DEPARTAMENTO DE ASTROFÍSICA

Universidad de La Laguna

# *Studying the outermost regions of galaxies to constrain their formation*

Memoria que presenta
Ignacio Martín-Navarro
para optar al grado de
Doctor por la Universidad de La Laguna.


INSTITUTO Đ ASTROFISICA Đ CANARIAS
octubre de 2015

Examination date: Noviembre, 2015
Thesis supervisor: Dr. Alexandre Vazdekis

*A Alejandro, Jesús y Nacho.*

# Agradecimientos

Querido lector, aunque probablemente esta sea la única sección que te leas entera, espero por lo menos que le eches un ojo a las conclusiones, créeme que son más interesantes. Sin más, quiero agradecer primero y sobre todo a Alejandro Vazdekis. Cualquier frase que diga para contar lo que le debo sería seguro insuficiente. Al contrario que nuestras interminables reuniones seré breve, gracias Alejandro. Quiero agradecer también al que ha sido referente y látigo durante estos cuatro años, Nacho Trujillo, aunque la versión 2.0 parece que no ha llegado a superar a la primera, o sí. Creo que mi mayor suerte ha sido llegar a conocer dos puntos de vista y maneras de trabajar tan distintas como la de ustedes. Gracias a los dos. Y el último de los tres pero probablemente más importante, a Jesús Falcón-Barroso, que me enseñó que se puede ser un gran investigador y llevar una vida normal. Creo Jesús que no te podré agradecer nunca lo suficiente. Dar las gracias a Mike Beasley, porque la ciencia de verdad se hace fuera de los focos. Desde luego, a Francesco La Barbera, por los ánimos, los consejos, los miles de e-mails, por todo. Muchas gracias Francesco. A Ignacio Ferreras, el último de los responsables de toda la locura de estos tres últimos años. Si pudiera elegir a un investigador en quién convertirme con los años, sería sin duda él. A Mariya Lyubenova, por cuidarme y enseñarme con un café en la mano. A Glenn van de Ven, porque aunque me siga dando miedo hablar con él, siempre merece la pena el mal trago. A Patricia Sánchez-Blázquez y a Javier Cenarro porque han sido modelos a seguir, con la suerte de poder contar con ellos. A Pablo Pérez-González por abrirme el universo a alto $z$ y por enseñarme como comunicar los resultados. A Sebastián Sánchez, por los dolores de cabeza que te hemos dado. A Evencio Mediavilla y a Clara Régulo, por no desesperar con nuestras prisas. Mención especial también para editores y referees de Nature, por descubrirme todos y cada uno de los problemas inherentes a la síntesis de poblaciones estelares; no creo que fuera esa su intención pero hemos aprendido mucho en el camino. A mis referentes en el mundo de las poblaciones estelares, R. Peletier, G. Worthey, S. Faber, C. Conroy, A. Renzini... porque solo se llega lejos si se apunta alto. A Jean Brodie y a Aaron Romanowsky, por confiar en mí. Quisiera por último darles las gracias a Lourdes y a Eva, esta tesis y el IAC hubieran colapsado sin ellas.

Agradecer el apoyo callado de mi familia. A mi madre y a mi padre, por aguantar sin preguntar (mucho) mis malos humores los fines de semana. Gracias sister por estar siempre ahí. A Jorge, profesor y compañero de estrellas, por encender, cuidar y alimentar la llama. A la vieja guardia, porque a veces sobran buenas palabras en el mundo y el insulto puede ser un abrazo. A Mar y a Pau, mis lolos de cabecera, por estos tres últimos años; por las acampaditas

en Guaria, por Comando 25 y por La Silla. Gracias. Para ti Marja, creo que no te haces una idea de lo que me has ayudado a ser quién soy ahora mismo. Te debo una vida. Peralta, guapo, sabes que esto es gran parte tuyo, creo que podrías ser coautor (o por lo menos defender) cada uno de los artículos de esta tesis. Gracias Bea, por ser hermana y madre estos años. Víctor, Javi, Paulo, Andreas, Rosa, Laura, Saras, Alba, a ustedes como los quiero menos, los pongo juntos. A Irantzu por el café de las mañanas; a Marins y a María por la suerte de haberlas conocido. A Mela, que se subió tarde (como no) en el tren pero que le ha dado color a este último año. A mis cordadas, Alberto, Eneko, Pablo y Carlos, por los encadenes y las comidas en el bar de Antonio. A Antonio. Gracias en general a todos los que han contribuido a allanar este camino y a todos los que he podido conocer en él; esto es solo el principio.

Summary

The properties of the stellar populations within galaxies contain important information about how they formed and evolved. In this thesis we study the stellar content of the two most characteristic morphological types, namely spiral and early-type galaxies, in order to understand their formation path. In particular, we make use of the radial variations in their relevant structural, kinematical and stellar population parameters. The study of these radial gradients provide deep insights into the physical processes driving galaxy evolution. Among all the explored parameters, we paid special attention to the stellar initial mass function. It determines the mass spectrum of stars at birth, and it is crucial to understand the chemical evolution of galaxies, to determine their masses, and to interpret $z \sim 0$ observations. Being a key and virtually unconstrained parameter in modern Astrophysics, it is necessary to characterize the IMF behaviour in different environments.

To observationally investigate the formation and evolution of galaxies we have made use of a wide variety of data and techniques. The study of the radial light distribution of spirals is based on photometric data from the Sloan Digital Sky Survey and from the *Spitzer* Survey of Stellar Structure in Galaxies. For studying the stellar population properties of early-type galaxies, we have analyzed spectroscopic data acquired with 10-meter class telescopes, integral field spectroscopy from the CALIFA survey and slit-less data obtained with the Hubble Space Telescope. The high quality of both spectroscopic and photometric data sets allows us to investigate the outer regions of nearby galaxies in great detail, and to probe the properties of galaxies at high ($z \sim 1$) redshift. To derive stellar population properties, these data were compared to state-of-the-art stellar population synthesis models using different techniques, from spectral energy distribution fitting to the detailed analysis of line-strength indices, including also full spectral fitting.

We find that breaks and truncations previously reported in face-on and edge-on spirals, respectively, are two different phenomena. Both of them can simultaneously coexist in the same spiral galaxy, and it is because a projection effect that truncations are not observed in face-on galaxies. We propose a simple *stellar disk plus halo* model that can explain at the same time all face-on and edge-on observations.

Regarding the stellar population of early-type galaxies, we find that the stellar initial mass function is a local property. This increases the existing tension between the commonly accepted assumption of a universal initial mass function and observations of massive early-type galaxies. Moreover, by analysing the stellar population gradients of the massive relic galaxy NGC 1277, we find

that the local velocity dispersion is not the main driver behind the stellar initial mass function variations, in contrast to the recently reported relation between central velocity dispersion and initial mass function slope. We use a sample of early-type galaxies from the CALIFA survey to better characterize the behaviour of the initial mass function, finding that its slope is tightly related to the total metallicity of the underlying stellar population. Deep implications would follow an initial mass function – metallicity relation. In particular, it predicts a flat slope during the first Myrs of galaxy formation, while the rapid initial metal enrichment of the galaxy was taking place. This early phase would be then followed by second stage regulated by a steeper initial mass function. By analysing a sample of high redshift galaxies, we confirm that, at $z \sim 1$, the initial mass function of massive galaxies was indeed as steep as in the local Universe, following the same trend with galaxy mass.

With this thesis we have reinforced an emerging picture of the formation and evolution of massive galaxies. Their central regions are proposed to be the result of an early monolithic-like collapse, which would explain the tight scaling relations and the enhanced abundance pattern observed in nearby objects. Later, the accretion of smaller structures contributed to the build-up of the outskirts of more massive objects, effectively altering their radial gradients. The combination of these two processes would naturally explain the bulk of the observations, reconciling the advantages of hierarchical and monolithic models of galaxy formation. This emerging picture will be tested and refined in the upcoming years by better and more extended observations, complemented with more detailed high-redshift measurements.

## Resumen

Las poblaciones estelares son una valiosa fuente de información acerca de cómo las galaxias se forman y evolucionan. En esta tesis nos centraremos en el estudio de los dos tipos morfológicos más característicos, esto es, las galaxias espirales y las de tipo temprano, con el fin de entender sus procesos de formación. En particular, prestamos especial atención al estudio de las variaciones radiales en distintas propiedades de las galaxias, tanto estructurales, como cinemáticas y poblacionales, ya que estos gradientes aportan importantes pistas acerca de los procesos que gobiernan la evolución galáctica. De entre todos los parámetros considerados, tiene un papel fundamental estudio de la función inicial de masa. Esta determina el espectro de masas de las estrellas en el momento de su formación y es un ingrediente clave para entender la evolución química de las galaxies, para determinar su masa y para interpretar las observaciones en el universo local. Siendo un parámetro tan importante y observacionalmente poco entendido, es necesario caracterizar su comportamiento en distintos entornos.

A la hora de investigar la formación y evolución de las galaxias, hacemos uso de un variado conjunto de datos y técnicas. Por un lado, el estudio de los perfiles de brillos en galaxias espirales se basa en los datos fotométricos de los cartografiados Sloan Digital Sky Survey y *Spitzer* Survey of Stellar Structure in Galaxies. Para el estudio de las poblaciones estelares en galaxias de tipo temprano hemos analizado datos obtenidos con telescopios de gran diámetro, datos de espectroscopía de campo integral del cartografiado CALIFA y espectros del telescopio espacial Hubble. La calidad de datos, tanto de los fotométricos como de los espectroscópicos, nos permite estudiar en gran detalle las regiones más externas en galaxias cercanas, así como explorar las características de las galaxias a alto desplazamiento al rojo ($z \sim 1$). Con el fin de derivar las propiedades de las poblaciones estelares, hemos hecho uso de los modelos de síntesis de poblaciones estelares más avanzados hasta la fecha, comparándolos con los datos mediante distintas técnicas que incluyen desde el ajuste de distribuciones espectrales de energía hasta el análisis detallado de índices espectrales, pasando también por ajustes al espectro completo de las galaxias.

Encontramos que los *breaks* y truncamientos, previamente detectados en galaxias espirales vistas de frente y de canto, respectivamente, son en realidad fenómenos distintos. Ambos pueden existir de manera simultánea en una misma galaxia y es únicamente un efecto de proyección lo que evita que veamos truncamientos en espirales vistas de frente. Así mismo, proponemos un modelo simple, consistente en un disco y un halo estelar, que permitiría explicar al mismo tiempo las observaciones tanto de galaxias vistas de canto y como vistas de frente.

En lo que respecta a las poblaciones estelares en galaxias de tipo temprano, encontramos que la función de masa estelar es una propiedad local. Este hecho incrementa la tensión existente entre la comúnmente aceptada suposición de una función inicial de masa universal y las observaciones de galaxias masivas de tipo temprano. Además, el análisis de los gradientes en las poblaciones estelares de la galaxia masiva NGC 1277 demuestra que no es la dispersión de velocidades local lo que determina las variaciones en la función inicial de masa, hecho que contrasta con resultados recientes que sugieren una relación entre la dispersión de velocidades central de las galaxias y la pendiente de la función inicial de masa. Así mismo, usamos una muestra de galaxias de tipo temprano del cartografiado CALIFA para caracterizar las variaciones en la función inicial de masa, encontrando que el valor de su pendiente está altamente correlacionado con la metalicidad total de la población estelar subyacente. Las implicaciones que una relación entre función inicial de masa y metalicidad tendría en la formación y evolución de las galaxias son críticas. En particular, predeciría una pendiente plana en los primeros mega-años de la formación de las galaxias, durante el enriquecimiento químico inicial. A esta primera fase seguiría una segunda etapa de formación estelar regulada por una función inicial de masa con pendiente más pronunciada. Analizando una muestra de galaxias a alto desplazamiento al rojo, hemos comprobado que efectivamente, a $z \sim 1$, la función inicial de masa era ya tal y como se observa en el Universo local, obedeciendo la misma misma relación con la masa de la galaxias.

Con esta tesis hemos contribuido a reforzar una nueva imagen de la formación y evolución de las galaxias masivas. En ella, las regiones centrales de las galaxias masivas serían el resultado de un colapso monolítico inicial, lo cual explicaría las relaciones de escala y el patrón de abundancias químicas observado en el Universo local. Posteriormente, el acrecimiento de estructuras más pequeñas habría contribuido al ensamblaje de las partes externas de galaxias más masivas, afectando con ello a sus gradientes radiales. La combinación de estos dos procesos explicaría de manera natural la mayoría de las observaciones, reconciliando las ventajas que los modelos jerárquicos y monolíticos ofrecen para explicar la formación de galaxias. En el futuro, esta idea será puesta a prueba y refinada mediante observaciones más precisas y completas en el universo cercano, así como medidas cada vez más detalladas a alto desplazamiento al rojo.

# Contents

# List of Figures

# List of Tables

# 1

# Introduction

*Las estrellas para quien las trabaja*
J. C. Mestre

## 1.1 Scientific motivation

Since first appeared in the early ($z \sim 10$) Universe, galaxies have formed and evolved following various channels. The different physical processes driving the formation and evolution of galaxies leave measurable imprints, being the aim of this thesis to observe, characterize and understand them.

Observationally, galaxy evolution can be investigated in two ways. On the one hand, observations of galaxies can be made at all redshifts, probing *in situ* their properties while evolving. A clear advantage of this approach is that evolution can be traced without any assumption, but only based on measurements at different redshifts. However, obtaining deep enough data at high redshift is observationally challenging and expensive. In addition, galaxy evolution can only be studied through snapshots of the Universe at different redshifts, but in principle it is not warranted a causal connection between consecutive redshift measurements. This inherent limitation to trace back the evolution of individual objects has to be always taken into account while interpreting high redshift observations. Alternatively, a detailed analysis of the properties of nearby galaxies can be used to infer their evolutionary path. The main advantage of this so-called *galactic archaeology* is that high-quality data can be compared in detail with model predictions, and therefore, a precise understanding of the

physical mechanisms shaping galaxy evolution can be obtained. The obvious disadvantage of this method is that many physical processes could lead to the same, or very similar, properties of galaxies at $z \sim 0$. To break this degeneracy in the nearby Universe, usually strong assumptions have to be made to interpret observations. This thesis is mostly based on this latter *archaeological* approach, but with brief incursions to the high redshift Universe.

Favoured by the advent of numerical simulations, the Λ-Cold Dark Matter (CDM) paradigm has become the leading interpretative framework for galaxy formation and evolution (Springel et al. 2005). Within the Λ-CDM context, once matter decoupled from radiation, baryons started to fall onto pre-existing dark matter halos (Navarro et al. 1997) forming the first stars and galaxies. Then, consecutive mergers of these dark matter halos and baryons built up larger structures, and in particular, galaxies. Therefore, within this paradigm, the observed properties of galaxies at $z \sim 0$ are the result of this hierarchical, bottom-up formation scheme, where more massive galaxies would emerge from the fusion of smaller components (White & Rees 1978). The Λ-CDM framework has been very successful at explaining a wide variety of observations, from the large scale structure of the Universe to its primordial chemical composition. However, it faces important challenges in the nearby Universe, some of them particularly tied to the aim of this thesis. Since most massive galaxies are the result of a continuous process of mergers, a naive expectation from this hierarchical scenario is that they should be younger and with more extended formation histories than low-mass galaxies. However, observations in the nearby Universe undoubtedly show the opposite: massive galaxies are old and have experienced very short formation events (Vazdekis et al. 1997; Thomas et al. 2005). Moreover, a purely hierarchical formation scenario is unable to explain the tight scaling relations observed a $z \sim 1$ (Blakeslee et al. 2003), and the stellar population properties of nearby dwarf galaxies are not consistent with being the building blocks of local massive galaxies (Ryś et al. 2015). To reconcile this apparent inconsistency between theory and observations, various recipes have been proposed to model the physics of baryons within galaxies(De Lucia et al. 2006), including active galactic nucleus (Di Matteo et al. 2005) and stellar (Conroy et al. 2015) feedback. However, state-of-the-art numerical simulations still fail to reproduce well-established observational results involving complex baryonic processes such as star formation (Schaye et al. 2015; Genel et al. 2014).

Aiming a comprehensive understanding of the formation an evolution of galaxies, this work is focused on the two most relevant morphological types: spiral and early-type (ETG) galaxies. Whereas the first constitute the most common morphology in the local Universe, the bulk of the stellar mass is con-

tained in the latter (Conselice et al. 2004). The clear morphological separation between spiral galaxies and ETGs arises from two completely different formation mechanisms, ultimately determined by the amount of gravitational binding energy dissipated in the process. If energy dissipation dominates the collapse of the protogalactic cloud, stars will form within a *cold* structure (Silk 1977), leading to the formation of rotationally supported spiral galaxies. On the contrary, if star formation surpasses energy dissipation, most of the stars will be formed before the collapse takes place. Since stars can not efficiently dissipate their kinetical energy, such a dissipationless channel for galaxy formation will result into a *hot* ETG, dominated by the random motions of the individual stars (Larson 1974).

Observationally, these two formation mechanisms translate into significant differences between ETGs and spiral galaxies. In ETGs, the radial light distribution decays approximately as $r^{\frac{1}{4}}$, following the so-called de Vaucouleurs (de Vaucouleurs 1948) profiles, and their internal kinematics is dominated by the stellar velocity dispersion. In contrast, spiral galaxies exhibit prominent rotation curves, with surface brightness profiles reasonably well represented by one or more exponential disks (Freeman 1970). Differences between ETGs and spirals are also obvious while analyzing their stellar population properties. Whereas in the local Universe ETGs are old, passively evolving systems, spiral disks are young and star-forming. These differences in the stellar population content of spiral and ETGs are schematically represented the color–galaxy mass diagram shown in Fig. 1.1: ETGs constitute a separated *red sequence*, while spiral galaxies gather around the so-called *blue cloud*.

Despite of the clear differences between spirals and ETGs, both morphological types share important similarities. Historically, the merger of two spiral galaxies has been thought to be a major channel for the ETG formation. Although this scenario struggles to reproduce some observed scaling relations such as the [Mg/Fe]–galaxy mass (Peletier 1989; Worthey et al. 1992), it is in agreement with the decreasing number of ETGs with increasing redshift. Moreover, it is a natural way of transforming the angular moment of a system into the random motions of stars (pressure) that support ETGs. In fact, when both rotation velocity and velocity dispersion are taken into account, ETGs and spirals unify into a continuous sequence as a function of $\sqrt{V^2 + 2\sigma^2}$, as shown in Fig. 1.2. From the point of view of the stellar populations, some properties of the outskirts of ETGs are remarkably similar to spiral galaxies. In particular, the old and metal-poor stars of the Milky Way halo are consistent with measurements of the outer parts of nearby ETGs (Sánchez-Blázquez et al. 2007). Therefore, although the central parts of both spirals and ETGs might represent two extreme examples of how galaxies formed, the analysis of their

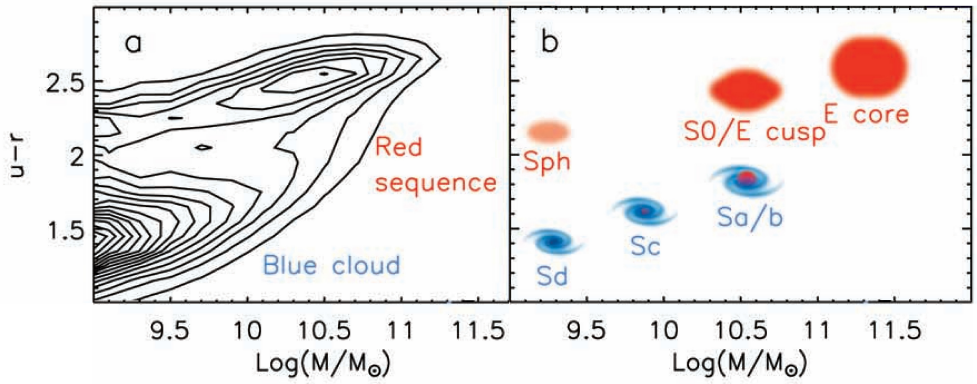


Figure 1.1: Color–galaxy mass relation, adapted from Kormendy & Bender (2012). The old stellar component of ETGs translates into red colors, and therefore ETGs mainly populate the red sequence. On the contrary, young stars dominating the light spiral galaxies ultimately lead to the formation of the blue cloud. Notice that, apart from the age effect, the final distribution of galaxies in a color-galaxy mass diagram depends also on the galaxy mass–metallicity relation.

radial gradients suggest a much richer formation picture, where star formation and accretion shape the observed properties of nearby galaxies. Recently, numerical simulations have suggested that the competing effect of *in situ* and *ex situ* formed stars results into a two-stages galaxy formation scenario (Oser et al. 2010; Navarro-González et al. 2013), where the properties of the inner regions of galaxies are driven by internal processes but their outskirts are determined by latter accretion of external material.

Therefore the study of the stellar population properties, and in particular of their radial gradients, appears as a promising route to understand and constrain the formation and evolution of nearby galaxies. Within the Λ-CDM framework, small structures, because of differences in density, will be deposited in the outskirts of more massive galaxies, effectively altering the pristine gradients. The comparison between observed and simulated stellar population properties has raised concerns on how the star formations is numerically treated Cole et al. (1994); Somerville et al. (2001). Moreover, the radial variations in the stellar population properties can be also used to determine the speed and effectiveness of star formation within galaxies (Pipino & Matteucci 2004; Kobayashi 2004), the degree of energy dissipation (Bekki & Shioya 1998; Naab et al. 2009), and the properties of the interstellar meduin (ISM) from where stars were formed. Finally, a proper characterization of the radial gradients will not only help to

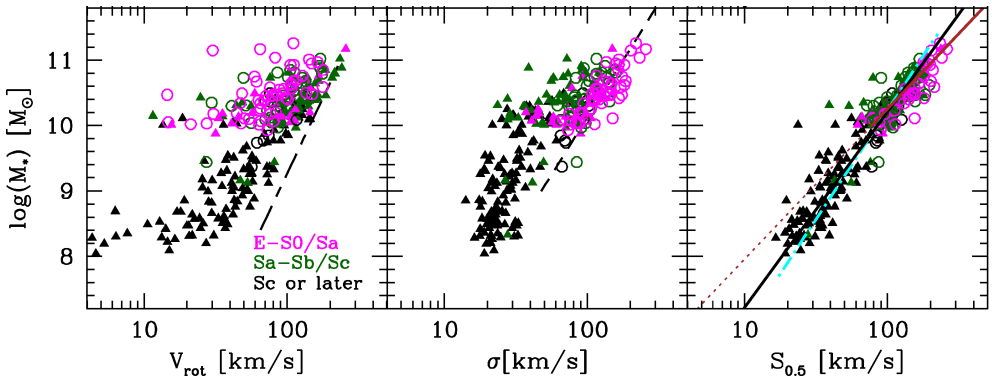


Figure 1.2: Galaxy mass as a function of different kinematical quantities, from Cortese et al. (2014). The differences in the kinematics between early and late type galaxies disappear when both rotation velocity ($V_{rot}$) and velocity dispersion ($\sigma$) are considered, in this case in the form of the $S_{0.5}$ parameter ($S_{0.5} = \sqrt{0.5V_{rot}^2 + \sigma^2}$). The fact that both spirals and ETGs share the same scaling relation (right panel) suggests some similarities in their formation processes.

understand the *ex situ* vs *in situ* star formation question, but given the similar properties of their outskirts, it will also allow to investigate the connection between spirals and ETGs since they were formed.

How did ETGs and spirals formed? Did they emerge from completely independent processes or are they extreme cases of a continuous mode of galaxy formation? Are ETGs the result of a pure monolithic collapse in the early Universe? What is the role of mergers in shaping the observed properties of nearby galaxies? To address these fundamental questions, in this thesis we have investigated the stellar population properties of ETGs and spiral galaxies, both locally and at high redshift, paying special attention to their radial gradients. The apparent simplicity of the stellar populations in ETGs allowed us to perform a detailed analysis of their properties based on the analysis of their spectral features. In contrast, the stellar populations in spiral galaxies are complex, with a mixture of young and old populations and extended star formation histories. Moreover, the effect of gas emission, dust absorption and integration along the line of sight (which can be dominant in highly asymmetric systems like spiral galaxies) highly complicates a precise stellar population analysis. Thus, we used the photometric structure of spiral galaxies as a first-order proxy to investigate their formation history. In the future, deep spectroscopic information will be analysed to complement the results derived in this thesis. In the following subsections, a more detailed introduction will be provided for the luminous structure of spiral galaxies (§ 1.1.1) and for the stellar population

characteristics of ETGs (§ 1.1.2), describing the different observational and interpretative scenarios.

### 1.1.1 Spiral galaxies

Since the radial light distribution of spiral disks decays roughly in an exponential manner, their light is not as concentrated as in ETGs and it is easier to explore larger radii. Although the central regions of spirals do not differ much from their outskirts, either due to secular evolution or to the early collapse, spheroid-like structures are usually detected in their centers. These bulges (and pseudo-bulges) are usually dominated by an old stellar population, similar to the cores of ETGs. Also, because of disk instabilities, bars are observed in the central regions of spiral galaxies bar-like, affecting also the inner structure of the disk.

Away from their very central regions, the vast majority of spiral galaxies do not follow a radial surface brightness decline mimicking a perfect exponential law as proposed by Patterson (1940); de Vaucouleurs (1958) & Freeman (1970). Depending on the shape of the surface brightness distribution, a classification for face-on galaxies has been developed by Erwin et al. (2005) and Pohlen & Trujillo (2006). It distinguishes three different types of profiles. Type I (TI) is the classical case, with a single exponential describing the entire profile; Type II (TII) profiles have a downbending brightness beyond the break. Type III (TIII) profiles are characterized by an upbending brightness beyond the break radius. Relative frequencies for each type are 10%, 60% and 30% (Pohlen & Trujillo 2006) in the case of late-type spirals.

Photometric studies of TII galaxies reveal that the radial scalelength of the surface brightness profiles changes when a characteristic radius ($\sim$10 kpc) is reached. This so called break radius is described in several studies of face-on galaxies (Erwin et al. 2005; Pohlen & Trujillo 2006; Erwin et al. 2008) and is also found if galaxies are observed in edge-on projections (van der Kruit & Searle 1982; de Grijs et al. 2001; van der Kruit 2007). Using faint magnitude stars, Ferguson et al. (2007) found also a break in the surface brightness profile of M 33. On the contrary, no break was detected by star counting neither in NGC 300 (Bland-Hawthorn et al. 2005; Vlajić et al. 2009) nor in NGC 7793 (Vlajić et al. 2011). Works on galaxies beyond the nearby Universe (Pérez 2004; Trujillo & Pohlen 2005; Azzollini et al. 2008) show the presence of a break at redshifts up to $z \sim 1$. These results suggest that breaks, once formed, must have been stable for the last 8 Gyrs of galaxy evolution. Cosmological simulations (Governato et al. 2007; Martínez-Serrano et al. 2009) as well support the idea of a break in the light distribution of disk galaxies.

Different mechanisms explaining the origin of TII breaks have been proposed. All those theories can be sorted into two families. A possible scenario is that the break could be located at a position where a threshold in the star formation occurs (Fall & Efstathiou 1980; Kennicutt 1989; Elmegreen & Parravano 1994; Schaye 2004; Elmegreen & Hunter 2006). A change in the stellar population would thus be expected at the break radius, but not necessarily a downbending of the surface mass density profile as shown by some simulations (Sánchez-Blázquez et al. 2009; Martínez-Serrano et al. 2009). Supporting this, Bakos et al. (2008) found that in a sample of 85 face-on galaxies (see Pohlen & Trujillo 2006), the $(g' - r')$ Sloan Digital Sky Survey (SDSS) color profile of the TII galaxies is, in general, U-shaped, with a minimum at the break radius, hinting at a minimum also in the mean age of the stellar population at the break radius. This is in agreement with studies on resolved stellar populations across the break (de Jong et al. 2007; Radburn-Smith et al. 2012a). Furthermore, the surface mass density profile recovered from the photometry shows a much smoother behavior, in which the break is almost absent compared to the surface brightness profile. Numerical simulations (Debattista et al. 2006; Roškar et al. 2008; Sánchez-Blázquez et al. 2009; Martínez-Serrano et al. 2009) reveal how the secular redistribution of the angular momentum through stellar migration can drive the formation of a break. In the papers of Roškar et al. (2008) and Sánchez-Blázquez et al. (2009), a minimum in the age of the stellar population is found at the break radius, in agreement with the results of Bakos et al. (2008). It is also remarkable that the mean break radius in the simulations of Roškar et al. (2008) is very close (2.6 $h_{\rm r}$) to the observational result (2.5±0.6 $h_{\rm r}$) measured by Pohlen & Trujillo (2006), where the values are given in radial scalelength units ($h_{\rm r}$). However, van der Kruit & Searle (1982) showed that the Goldreich-Lynden-Bell criterion for stability of gas layers offered a poor prediction for the truncation radius in their sample of edge-on galaxies. Focusing on these high inclined galaxies, van der Kruit (1987, 1988) proposed an alternative scenario where the break could be related to the maximum angular momentum of the protogalactic cloud, leading to a break radius of around four or five times the radial scalelength. This mechanism would also lead to a fast drop in the density of stars beyond the break. Observations of edge-on galaxies, such as those by van der Kruit & Searle (1982), Barteldrees & Dettmar (1994) or Kregel et al. (2002), place the break at a radius around four times the radial scalelength, supporting this second explanation.

There is a clear discrepancy between the positions of the breaks located in the face-on view compared to those breaks found in the edge-on perspective. In the face-on view, the breaks are located at closer radial distances of the center than in the edge-on cases. Are the two types of breaks the same phenomenon?

On the one hand, the edge-on observations tend to support the idea of the maximum angular momentum as the main actor in the break formation. On the other hand, face-on galaxies, supported by numerical simulations, favor a scenario where the break is associated with some kind of threshold in the star formation along the disk. Only a few studies have attempted to give a more global vision of the problem (Pohlen et al. 2004, 2007) by deprojecting edge-on surface brightness profiles. Pohlen et al. (2007) and Comerón et al. (2012) found that the classification exposed at the beginning of the current chapter into TI, TII and TIII profiles is basically independent of the geometry of the problem. Consequently, the difference between the position of the break radius obtained from the edge-on galaxies and the one from the face-on galaxies can not be related to the different inclination angle. More details on the current understanding of breaks and truncations can be found in the review by van der Kruit & Freeman (2011, §3.8).

### 1.1.2 Early-type galaxies

There is a clear observational connection between the dynamics, structure and stellar population properties of ETGs, e.g., as suggested by the color-magnitude relation (Bower et al. 1992) and the fundamental plane (Bender et al. 1992). In addition, ETGs have been traditionally considered as landmarks for the stellar population analysis since, unlike other morphological types, they are well represented by simple star formation histories. Observations suggest that ETGs harbour old and metal-rich populations, with more massive systems being older and more metallic than low-mass ETGs (e.g. Renzini 2006). The study of absorption lines in the spectrum of ETGs has also revealed a tight correlation between the strength of Mg absorption features and galaxy velocity dispersion or luminosity (Bender et al. 1993; Worthey & Collobert 2003), which has been interpreted as an increasing $\alpha$-elements to iron ratio with increasing galaxy mass (Worthey et al. 1992; Thomas et al. 1999).

Over the last years, and thanks to large enough telescopes and accurate stellar population synthesis models, a fundamental quantity has been probed for the first time in nearby ETGs: the stellar initial mass function (IMF), which characterises the distribution of stellar masses at birth in star forming regions. The IMF is therefore a crucial ingredient of galaxy formation and evolution. It sets the mass-scale of galaxies, determining their (stellar) mass-to-light ratio, and drives stellar feedback as well as chemical enrichment into the ISM.

While resolved stellar population studies support the idea of an invariant IMF in environments with quite different local properties such as metallicity or density (Kroupa 2002; Bastian et al. 2010; Kroupa et al. 2013); recent studies

of ETGs, based on both dynamics (Cappellari et al. 2012; Thomas et al. 2011b; Wegner et al. 2012; Dutton et al. 2013; Tortora et al. 2013) and stellar populations (Saglia et al. 2002; Cenarro et al. 2003; van Dokkum & Conroy 2010; Spiniello et al. 2012; Ferreras et al. 2013; La Barbera et al. 2013) have found that the IMF varies with galaxy mass. The same result has also been obtained by a combination of gravitational lensing and dynamical studies (Treu et al. 2010; Auger et al. 2010, but see Smith & Lucey 2013). In particular, dynamical studies have found a significant increase of the stellar mass-to-light ratio, with respect to that expected for a "standard", Milky-Way-like IMF, towards high-mass systems. The analysis of gravity-sensitive features in the integrated spectra of ETGs has revealed that this trend in the "normalization" of the IMF is driven by an increase of the fraction of dwarf-to-giant stars, i.e. a change towards steeper IMF slopes with higher velocity dispersion (Cenarro et al. 2003; Falcón-Barroso et al. 2003; Cappellari et al. 2012; Ferreras et al. 2013; La Barbera et al. 2013, hereafter LB13). Although some discrepancies can be found between dynamical and stellar population studies, the agreement is remarkable, considering the fundamental differences of both approaches (Smith 2014).

## 1.2 Data types

Because of the broad goals of this thesis, three different type of data have been used, always focused on the study of the dim structures, either locally or at high redshift.

### 1.2.1 Photometry

Chapters 2 and 3 are based on photometric data from the Sloan Digital Sky Survey (Abazajian et al. 2009) and from the *Spitzer* Survey of Stellar Structure in Galaxies (Sheth et al. 2010). Compared to spectroscopic data, the use of broad band photometry allows us to probe much fainter regions with minimum observational cost. For example, with a 10-meter class telescope, less than one minute is necessary to photometrically reach a surface magnitude of $\mu \sim 26$ mag arcsec$^2$, whereas the same surface brightness can only be reached after 20 hours of (intermediate resolution) spectroscopic integration. In contrast, the capacity of broad band colors to retrieve stellar population information is limited, being dominated by the age-metallicity degeneracy (Worthey 1994), as shown in Fig. 1.3. Therefore, deep photometry is a powerful tool to investigate extremely dim features, but without great detail in terms of stellar population properties. It is usually employed as a zero-order proxy, before the use of more accurate, but observationally more expensive, spectroscopic data. Since breaks

and truncations in spiral galaxies occur at very low surface brightness ($\mu \sim 26$ mag arcsec$^2$), the use of photometric data was the natural choice, while waiting for deep enough spectra.

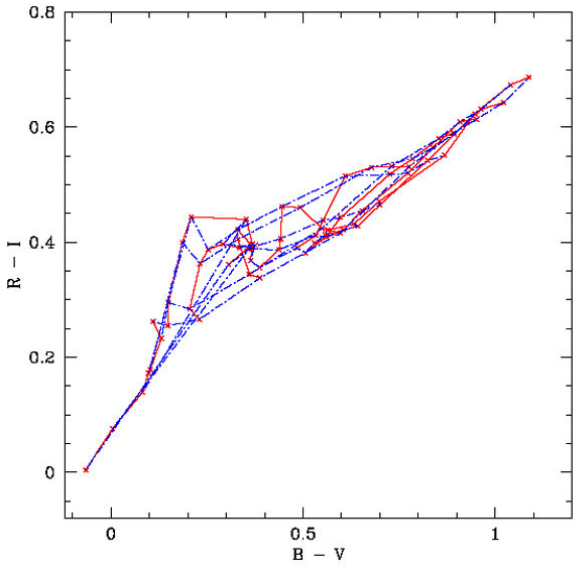


Figure 1.3: Color–color diagram for a grid of single stellar populations (SSPs) with different ages and metallicities, based on the MILES models (Vazdekis et al. 2010). The age-metallicity degeneracy is clear, and becomes more significant for old and metal-rich populations (top right corner of the diagram), as expected in the central parts of ETGs. Figure from Peletier (2013).

### 1.2.2 Long-slit spectroscopy

Whereas broad band photometry is only sensitive to spectral variations in scales of a few hundred Å, the use of medium or high resolution spectroscopic data probes much finer spectral features which partially breaks the degeneracies between the different stellar population parameters. In particular, Fig. 1.5 shows how a careful selection and comparison of different line-strength indices provides a much orthogonal model grid than a color-color diagram (Fig. 1.3). This clear advantage over photometry has been exploded over the last 30 years to investigate the stellar populations of nearby galaxies. However, as stated above, it is observationally expensive and only recently, the development of new telescopes and facilities has allowed us to spectroscopically probe local galaxies beyond their effective radius (Sánchez-Blázquez et al. 2007; Roediger et al. 2012).

Moreover, to measure the subtle IMF effect on long-slit data, we require a signal-to-noise ratio $\sim 100$ per Å. A proper analysis of longs-slit data is further complicated by the presence of strong emission and absorption telluric features in the optical wavelengths. Thus, not only long exposures in large telescopes are needed, but also careful observational strategies and intermediate-to-high ($R \sim 2000$) spectral resolution to clean the observed spectrum from telluric contamination. The typical absorption and emission telluric spectrum in the red end of the optical wavelength range are shown in Fig. 1.4. For this purposes of this thesis, the telluric contamination is particularly relevant beyond $\lambda \sim 8000$ Å, where the most important IMF sensitive features (like the NaI 8190 and the CaT lines) appear in heavily contaminated regions.

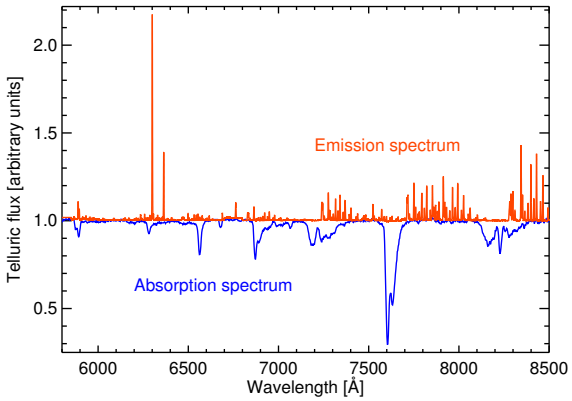


Figure 1.4: Typical emission (red) and absorption (blue) telluric spectra. Beyond $\lambda \sim 600$ nm, stellar population sensitive features appear in spectral regions dominated by telluric contaminations. To overcome this problem, it is mandatory the use of intermediate-to-high resolution spectrographs to properly clean the data.

Therefore, in order to investigate the stellar population properties of nearby ETGs, in this thesis we made use of extremely deep long-slit data acquired with the Gran Telescopio Canarias (GTC). These high quality data facilitated the derivation of precise stellar population parameters up to the effective radius, and kinematical measurements reaching two effective radii. Apart from its observational cost, long-slit data present an inherent limitation: the lack of two dimensional spatial information. Because of the use of a narrow slit to increase the spectral resolution, only spatial information along the slit is conserved. Thus, the symmetry of the source plays a crucial role. For example, a slit perpendicular to an edge-on spiral will probe completely different properties

than if placed along the disk.

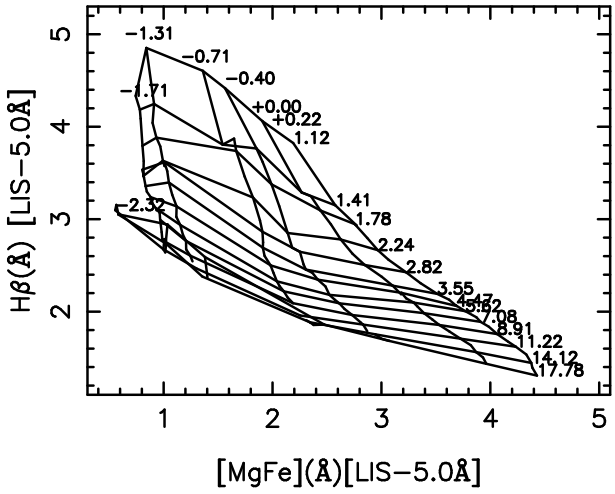


Figure 1.5: Index–index ($H_\beta$–[MgFe]) diagram for a grid of SSPs with different ages and metallicities, from (Vazdekis et al. 2010). In contrast to Fig. 1.3, the iso-age (∼horizontal) and iso-metallicity (∼vertical) lines are almost orthogonal, minimizing the effect of the age–metallicity degeneracy. The analysis of spectroscopic data is therefore crucial for detailed stellar population studies.

### 1.2.3 Integral Field spectroscopy

With two spatial and one spectral dimension, integral field spectroscopy (IFS) has become a popular alternative to the standard long-slit spectroscopy. Although both approaches share similar characteristics, the IFS spectroscopic offers two important advantages. First, because of the full spatial coverage (not limited to one dimension), no assumptions about the symmetry of the observed object have to be made. In this regard, IFS surveys as ATLAS$^{3D}$ (Cappellari et al. 2011) or CALIFA (Sánchez et al. 2012) have revealed an unexpected variety of kinematical and stellar population structures within nearby galaxies (Fig. 1.6). Second, and particularly relevant for the goals of this thesis, the radial binning of IFS data offers a significant increment in the signal-to-noise compared to the long-slit technique. In particular, at a radial distance $R$ from the centre of a galaxy, the signal-to-noise expected from an IFS is roughly a factor of $\sim \sqrt{2\pi R}$ larger. Therefore, IFS data can be used to probe the outskirts of nearby galaxies in a much more efficient way than the standard long-slit spectroscopy.

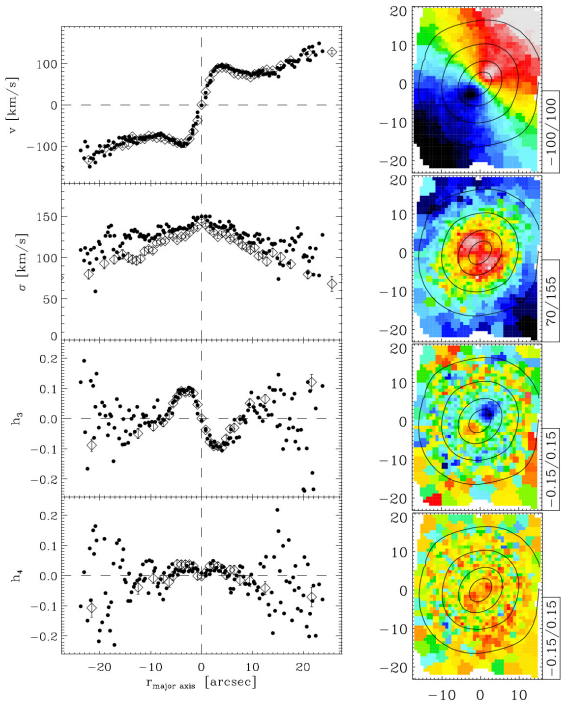


Figure 1.6: Comparison between the 1D- (long-slit) and 2D- (IFS) based kinematics of NGC 3385, from de Zeeuw et al. (2002) and Emsellem et al. (2004). The apparent simplicity of the one-dimensional maps contrasts with the kinematical complexity revealed by the IFS spectroscopy. Moreover, at the same radial distance, the IFS data allows to combine more information, which translates into an improved signal-to-noise ratio with respect to the long-slit approach. This greatly facilitates the study of the outermost regions of nearby galaxies.

The last chapter of this thesis is based on the aforementioned CALIFA IFS survey. These data were acquired using two different set-ups of the PMAS/PPAK integral field unit: the V500 and the V1200 gratings. Whereas the V500 configuration offers a wide wavelength range with a lower spectral resolution (best suited for the stellar population analysis), the V1200 grating has a higher resolution but in a narrower spectral range (ideal for kinematical measurements). The combination of these two gratings was crucial to accurately determine kinematical and stellar population parameters. Note that, in the outermost regions of galaxies, a large radial binning is necessary to achieve the required signal-to-noise ratio. Thus, precise kinematical measurements are needed to avoid

spurious line broadening due to different kinematics along one radial aperture.

## 1.3 Models and techniques

In this section we describe the models and techniques used during the thesis to determine stellar population parameters from photometric and spectroscopic data. Although a detailed description of the stellar population analysis is provided in particular for each chapter, here we present a brief introduction to the basic ingredients and concepts that will be use hereafter.

### 1.3.1 Models

To derive stellar population parameters from a given data set it is necessary to compare them with stellar populations models. To this end, two main approaches have been developed. On the one hand, the spectrum of a galaxy can be fitted by a unconstrained combination of stars drawn from a (stellar) spectral library (see e.g. O'Connell 1986). The main advantage behind these so-called empirical models is the fact that no assumptions are made on the star formation history or on the stellar evolution. However, the large number of degrees of freedom in the problem can lead to strong degeneracies in the recovered stellar population parameters. On the other hand, stars from the spectral library can be also combined attending to their position on the H-R diagram, following theoretical isochrones. This evolutionary approach relies on our (incomplete) knowledge about stellar evolution, but it significantly reduces the degeneracies in the inferred parameters. Thus, throughout this thesis, we base our analysis on this latter approach.

*Evolutionary* stellar population synthesis models

Evolutionary stellar population synthesis (SPS) models consist on three basic ingredients: the stellar spectral library, the isochrones and the IMF. For a given age, metallicity and abundance pattern, stellar evolution predicts the $\log g$–$\mathrm{T_{eff}}$ distribution of stars according to their masses, which can be translated into an observational plane following either empirical or theoretical prescriptions. The summation of the stellar spectra of this distribution, weighted by the IMF, results into a single stellar population (SSP) model, which is the basis of any SPS analysis. In other words, SPS models can predict the spectrum of an instantaneous star formation event, with a single metallicity and abundance pattern, for any given age. The basic scheme of a SPS model is show in Fig. 1.7, but it be further sophisticated to include dust attenuation, nebular gas emission

and extended star-formation histories. Although there are multiple flaws in this approach (e.g. poorly understood stellar evolutionary phases, unconstrained stellar structure parameters or non-canonical evolutionary tracks), SPS can be used in a wide range of ages and metallicities to investigate the stellar content of galaxies at all redshift.

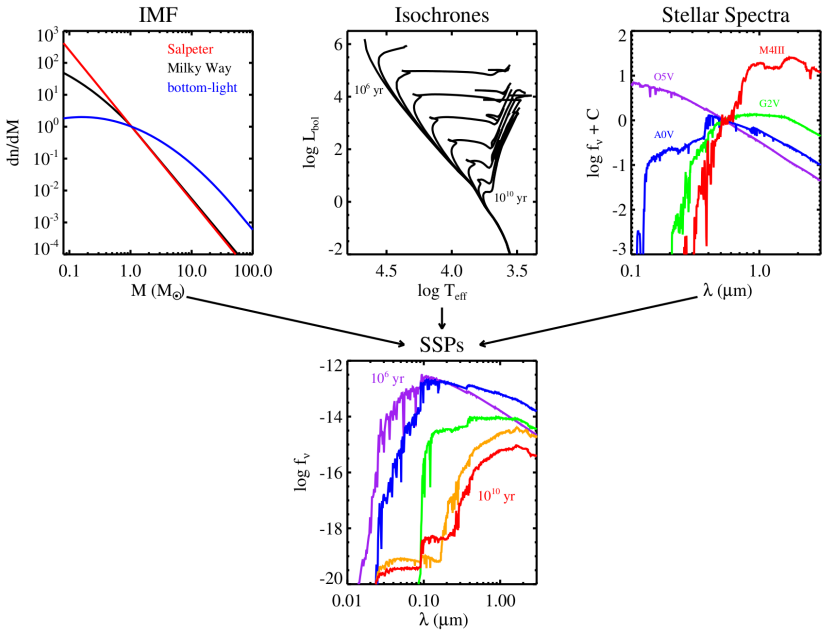


Figure 1.7: Basic scheme of an evolutionary SPS model, from Conroy (2013). Stellar spectra along an isochrone are combined, according to an IMF, to produce an SSP model. A major advantage of these models is the use of the stellar physics which, although introduces some uncertainties, greatly reduces the underlying degeneracies. in the determination of the stellar population parameters. The evolutionary SPS models have become the preferred option in most of current studies.

### The MILES models

From all the available models in the literature (e.g. Bruzual & Charlot 2003; Thomas et al. 2003; Conroy & van Dokkum 2012b), the bulk of the work of this thesis is based on the MILES models (Vazdekis et al. 2010, 2012). The MILES models are evolutionary stellar population synthesis models, and they make use of the empirical MILES stellar library (Sánchez-Blázquez et al. 2006). Four im-

portant characteristics make them well suited for the goals of this thesis. First of all, they rely on an empirical stellar library, which eliminates uncertainties due to failures in the modelling of theoretical stellar atmospheres. Second, they provide intermediate resolution spectra along a wide wavelength range, which facilitates the use of full-spectral fitting techniques (see below). Third, they are not limited to solar metallicity, being crucial to study the metal-poor outskirts of ETGs. Finally, they allow for IMF variations. This last point is particularly relevant for the purposes of the thesis.

MILES models and their extension to the near-IR (MIUSCAT) have a nominal resolution of 2.51Å along the whole wavelength range, i.e., from 3465Å to 9469Å, and they are accurately flux calibrated. The *base* MILES models follow the abundance pattern of the solar neighbourhood, which implies that metal-poor SSP predictions ([M/H]∼-0.4) are alpha-enhanced ([Mg/Fe]∼0.4). Although a new version of the MILES models allowing for abundance pattern variations has been recently released (Vazdekis et al. 2015), we stuck to the base models, avoiding then uncertain corrections based on theoretical stellar atmospheres.

The stellar initial mass function

Among the three ingredients to be considered in a SSP model, in this thesis we pay special attention to the IMF, where two main parametrization have been considered: unimodal and bimodal. In the unimodal or single power-law IMF, the number of stars per logarithmic mass bin is

$$\phi(\log m) \stackrel{\text{def}}{=} \frac{\mathrm{d}\mathcal{N}}{\mathrm{d}\log m} \propto m^{-\Gamma}$$

Motivated by the pioneering work of Salpeter (1955), the standard IMF slope value under this unimodal shape is $\Gamma = 1.35$. However, when more detailed studies were able to probe lower masses in the IMF of the Milky Way, it was shown that the IMF flattened for low stellar (M∼ $0.5\mathrm{M}_\odot$) masses (Chabrier 2003; Kroupa 2002). Following these later works, we also assumed a bimodal IMF, parametrised as a two-segment function (Vazdekis et al. 1996), where the star number per logarithmic mass bin is given by

$$\phi(\log m) \stackrel{\text{def}}{=} \frac{\mathrm{d}\mathcal{N}}{\mathrm{d}\log m} \propto \begin{cases} m_{\mathrm{p}}^{-\Gamma_{\mathrm{b}}} & m \leq 0.2\,\mathrm{M}_\odot \\ p(m) & 0.2\,\mathrm{M}_\odot < m \leq 0.6\,\mathrm{M}_\odot \\ m^{-\Gamma_{\mathrm{b}}} & m > 0.6\,\mathrm{M}_\odot \end{cases}$$

where $m_{\rm p}$ determines the turning-point mass, set to $m_{\rm p} = 0.4\,{\rm M}_{\odot}$ in the Vazdekis et al. (2010, 2012) models. $p(m)$ is a spline function satisfying a set of boundary conditions so that $\phi(m)$ is continuous:

$$\begin{aligned} p(0.2\,{\rm M}_{\odot}) &= m_{\rm p}^{-\Gamma_{\rm b}} \\ p'(0.2\,{\rm M}_{\odot}) &= 0 \\ p(0.6\,{\rm M}_{\odot}) &= 0.6^{-\Gamma_{\rm b}} \\ p'(0.6\,{\rm M}_{\odot}) &= -\Gamma_{\rm b} 0.6^{-(\Gamma_{\rm b}+1)} \end{aligned}$$

Under this parametrisation, the standard Kroupa-like IMF is well represented by a slope of $\Gamma_{\rm b} = 1.3$. Note that such a tapered IMF allows to increase the number of low-mass stars while keeping the mass-to-light ratio within reasonable values. In Fig. 1.8 we show the comparison between these bimodal and unimodal parametrisations, and a Kroupa IMF.

### 1.3.2 Techniques

Depending on the nature of the available data, the way of comparing them to models might differ. We detail next the three main techniques employed in this thesis to retrieve stellar population parameters from photometric and spectroscopic data.

#### Spectral Energy Distribution fitting

Among the three explored techniques, the spectral energy distribution (SED) fitting is the least accurate since it relies on broad to narrow photometric information. However, it is observationally the most efficient, and therefore is best suited for high-redshift objects, dim structures, or for studying a large sample of objects. In these cases, an spectroscopic approach is not affordable, and the use of photometric data is necessary. The SED fitting consist on using many photometric bands, along a spectral range as large as possible, to obtain a raw estimation of the most important stellar population parameters, namely, age and metallicity. In general, SED fits are more sensitive to age (or related quantities such as star formation histories) than to metallicity variations. Note that, if infrared data are included, SED fitting can be dominated by the presence of asymptotic giant branch, a poorly understood evolutionary stage. Moreover, the UV excess observed in some ETGs could also distort the inferred stellar population parameters.

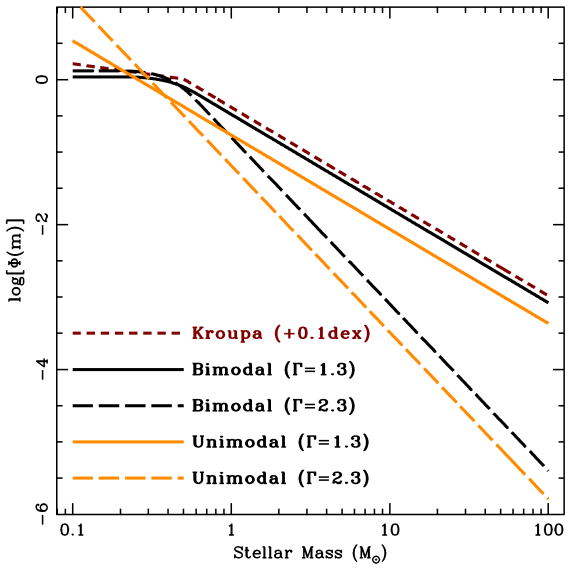


Figure 1.8: Different IMF paremetrizations, from La Barbera et al. (2013). Our favoured bimodal IMF shape is compared to a single power-law (unimodal) IMF and to the standard Kroupa IMF. The bimodal parametrization is able to simultaneously show an enhanced fraction of low-mass stars and a reasonable mass-to-light ratio. In the unimodal case, the large amount of extremely-low-mass stars leads to unphysical mass-to-light ratios for steep IMF slope values.

### Full spectral fitting

The full spectral fitting (FSF) technique is similar to the SED fitting, but applied to intermediate-to-high resolution spectra. Since spectral lines are fitted instead to large-scale photometric features, the FSF is significantly more accurate in deriving stellar population parameters than SED fits. FSF can be used even if with relatively low signal-to-noise data, behaving in this case even better than the line-strength analysis (Sánchez-Blázquez et al. 2011), as show in Fig. 1.9. In addition, the FSF can be useful to derive ages when gas emission dominates the Balmer lines. In contrast, it suffers from flux calibration uncertainties, and it is also affected by the presence of dust. Finally, it is worth noting that fits to different spectral regions might lead to different results, e.g. when comparing UV to infrared data, suggesting the presence of composite stellar populations.

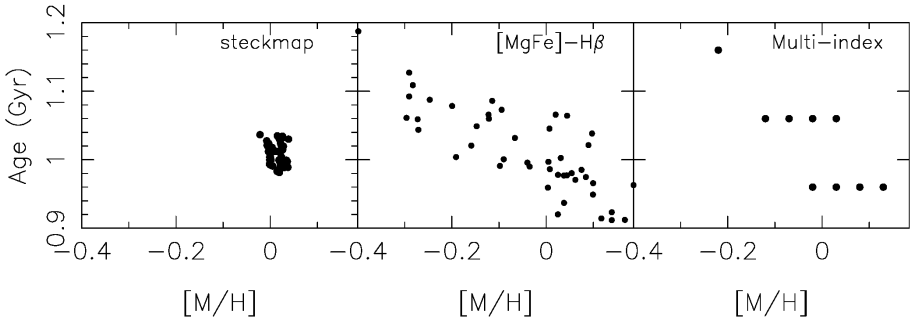


Figure 1.9: Age–metallicity degeneracy using FSF (left), an $H_\beta$-[MgFe] diagram, and a combination of line-strength indices, from Sánchez-Blázquez et al. (2011). If, as in this example, the signal-to-noise of the data is not high enough, the use of line-strength indices leads to a strong age–metallicity degeneracy, which is minimized if FSF is applied instead.

### 1.3.3 Line-strength indices

Line-strength indices have been the main tool to investigate with great detail the stellar population properties of nearby ETGs over the last 30 years. In unresolved galaxies, where line broadening due to the stellar velocity dispersion is usually larger than $\sim$50 km s$^{-1}$, line-strength indices probe the smallest uncorrelated spectral features. Therefore, they can provide extremely accurate estimations of the stellar population parameters. This is particularly important for second-order parameters like [$\alpha$/Fe] or IMF, whose effect is restricted to very small scales or color-wide features. In fact, La Barbera et al. (2013) showed that the ability to retrieve IMF information vanishes when FSF techniques (which probe intermediate scales) are applied instead of line-strength indices and colours. In contrast, given the small number of independent index (measurements), the assumption of a SSP is normally made when working with line-strength indices. This is certainly not the case of spiral galaxies with extended star formation histories, where line-strength analysis will provide strongly biased, luminosity weighted quantities. Therefore, the use of line-strength indices is best suited for the study of ETGs.

In practice, line-strength indices usually measure the effective width of a certain absorption feature. Therefore, their definition includes two continuum bands and a bandpass, although they can also be defined as a *contrast* or jump between two spectral regions. As an example, in Fig. 1.10 we show the standard definition of the index around the $TiO_2$ molecular band. Index definitions can not be arbitrary, and their dependence on stellar population, kinematical and observational parameters have to be taken into account. Note that our index

definitions are based on flux calibrated predictions, in contrast to the classic LICK-IDS system.

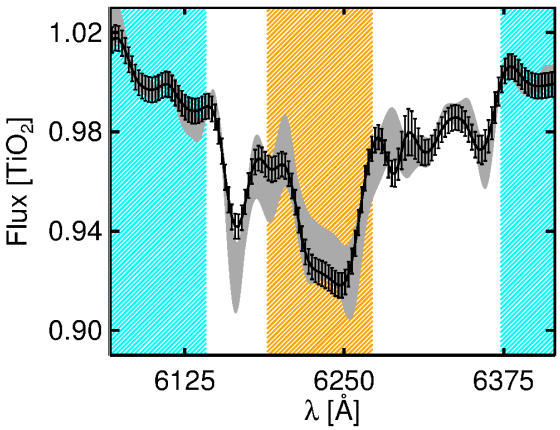


Figure 1.10: $TiO_2$ line-strength index definition. The two pseudo-continua are marked in blue and the central bandpass is indicated in orange. Indices usually measure the equivalent width of a certain feature, and they can provide very accurate information about stellar population parameters. In particular, this $TiO_2$ molecular band is very sensitive to IMF variations, depending mildly on the age and on the [Ti/Fe] abundance ratio.

## 1.4 Goals

Motivated by the observational and theoretical arguments detailed above, this thesis aims to deepen in our knowledge of galaxy formation and evolution by investigating the radial variations of the stellar population properties of nearby galaxies, combined with direct probes of the high redshift Universe. The goals of the thesis can be summarized as follows:

- To analyze the surface radial profiles of a sample of nearby edge-on spirals in order to investigate the nature and origin of the abrupt changes in their radial light distributions. In addition, to understand the relation between these changes and the formation processes followed by spiral galaxies.

- To study the radial variations in stellar population of nearby ETGs, deriving the radial gradients out to $\sim 1R_e$. Both kinematical (rotational velocity and velocity dispersion) and stellar population properties (age, metal content, abundance pattern and IMF) will be derived.

- To understand the evolution in the stellar population properties since the formation epoch of massive ETGs until $z \sim 0$. To this end, two approaches will be combined:

  - To compare the properties of nearby massive ETGs to those massive galaxies that, in the local volume, have not experienced any major merger event since their formation. This will allow us to isolate the effect of the accreted material on the typical radial gradients observed at $z \sim 0$.
  - To directly probe the properties of massive ETGs at high redshift by using spectro-photometric information. Albeit being observationally expensive, this approach will provide a valuable information about ETG evolution since $z \sim 1$.

- To empirically characterize the observed variations in the IMF of ETGs, through the analysis of line-strength indices. To interpret these variations on the basis of the different theoretical frameworks.

- To evaluate the implications of the findings above on the standard picture of galaxy formation.

# 2

# A unified picture of breaks and truncations in spiral galaxies

This chapter has been published as *Martín-Navarro et al. 2012, MNRAS, 427, 1102*

Despite truncations and breaks in the radial light distributions of edge-on and face-on galaxies, respectively, have been traditionally considered equivalent features, our aim in the current chapter is to understand the already noticed observational differences, proposing a global and self-consistent understanding of the breaks. We use images in six different filters (five SDSS bands and the S$^4$G 3.6$\mu m$ band) to study the radial surface brightness distribution in a sample of 34 edge-on galaxies. We also measure the color and the stellar surface mass density profiles for each object, trying to constrain the most plausible mechanism for the break formation.

Throughout this chapter, we adopt a standard $\Lambda$CDM set of cosmological parameters ($H_0 = 70$ km s$^{-1}$ Mpc$^{-1}$; $\Omega_{\rm M} = 0.30$; $\Omega_\Lambda = 0.70$) to calculate the redshift dependent quantities. We have used AB magnitudes unless otherwise stated.

## 2.1 Sample and data

Our sample of galaxies has been selected to cover edge-on objects present both in the Sloan Digital SDSS Data Release 7 (Abazajian et al. 2009) and in the *Spitzer* Survey of Stellar Structure in Galaxies (S$^4$G) (Sheth et al. 2010). We

find 49 highly inclined (inclination $\gtrsim 88°$) objects satisfying this criterion. In this sense our sample is neither volume limited nor flux limited.

For each object, the morphological type, the corrected $B$-band absolute magnitude ($M_{\rm B}$) and the maximum velocity of the rotation curve were obtained from the HyperLeda database (Paturel et al. 2003). Using the NASA/IPAC Extragalactic Database (NED) (Helou et al. 1991) we obtained most distances from primary indicators, except for three cases (PGC 029466, UGC 5347 and UGC 9345) where the distance was obtained using the redshift.

Finally, from the original 49 galaxies, we keep only those objects brighter than $M_{\rm B} = -17$ mag and with morphological type Sc or later. Table 3.1 summarizes the general information available for each galaxy in the final sample. We focus our studies on late-type spiral galaxies. These late Hubble-types are known to have the most quiescent evolution during the cosmic time, hence the fossil records imprinted by the early galaxy formation and evolution processes likely survive to present day.

### 2.1.1 SDSS data

For all the galaxies in the sample, the SDSS data were downloaded in all the five available bands $\{u', g', r', i', z'\}$. SDSS observations are stored in the format of 2048×1489 pixel ($\sim$ 13.51'×9.83') frames that cover the same piece of sky in all bands. These frames are bias subtracted, flat-fielded and purged of bright stars, but still contain the sky background. These frames might not be large enough to contain extended objects completely. For this reason, to assemble mosaics that are large enough to study extended objects, we needed to download several adjacent frames from the SDSS archive. We estimate the sky background of these frames independently (see §2.2 for a more detailed description) and then, we assemble the final mosaics in all five bands, centered at the target galaxy, by using SWARP (Bertin et al. 2002).

The pixel size in the SDSS survey is 0.396 ", and the exposure time is $\sim$ 54 sec. From this, we calculated the surface brightness in the AB system as:

$$\begin{aligned} \mu_{\rm SDSS} &= -2.5 \times \log(counts) + ZP \\ ZP &= -2.5 \times 0.4 \times (aa + kk + airmass) \\ &\quad +2.5 \times \log(53.907456 \times 0.396^2) \end{aligned}$$

where *aa*, *kk* and *airmass* are the photometric zero point, the extinction term and the air mass, respectively. These parameters are stored in the header of each SDSS image.

| Galaxy | $M_{\rm abs}$ ($B$-mag) | Morph. type | Morph. code | Distance (Mpc) | $V_{\rm rot}$(max) (km s$^{-1}$) |
|---|---|---|---|---|---|
| IC 1197 | -18.56 | Sc | 6.0 | 25.7 | 87.9 |
| IC 2233 | -19.44 | SBc | 6.4 | 13.4 | 79.2 |
| NGC 3279 | -19.27 | Sc | 6.5 | 32.5 | 156.2 |
| NGC 3501 | -19.15 | Sc | 5.9 | 22.9 | 133.6 |
| NGC 3592 | -18.14 | Sc | 5.3 | 22.7 | 79.7 |
| NGC 4244 | -18.44 | Sc | 6.1 | 4.6 | 89.1 |
| NGC 4330 | -19.92 | Sc | 6.3 | 19.5 | 115.6 |
| NGC 4437 | -21.55 | Sc | 6.0 | 9.8 | 140.1 |
| NGC 5023 | -17.87 | Sc | 6.0 | 9.0 | 80.3 |
| NGC 5529 | -22.07 | Sc | 5.3 | 49.5 | 284.1 |
| NGC 5907 | -20.96 | Sc | 5.4 | 16.3 | 227.0 |
| PGC 029466 | -18.71 | Sc | 6.2 | 44.8 | 69.0 |
| UGC 01839 | -17.20 | Scd | 7.1 | 19.1 | 65.6 |
| UGC 01970 | -18.98 | Sc | 5.9 | 33.9 | 95.2 |
| UGC 04725 | -17.49 | Sc | 6.1 | 45.4 | 59.4 |
| UGC 04970 | -18.51 | Sc | 5.7 | 56.7 | 113.3 |
| UGC 05347 | -18.94 | Scd | 6.5 | 36.0 | 95.6 |
| UGC 06080 | -18.69 | Sc | 6.5 | 36.3 | 77.9 |
| UGC 06509 | -19.12 | Scd | 6.6 | 43.8 | 78.3 |
| UGC 06667 | -17.88 | Sc | 5.9 | 19.8 | 89.2 |
| UGC 06791 | -18.83 | Sc | 6.5 | 35.7 | 96.5 |
| UGC 06862 | -18.32 | Scd | 6.7 | 62.2 | 81.8 |
| UGC 07153 | -19.40 | Sc | 5.9 | 48.0 | 111.9 |
| UGC 07802 | -18.44 | Sc | 6.1 | 23.2 | 70.1 |
| UGC 07991 | -18.15 | Scd | 6.6 | 23.2 | 79.5 |
| UGC 08146 | -17.31 | Sc | 6.4 | 18.2 | 71.1 |
| UGC 08166 | -18.78 | Sc | 6.0 | 53.4 | 74.3 |
| UGC 09242 | -19.89 | Scd | 6.6 | 24.0 | 81.4 |
| UGC 09249 | -18.35 | Scd | 7.2 | 24.8 | 63.5 |
| UGC 09345 | -18.39 | Sc | 6.4 | 36.6 | 95.4 |
| UGC 09760 | -18.72 | Scd | 6.6 | 29.8 | 62.3 |
| UGC 09977 | -19.85 | Sc | 5.3 | 30.5 | 112.7 |
| UGC 10288 | -20.37 | Sc | 5.3 | 31.7 | 166.6 |
| UGC 12281 | -19.82 | Sd | 7.5 | 33.9 | 117.3 |

Table 2.1: Fundamental parameters of the final sample. The distances were collected from the NED database meanwhile the $B$-band absolute magnitude (corrected from extinction), the morphological type, the morphological code (T-type) and the maximum rotational velocity were obtained from the HyperLeda database.

### 2.1.2 S$^4$G data

The S$^4$G project is a survey of a representative sample of nearby Universe galaxies (D<40 Mpc) that collects images of more than 2000 galaxies with the *Spitzer* Infrared Array Camera (IRAC); Fazio et al. (2004). In particular, we are interested in the $3.6\mu m$ band (channel 1) which is less affected by dust than the SDSS optical bands and is a good tracer for the stellar mass in our galaxies. The fact that the optical depth in this band is lower than in the SDSS images is crucial as we are dealing with edge-on objects, with a lot of dust along the line of sight. The IRAC $3.6\mu m$ images were reduced by the S$^4$G team. They have a pixel scale of 0.75 "/pix and a spatial resolution is $\sim$ 100 pc at the median distance of the survey volume. Also, the azimuthally-averaged surface brightness profile typically traces isophotes down to a ($1\sigma$) surface brightness limit $\sim$ 27 mag arcsec$^{-2}$ (see Sheth et al. 2010). The conversion to AB surface magnitudes is given by:

$$\mu_{\mathrm{S^4G}} = -2.5 \times \log(counts) + 20.472$$

## 2.2 Data handling and results

Sky subtraction

Since the breaks are expected to happen at low surface brightness (a typical value of $\sim$ 24 mag arcsec$^{-2}$ in the SDSS $g'$ band was found by Pohlen & Trujillo 2006 for face-on galaxies), a very careful sky estimation is needed to obtain reliable results. In this context, working with data taken with different instruments at different wavelengths, requires a different treatment for the SDSS and S$^4$G data.

In the case of the SDSS images, after removing the 1000 counts of the SOFTBIAS added to all SDSS chips, we measure the fluxes in about ten thousand randomly placed, five pixel wide apertures. We apply a resistant mean[1] to the distribution of the aperture fluxes, and carry out several iterations to get rid of the fluxes biased by stars, and other background objects. The mean of the bias-free distribution provides accurate measurement of the sky background, and is then subtracted from the chips.

For the S$^4$G data, the sky treatment was completely different because of the presence of important gradients across the images (see Comerón et al. 2011). The adopted strategy was to mask every object in the image and then make a low order polynomial fit of the background in the same way that Comerón

[1]The resistant mean trims away outliers using the median and the median absolute deviation. It is implemented as an Interactive Data Language (IDL) routine.

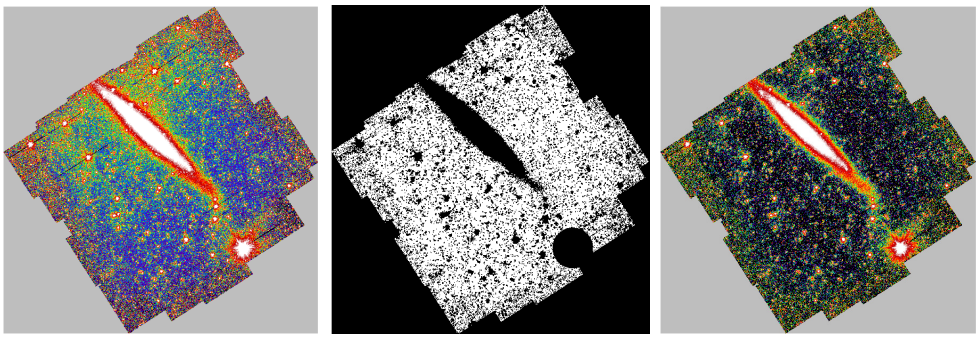

Figure 2.1: Sky subtraction steps for NGC 4244 (3.6$\mu m$ band). From left to right: 1- Original image. 2- Image mask where white pixels are those used to estimate the background shape. 3- Image after the subtraction of one of the polynomial fittings (3rd order).

et al. (2011) did in their study of NGC 4244. In order to establish a threshold between sky/non-sky pixels, we built the histogram of the image and, with the assumption that this histogram is dominated by the sky pixels, we calculated the maximum and the FWHM of this distribution. The FWHM measured in that way can be associated with an effective sigma ($\sigma_{\rm e}$) that we supposed representative of the standard deviation of the background. After this, we performed five two-dimensional fits with five different polynomial orders ($\mathcal{O} = \{0, 1, 2, 3, 4\}$), including only those pixels with a value between the maximum of the histogram $\pm 3\sigma_{\rm e}$. The outcome of this stage was five sky-subtracted images, each one derived from one of the fits. The difference between these images was used (see §2.2.1) to establish the surface brightness limit in the 3.6$\mu m$ surface brightness profile. In Fig. 2.1 we show a raw S$^4$G image (left) where the gradients across the image are obvious; the mask image (center) with the pixels used to fit the background represented in white and, as an example, the 3rd order sky subtracted image (right).

### Estimating the position angle of the slit

Our aim is to extract surface brightness profiles along the disk in a slit that represents the same physical distance (1.2 kpc) vertically in all galaxies. For this reason, this slit has to be aligned accurately with the disk of our galaxies. The position angle (PA) was defined as the angle that maximizes the total number of non-sky pixels within the previously fixed slit. This definition is consistent with the idea followed in the surface brightness profile calculation. The measurement will be robust if the size of the galaxy is large enough compared to the field

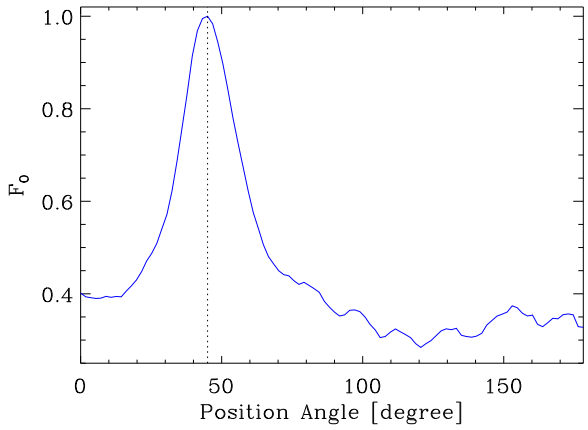


Figure 2.2: The fraction of non-background pixels within the slit aperture ($F_O$) as a function of the position angle of the slit for NGC 4244 ($r'$-band). The vertical dashed line marks the center of the angular interval used to refine the measurement of the final PA.

of view. As in §2.2, we distinguished sky pixels from non-sky pixels, setting them to 0 and 1 respectively. We rotated the image by a certain angular step and then sum the value of all the pixels within the slit. The desired angle corresponds to the maximum of this distribution.

In order to obtain the PA with enough accuracy, but with an acceptable computational cost, the process was divided into two phases. In the first one, a low resolution profile was obtained by rotating the galaxy between 0° and 180° in 100 consecutive steps. We then defined an angular interval around the maximum of the resulting low resolution profile and used a high resolution step of 0.2°. The maximum found in this second phase is the PA of the galaxy. Fig. 2.2 shows the normalized fraction of flux within the aperture vs the slit position angle profile for the case of NGC 4244, with a peaked distribution around the maximum (PA = 47.2°).

As the galactic plane is expected to be dust attenuated, we employed the $3.6\mu m$ S$^4$G images to calculate the PA. The PA derived form the SDSS data was in all the cases compatible with the S$^4$G measurements taking into account the associated errors. In addition, we repeated the measurement of the PA changing the threshold used to distinguish the sky pixels, taking at the end the average of the resulting values.

The PA calculated in this way is intuitive but is sensitive to the presence of extended objects in the field and to asymmetries in the light distribution

of the galaxy. For that reason, we had to manually set the PA in seven cases to completely align the galactic plane with the slit, with a typical deviation with respect to the automatic measurement $\langle PA_{\rm final} - PA_{\rm auto} \rangle = 0.5 \pm 0.1°$. The PA here calculated is compared in Table 2.2 with the position angle from HyperLeda[2] for each galaxy in the sample, showing a mean difference between our measurements and the PA from HyperLeda $\sim 0.7°$. It is worth noting here that the PA given by HyperLeda is the result of averaging all entries in the database for each object, sometimes with very different values (e.g. for NGC 4244, the HyperLeda PA (42.2°) is the average of four significantly different measurements: 48°, 48°, 27° and 45.2°).

#### Image masking

To study the outskirts of the galaxies with the desired precision it was necessary to mask objects that clearly do not belong to the galaxy (foreground stars, background galaxies). This masking process allowed us to obtain cleaner surface brightness profiles and also to avoid the contamination of the faintest parts by external objects.

For the S$^4$G images, the masks were supplied by the S4G team and are described in Sheth et al. (2010). In the case of the SDSS images, we generated the masks using the package SEXTRACTOR (Bertin & Arnouts 1996). Background objects and foreground stars were detected using a master image composed of all five SDSS bands, scaled to the $r'$-band flux. Then, over-sized elliptical masks were place onto the detected sources using SEXTRACTOR parameters such measured flux, elongation and similar. To increase the accuracy in this process, the masking was done in two consecutive steps. In the first one, the bigger and brighter background objects were masked. In the second step, we performed a more detailed detection process to mask any possible remaining object in the field. By doing this, we could successfully mask background objects within a wide range of sizes.

### 2.2.1 Surface brightness profiles

To extract the profile along the radial distance of the galaxies, a slit of constant physical width is placed over the galactic plane and then used to calculate how the flux varies along the slit. The width of the slit was fixed to 1.2 kpc following the assumption of a vertical scalelength equal to 0.6 kpc (Kregel et al. 2002).

[2]By definition, the PA increases (from 0° to 180°) from the North to the East, i.e., counterclockwise.

| Galaxy | PA (HyperLeda) | PA (This chapter) |
|---|---|---|
| IC 1197 | 56.6 | 56.3 |
| IC 2233 | 172.3 | 171.5 |
| NGC 3279 | 152.0 | 152.0 |
| NGC 3501 | 28.0 | 27.1 |
| NGC 3592 | 117.7 | 116.5 |
| NGC 4244 | 42.2 | 47.2 |
| NGC 4330 | 60.0 | 57.9 |
| NGC 4437 | 85.7 | 82.3 |
| NGC 5023 | 28.3 | 27.8 |
| NGC 5529 | 114.3 | 113.4 |
| NGC 5907 | 155.5 | 154.5 |
| PGC 029466 | 179.9 | 180.0 |
| UGC 01839 | 43.5 | 45.8 |
| UGC 01970 | 22.7 | 22.6 |
| UGC 04725 | 66.2 | 67.3 |
| UGC 04970 | 104.6 | 104.8 |
| UGC 05347 | 17.0 | 18.2 |
| UGC 06080 | 129.4 | 127.2 |
| UGC 06509 | 79.0 | 78.9 |
| UGC 06667 | 87.2 | 87.2 |
| UGC 06791 | 0.5 | 0.8 |
| UGC 06862 | 103.7 | 103.5 |
| UGC 07153 | 165.8 | 166.3 |
| UGC 07802 | 56.4 | 56.1 |
| UGC 07991 | 172.6 | 170.5 |
| UGC 08146 | 30.6 | 30.5 |
| UGC 08166 | 156.5 | 156.3 |
| UGC 09242 | 70.8 | 71.1 |
| UGC 09249 | 85.5 | 185.5 |
| UGC 09345 | 141.7 | 140.4 |
| UGC 09760 | 61.2 | 55.0 |
| UGC 09977 | 80.4 | 77.4 |
| UGC 10288 | 90.2 | 90.0 |
| UGC 12281 | 30.3 | 29.7 |

Table 2.2: Position angles (in degrees) calculated in this chapter and from HyperLeda for our sample of galaxies. The PA is measured from the North to the East (between 0° and 180°). The mean difference between our measurements and those from HyperLeda is 0.7°.

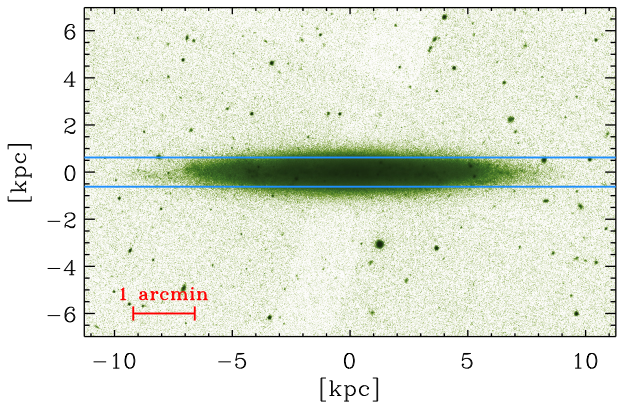


Figure 2.3: The galaxy NGC 5023 is shown with the region (slit) used to calculate the surface brightness profile delimited by the solid blue lines.

For illustrative purposes, in Fig. 2.3 the slit position (in blue) is shown over the $r'$-band image of NGC 5023.

In general, the process to obtain the surface brightness profiles was the same for the SDSS and for the S$^4$G data. The first step was to divide the slit along the major axis in cells of 0.3" radial width. The averaged value of the flux within each cell was calculated using a $3\sigma$ rejection mean. This first stage yields a crude estimate of the surface brightness profile. The center of the galaxy was supposed to correspond to the brightest cell of this profile and, to avoid any kind of misalignment between the different filters, we took the right ascension and declination of the S$^4$G brightest cell as the center in all the other profiles. The sky was again measured on the left and right sides of the galaxies in order to, later, remove any possible residual contribution after the initial sky subtraction (§2.2).

After that, we calculated the *right* and *left* surface brightness profiles with the size of the bins linearly increasing with a factor 1.03 between consecutive cells to improve the signal to noise ratio in the outskirts of the galaxies. The right/left residual sky value measured at the beginning of the process was also subtracted for the right/left profiles to obtain the final surface brightness distributions. The surface brightnesses of this residual sky corrections were typically $\sim$ 30 mag arcsec$^{-2}$ for the $g'$-band and $\sim$ 29 mag arcsec$^{-2}$ for the 3.6$\mu m$ band.

Finally, a mean profile was constructed as the average of the left and right

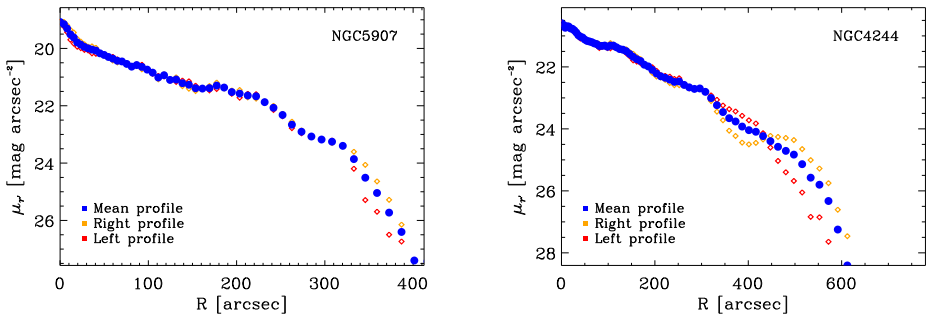


Figure 2.4: Surface brightness profile for the galaxies NGC 5907 (upper panel) and NGC 4244 (bottom panel) in the $r'$ band. In blue it is shown the mean profile, whereas left and right profiles are represented in red and yellow respectively.

profiles. These averaged profiles are the ones used in this study. Looking at the individual right/left profiles of all our sample, it was clear that in some cases (e.g. NGC 4244) there are considerable asymmetries (up to 0.8 $r'$-mag arcsec$^{-2}$ difference between the averaged profile and the right/left profiles at $r = 550$ arcsec for that object) but as we wanted to explore the surface brightness profiles down to very faint regions, the combination of the two sides of the galaxies is necessary. As an example, in Fig. 2.4 we represent the mean, left and right surface brightness profile in the SDSS $r'$-band for a symmetric case (NGC 5907) in opposition to the more asymmetric galaxy NGC 4244.

Beyond a certain radius, the sky subtraction becomes a dominant factor at determining surface brightness profiles. Having used different sky subtractions techniques, the maximum radial extension of a reliable surface brightness profile needs to be measured separately for the SDSS and for the S$^4$G data.

SDSS surface brightness limit

To estimate how faint we can explore the SDSS profiles, we defined a certain critical surface magnitude ($\mu_{\rm crit}$) that sets the limit for our profiles. Following Pohlen & Trujillo (2006), we defined $\mu_{\rm crit}$ as the surface brightness where the two profiles obtained by under/over subtracting the sky by -1/+1 $\sigma_{\rm sky}$ start to differ by more than 0.2 mag arcsec$^{-2}$ where $\sigma_{\rm sky}$ is given by

$$\sigma^2_{\rm sky} = \sigma^2_{\rm sky,\ left} + \sigma^2_{\rm sky,\ right}$$

with $\sigma_{\rm sky,\ left}$ and $\sigma_{\rm sky,\ right}$ the standard deviation of the residual sky measured on the left and right sides of the galaxy. On average, we could reach a surface

brightness magnitude limit equal to 26.1 ± 0.1 mag arcsec$^{-2}$ in the SDSS $r'$ band. This value is a characteristic limit for the $g'$, $r'$ and $i'$ SDSS data, with the remaining SDSS images being typically shallower (e.g. $\langle \mu_{u',\mathrm{lim}} \rangle = 25.7$ mag arcsec$^{-2}$ ; $\langle \mu_{z',\mathrm{lim}} \rangle = 24.2$ mag arcsec$^{-2}$ ).

S$^4$G surface brightness limit

The limit for the S$^4$G data had to be more strictly defined because of the presence of gradients across the S$^4$G images. As discussed in §2.2, we have, for each object, five images from five different polynomial fits to the background. The limit was established where the function

$$\mu_{\mathrm{crit}} = \frac{1}{5} \sum_{n=0,..,4} |\mu_n - \langle \mu \rangle |$$

became greater than 0.2 mag arcsec$^{-2}$. In other words, the limit for the S$^4$G profiles was placed where the mean difference between the five profiles and the mean one was greater than 0.2 mag arcsec$^{-2}$. A typical value of 26.1 ± 0.2 mag arcsec$^{-2}$ was found for this limit in the S$^4$G 3.6$\mu m$ band.

The limit defined in this a way is not necessarily the same for the left and right sides of a galaxy. The mean profile is in fact the average of two profiles until the surface magnitude limit of the "shallower" side. Beyond that, the mean profile is only that of the "deeper" side of the galaxy.

### 2.2.2 Color profiles

From the surface brightness profiles one can directly obtain the radial color profiles of an object. However, the interpretation of the edge-on color profiles is not straightforward. On the one hand, the presence of dust in the galactic plane will generate redder colors and change the actual shape of the color profile compared to that expected in its absence. On the other hand, effects related to the edge-on projection (integration of light from different radii along the line of sight and a bigger optical depth because of the presence of dust) are difficult to handle and to account for in an edge-on color profile.

In this chapter, we have focused only on those profiles that could reach the lowest surface brightness values (i.e., the color profiles derived from the deepest surface brightness profiles). In particular, we calculated for each galaxy the $(g' - r')$, $(r' - i')$ and $(r' - 3.6\mu m)$ color profiles.

### 2.2.3 Stellar surface mass density profiles

The final quantity that we obtained from the images is the stellar surface mass density ($\Sigma_\lambda$). We can relate $\Sigma_\lambda$ with the surface brightness at a certain wavelength ($\mu_\lambda$) and with the mass to luminosity ratio $(M/L)_\lambda$ at that given $\lambda$ (see Bakos et al. 2008) using the following expression:

$$\log \Sigma_\lambda = \log(M/L)_\lambda - 0.4(\mu_\lambda - m_{\mathrm{abs}\ \odot,\lambda}) + 8.629$$

where $\Sigma_\lambda$ is given in $M_\odot$ pc$^{-2}$. Having $\mu_{r'}$ from the photometry, one just needs to know the value $(M/L)_{r'}$ along the galaxy to get the $\Sigma_\lambda$ profile. We used the relation proposed by Bell et al. (2003) to estimate $(M/L)_{r'}$ as follows

$$\log(M/L)_{r'} = [a_{r'} + b_{r'} \times (g' - r')] - 0.15$$

where $a_{r'}$ and $b_{r'}$ are $-0.306$ and 1.097 respectively. We have then the stellar surface mass density as a function of all known variables.

As mentioned in §2.2.2, the interpretation of edge-on color profile is not as direct as in the face-on case. The dust attenuation and the error propagation in this kind of profiles are very important and thus, one has to be aware of all these effects while interpreting the surface mass density profiles.

### 2.2.4 Presentation of the results

Shortly below we will show some examples of the profiles extracted in this chapter. For the rest of the galaxies, we refer to the reader to Appendix A. Upper left panels in these figures show the six bands surface brightness profiles used in this chapter. The dashed vertical lines mark those radii where a change in the exponential behavior happens defined as described in §2.3.3.

On the bottom left panel we represent the color profiles. The color profile are shown down to the distance where data points have an error less than or equal to 0.2 mag, with the error calculated as the quadratic sum of the errors in the individual surface brightness profiles.

The bottom right panel is occupied by a $g'$-band image of the galaxy, with vertical lines marking the characteristic radii, in the same way as in the surface brightness profiles. The angular distance from the center of the galaxy to those lines is shown at the top of the image.

Finally, the upper right panel shows the stellar surface mass density profile. In the same panel is over-plotted the $3.6\mu m$ surface brightness profile, that is expected to be a good tracer of the stellar mass density. In this panel we have not limited the extent of the profiles and therefore the farthest points have to be considered with caution.

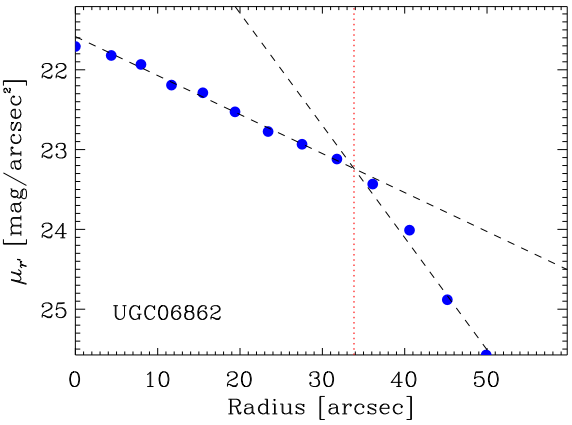


Figure 2.5: Fit of the $r'$-band surface brightness profile of UGC 06862. The fit of the two characteristic regions is shown as a black dashed line, while the radius where the change in the slope occurs is marked with a red dotted line. We have defined this radius as the intersection point between the two linear fits.

## 2.3 Analysis

### 2.3.1 Break radius and scalelengths

In order to quantify the radial distance where the change in exponential scalelength occurs, we have linearly fitted the $r'$-band averaged surface brightness profile of each galaxy. We have visually selected all the disk regions showing a differentiated exponential behavior and then we have made an independent linear fit over each one of those regions. The characteristic radius where the exponential scalelength changes is set at the intersection point between two straight lines derived from the fit of two adjacent regions. Fig. 2.5 shows, as an example, the fit for UGC 06862. The black dashed lines represent the linear fit of each part of the disk. The red dotted line marks the intersection point between the two fits. Table 2.3 lists the regions of the disk where the fits were made for each individual galaxy. In addition, Tables 2.4 and 2.5 list where all characteristic radii occur in each galaxy in the sample.

Apart from identifying different characteristic radii, we have measured $r_{\rm max}$ as the radial distance where a hint of a new change in the exponential behavior is present but there were not enough points to perform a reliable fit because it occurs at a surface magnitude too close to the surface brightness limit. If no such hint is detected, $r_{\rm max}$ represents then a lower limit for a potential new

| Galaxy | $r_1$ (arcsec) | $r_2$ (arcsec) | $r_3$ (arcsec) | $r_4$ (arcsec) | $r_5$ (arcsec) | $r_6$ (arcsec) |
|---|---|---|---|---|---|---|
| IC 1197 | 0.0 | 40.6 | 49.9 | 86.8 | 86.8 | 98.7 |
| IC 2233 | 0.0 | 111.3 | 111.3 | 138.6 | 145.9 | 169.2 |
| NGC 3279 | 11.7 | 45.2 | 49.9 | 86.8 | 86.8 | 104.9 |
| NGC 3501 | 11.7 | 64.8 | 64.8 | 104.9 | 104.9 | 131.5 |
| NGC 3592 | 0.0 | 40.6 | 31.8 | 64.8 | 64.8 | 81.1 |
| NGC 4244 | 0.0 | 296.3 | 308.1 | 552.4 | 552.4 | 612.2 |
| NGC 4330 | 0.0 | 98.7 | 92.6 | 161.2 | - | - |
| NGC 4437 | 0.0 | 203.5 | 212.6 | 372.8 | 372.8 | 416.3 |
| NGC 5023 | 0.0 | 111.3 | 111.3 | 212.6 | - | - |
| NGC 5529 | 8.0 | 98.7 | 92.6 | 177.4 | 177.4 | 194.5 |
| NGC 5907 | 19.4 | 222.1 | 222.1 | 320.3 | 320.3 | 401.4 |
| PGC 029466 | 0.0 | 15.5 | 19.4 | 36.1 | - | - |
| UGC 01839 | 4.4 | 45.2 | 40.6 | 64.8 | - | - |
| UGC 01970 | 4.4 | 27.5 | 27.5 | 49.9 | 54.7 | 70.1 |
| UGC 04725 | 0.0 | 19.4 | 19.4 | 36.1 | 40.6 | 49.9 |
| UGC 04970 | 0.0 | 40.6 | 40.6 | 54.7 | - | - |
| UGC 05347 | 0.0 | 23.4 | 19.4 | 36.1 | 40.6 | 54.7 |
| UGC 06080 | 0.0 | 40.6 | 45.2 | 59.7 | - | - |
| UGC 06509 | 0.0 | 49.9 | 49.9 | 75.5 | - | - |
| UGC 06667 | 0.0 | 45.2 | 45.2 | 92.6 | 98.7 | 131.5 |
| UGC 06791 | 0.0 | 31.8 | 40.6 | 54.7 | 54.7 | 64.8 |
| UGC 06862 | 4.4 | 31.8 | 36.1 | 49.9 | - | - |
| UGC 07153 | 0.0 | 49.9 | - | - | 54.7 | 70.1 |
| UGC 07802 | 4.4 | 40.6 | 40.6 | 59.7 | 59.7 | 75.5 |
| UGC 07991 | 4.4 | 31.8 | 40.6 | 75.5 | - | - |
| UGC 08146 | 0.0 | 70.1 | 75.5 | 111.3 | 111.3 | 124.6 |
| UGC 08166 | 0.0 | 27.5 | 27.5 | 40.6 | - | - |
| UGC 09242 | 0.0 | 104.9 | 124.6 | 177.4 | - | - |
| UGC 09249 | 4.4 | 49.9 | 54.7 | 75.5 | - | - |
| UGC 09345 | 8.0 | 27.5 | 31.8 | 49.9 | - | - |
| UGC 09760 | 0.0 | 49.9 | 64.8 | 81.2 | - | - |
| UGC 09977 | 11.7 | 98.7 | - | - | 111.3 | 131.5 |
| UGC 10288 | 11.7 | 92.6 | 98.7 | 138.6 | 153.5 | 169.2 |
| UGC 12281 | 0.0 | 40.6 | 40.6 | 98.7 | 98.7 | 111.3 |

Table 2.3: Boundaries enclosing the different regions in each galaxy. The $[r_1, r_2]$ interval marks the limits between the galactic centre and the break, $[r_3, r_4]$ the limits between the break and the truncation and $[r_5, r_6]$ between the truncation and the end of the brightness profile.

| Galaxy | Type | $r_B$ | | $r_T$ | |
|---|---|---|---|---|---|
| | | (kpc) | (arcsec) | (kpc) | (arcsec) |
| IC 1197 | II | 5.6 | 45.0 | 10.7 | 86.0 |
| IC 2233 | II | 7.48 | 115.5 | 9.17 | 141.7 |
| NGC 3279 | II | 7.64 | 48.4 | 12.61 | 80.0 |
| NGC 3501 | II | 7.41 | 66.8 | 11.12 | 100.2 |
| NGC 3592 | II | 3.19 | 29.0 | 6.59 | 59.8 |
| NGC 4244 | II | 6.50 | 289.5 | 12.30 | 548.1 |
| NGC 4330 | II | 8.53 | 90.2 | *nd* | *nd* |
| NGC 4437 | II | 9.89 | 209.0 | 16.90 | 357.2 |
| NGC 5023 | II | 4.51 | 103.7 | *nd* | *nd* |
| NGC 5529 | II | 23.33 | 97.2 | 43.37 | 180.6 |
| NGC 5907 | II | 18.95 | 237.2 | 26.14 | 327.2 |
| PGC 029466 | II | 2.75 | 13.2 | *nd* | *nd* |
| UGC 01839 | II | 3.70 | 39.9 | *nd* | *nd* |
| UGC 01970 | III | 3.89 | 23.7 | 8.75 | 53.3 |
| UGC 04725 | III | 4.23 | 19.2 | 8.74 | 39.7 |
| UGC 04970 | II | 10.69 | 38.9 | *nd* | *nd* |
| UGC 05347 | II | 2.99 | 17.9 | 6.20 | 37.1 |
| UGC 06080 | II | 7.51 | 42.7 | *nd* | *nd* |
| UGC 06509 | II | 10.53 | 49.7 | *nd* | *nd* |
| UGC 06667 | II | 5.21 | 54.4 | 9.22 | 96.3 |
| UGC 06791 | II | 5.33 | 30.8 | 9.37 | 54.1 |
| UGC 06862 | II | 10.20 | 33.8 | *nd* | *nd* |
| UGC 07153 | I | - | - | 12.74 | 54.8 |
| UGC 07802 | II | 4.06 | 36.1 | 6.76 | 60.2 |
| UGC 07991 | II | 4.22 | 37.5 | *nd* | *nd* |
| UGC 08146 | II | 6.72 | 76.1 | 9.96 | 112.7 |
| UGC 08166 | III | 6.85 | 26.4 | *nd* | *nd* |
| UGC 09242 | II | 13.25 | 113.9 | *nd* | *nd* |
| UGC 09249 | II | 6.51 | 54.2 | *nd* | *nd* |
| UGC 09345 | II | 3.84 | 22.6 | *nd* | *nd* |
| UGC 09760 | III | 8.26 | 57.2 | *nd* | *nd* |
| UGC 09977 | I | - | - | 15.50 | 104.8 |
| UGC 10288 | II | 13.50 | 87.7 | 23.40 | 152.1 |
| UGC 12281 | II | 5.89 | 35.9 | 15.72 | 95.8 |

Table 2.4: Types of profiles and break (B subscript) and truncation (T subscript) radii. *nd* represents a non-detected truncation.

| Galaxy | $\mu_{\rm B}$ $\left(\frac{r'\rm mag}{\rm arcsec^2}\right)$ | $\mu_{\rm T}$ $\left(\frac{r'\rm mag}{\rm arcsec^2}\right)$ | $(g'-r')_{\rm B}$ (ABmag) | $(g'-r')_{\rm T}$ (ABmag) |
|---|---|---|---|---|
| IC 1197 | 21.9 | 24.7 | 0.41 | 0.35 |
| IC 2233 | 23.20 | 24.31 | 0.11 | 0.07 |
| NGC 3279 | 21.21 | 23.58 | 0.76 | 0.62 |
| NGC 3501 | 21.73 | 23.09 | 0.54 | 0.44 |
| NGC 3592 | 21.84 | 23.57 | 0.54 | 0.62 |
| NGC 4244 | 22.70 | 25.75 | 0.25 | 0.28 |
| NGC 4330 | 22.05 | *nd* | 0.49 | *nd* |
| NGC 4437 | 22.00 | 25.13 | 0.60 | 0.61 |
| NGC 5023 | 22.56 | *nd* | 0.36 | *nd* |
| NGC 5529 | 22.69 | 24.17 | 0.54 | 0.63 |
| NGC 5907 | 21.98 | 23.65 | 0.50 | 0.29 |
| PGC 029466 | 22.24 | *nd* | 0.25 | *nd* |
| UGC 01839 | 23.07 | *nd* | 0.39 | *nd* |
| UGC 01970 | 21.94 | 23.19 | 0.74 | 0.59 |
| UGC 04725 | 23.13 | 24.40 | 0.31 | 0.27 |
| UGC 04970 | 23.38 | *nd* | 0.31 | *nd* |
| UGC 05347 | 21.42 | 23.16 | 0.47 | 0.40 |
| UGC 06080 | 23.01 | *nd* | 0.30 | *nd* |
| UGC 06509 | 23.19 | *nd* | 0.14 | *nd* |
| UGC 06667 | 22.53 | 23.98 | 0.52 | 0.61 |
| UGC 06791 | 21.90 | 23.85 | 0.43 | 0.41 |
| UGC 06862 | 23.27 | *nd* | 0.38 | *nd* |
| UGC 07153 | - | 23.49 | 0.84 | 0.23 |
| UGC 07802 | 22.65 | 24.42 | 0.35 | 0.36 |
| UGC 07991 | 22.15 | *nd* | 0.58 | *nd* |
| UGC 08146 | 23.61 | 25.59 | 0.14 | 0.36 |
| UGC 08166 | 23.89 | *nd* | 0.25 | *nd* |
| UGC 09242 | 23.49 | *nd* | 0.25 | *nd* |
| UGC 09249 | 23.50 | *nd* | 0.15 | *nd* |
| UGC 09345 | 22.47 | *nd* | 0.38 | *nd* |
| UGC 09760 | 23.77 | *nd* | 0.25 | *nd* |
| UGC 09977 | - | 23.28 | 1.57 | 0.43 |
| UGC 10288 | 22.63 | 24.57 | 0.63 | 0.41 |
| UGC 12281 | 21.82 | 23.64 | 0.53 | 0.27 |

Table 2.5: Measured quantities at the break distance (B subscript) and at the truncation radius (T subscript). *nd* represents a non-detected truncation. The typical error for the $(g'-r')$ color profile is 0.10 AB mag at the break radius and 0.22 AB mag at the truncation radius.

characteristic radius detection.

### 2.3.2 Overall behavior

To exemplify the findings of our chapter, we will focus on the interpretation of those objects that, in particular, better reflect the general behavior of the surface brightness profiles of our sample. In any case, the same information is available for all the galaxies in Appendix A.

A paradigmatic example of the behavior found in the surface brightness profiles is found in NGC 4244 (Fig. 2.6). In the inner parts of the galaxy, the shape of the surface brightness profile is dominated by an exponential decline but, reaching a break radius $r \sim 290$" (red vertical line in Fig. 2.6), the slope becomes more pronounced. If we keep moving farther away, we find a second change in the exponential behavior (blue line) happening at $r \sim 550$". In the image of the galaxy shown in the bottom right panel, we can see how the first break radius (red lines) marks an inner disk, while the second break radius is very close to the visual edge of the galaxy for this exposure. It is worth noting here that the asymmetry of the brightness distribution in this object (see §2.2.1) makes the break radii different for the two sides of the galaxy. This has been already noticed in several studies (de Jong et al. 2007; Comerón et al. 2011; Holwerda et al. 2012). While Holwerda et al. (2012) noted a bright star-forming knot on either side of this galaxy but at slightly different radii, Comerón et al. (2011) stated that this asymmetry "can be explained by a combination of the galaxy not being perfectly edge-on and a certain degree of opacity of the disk". de Jong et al. (2007) proposed this asymmetry as the cause of the difference between their measurements for the break radial distance of the "shorter" galactic side, and the results of van der Kruit & Searle (1981) and Fry et al. (1999), who placed the break radius at around 570" as a consequence of averaging both sides of the galaxy. It is worth noting that this asymmetry makes the breaks smoother that in the case of more symmetric galaxies.

Lastly, in the stellar surface mass density plot, the second radius is associated with a steeper drop in both profiles than the first break, which has only a minor feature in Fig. 2.6 like that in the surface brightness profiles.

Another representative example (in this case a symmetric galaxy) is NGC 5907 (Fig. 2.7). The surface brightness profiles resemble a typical TII, with the inner break around 240". As in the case of NGC 4244, there is a second change in the exponential behavior at a radius $r \sim 330$".

A clear difference with NGC 4244 are the high values of the $(r' - 3.6\mu m)$ color in the central region of the galaxy. Knowing that the IR band is less sensitive to dust attenuation, this red value of the $(r' - 3.6\mu m)$ color could

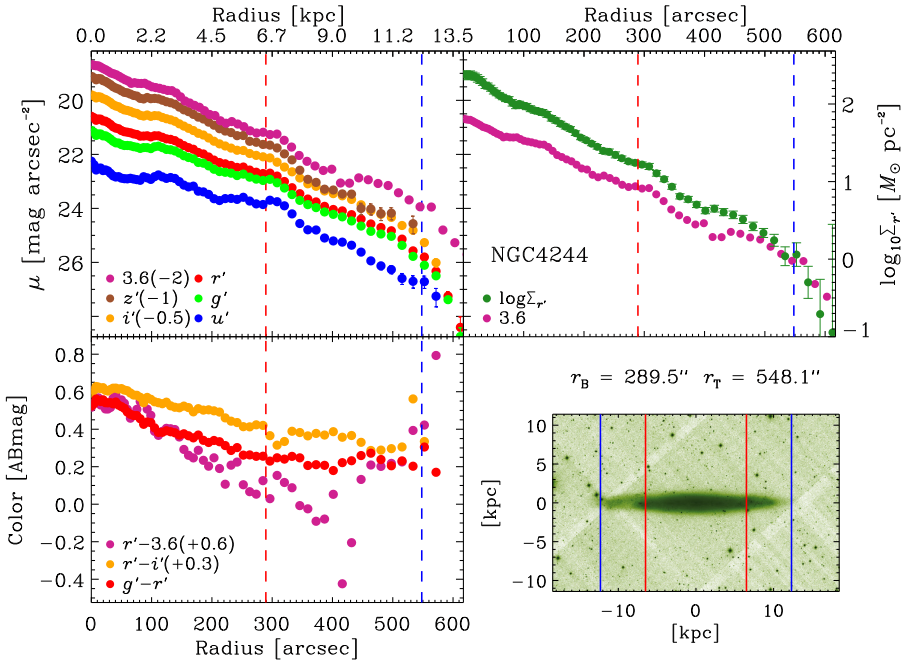


Figure 2.6: Surface brightness, color and stellar surface mass density profiles of NGC 4244. The upper left panel shows six surface brightness profiles from the different photometric bands used in the current chapter. Dashed vertical lines mark where a change in the exponential behavior happens. On the upper right panel are simultaneously plotted the stellar surface mass density profile and the $3.6\mu m$ surface brightness profile. The bottom left panel shows the three deeper color profiles from the available photometric bands. Lastly, the bottom right panel is occupied by a $g'$-band image of the galaxy. For this object the surface brightness distribution shows two clearly differentiated regions: one inner region before the red line and a second outer region after the blue line. The position of the two breaks is shown on the bottom right panel. The last characteristic radius is near to the visible edge of the galaxy and it is reflected as a drop in the stellar surface mass density profile. On the other hand, the first break is clearly within the galactic disk and does not seem to affect dramatically the behavior of the mass distribution.

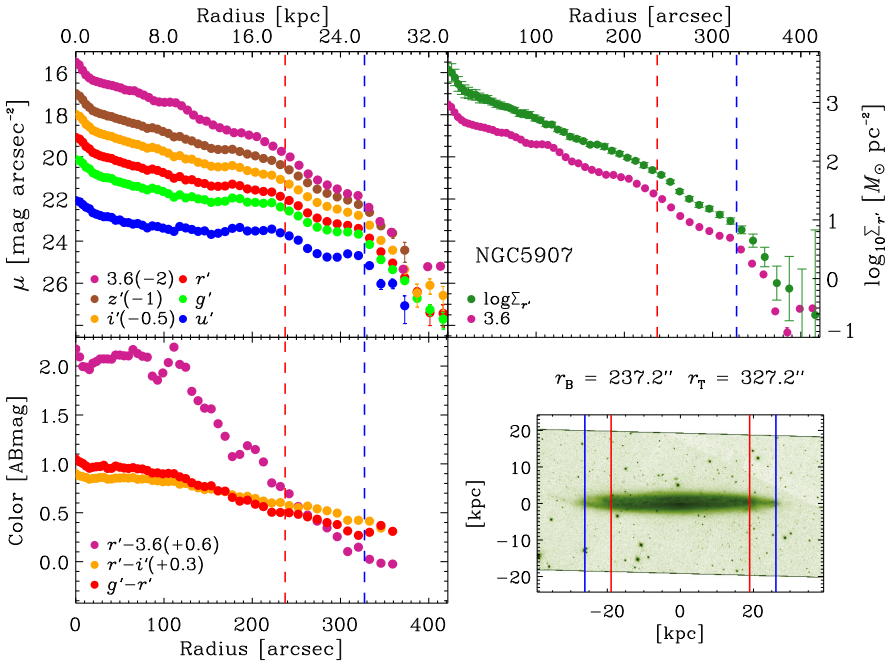


Figure 2.7: As in Fig. 2.6, now for NGC 5907. The first break radius is placed at around 240". The farther break radius can be found at $\sim 330''$. Contrary to what we observe in NGC 4244, there is a big difference between the values of the optical color profiles and the $(r' - 3.6\mu m)$ color profile that could be related to a stronger dust attenuation of the inner parts of this galaxy compared to NGC 4244.

be explained by the attenuation of dust in the optical bands. This is a very common behavior among our sample of galaxies since it is clearly present in, at least, 12 objects (see Appendix A). Paying attention to the stellar surface mass density plot, one can see again how the change in the slope is much pronounced at the second break radius compared to the change at the inner break radius. This time, being the galaxy very symmetric, this change is clearly visible.

### 2.3.3 Feature classification

Many of our galaxies (18 out of 34) show two break radii in their profiles. The characteristics of the breaks seems to be different (see §2.3.2) depending whether they are in the inner or in the outer regions of the disk. For this reason we attempt to establish an observational classification for these features. Assuming that both breaks have a different physical origin, we have studied their characteristics in those cases when it was easy to distinguish one type from the other, i.e., when both breaks appear simultaneously in the same galaxy. Having characterized the type of the break, that allowed us to extent the classification to those galaxies where only one break was present in the surface brightness profile.

We labeled the first radius as the break radius ($r_{\rm B}$) and the second radius as the truncation radius ($r_{\rm T}$). In order to define an empirical criterion, we have investigated the distributions of these breaks and truncations as a function of two different parameters: $h_0/h_{\rm feature}$ (with $h_0$ the innermost scalelength and $h_{\rm feature}$ the scalelength after the break ($h_{\rm B}$) or the truncation ($h_{\rm T}$)) and $r_{\rm feature}/h_{\rm feature}$ (with $r_{\rm feature}$ representing $r_{\rm B}$ or $r_{\rm T}$, i.e., the radial distance from the galactic center to the break or the truncation position). The meaning of each parameter is exemplified in Fig. 2.8.

Fig. 2.9 shows the histograms for the breaks and truncation vs each one of the above defined ratios, measured in the SDSS $r'$-band surface brightness profiles. The breaks distribution is shown in red while the truncations are represented by a blue histogram. It is clear from Fig. 2.9 that breaks and truncations are partially degenerated when using the $h_0/h_{\rm feature}$ parameter but both characteristic radii are fully differentiated using the $r_{\rm feature}/h_{\rm feature}$ parameter. We find $r_{\rm feature}/h_{\rm feature} = 5$ as a typical value defining the break-truncation boundary.

We define, then, a break on the surface brightness profile as a slope change (from $h_0$ to $h_{\rm B}$), occurring at a radial distance $r_{\rm B}$, if the ratio between $r_{\rm B}/h_{\rm B}$ is less than 5. Conversely, truncations are changes in the slope ($h_{\rm T}$) of the surface brightness profiles happening at a radius $r_{\rm T}$, with a ratio $r_{\rm T}/h_{\rm T}$ greater than 5. Applying this recipe to the whole sample of galaxies, we can analyze separately

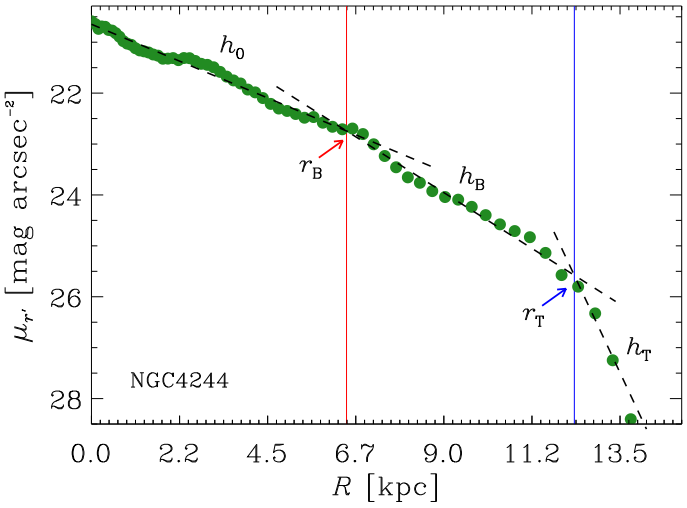


Figure 2.8: Exemplification of the meaning of the parameters $h_0$, $h_B$, $h_T$, $r_B$ and $r_T$ using the $r'$-band surface brightness profile (NGC 4244).

both features and study whether they are actually different phenomena. We note that in Comerón et al. (2012) they use a slightly different notation in which "break" describes all changes in slope, with Type II breaks being termed "truncation" and Type III breaks being called "antitruncations". Our galaxies have been traced out further than in most previous studies, and this leads to our recognition of a second break in some cases. Breaks with $r_B/h_B > 5$ are called truncation in keeping with previous nomenclature even if there is no clear evidence for a sharp end to the disk. In fact, most of our truncations are transitions to a far-outer region that may be as exponential as the inner regions, although with a steeper decline. Studies extending outer disk surface photometry to greater radii with star counts do not find a sudden drop-off either (Richardson et al. 2008; Saha et al. 2010; Grossi et al. 2011; Barker et al. 2012; Radburn-Smith et al. 2012a).

In Fig. 2.10 we show three examples of a galaxy with break *and* truncation (top), a galaxy where only the break has been detected (middle) and a galaxy with just a truncation (bottom) using our criteria. The red and blue lines mark the break and truncation radii (respectively) in both the surface brightness profiles and in the galaxy images. It its clear from Fig. 2.10 that the break occurs closer to the galactic centre compared to the truncacion which appears

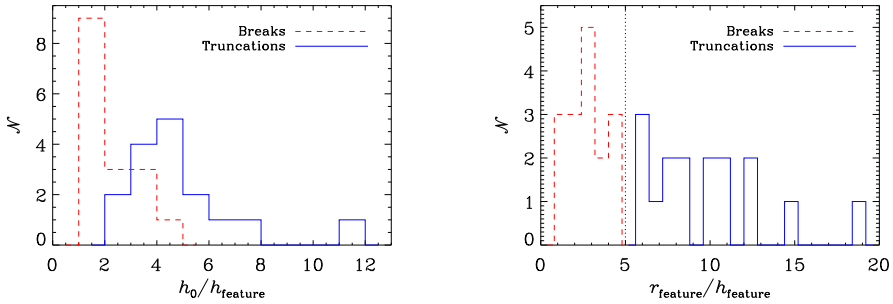


Figure 2.9: Histograms representing the distribution of breaks and truncation versus the $h_0/h_{\rm feature}$ (left) and the $r_{\rm feature}/h_{\rm feature}$ (right) parameters where $h_0$ is the innermost exponential scalelength (between the galactic center and the first break) and $h_{\rm feature}$ is the exponential scalelength after the first break (*break*) or after the second break (*truncation*), measured in the SDSS $r'$-band. $r_{\rm feature}$ represents the distance from the center of the galaxy where the break or the truncation is measured. The degeneracy shown in the left panel between both features is broken in the right panel.

near the very end of the optical disk. Also, the change in the exponential scalelength seems to be stronger after the truncation than after the break.

We show in Tables 2.4 and 2.5 the summary of all the measurements and the derived quantities for breaks and truncations.

### 2.3.4 Inner break analysis

Looking at the relative frequencies of the different profile types around the inner break radius, 82±16%[3] (28 cases) of our galaxies can be classified as TII (i.e., after the break there is a downbending on their surface brightness distribution). For the TI and TIII we found frequencies of 6±4% (2 cases) and 12±6% (4 cases) respectively. These values are different than those found by Pohlen & Trujillo (2006) (10%/60%/30% for TI/TII/TIII) but two factors must be taken into account. On one hand, having 34 galaxies, the statistical analysis is not as robust as in the case of Pohlen & Trujillo (2006). On the other hand, the study of Pohlen & Trujillo (2006) includes morphological types from Sb to Sdm while our sample only collects Sc or later spiral types. It is well established (Pohlen & Trujillo 2006; Gutiérrez et al. 2011) that there exists a trend in the sense that TII becomes dominant in late-type galaxies. If the statistics of Pohlen &

[3]The errors are given by $\Delta T_{\rm i} = \sqrt{N_{\rm T_i}}/N_{\rm S}$ where $N_{\rm T_i}$ is the number of $\rm T_i$ profiles in a sample of $N_{\rm S}$ elements.

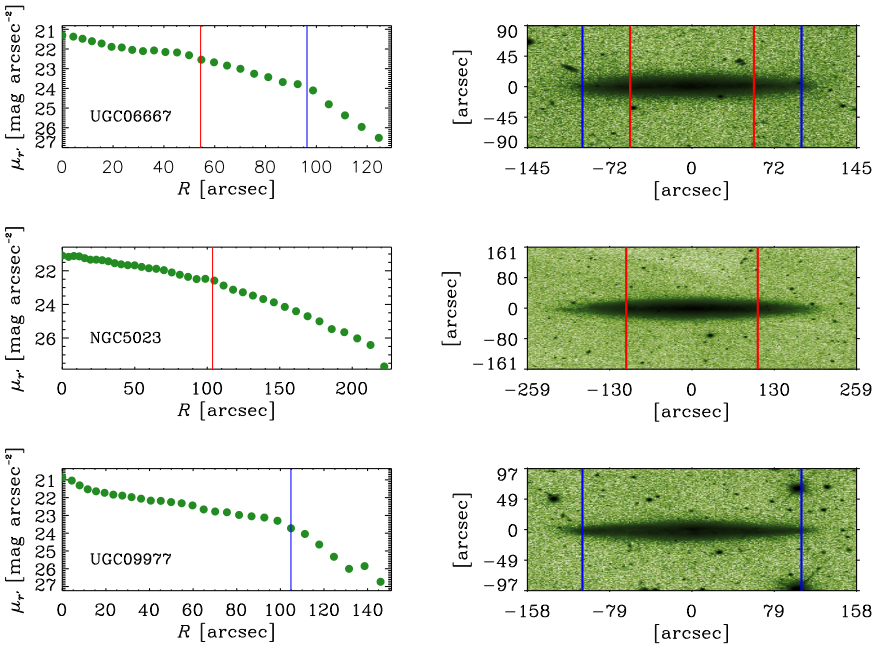


Figure 2.10: Upper panel: UGC 6667 showing both a break (red line) and a truncation (blue line). Middle panel: The galaxy NGC 5023 with a break marked in red. There is a hint of a truncation around $r \sim 210$ arcsec but as there were not enough points above the surface brightness limit, we did not perform a fit over that region. Lower panel: Galaxy UGC 9977 where we only detected a truncation. The right column shows the position of the breaks and truncations over the galaxy images.

| Band | Break $\left(\frac{\text{mag}}{\text{arcsec}^2}\right)$ | $\pm\Delta$ $\left(\frac{\text{mag}}{\text{arcsec}^2}\right)$ | Truncation $\left(\frac{\text{mag}}{\text{arcsec}^2}\right)$ | $\pm\Delta$ $\left(\frac{\text{mag}}{\text{arcsec}^2}\right)$ |
|---|---|---|---|---|
| $u'$ | 24.0 | 0.1 | 25.7 | 0.2 |
| $g'$ | 22.9 | 0.1 | 24.6 | 0.2 |
| $r'$ | 22.5 | 0.1 | 24.2 | 0.2 |
| $i'$ | 22.3 | 0.2 | 23.9 | 0.2 |
| $z'$ | 22.1 | 0.2 | 23.7 | 0.2 |
| $3.6\mu m$ | 22.7 | 0.2 | 24.5 | 0.2 |

Table 2.6: Mean surface brightness at the break (second column) and at the truncation (fourth column) radius in the six photometric bands employed in this chapter.

Trujillo (2006) are re-calculated for the same morphological range as used in the current chapter, we find that the relative frequencies become compatible (6±4% vs 12±7% for TI, 82±16% vs 76±17% for TII and 12±6% vs 12±7% for TIII)

The mean surface brightness value for the TII inner breaks is 22.5 ± 0.1 mag arcsec$^{-2}$ in the $r'$ band. For the others bands employed in the current chapter, the mean surface brightness at the break radius are listed in Table 2.6. We find a mean radius equal to 7.9 ± 0.9 kpc which is in agreement with the result of Pohlen & Trujillo (2006) who found a typical radius of 9 ± 3 kpc. The break scalelength $h_{\rm B}$ has a mean value of $2.7 \pm 0.3$ kpc.

Fig. 2.11 shows the values for the $r'$-band surface brightness, the $(g' - r')$ color and the radial distance $\{\mu_{r'}$, $(g' - r')$, $r_{\rm B}\}$ measured at the break radius (only TII profiles), plotted against the $M_{\rm B}$ and the maximum rotational velocity of the galaxy. In each plot it is over-plotted the Spearman's rank correlation coefficient[4]. Significant correlations are found between the break radius and $M_{\rm B}$, and between the $(g' - r')$ color at the break and the maximum rotational velocity (top right and bottom left panels, respectively).This correlation between the break radius and $M_{\rm B}$, and the fact that our sample is limited to objects brighter than $M_{\rm B} = -17$ can explain why we marginally measure a mean break radius smaller than Pohlen & Trujillo (2006), whose galaxies were brighter than $M_{\rm B} = -18.4$

[4]The Spearman's rank correlation coefficient varies between -1 and 1. The closer its absolute value is to one, the stronger the correlation.

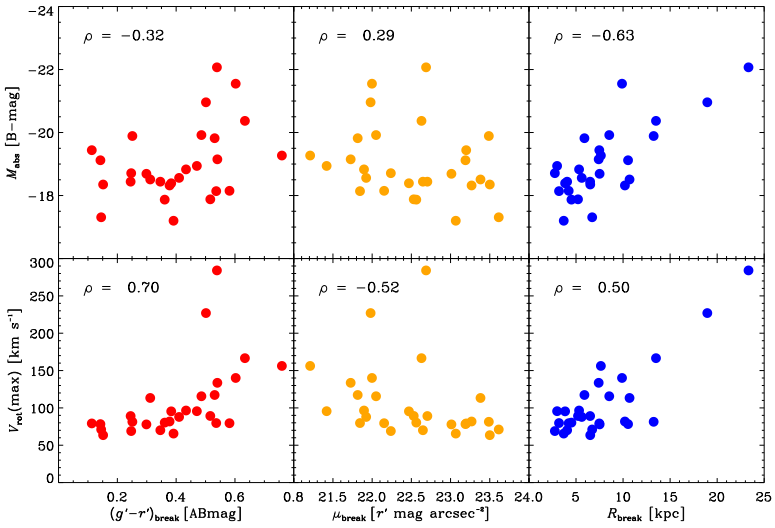


Figure 2.11: *Breaks:* correlations between $(g' - r')$ (left), $\mu_{r'}$ (center) and $r_{\rm B}$ (right) with the $B$-band absolute magnitude $M_{\rm B}$ (top) and with the maximum rotational velocity (bottom). The Spearman's rank correlation coefficient ($\rho$) is over-plotted.

### 2.3.5 Truncation analysis

We found that all the profiles are downbending and steeper after the truncation than after the inner break, with a mean value for the scalelength $h_{\rm T}$ equal to 1.5±0.1 kpc. The $r'$-band surface brightness has a mean value at the truncation radius of 24.1 ± 0.2 mag arcsec$^{-2}$ (see Table 2.6 for the mean values in the other bands) and the averaged radial distance is $14 \pm 2$ kpc. In average, the $3\sigma$ sky level in the $r'$-band is $\sim$ 3.5 mag arcsec$^{-2}$ dimmer than the typical surface brightness of the truncations so our results are not strongly affected by the sky subtraction process. The typical signal to noise ratio at the truncation radius is $\sim$ 10 in the $r'$ band.

In the case of the truncations, we also looked for correlations between the same set of parameters as in Fig. 2.11, but measured obviously at the truncation radius. The results of the analysis are in Fig. 2.12, where strong correlations appears between $M_{\rm B}$ and the maximum rotational velocity, and the radius where the truncation occurs.

It should be noted that the statistics derived in Figs. 2.11 and 2.12 are heavily influenced by a couple of points due to NGC 5907 and NGC 5529. The latter has a boxy/peanut bulge and a warped outer disk while NGC 5907 shows

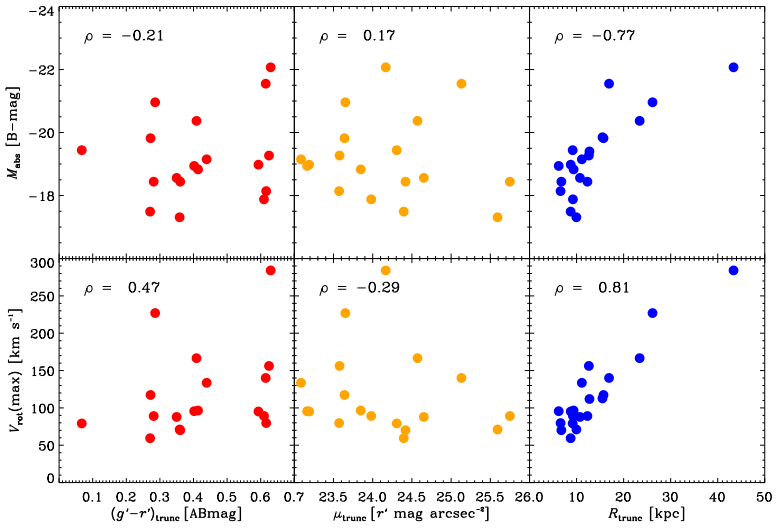


Figure 2.12: *Truncations:* correlations between $(g' - r')$ (left), $\mu_{r'}$ (center) and $r_{\rm T}$ (right) with the $B$-band absolute magnitude $M_{\rm B}$ (top) and with the maximum rotational velocity (bottom). The Spearman's rank correlation coefficient ($\rho$) is over-plotted.

a bulge and a small warp too. If we exclude those two galaxies from the statistical analysis, the Spearman's rank correlation coefficient changes from 0.50 to 0.44 in the $V_{\rm rot}$(max) vs $r_{\rm B}$ relation and from 0.81 to 0.73 in the $V_{\rm rot}$(max) vs $r_{\rm T}$ relation.

## 2.4 Discussion

### 2.4.1 Comparison with previous studies

Inner breaks and truncations, as defined in §2.3.3, have different characteristic parameters. Breaks appear closer to the galactic center compared to truncations ($r_{\rm B} \sim 8$ kpc; $r_{\rm T} \sim 14$ kpc) and the typical exponential scalelength is also smaller after the breaks than after the truncations ($h_{\rm B} \sim 3$ kpc; $h_{\rm T} \sim 1.5$ kpc). In addition, we have found that the ratio between the mean radius for breaks and truncations ($\langle r_{\rm T} \rangle / \langle r_{\rm B} \rangle = 1.8 \pm 0.5$ among our sample of galaxies) is very similar to the ratio $\langle r_{\rm EO}/h_0 \rangle / \langle r_{\rm FO}/h_0 \rangle = 1.8 \pm 0.9$ between the break radii in edge-on galaxies by van der Kruit (1987) and those in face-on galaxies by Pohlen & Trujillo (2006). Since the latter results are normalized to the innermost exponential scalelength, this quotient between edge-on and face-on measurements

can be only fairly compared to our results if the innermost scalelength $h_0$ remains unchanged while looking at a galaxy in both projections. In this sense, Pohlen et al. (2007) found that their de-projected $h_0$ values match with the range given by Pohlen & Trujillo (2006) if the influence of dust is taken into account.

It is possible, then, that the previous discrepancies found for the position of the breaks between edge-on and face-on studies can be explained as follows. Face-on studies usually measure the break radius but the truncation happens (due to the orientation) at very low surface brightness (typically $\sim$ 26.5 mag arcsec$^{-2}$), probably beyond the surface brightness limit. On the contrary, thanks to the line of sight integration, in the edge-on observations the truncation appears at higher surface brightness and it can be detected. The transition to a steeper decline after the break in the edge-on profiles can be smoothed because of this particular projection too, making it more difficult to detect this feature in edge-on galaxies than in the face-on counterpart and for this reason may have remained unnoticed in previous papers (but see Comerón et al. 2012).

A natural prediction of our analysis is that truncations should be systematically observed in face-on projections if the images were deep enough. Just recently Bakos & Trujillo (2012) used very deep data from SDSS Stripe82 to explore the very faint regimes of disks in face-on projections by obtaining surface brightness profiles down to $\sim$ 30 $r'$-band mag arcsec$^{-2}$. Bakos & Trujillo have not found any clear evidence for a truncation on these profiles but they have reported that the surface brightness profiles of the stellar disks show a smooth continuation into what they have identified as stellar halos. These stellar halos start to dominate the surface brightness profiles at $\sim$ 27.5. $r'$-band mag arcsec$^{-2}$ Coincidently, this means that observing truncations in face-on projections could be hindered due to the lack of contrast between the disk and the stellar halo components. The result of Bakos & Trujillo (2012) would, if confirmed, point out that our only opportunity of studying truncations in spiral galaxies could be limited to edge-on observations, unless an accurate parametrization and subtraction of the stellar halo component can be performed.

### 2.4.2 Break-truncation scenario

If breaks and truncations are actually two differentiated features, the two main theories (see Chapter 1, §1.1.1) proposed to explain the break formation are not mutually exclusive, each playing a role at different distances from the galactic center. On the one hand, the averaged value found here for the break radius is compatible with the face-on picture of a break caused by a threshold for the star

formation in the disk. On the other hand, we have found a mean truncation radius which is extremely well correlated with the maximum rotational velocity of the galaxy ($\rho = 0.81$). The above ideas are reinforced if we look at the different degree of correlations between the break/truncation radius and the maximum rotational velocity.

We can calculate the specific angular momentum of the disk to exemplify the differences between the two breaks by following the empirical expression given by Navarro & Steinmetz (2000):

$$j_{\rm disk} \approx 1.3 \times 10^3 \left[\frac{V_{\rm rot}({\rm max})}{200\ {\rm km \cdot s^{-1}}}\right]^2 {\rm km\ s^{-1}\ h^{-1}\ kpc}$$

Note that, following the equation above, the derived specific angular momentum of the disk is just a re-scaling of the maximum rotational velocity of the galaxy. Then, this specific angular momentum is showed as auxiliary information but it has not influence in further results.

Fig. 2.13 shows how the break and truncation radii correlate with the maximum rotational velocity and with the specific angular momentum of the disk. The Spearman's rank coefficient reveals a very strong correlation ($\rho_{\rm trunc} = 0.81$) between the maximum rotational velocity (and the specific angular momentum of the disk) and the truncation radius. On the contrary, the correlations between the same dynamical parameters and the break radius are significantly weaker ($\rho_{\rm break} = 0.50$).

From Fig. 2.13 it is clear that the truncation radius correlates with the maximum rotational velocity for the whole range of values in the sample but the break radius correlates well only for those galaxies with $r_{\rm B} \gtrsim 8$ kpc. Below this value, the break distance seems to be decoupled from the rotational velocity. In other words, for small disks, with $V_{\rm rot} < 100$ km s$^{-1}$, $r_{\rm B}$ and $V_{\rm rot}$ are not linked. The break radius seems to be strongly related to the maximum rotational velocity only when it happens in a galaxy with a significant angular momentum. This behavior supports the picture of truncations caused by the distribution of the galactic angular momentum and the break most likely related with a threshold in the gas density. Only when the rotational velocity is significant, the threshold in the star forming gas seems to be affected by the angular momentum distribution.

In the stellar surface mass density profile, the break has almost disappeared in many cases compared to the surface brightness profiles but the truncation barely changes (see Figs. 2.6 and 2.7). In particular, we find a typical value for the ratio $\langle h_0/h_{\rm B}\rangle_{\log\Sigma} = 1.6 \pm 0.1$ at the break distance. Truncations on the contrary, show a ratio $\langle h_0/h_{\rm T}\rangle_{\log\Sigma} = 2.8 \pm 0.3$, associated with a quicker drop

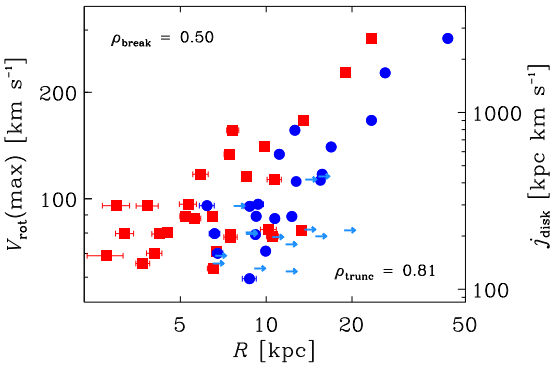


Figure 2.13: Correlations between the positions of the inner breaks (red squares) and the radial position of the truncations (blue dots) versus the maximum rotational velocity and vs the specific angular momentum of the disk. Light blue arrows represent $r_{\rm max}$ as defined in §2.3.1. These arrows correspond to those galaxies where no truncation has been detected (so, they should be considered as a lower limit for the truncation radius). The Spearman's rank correlation coefficients for breaks (top left) and truncations (bottom right) are over-plotted.

in the stellar surface mass density profile than in the break case. This is also in agreement with this *break-truncation* scenario where a fast drop in the density of stars is expected after the truncation but not necessarily after the breaks.

However, two things must be noted here about the physical origin of breaks and truncations. First of all, finding a feature in a modern disk is not very clearly tied to cosmological accretion because the disk can adjust its mass distribution during its life (e.g. Roškar et al. 2008). Thus, the origin of truncations related to the angular momentum of the protogalactic cloud should be treated carefully. Also, regarding the formation of breaks, there are observational evidences that point to some level of star formation in the outskirts of spiral galaxies (Bush et al. 2010; Barker et al. 2011), arguing against a completely quenched star formation after the break radius.

Another important point regarding the break-truncation differentiation is that we have measured an averaged ratio between the scalelength after the breaks ($h_{\rm B}$) and after the truncations ($h_{\rm T}$) equal to $\langle h_{\rm B}/h_{\rm T}\rangle = 1.9 \pm 0.4$. This means that the change in the slope of the surface brightness profile is a factor of $\sim$ 2 stronger for truncations than for breaks. This result could explain why van der Kruit & Searle (1981), studying edge-on galaxies, found a sharp *cut-off* (truncation) in their surface brightness profiles while face-on studies find a feature (break) which corresponds to a softer *break* in the radial light

distribution (see Pohlen & Trujillo 2006, §6 in that paper).

The fact that the ratio $r_{\rm feature}/h_{\rm feature}$ is a good indicator to separate breaks from truncations (see Fig.2.9) can be fully understood now. For the truncations, the numerator $r_{\rm feature}$ is larger and the denominator $h_{\rm feature}$ is smaller compared to the breaks. The ratio between both quantities has then, a significantly higher value for the truncations than for the breaks:

$$\left[\frac{r_{\rm B}(\downarrow)}{h_{\rm B}(\uparrow)}\right](\Downarrow) \;\leftrightsquigarrow\; \left[\frac{r_{\rm T}(\uparrow)}{h_{\rm T}(\downarrow)}\right](\Uparrow)$$

We can conclude also that the edge-on orientation is better to study the outermost parts of galaxies because it allows us to reach the outskirts with a higher surface brightness than in the face-on case. A disadvantage of this edge-on projection is that the study of the color and stellar surface mass density profiles is less robust than in the face-on case due to the strong, yet measurable, influence of dust and line of sight integration problems (see §2.2.2). As an example, we can compare Fig. 2 in the paper of Bakos et al. (2008) with Fig. 2.11 and Fig. 2.12 (top-left panels) in this chapter. Unlike Bakos et al. (2008), we did not find any clear correlation between the $(g' - r')$ color at the break radius and the $M_{\rm B}$ of the galaxy.

To sum up, two differentiated features can be found in the light distribution of the disk in spiral galaxies: breaks and truncations. Face-on galaxies seem to be the perfect candidates to study breaks because both the surface brightness profile and the color profiles are available, with moderate dust influence. The advantage of integrating along the line of sight is crucial in the case of truncations, since a truncation is a feature that happens at very low surface brightness. However, the color profiles in the edge-on projection have to be interpreted with great care. Also, in the edge-on projection, it is not possible to classify the breaks depending on the morphology of the galaxy (see Pohlen & Trujillo 2006, their section 4.1) unless a two-dimensional disk decomposition is made (Gadotti 2012).

## 2.5 Conclusions

Using SDSS and S$^4$G imaging, we have found the following important aspects regarding the behaviour of surface brightness profiles in edge-on late-type spirals:

1. The majority of our galaxies ($82 \pm 16\%$) show a TII surface brightness profile as those found in photometric studies of face-on galaxies, with the

break occuring at a mean radial distance from the galactic center equal to 7.9 ± 0.9 kpc.

2. Truncations, previously described in edge-on galaxies as a quick drop in the surface brightness profile, have been found in 20 of the 34 galaxies in our sample. This drop, also observed in the stellar surface mass density profile, occurs at an average radial distance of 14 ± 2 kpc.

3. For many galaxies, breaks and truncations coexist as two differentiated features in the light distribution of the disks in spiral galaxies.

4. Strong correlations exist between the truncation radius and the maximum rotational velocity, and the specific angular momentum of the disk. These correlations are, however, less strong in the case of breaks. This result reinforces the idea that breaks are more likely a phenomena related to a star formation threshold whereas truncations have a strong connection with the maximum angular momentum of the galaxy.

5. Color and stellar surface mass density profiles are both very sensitive to the line of sight projection and to the presence of dust. Their interpretation in edge-on systems is not trivial and could be the cause of the differences between some of our results and those found in face-on works (e.g. correlations between $M_{\rm B}$ and break radius).

# 3

# Stellar haloes outshine disc truncations in low-inclined spirals

This chapter has been published as *Martín-Navarro et al. 2014, MNRAS, 441, 2809*

The access to deep and high-quality imaging from both the Sloan Sky Digital Survey (SDSS) Data Release 7 (Abazajian et al. 2009) and the *Spitzer* Survey of Stellar Structure in Galaxies ($S^4G$) (Sheth et al. 2010) has allowed to shed more light on the break-truncation dichotomy. Thanks to these surveys, Martín-Navarro et al. (2012) and Comerón et al. (2012) have shown that both breaks and truncations can be observed simultaneously in edge-on galaxies. Consequently, there is growing consensus that truncations, usually observed in edge-on galaxies, and breaks, initially measured in face-on systems, are not the same phenomenon. However, an unavoidable question remains unanswered: Why are we able to detect both breaks and truncations in edge-on galaxies but only the former in face-on orientations?

To complete the observational picture of the radial light distribution of spiral galaxies it is necessary to take into account the stellar halo. Only a few photometric studies (e.g., Zibetti et al. 2004; Zibetti & Ferguson 2004; Jablonka et al. 2010; Zackrisson et al. 2012; Bakos & Trujillo 2012; Trujillo & Bakos 2013; Peters et al. 2014) have been able to reach surface brightnesses $\mu_{\rm r} \sim 30$ mag arcsec$^{-2}$, deep enough to study the stellar halo properties. Although the formation and evolution of stellar haloes around spiral galaxies remains an open question, most observations point to old and moderately metal-poor

stars as the main component of these stellar haloes, probably assembled in merger/accretion events at redshifts $z > 1$ (Zibetti et al. 2004; Trujillo & Bakos 2013; Bakos & Trujillo 2012).

Trying to reconcile all the previous observational results, we have built a 3D disc galaxy model using an *exponential disc* plus *stellar halo*. Our model comfortably fits the current observational constraints on the photometrical structure of spiral galaxies. We show how this simple model is able to explain why different disc orientations prevent the general detection of truncations in low-inclined galaxies. Basically, the expected surface brightness of the stellar disc at the position of the truncation in a face-on orientation is so faint that this feature is outshone by the brightness of the stellar halo at that radial distance.

In Section 2 we present a compilation of observational results of face-on and edge-on galaxies; in Section 3 we describe the model and finally, in Section 4 we derive the main conclusions of this chapter.

## 3.1 Observational constraints to the model

To introduce the observational framework regarding breaks, truncations and stellar haloes in spiral galaxies, we compile in this section the current observational constraints that describe these features.

### 3.1.1 Breaks

Pohlen & Trujillo (2006) found in their sample of 85 low-inclined galaxies that downbending breaks appear, on average, at a radial distance of $2.5 \pm 0.6\ h_{\rm in}$, where $h_{\rm in}$ is the exponential scalelength before the break radius. Yoachim et al. (2012) measured a quite similar value of $2.5 \pm 0.2\ h_{\rm in}$ for the break radius among a sample of 12 nearby galaxies, while Erwin et al. (2008) and Gutiérrez et al. (2011) found slightly lower values ($1.8 \pm 0.2\ h_{\rm in}$ and $2.1 \pm 0.5\ h_{\rm in}$, respectively) for the break radius of early-type galaxy discs (with morphological types from S0 to SB). Breaks also present a characteristic ratio between the exponential scalelength before and after the break radius ($h_{\rm in}/h_{\rm out}$). In this sense, low-inclined spiral galaxies show a value for $h_{\rm in}/h_{\rm out} \sim 2$, with values typically varying from $h_{\rm in}/h_{\rm out} = 2.6 \pm 0.3$ (Erwin et al. 2008) to $h_{\rm in}/h_{\rm out} = 1.7 \pm 0.1$ (Gutiérrez et al. 2011). This scatter lies within the measurements of Pohlen & Trujillo (2006) who found a mildly peaked distribution ranging between $h_{\rm in}/h_{\rm out} = 1.3$-$3.6$

### 3.1.2 Truncations

The first results of van der Kruit & Searle (1982) placed the truncation radius at a radial distance of 4.2 ± 0.6 $h_{\rm in}$, significantly larger than the break radius. Barteldrees & Dettmar (1994) proposed a truncation radius of 3.7 ± 1.0 $h_{\rm in}$ which is compatible also with the results of Pohlen et al. (2000), who found an averaged truncation radius of 2.9 ± 0.7 $h_{\rm in}$. As discussed in Chapter 1, truncations are principally detected in edge-on galaxies. Nevertheless, Martín-Navarro et al. (2012) and Comerón et al. (2012) have shown that edge-on galaxies can simultaneously host breaks too. Thus, if no distinction is made between breaks and truncations while studying edge-on systems, the measurements can be confusing both features (breaks and truncations). This could be the reason for the large scatter in the values of the truncation radii found in the literature. For the ratio $h_{\rm in}/h_{\rm out}$ between the exponential scalelengths before and after the truncation radius, Martín-Navarro et al. (2012) found a mean value of 1.9 ± 0.4, very similar to the observed change in the exponential scalelength around the break radius. This measurement is in agreement with Comerón et al. (2012) who did not find significant differences between the $h_{\rm in}/h_{\rm out}$ distributions for breaks and truncations.

### 3.1.3 Stellar haloes

The current observational constraints on stellar haloes are not as strong as those on breaks and truncations because of the very low surface brightnesses where these haloes start to be visible, typically below $\mu \sim 28$ mag arcsec$^{-2}$ in the R band. Stellar haloes are usually detected as an excess of light with respect to the exponential decline of the discs in the outer parts of spiral galaxies ($R \gtrsim 15$ kpc) and they are observed not only in images (e.g., Trujillo & Bakos 2013; Bakos & Trujillo 2012; Peters et al. 2014), but in particular using star-counting techniques (e.g., Ferguson et al. 2002; Mouhcine et al. 2005; Ferguson et al. 2007; Ibata et al. 2009; Jablonka et al. 2010). The shape and the surface brightness of the stellar haloes are the same in edge-on and face-on galaxies. For example, Bakos & Trujillo (2012) found them at around $R \sim 20$ kpc, with a typical surface brightness in the SDSS $r'$-band of $\mu_{r'} \sim 28$ mag arcsec$^{-2}$ in a sample of low-inclined disc galaxies. In the edge-on galaxy NGC 3957, Jablonka et al. (2010) measured the stellar halo above 20 kpc above the galactic plane, at a surface brightness of $\mu_R = 28.5$ mag arcsec$^{-2}$. Wu et al. (2002) detected the stellar halo of the edge-on spiral NGC 4565 at 22 kpc measured along the minor axis, having a surface brightness of $\mu_{6660\text{Å}} = 27.5$ mag arcsec$^{-2}$

## 3.2 Model

To explain the proposed model in a clear way, this section is split into two parts. In the first subsection we describe the mathematical formulation of the model, along with the required information regarding the vertical distribution of the disc and the dust component. In the second part, we use this same model to reproduce the observed characteristics of two galaxies with similar properties in the $r'$-band, one seen with a low inclination (UGC 00929) and the other one observed in an edge-on orientation (UGC 00507).

### 3.2.1 Mathematical description

The disc component of our model is parametrised as an exponential function in both the radial (Freeman 1970; van der Kruit 1988; Pohlen et al. 2007) and the vertical direction (Wainscoat et al. 1989; de Grijs et al. 1997, 2001). Although the vertical exponential scalelength can vary with galactocentric distance (see de Grijs & Peletier 1997), for simplicity, we assume it is constant along the whole disc (van der Kruit & Searle 1981, 1982; Shaw & Gilmore 1990). In the radial direction, the model is characterised by two changes (a *break* and a *truncation*) in the exponential behaviour. Thus, the three-dimensional light distribution of our synthetic galaxy can be expressed in cylindrical coordinates $(R, z)$ as:

$$L(R, z) = L_0 \; L(R)\, e^{-|z|/h_{\rm z}} \; , \tag{3.1}$$

where $L_0$ is the luminosity at the centre of the disc and the radial light distribution is given by:

$$L(R) = e^{-R/h_{\rm I}} \Pi_{0,r_{\rm B}} + \; e^{-R/h_{\rm B}} \Pi_{r_{\rm B},r_{\rm T}} + \; e^{-R/h_{\rm T}} \Pi_{r_{\rm T},\infty} \; . \tag{3.2}$$

As mentioned before, Eq. (3.2) shows two changes in the exponential behaviour: the first one (*break*) is located at a radial distance $R = r_{\rm B}$, while the second change (*truncation)* occurs at $R = r_{\rm T}$. The light distribution is parametrised by the vertical exponential scalelength ($h_{\rm z}$) and also by the radial exponential scalelength before the break radius ($h_{\rm I}$), after the break radius ($h_{\rm B}$) and after the truncation radius ($h_{\rm T}$). The boxcar function $\Pi_{a,b}$ is defined as:

$$\Pi_{a,b} = \begin{cases} C_{a,b} & \text{if } a \leq R < b \\ 0 & \text{otherwise} \; , \end{cases}$$

where $C_{a,b}$ is constant, and $L(R)$ is continuous over the whole $R$-domain.

Although a certain level of clumpyness is expected in the dust distribution, we have only considered the diffuse component for the dust attenuation,

parametrising the extinction with a continuous spatial exponential function (Xilouris et al. 1997, 1998). This exponential approach has properly described the dust distribution in edge-on galaxies (Xilouris et al. 1999; Misiriotis et al. 2001) and a very careful description can be found in Popescu et al. (2011, §2.1). The extinction of the dust disc can be written as:

$$\kappa^{\rm dust}(\lambda, R, z) = \kappa^{\rm dust}(\lambda, 0, 0)\, e^{-R/h_R^{\rm dust}}\, e^{-|z|/h_z^{\rm dust}} \ , \tag{3.3}$$

where $\kappa^{\rm dust}(\lambda, 0, 0)$ is the extinction at the centre of the disc and $h_R^{\rm dust}$ and $h_z^{\rm dust}$ are the dust scalelengths in the radial and vertical directions.

Finally, the surface brightness profile of the stellar halo is modelled using a Sérsic (1968) law which has been widely used as a proxy for the projected light distribution of this component in spiral galaxies (e.g, de Jong 2008; Courteau et al. 2011; Bakos & Trujillo 2012). We do not describe the 3D structure of the halo (as we have done before for the disc) but we only model its projected surface brightness distribution. For simplicity, we assume that the stellar halo is spherical. The projected light distribution of the stellar halo is described as follows:

$$I^{\rm halo}(R) = I_{\rm eff}^{\rm halo} \exp\left\{-b_{\rm n}\left[\left(\frac{R}{R_{\rm eff}}\right)^{1/n} - 1\right]\right\} \ , \tag{3.4}$$

where $I_{\rm eff}$ is the intensity at the effective radius $R_{\rm eff}$, $n$ is the so-called Sérsic index and $b_{\rm n}$ is a function of the Sérsic index that, in good approximation, is given by $b_{\rm n} \simeq 2n - 0.324$ (e.g., Trujillo et al. 2001). To have a fair comparison with previous studies, we fixed the Sérsic index of the stellar halo to n=1. This choice properly represents the shape of the stellar halo surface brightness profile (Irwin et al. 2005; Ibata et al. 2007; Tanaka et al. 2010; Peters et al. 2014).

Eqs. (3.1) to (3.4) completely define the three-dimensional light distribution in our model. The observed surface brightness profile is given by the integration along the line of sight (LOS) of Eq. (3.1), attenuated by the dust component following Eq. (3.3) plus the contribution of the stellar halo in Eq. (3.4). Thus, the radial surface brightness profile of our synthetic galaxy, observed in an arbitrary orientation, can be written as:

$$I^{\rm obs}(R) = I^{\rm halo}(R) + \int_{\rm LOS} L(R, z) e^{-\tau(\xi,\lambda)}\, {\rm d}\xi \ , \tag{3.5}$$

where the optical depth $\tau(\xi, \lambda)$ is given by:

$$\tau(\xi, \lambda) = \int_{\rm LOS} \kappa^{\rm dust}(\lambda, R, z)\, {\rm d}\xi \ . \tag{3.6}$$

| Galaxy | $M_{\rm abs}$ ($B$-mag) | Morph. type | *incl* (deg) |
|---|---|---|---|
| UGC 00507 | -20.34 | Scd | 80.0 |
| UGC 00929 | -20.60 | SABc | 24.7 |

Table 3.1: Global parameters of the two galaxies analysed in this chapter (from the HyperLeda database).

### 3.2.2 Comparison with the data

The above model can simultaneously reproduce the typical surface brightness profiles of low and highly inclined spiral galaxies. In order to illustrate this, we have selected two galaxies, UGC 00929 (low-inclined) and UGC 00507 (highly-inclined), from the SDSS Stripe 82. The SDSS Stripe82 is a very deep photometric survey covering 275 deg$^2$ around the Celestial Equator and reaching $\sim$ 2 magnitudes deeper than the standard SDSS survey. These ultra-deep data are crucial to constrain the model since, as mentioned in §3.1.3, the stellar halo starts to dominate the surface brightness distribution at around $\mu_{r'} \sim 28$ mag arcsec$^{-2}$. Table 3.1 summarises the basic information about these two objects, found in the HyperLeda database (Paturel et al. 2003).

The SDSS $r'$-band radial surface brightness profiles were calculated in the same way that Bakos & Trujillo (2012) and Martín-Navarro et al. (2012) did for low and highly inclined spiral galaxies, respectively[1]: for UGC 00929 elliptical apertures were placed along the galaxy disc, while for the edge-on galaxy, UGC 00507, the profile was measured by placing a constant-width slit onto the galactic plane. The latter profile is noisier than the first one since, at the same radial distance, the number of pixels within a slit is much lower than within an elliptical aperture. This means that, by measuring the radial profile through a slit, we are limited to surface brightnesses above $\mu_{r'} \lesssim 27$ mag arcsec$^{-2}$, where the stellar halo contribution to the total surface brightness profile of the galaxy just starts to be important. To address this problem and complete the edge-on galaxy model below $\mu_{r'} \sim 27$ mag arcsec$^{-2}$, we measured the stellar halo of UGC 00507 by using circular apertures centred on the galaxy.

Apart from these radial surface brightness profiles, additional information about the vertical light distribution and about the dust was required to fully constrain our model. Typically, the vertical exponential scalelength is found to be $h_{\rm z} \sim 1/10\ h_{\rm r}$ (van der Kruit & Searle 1982; de Grijs & van der Kruit

[1] An extensive explanation on the surface brightness profile calculation process can be found in these two papers.

| | Face-on case (UGC 00929) | | | Edge-on case (UGC 00507) | |
|---|---|---|---|---|---|
| $\mu_{r'}^{\rm break}$ | 24.7 | [mag arcsec$^{-2}$] | $\mu_{r'}^{\rm break}$ | 24.0 | [mag arcsec$^{-2}$] |
| $r_{\rm B}$ | 4.1 | [$h_{\rm I}$] | $r_{\rm B}$ | 3.0 | [$h_{\rm I}$] |
| $h_{\rm B}$ | 1.7 | [$h_{\rm I}$] | $h_{\rm B}$ | 2.1 | [$h_{\rm I}$] |
| $r_{\rm T}$ | 6.0 | [$h_{\rm I}$] | $r_{\rm T}$ | 4.5 | [$h_{\rm I}$] |
| $h_{\rm T}$ | 3.4 | [$h_{\rm I}$] | $h_{\rm T}$ | 3.6 | [$h_{\rm I}$] |

Table 3.2: Modelled structural parameters of the galaxies used in this chapter.

1996). For the dust distribution we followed Xilouris et al. (1999), assuming a characteristic vertical scalelength $h_z^{\rm dust} \sim 1/20\ h_{\rm r}$ and a radial scalelength $h_R^{\rm dust} \sim 2\ h_{\rm r}$.

Once the surface brightness profiles for the two galaxies were obtained, we built up two synthetic galaxies that reproduce both the face-on and the edge-on surface brightness distributions. The structural parameter set that defines our synthetic galaxy models is listed in Table 3.2.

In Fig.3.1 we show how our simple model is able to reproduce the surface brightness profiles of low and highly-inclined galaxies. The structural parameters listed in Table 3.2 were not obtained by a systematised fitting process of the data showed in Fig.3.1 (dark green filled circles) since providing a precise characterisation of the observed data is not in the scope of the present chapter. Following a simplified approach, we tuned the free parameters in our model (see §3.2.1) to obtain a reasonable representation of the data, taking into account the observational constraints detailed in §3.1. That is the reason why no uncertainties are given for the structural parameters showed on Table 2.

## 3.3 Discussion and Conclusions

We present in Fig. 3.2, qualitatively, the main idea of this chapter: truncations in the surface brightness profile of low inclined spiral galaxies are outshone by the light of the stellar halo component.

The explanation for the lack of observational evidence of truncations in the radial light distribution of low-inclined galaxies is based on the different response that the stellar disk and the stellar halo have to the LOS integration. Whereas the surface brightness profile of a highly symmetric stellar halo is almost independent of orientation with respect to the observer, we expect from the model that the stellar disc is $\sim 2$ mag arcsec$^{-2}$ dimmer in a face-on than in an edge-on projection. It is the absence of contrast between the stellar disc

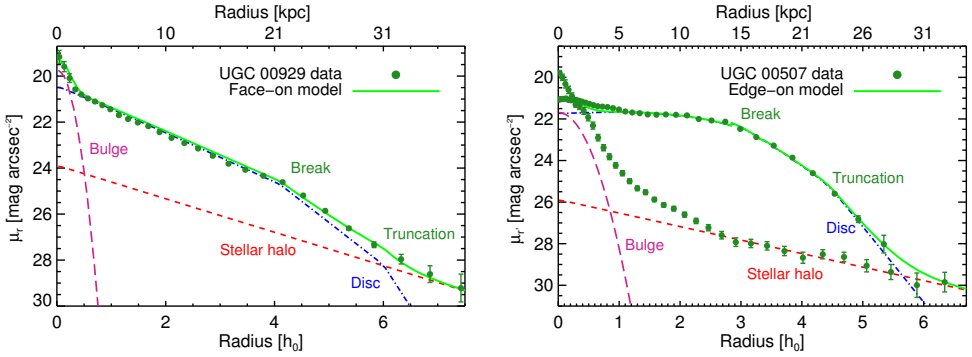


Figure 3.1: Surface brightness distributions of a face-on (UGC 00929) and an edge-on (UGC 00507) spiral galaxy. Our model fits to the surface brightness distribution are overplotted (green solid lines). We also show the different contributions to the final surface brightness profiles: blue dashed line for the disc, red dashed line for the stellar halo and purple dashed line for the bulge. Because of the LOS integration, the observed radial surface brightness profile of the edge-on galaxy is brighter, allowing us to measure the truncation in the radial light distribution of the stellar disk above the stellar halo contribution. However, the halo brightness outshines the truncation in the face-on case since the surface brightness of the stellar disk and the halo are similar at the radial distance where the truncation happens. Note that for UGC 00507, the stellar halo radial profile was obtained using circular apertures. This is a fair approach under the assumptions made in our model (see §3.2.1). Note, however, that the halo in UGC 00507 is $\sim$ 1 mag dimmer than in the face-on galaxy UGC 00929 at $\sim$ 30 kpc. This means that either the halo is intrinsically dimmer or that it does not obey a perfectly spherical symmetry.

and the stellar halo which prevents us from detecting truncations in the surface brightness profiles of low-inclined spiral galaxies.

However, our model does not necessary imply that truncations cannot be studied in face-on galaxies. The contribution of the stellar halo to the total light of a galaxy depends on the galaxy mass (see Fig.10 of Courteau et al. 2011). The lower the mass of the galaxy, the weaker the contribution of the stellar halo to the total light is. Low-mass spirals are then the most suitable candidates to distinguish between truncations and stellar haloes in face-on disc galaxies. Another option to detect truncations in low-inclined systems could be through the decomposition of the surface brightness profiles in separate components: bulge, thin and thick discs, stellar halo... However, since we do not yet have a complete characterisation of the radial light distribution of stellar haloes, the subtraction of such component from the observed surface brightness distribution of a galaxy may lead to misleading conclusions.

The properties of the underlying stellar population could be also a tool to

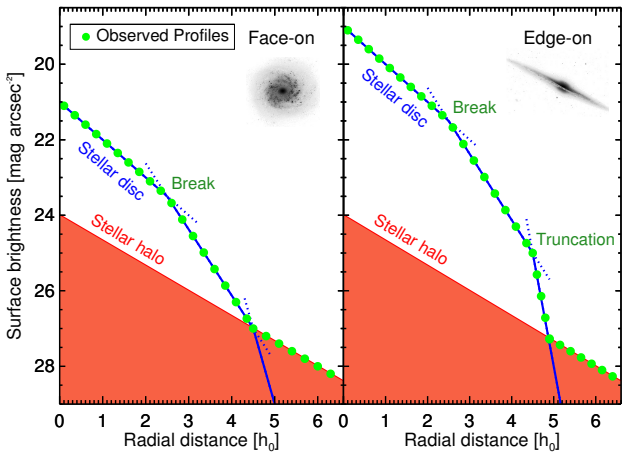


Figure 3.2: Schematic representation of the observed surface brightness profiles of a face-on and an edge-on disc galaxy according to our interpretation. The surface brightness profile of the stellar hallo component is the same in both cases since it is assumed to be spherically symmetric. The surface brightness profile of the edge-on galaxy is two magnitudes brighter than the face-on counterpart because of the LOS integration. This LOS integration brings the brightness of the galaxy at the truncation radius well above the stellar halo contribution, allowing us to detect it. In the face-on case, the truncation in the stellar disc is completely outshone by the brightness of the stellar halo.

study the mechanism behind the formation of breaks and truncations in face-on spiral galaxies, without the inherent problems associated to the edge-on projection (e.g., dust attenuation and the mixing of stellar properties because of the LOS integration). The stellar disc and the stellar halo are expected to have very different kinematical properties and that can be used to spectroscopically differentiate the two components. Also, since truncations are thought to be related to the total angular momentum of the protogalactic cloud (van der Kruit 1987, 1988), a detailed study of the kinematics around the truncation radii might bring precious information about the angular momentum distribution when galaxies were formed. In addition, in terms of $\alpha$-element overabundance, age and metallicity, stellar discs and stellar haloes might show significant differences (Radburn-Smith et al. 2012b), with the stars in the stellar halo probably being older, more metal-poor and more $\alpha$-enhanced than the stars in the stellar disc. Deep enough resolved spectroscopic surveys such as CALIFA (Sánchez et al. 2012) and MaNGA[2] might help to separately study truncations and stellar haloes. Finally the next generation of space (GAIA, James Webb Space

[2] *http://www.sdss3.org/future/manga.php*

Telescope) and ground based telescopes (European Extremely Large Telescope) will allow us to perform resolved stellar population analysis in the Milky Way and beyond the Local Group, opening the door to very detailed star counting studies of breaks and truncation up to the distance of the Virgo Cluster.

# 4

# Radial variations in the stellar initial mass function of early-type galaxies

*We've got beginner's luck*
Eels (Hombre Lobo)

This chapter has been published as *Martín-Navarro et al. 2015, MNRAS, 447, 1033*

So far, IMF results from stellar population studies are derived from integrated spectra, therefore correspond mostly to the bright central regions of ETGs. Therefore, the question of whether radial variations *within* a galaxy occur, follows naturally. Are these variations in the IMF driven by a large-scale (e.g. galaxy mass) or a local property (e.g. local velocity dispersion)? Despite the importance of this question to constrain the overall picture of galaxy formation and evolution, no reliable spatially-resolved measurement of the IMF has been performed so far. Only a few early attempts tried to investigate this issue. Carter et al. (1986) found strong radial gradients of Na and TiO spectral features in ETGs, interpreting it as the contribution from metal-rich populations of dwarf stars, concentrated towards the centres of the most massive galaxies. This interpretation was dismissed by Cohen (1979); Hardy & Couture (1988) and Delisle & Hardy (1992), who suggested instead metallicity alone as the driver of these radial trends. Due to the lack of accurate stellar population models and high-quality data at the time, these pioneering attempts remained inconclusive.

In the present chapter, we show that after considerable improvement in

the state-of-the-art stellar population synthesis models, analysis tools, observational facilities, and instrumentation, we are now able to address the issue of a radial variation of the IMF in unresolved stellar populations. Targeting a set of optical and Near-Infrared (NIR) gravity-sensitive spectral features in two high-$\sigma$ ($\sim 300\,\mathrm{km\,s^{-1}}$) and one low$-\sigma$ ($\sim 100\,\mathrm{km\,s^{-1}}$) ETGs, we find that variations in the IMF of these systems should be regarded as a local property.

## 4.1 Sample and data reduction

We obtained deep spectroscopic data of three nearby early-type galaxies, with different masses and different radial profiles of velocity dispersion. NGC 4552 and NGC 5557 are massive ETGs, with a velocity dispersion $\sigma \sim 300\,\mathrm{km\,s^{-1}}$ in their centre (Emsellem et al. 2011), whereas NGC 4387 is a lower-mass system with a central value of $\sigma \sim 100\,\mathrm{km\,s^{-1}}$ . The effective radii are, 18.″85, 36.″31 and 28.″84 for NGC 4387, NGC 4552 and NGC 5557, respectively (Cappellari et al. 2011). Because the spectra of NGC 5557 turned out to be significantly affected by telluric absorption, we analyzed its data following a different approach than for NGC 4552 and NGC 4387. While the kinematics of NGC 5557 is presented in Sec. 4.2.1, together with that for the other two galaxies, the analysis of the IMF is presented separately, in Appendix B. Throughout the chapter, we refer to NGC 4387 and NGC 4552 as our reference low- and high-mass ETGs. We notice that both NGC 4387 and NGC 4552 (as well as NGC 5557) are not peculiar in terms of either kinematics or stellar population properties (Cappellari et al. 2011).

The observations were carried out at the 10.4m Gran Telescopio Canarias, with the OSIRIS (Cepa et al. 2000) spectrograph. The spectra cover the range from 4500 to 10000 Åwith a resolution of $R = 2500$ for $\lambda < 6000$ Åand $R = 1,000$ otherwise. The slit used has $1.''0 \times 7.'8$ along the spectral and spatial directions, respectively. The wide wavelength range allows us to target IMF-sensitive absorption features that are sensitive to different chemical species (mostly, Na, Ca, and Ti). This is crucial to distinguish between the effect of a varying IMF and other effects possibly affecting gravity-sensitive indices, such as variations of elemental abundance ratios. Each target was observed for 1.5 hours, allowing us to achieve the high signal-to-noise ($S/N$) ratio required to analyze the IMF effect on absorption features.

Data reduction was done with the $\mathrm{R_ED^{uc}_mE}$ package (Cardiel 1999), allowing for a careful propagation of different sources of uncertainties during the reduction. This is crucial for our purposes, as we aim to explore different galactocentric regions – up to about one effective radius – where systematic ef-

fects might be potentially important because of the low surface brightness level. We performed the usual spectroscopic reduction steps, including bias subtraction, flat-fielding, cosmic ray cleaning, sky subtraction, C-distortion correction, wavelength calibration (better than $\Delta\lambda \sim 8$ %), S-distortion correction, extinction correction and flux calibration.

In order to measure the radial variation of the IMF, for each galaxy we produced averaged spectra in different radial bins. To this effect, we first corrected, line-by-line, the two-dimensional reduced spectrum to the rest-frame (removing both systemic and rotation velocity), and convolved each spectrum (i.e. each line) to match the maximum velocity dispersion of the galaxy (see §4.2.1 for details on the determination of the kinematics). Then, we defined radial bins adaptively, summing up the spectra along the slit position incrementally, until a target $S/N$ ratio $\geq 100$ per Å was reached for each bin.

## 4.2 Analysis

### 4.2.1 Kinematics

To measure the radial velocity and velocity dispersion profiles, we used the software pPXF (Cappellari & Emsellem 2004), which assumes that observed spectrum of a galaxy is well represented by the convolution of a set of model templates with a Gauss-Hermite series. The $S/N$ requirement for the measurement of the kinematics is lower than for the analysis of the stellar populations. Thus, as explained above, we corrected the differences in the kinematics of individual spectra within the radial bins to be used in the study of the stellar population properties. In Fig. 4.1 we show the profiles of velocity dispersion and radial velocity as a function of normalized galactocentric distance, $R/R_e$, for all three galaxies observed with GTC-OSIRIS. Our measurements are in agreement with previous results (Emsellem et al. 2011), with the massive galaxy NGC 4552, as well as the additional high-mass system NGC 5557 (Appendix B), being slow rotators ($\lambda_{Re}$ =0.049 for both galaxies), and the low-mass galaxy NGC 4387 classified as a fast rotator ($\lambda_{Re}$ =0.399).

### 4.2.2 Stellar population models

We analysed the spectra of each galaxy, at each galactocentric distance, with the Vazdekis et al. (2012) extended version of MILES stellar population models (Vazdekis et al. 2010), hereafter defined as MIUSCAT models. These models combine a variety of empirical stellar libraries over the spectral range $\lambda\lambda 3465 - 9469$ Å, at a nominal resolution of 2.51 Å FWHM, relying on solar-

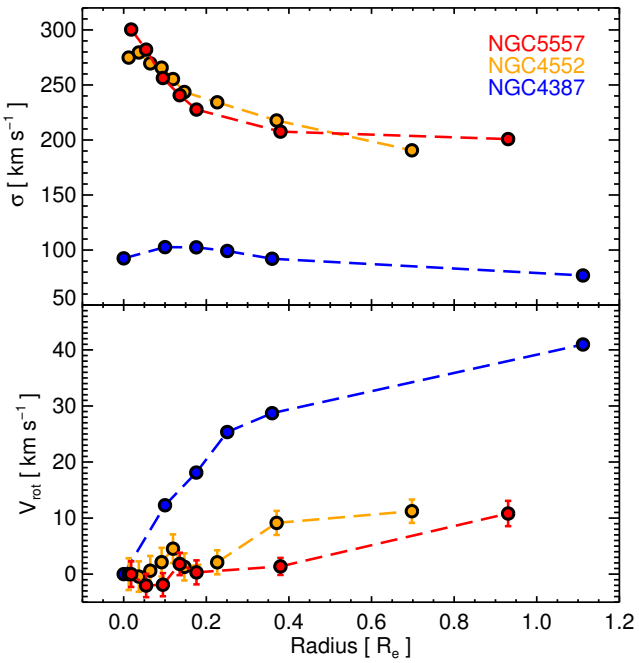


Figure 4.1: Radial gradients of velocity dispersion (top) and rotation velocity (bottom), from our GTC-OSIRIS observations, i.e. for NGC 4552, NGC 4387, and the additional massive galaxy NGC 5557. The profiles are plotted against the normalized galactocentric distance, $R/R_e$. The two massive galaxies, NGC 5557 and NGC 4552, show a decreasing $\sigma$ profile, while the low-mass system, NGC 4387, has an almost constant velocity dispersion profile. Error bars in $\sigma$ are smaller than the symbol size. Notice that the radial velocity is more important in the fast-rotator NGC 4387 than in the two massive slow-rotators ( NGC 4552 and NGC 5557). The increasing distance of radial bins reflects the signal-to-noise criterion imposed to perform an adaptive binning of the available spectra along the slit spatial direction.

scaled isochrones with stellar spectra following the abundance pattern of our Galaxy, i.e. approximately solar-scaled at solar metallicity. We consider a variety of extended MILES Simple Stellar Population (hereafter SSP) models covering a wide range of ages, from 0.5 to 14 Gyr, and metallicities, from [Z/H]$= -0.4$ to $+0.3$, as well as different IMF slopes. Notice that we did not use SSPs younger than 0.5 Gyr and with $[Z/H] < -0.4$, as our targeted ETGs are mostly composed of old, metal-rich, stellar populations. For metallicities above $+0.22$ – the maximum MILES value – SSPs are computed by linear extrapolation of the available models. However, our conclusions are not affected

at all by this extrapolation, as only the innermost radial bin of NGC 4552 benefits from it (see §4.3.2). For the present study, we consider the bimodal IMF (Vazdekis et al. 1996), consisting of a power law at high masses, with index $\Gamma_{\rm b}$, tapered off to a constant value at M$< 0.6\,{\rm M}_{\odot}$. Both bimodal and unimodal – i.e. single-segment, Salpeter-like IMFs (Salpeter 1955) – are able to describe equally well the gravity sensitive features of ETGs, but bimodal IMFs provide mass-to-light ratios in better agreement with dynamical constraints. For $\Gamma_{\rm b} \sim 1.35$, the bimodal IMF represents well the canonical, Kroupa-like, IMF (e.g. Kroupa 2001). Lower (higher) values of $\Gamma_{\rm b}$ correspond to top- (bottom-)heavy distributions, with an excess of high- (low-) mass stars. The lower and upper mass cutoffs of the IMFs are set to 0.1 and $100\,{\rm M}_{\odot}$, respectively, while the IMF slope, $\Gamma_{\rm b}$, is allowed to vary from $\Gamma_{\rm b} = 0.3$ to 3.3, where MILES models provide robust predictions (Vazdekis et al. 2012).

### 4.2.3 Fitting process

For each spectrum, i.e. each galaxy and radial bin, we infer the best-fitting slope of the bimodal IMF, $\Gamma_b$, by minimising the expression:

$$\chi^2(\Gamma_{\rm b}, [{\rm Z/H}], \delta{\rm Ti}) = \left[\frac{Age(\Gamma_{\rm b}) - Age_M}{\sigma_{Age}}\right]^2 + \sum_i \left[\frac{(EW_i - C_{\alpha,i}\cdot[\alpha/{\rm Fe}] - \Delta_{\rm Ti,i}\cdot\delta{\rm Ti}) - EW_{M,i}}{\sigma_{EW_i}}\right]^2, \quad (4.1)$$

where $Age(\Gamma_{\rm b})$ is the ($\Gamma_{\rm b}$-dependent) estimate of the age, obtained from spectral fitting (see Sec. 4.2.3 for details); $EW_i$ are the measured equivalent widths (i.e. line-strengths) for a selected set of spectral features (see Sec. 4.2.3); and $Age_M$ and $EW_{M,i}$ are the Age and equivalent widths of (MILES) SSP models; $C_{\alpha,i}$ is the observed sensitivity of the $i$-th index to [$\alpha$/Fe] (see Sec. 4.2.3); $\Delta_{\rm Ti,i}$ is the expected sensitivity (from Conroy & van Dokkum 2012a, hereafter CvD12, theoretical stellar population models) to [Ti/Fe] abundance, and $\delta$Ti is a "residual" TiO-based abundance correction [1] (i.e. not accounted for by the $C_{\alpha,i}$ terms, see La Barbera et al. 2013). The $\chi^2$ minimization is performed over a range of SSP models, with varying age, metallicity, and IMF (see Sec. 4.2.2). The $\sigma_{Age}$ is a rescaled uncertainty on $Age(\Gamma_{\rm b})$, defined by dividing the 1-sigma error on age ($\sigma'_{Age}$, as estimated from spectral fitting, see Sec. 4.2.3 below) by the root square of the number of indices used in the fitting. In practice, this procedure ensures that the age of the SSP model that minimizes the $\chi^2$ (Eq. 4.1)

[1] Notice, also, that $\delta$Ti *is not* a Titanium abundance measurement ([Ti/Fe]), since $\delta$Ti strongly depends on flux calibration at the level of a few percent (see §4.4 and §D).

is always close to the age estimate from spectral fitting, i.e. that the age of the preferred SSP model is *not* driven by the IMF-sensitive features (e.g. TiO1, TiO2, and Mg4780, whose sensitivity to age, in addition to IMF slope, is also significant; see Sec. 4.2.3).

The free fitting parameters are therefore IMF slope ($\Gamma_{\rm b}$); total metallicity ([Z/H]); and a Ti-related correction ($\delta$Ti), whereas age is a constrained fitting parameter (its value being constrained, within $\sigma_{Age}$, to the estimate obtained from spectral fitting, for each $\Gamma_{\rm b}$). Uncertainties on best-fitting parameters are estimated by shifting the $EW_i$'s and $Age(\Gamma_{\rm b})$ (see Eq. 4.1) according to their errors ($\sigma_{EW_i}$ and $\sigma'_{Age}$, respectively), and repeating the $\chi^2$ minimization procedure. The uncertainty of a given parameter is bootstrapped from the standard deviation of best-fitting repeated estimates. The term $C_{\alpha,i}\cdot$ [$\alpha$/Fe] corrects the observed line-strengths to [$\alpha$/Fe]=0, allowing a more direct comparison to the reference, solar-scaled, MILES models. The term $\Delta_{\rm Ti,i}\cdot\delta$Ti removes the effect of residual [Ti/Fe] abundance (and flux calibration effects, see details in §4.4) from line-strengths. The crucial aspects of Eq. 4.1, and the rationale beyond all different terms in it, are explained in the following subsections. We remark that for NGC 5557, because of significant contamination from telluric absorption in the spectra, we have analyzed the spectra separately, with a different set of indices, as detailed in Appendix B.

### Spectral indices

The spectral features we use in the $\chi^2$ minimization procedure include the total metallicity indicator [MgFe]$'$ (Thomas et al. 2003), and the following set of gravity-sensitive features: Mg 4780 (Serven et al. 2005), $\rm TiO_1$ (Trager et al. 1998) ($\lambda\sim5960$ Å), $\rm TiO_2$ (Trager et al. 1998) ($\lambda\sim6230$ Å), and $\rm Ca_2$ (Cenarro et al. 2001) ($\lambda\sim$ 8540 Å), all of them showing a significant response to a varying fraction of low- to high-mass stars in the IMF. We note that other (gravity-sensitive) NIR Calcium absorption lines, $\rm Ca_1$ ($\lambda\sim8500$ Å) and $\rm Ca_3$ ($\lambda\sim8660$ Å), entering the definition of the Calcium triplet (CaT$\equiv\rm Ca_1{+}Ca_2{+}Ca_3$; see Cenarro et al. 2001), are severely contaminated by airglow in the spectra of our sample of ETGs, and thus are not considered in this chapter. Other well-known gravity-sensitive features, including the optical Na doublet NaD ($\lambda\sim5900$ Å), and the NIR Na I doublet feature (Schiavon et al. 2000) NaI8190 ($\lambda\lambda$ 8183,8195 Å), are also contaminated by airglow and telluric absorption. However, as shown in Appendix C, the contamination mostly affects the absolute value of the indices, while their radial variation (i.e. the gradient) is robust. Therefore, while we do not include Na features in the $\chi^2$ minimization

procedure, we compare their observed gradients to model gradients, accounting for the radial variations of age, metallicity, and IMF as inferred from our fiducial set of spectral features (see Appendix C). Notice that the NaI 8190 feature, together with the Wing-Ford band at $\lambda \sim$9900 Å, have been actually used by van Dokkum & Conroy (2010) to infer an enhanced population of low-mass stars in the centre of elliptical galaxies. Unfortunately, in the spectra of our samples of ETGs, similar issues as for the Na features also affect the gravity-sensitive spectral indices, CaH1 ($\lambda \sim 6380$ Å), CaH2 ($\lambda \sim 6850$ Å) and aTiO ($\lambda \sim 5500$ Å), recently proposed by Spiniello et al. (2014). In particular, both CaH lines are affected by telluric absorption, CaH1 is also affected by emission, whereas the aTiO passband encompasses a strong sky emission line ($\lambda \sim 5576$ Å). We note that the spectal index, bTiO, of Spiniello et al. (2014) is very similar to the Serven et al. 2005 Mg 4780 index, that we already include in the $\chi^2$ minimization procedure. In Appendix C, we show that, in spite of these problems, the gradients of CaH2 and aTiO can be safely estimated (the latter with large error bars), while for CaH1 the radial gradient is more uncertain (being more dependent on the way we perform sky subtraction). Nevertheless, we can obtain useful constraints on the radial variation of this index. Therefore, we treat CaH1, CaH2 and aTiO in the same way as Na features, i.e. we do not include them in the $\chi^2$ minimization procedure, but we compare instead the observed gradients with model predictions for our fiducial set of spectral features, breaking the degeneracy between IMF and the other stellar population parameters (e.g. elemental abundances).

### Age determination

The age determination of a stellar population is often performed by means of the hydrogen Balmer lines, whose line-strengths might replace the first term on the right hand side of Eq. 4.1 in the $\chi^2$ minimisation procedure. In practise, we do not use this approach here, as (i) H$\beta$ appears significantly contaminated by nebular emission for NGC 4552, with the emission correction being rather uncertain for this galaxy (Sarzi et al. 2006); and (ii) higher-order Balmer lines (i.e. H$\gamma$ and H$\delta$), which are virtually unaffected by nebular emission, do not fall within the observed spectral range.

We constrain instead the age by direct-fitting of each spectrum in the wavelength region $\lambda \sim 4600 - 5600$ Å, where prominent age and metallicity features are found, using a single SSP multiplied by a tenth-degree polynomial. We perform the fit for each of the ten bimodal IMFs [2] provided by MIUSCAT

[2] with slopes $\Gamma_b = \{0.3, 0.8, 1.0, 1.3, 1.5, 1.8, 2.0, 2.5, 2.8, 3.0\}$,

models (Sec. 4.2.2). For a given IMF, the best-fitting parameters are the age and metallicity of the SSP, as well as the polynomial coefficients. Notice that the multiplicative polynomial accounts for deviations between the continua of data and models (e.g. flux calibration uncertainties in the data). For each IMF, we perform 1000 iterations of the fitting procedure, shifting randomly the flux values in the spectra according to their uncertainties. This procedure provides an age estimate (i.e. $Age(\Gamma_{\rm b})$ in Eq. 4.1), along with its uncertainty [3], $\sigma'_{Age}(\Gamma_{\rm b})$, as a function of $\Gamma_{\rm b}$. Notice that $\sigma_{Age}$ in Eq. 4.1 is obtained by dividing $\sigma'_{Age}$ by the root square of the number of spectral indices fitted, in order to give a similar weight to the first term on the right hand side of Eq. 4.1 with respect to the second term (i.e. the index summation), that contains most of the information on the IMF. Although the age can not be derived directly from the line-strengths (i.e. Balmer lines, see above), the IMF inference is very robust against a variety of age determination methods, with different methods providing consistent $\Gamma_b$ gradients (see §4.4). For NGC 4387, where the emission correction to H$\beta$ is negligible ($< 0.03$ Å), we verified that replacing the $Age$ term in the $\chi^2$ definition (Eq. 4.1) with an additional term in the equivalent widths corresponding to the H$\beta$ line, does not change the inferred values of $\Gamma_{\rm b}$ (also providing very consistent age estimates, within $\sim$1 Gyr[4], to those derived from spectral fitting). Hence, our procedure is robust, and general enough, to constrain the age for all available spectra.

Chemical abundances and temperature effects

Chemical abundances can partly mimic the effect of a varying IMF. Moreover, we want to rely on empirical (rather than theoretical), solar-scale, stellar population (MILES) models to analyse the spectra. We take the abundance issue into account in two ways.

First, using the semi-empirical correction procedure described in La Barbera et al. (2013), we correct the observed line strengths to solar scale. The corrections to line strengths are the terms $C_{\alpha,i}\cdot[\alpha/{\rm Fe}]$ in Eq. 4.1, where $C_{\alpha,i}$ are semi-empirical correction coefficients, given by the slopes of the correlations of line strengths with $[\alpha/{\rm Fe}]$, at fixed velocity dispersion – from stacked spectra of ETGs in the Sloan Digital Sky Survey (see La Barbera et al. 2013 for details). For each spectrum, we estimate $[\alpha/{\rm Fe}]$ (and plug it into $C_{\alpha,i}\cdot[\alpha/{\rm Fe}]$)

[3] computed as the standard deviation of age estimates from the 1000 iterations

[4] The same test was also performed on the additional high-mass galaxy, NGC 5557, for which results are only presented in Appendix B. The emission correction for this galaxy is negligible, and we find very consistent $\Gamma_{\rm b}$'s (within the errors, see Appendix) when constraining the age by either H$\beta$ or spectral fitting.

by a solar-scale proxy, $[Z_{\rm Mg}/Z_{\rm Fe}]$, defined as the difference of the metallicities estimated with either Mg or Fe lines, for a fixed Kroupa IMF, with MILES models. Notice that the [$\alpha$/Fe] correction procedure assumes that the $C_{\alpha,i}$'s, derived in galaxy central regions (SDSS), are the same at different galactocentric distances. Although this assumption is not necessarily true, the terms $C_{\alpha,i}\cdot$[$\alpha$/Fe] vanish outwards in our sample of ETGs (as [$\alpha$/Fe]$\sim$0 at the largest radii probed). Thus, the computation of $C_{\alpha,i}$ does not affect significantly our conclusions. The correction for non-solar [$\alpha$/Fe] abundance ratios is negligible for TiO features, while it tends to increase the EWs of Mg 4780 and $\rm Ca_2$, especially in the centre of the massive galaxies, where [$\alpha$/Fe] is high.

In addition, to allow for residual abundance variations, we also include the effect of varying [Ti/Fe] abundance, as an extra fitting parameter, in Eq. 4.1 (see La Barbera et al. 2013 for details). The reason for including [Ti/Fe], rather than any other single element, in the analysis is that according to different theoretical stellar population models (Conroy & van Dokkum 2012a; Johansson et al. 2012), titanium is the main element whose individual abundance ratio affects the strength of TiO features, and, in fact, an increase of [Ti/Fe] with (central) velocity dispersion has been detected in ETGs (Johansson et al. 2012; La Barbera et al. 2013). Notice that TiO features might also be affected by [O/Fe] abundance (Conroy et al. 2014). Since oxygen closely follows magnesium, with deviations smaller than 0.1 dex, in both our Galaxy (independent of metallicity as shown by Bensby et al. 2004) and early-type galaxies (Johansson et al. 2012), the effect of [O/Fe] is already accounted for by our solar-scale proxy correction (see above). Moreover, at least some stellar population models (Johansson et al. 2012) do not predict any dependence of either $\rm TiO_1$ or $\rm TiO_2$ on [O/Fe]. Notice that the [Ti/Fe] abundance term in Eq. 4.1 does only affect $\rm TiO_1$ and $\rm TiO_2$, while it is negligible for $\rm Ca_2$ and Mg 4780. For what concerns $\rm Ca_2$, this feature might also be affected by Ca abundance variations. In contrast to Ti, no *residual* variation (i.e. not accounted for by our solar-scale correction) with (central) velocity dispersion has been detected with Ca. Therefore, we have not included Ca abundance in the analysis. The Mg 4780 index could be affected by radial gradients of several chemical species (e.g. C and Si), that are difficult to analyse even with the latest state-of-art stellar population models. For simplicity, we do not consider any of these effects here.

Finally, we note that gravity-sensitive features are also sensitive to the effective temperature of RGB stars, $T_{\rm eff}$. Decreasing $T_{\rm eff}$, at optical wavelengths, mimics the effect of steepening the IMF, but this degeneracy breaks down completely in the red part ($>$ 7500 K) of the spectrum (Spiniello et al. 2014). The fact that both optical and NIR features (e.g. NaI 8190) suggest an IMF radial gradient in our massive galaxies (see Appendix B), excludes $T_{\rm eff}$ as the main

source for the radial variation of TiO features. Also, one should note that two of the main sources of possible variations of the $T_{\rm eff}$ of the RGB, i.e., Mg abundance and total metallicity (VandenBerg et al. 2012) (besides Si abundance), are already accounted for in the analysis by means of the solar-scale correction procedure (that virtually removes all effects tightly related to Mg abundance) and because we adopt stellar population models with varying total metallicity.

## 4.3 Results

We start discussing below, in a qualitative manner, the radial behaviour of the IMF-sensitive TiO2 feature (Section 4.1). In Section 4.2, we perform a quantitative comparison of best-fitting and observed line-strengths, for all selected IMF-sensitive features, following the approach described in Section 4.2. The main results of the present chapter are presented in Section 4.3, where we contrast the radial trends of IMF slope for the low-mass galaxy, NGC 4387, and our best high-mass candidate, NGC 4552. Results for our additional high-mass galaxy, NGC 5557, are presented separately in Appendix B, as this galaxy has been analyzed with a different methodology than NGC 4387 and NGC 4552. Appendix C also shows that the NIR Na8190 doublet, as well as other optical features, provide (independent) radial constraints to the IMF, that are fully consistent with those from our fiducial set of spectral features.

### 4.3.1 Line-strength gradients: qualitative analysis

In Fig. 4.2 the spectral region around the IMF-sensitive $TiO_2$ spectral feature (Trager et al. 1998) is shown, for two radial bins corresponding to the centre (top) and one half of the effective radius ($0.5\,R_e$, bottom) for NGC 4387 (left) and NGC 4552 (right), respectively. The $TiO_2$ index measures the absorption strength of a TiO molecular band, prominent in the atmospheres of low-mass cool stars (Mould 1976), and therefore, when detected in the integrated light of a stellar population, provides a sensitive tracer of the ratio of dwarf-to-giant stars. This ratio is a surrogate of IMF slope: the higher the ratio, the steeper the IMF.

The grey shaded regions in Fig. 4.2 show the allowed range in the $TiO_2$ feature for a wide range of age (7–14 Gyr), metallicity ($-0.4$ to $+0.2$ dex) and titanium abundance (from $-0.5$ to $+0.2$ dex), encompassing those measured from our data, but keeping the IMF fixed at the Milky-Way "standard" distribution. We find that: (i) the $TiO_2$ spectral region of the low-mass galaxy is well reproduced by Kroupa-like IMF models at all radii; (ii) on the contrary, for our reference high-mass galaxy, a significant $TiO_2$ mismatch towards a bottom-

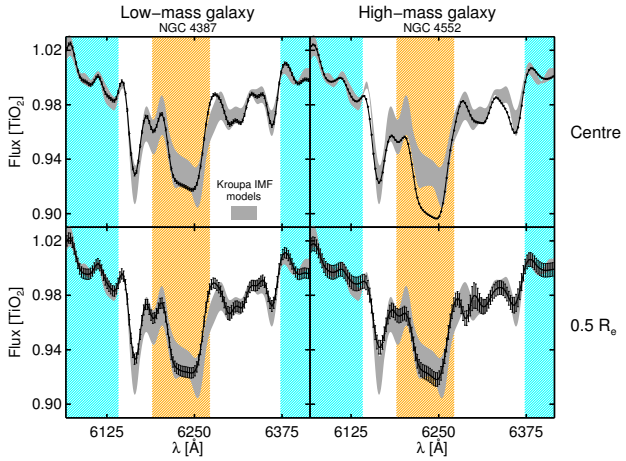


Figure 4.2: Spectral region surrounding the $TiO_2$ absorption band. The Figure compares the spectra (black curves with $1\,\sigma$ error bars) for the low-mass (left) and the high-mass (right) galaxies, in their centre (top) and at half of the effective radius (bottom). The grey region shows how the $TiO_2$ feature changes for Simple Stellar Population (SSP) models with fixed, standard (Milky-Way like) IMF over a wide range of ages and chemical compositions. Note that any linear superposition of SSPs will also fall within the grey regions. Observed and model spectra are normalised to the blue flanking regions of the (orange-hatched) $TiO_2$ band, where the IMF information is encoded. In the low-mass galaxy the $TiO_2$ can be well fitted with a universal IMF (grey region) at all radii. In contrast, the massive galaxy shows a significant gradient of $TiO_2$: a stronger absorption is detected in the centre, revealing an enhanced dwarf-to-giant ratio. At R$\sim 0.5\,R_e$, $TiO_2$ absorption is instead consistent with the range expected for a standard IMF.

heavy IMF is detected in the central region. This $TiO_2$ gradient can only be explained by a change of IMF slope with radius (see §4.5).

### 4.3.2 Best-fits to IMF-sensitive spectral indices

Fig. 4.3 illustrates the spectral analysis for our reference low- and high-mass galaxies, NGC 4387 (empty symbols) and NGC 4552 (solid symbols), respectively. Symbol colours vary from red, in the innermost, to blue, in the outermost radial bins. The triangles mark the measured equivalent widths, while circles plot the quantities $[EW_i - C_{\alpha,i} \cdot [\alpha/\mathrm{Fe}] - \Delta_{\mathrm{Ti,i}} \cdot \delta\mathrm{Ti}]$ in Eq. 4.1, i.e. the observed EWs corrected for $[\alpha/\mathrm{Fe}]$, and with the TiO-based residual term removed. As mentioned above, the correction in $[\alpha/\mathrm{Fe}]$ affects only Mg 4780 and $Ca_2$, and is negligible for TiO features ($\sim$0.005 mag for the bin with the largest $[\alpha/\mathrm{Fe}]$ correction). $\Delta_{\mathrm{Ti,i}}$ is different from zero only for TiO-based indices, and

in particular for $TiO_1$ (when compared to its radial gradient; see the large differences among triangles and circles in panel b).

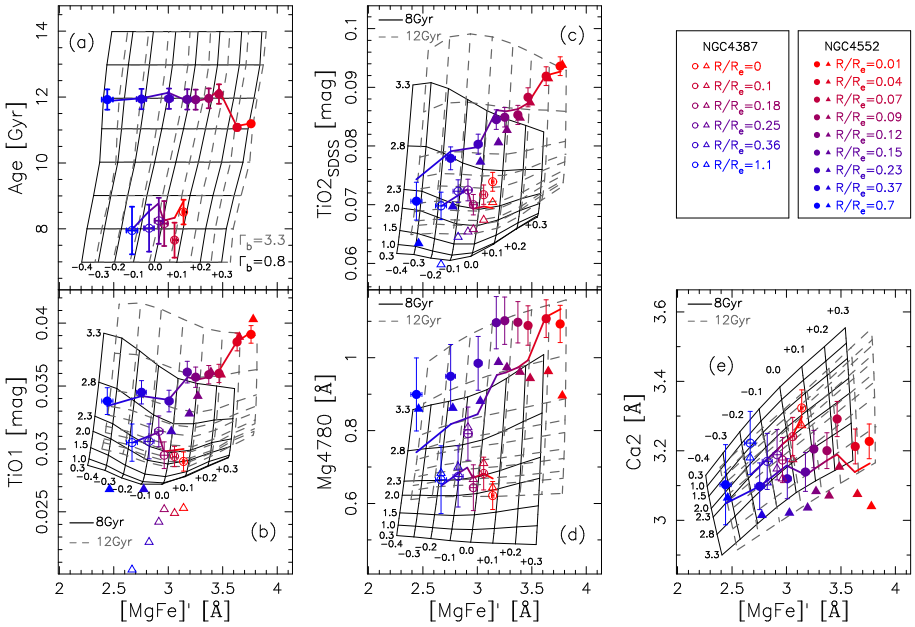


Figure 4.3: Fitting results for our low- (NGC 4387; open symbols) and high-mass (NGC 4552; filles symbols) galaxies. Panel a: coloured symbols, with error bars, are age estimates from spectral fitting. Notice that the age estimates depend on the assumed IMF (see the text). Hence, for each galaxy, and each radial bin, the plot shows the age estimate for the corresponding, best-fitting, IMF. The grids show the effect of varying metallicity on the [MgFe]′ index, for SSPs with different ages, and two extreme IMFs (grey-dashed and solid-black grids, as labeled). Panels (b-e): IMF-sensitive line-strengths vs. the total metallicity indicator [MgFe]′. Triangles show the raw line strengths, whereas circles (with error bars) show the line strengths corrected for [$\alpha$/Fe], and with the best-fit residual TiO-based abundance term ($\delta$Ti in Eq. 4.1) subtracted off. The solid-coloured curves show the best-fit solutions, with colour varying from red, in the galaxy centre, through blue, at larger galactocentric distances (see legend in the upper–right corner of the plot). Solid and dashed grids plot line strengths for SSP models with varying $\Gamma_b$ and [Z/H], for two ages of 8 (representative of NGC 4387; see panel a) and 12 Gyr (oldest representative age for NGC 4552), respectively.

For NGC 4552, the best-fitting $\delta$Ti shows an overall gradient of about $-0.7$ dex. Interestingly, this is similar to the total metallicity gradient of this galaxy. Note that despite of the large $\delta$Ti radial variation, the gradient of $TiO_2$, after the residual abundance term is subtracted off, is still very significant (filled circles in panel c), and can only be explained by a radial gradient of IMF slope. In fact, to mimic the radial variation of $TiO_2$ with a fixed IMF, we

would require a large radial gradient, more than +2 dex in $\delta$Ti. Such a strong gradient (at fixed IMF) would be inconsistent with the observed radial gradient of $TiO_1$ (see details in §4.5).

For $Ca_2$, our best-fitting solutions (Fig. 4.3) are fully consistent ($1\,\sigma$) with the data in each radial bin. Note that this index decreases with metallicity, and thus, because elliptical galaxies have negative metallicity gradients (see panel a of Fig. 4.3), one would expect a negative radial gradient of $Ca_2$. Apart from the outermost radial bin, where the error bar reflects a large uncertainty in sky subtraction, such a negative gradient is clearly observed for the low-mass galaxy. On the contrary, a flatter trend is found in NGC 4552, despite of its stronger metallicity gradient. Considering that $Ca_2$ decreases with $\Gamma_b$ (Vazdekis et al. 2003), the mild $Ca_2$ gradient for the high-mass galaxy is fully consistent with the result that the slope of its IMF tends to decrease outwards. The case of Mg 4780 is less clear, as this index still shows a radial gradient in NGC 4552, possibly consistent with a less bottom-heavy IMF outwards. The gradient is mild, and only marginally consistent with the other indices, as one can see by comparing the filled circles and the best-fitting solution for NGC 4552 (upper curve) in panel (d) of Fig. 4.3. Based on stellar population models with varying abundance ratio (Conroy & van Dokkum 2012a), we expect that this index anti-correlates with several chemical abundances, like [C/Fe] and [Si/Fe]. Hence, negative gradients, like those observed for [Z/H] and $\delta$Ti, might be pushing this index towards higher values at large galactocentric distances. Since the effect is mild, and we still observe a gradient in Mg 4780, for the purpose of the present chapter, we do not attempt any further analysis.

### 4.3.3 IMF radial gradients

The main result of this chapter is shown in Fig. 4.4, where the radial trends of bimodal IMF slope, $\Gamma_b$, are presented for both NGC 4552 and NGC 4387, respectively.

For the massive galaxy NGC 4552, the IMF slope decreases, by $\Delta\Gamma_b = -1.5$, from the centre to $0.7\,R_e$. In the innermost radial bins, the inferred IMF slope ($\Gamma_b = 3.05 \pm 0.2$), implies a bottom-heavy distribution, consistent with previous work. In constrast, for the outermost bin, the best-fit ($\Gamma_b = 1.9 \pm 0.4$) is higher, but still consistent at the $1.5\sigma$ level, with the value corresponding to a Kroupa-like distribution ($\Gamma_b \sim 1.35$). As shown in Appendix B, the additional massive galaxy (NGC 5557) also exhibits a decrement of $\Gamma_b$ between the central part and the outer region, with $\Delta\Gamma_b = -1.5(-0.8)$, from the centre to $1(0.7)\,R_e$. In contrast, the low-mass ETG, NGC 4387, shows almost no radial dependence of IMF within the uncertainties, with $\Delta\Gamma_b = -0.3$. In Appendix D, we also

show that the correlation of uncertainties between the best-fitting parameters (mainly, age, $\delta$Ti, and IMF) cannot explain, by itself, the radial IMF gradient detected in NGC 4552, i.e. the radial trend in Fig. 4.4 is not just the result of marginalizing the uncertainties along a given direction of the parameter space. We also notice that the inferred IMF slope for NGC 4387 is higher than that expected for its velocity dispersion (see La Barbera et al. 2013). However, while absolute values of $\Gamma_{\rm b}$ are significantly dependent on the set of adopted spectral features in the analysis (Spiniello et al. 2014), it is expected that IMF slope variations (i.e. the radial gradients) are constrained in a much more robust way. In addition, one may notice that (i) for a bimodal IMF, the difference of IMF normalization (i.e. the stellar mass-to-light ratio) between $\Gamma_{\rm b} = 1.35$ (i.e. a Kroupa-like distribution) and $\Gamma_{\rm b} \sim 2$ (as we measure for NGC 4387) is only 0.1 dex (SDSS $r$-band, Ferreras et al. 2013), and (ii) for a Kroupa-like slope ($\Gamma_{\rm b} = 1.35$), IMF-sensitive features are much less sensitive to a given variation of $\Gamma_{\rm b}$, than for a bottom-heavy IMF (e.g. $\Gamma_{\rm b} \sim 3$). Hence, our results for the low-mass galaxy do not contradict independent constraints from dynamical studies (e.g. the results from the ATLAS3D survey), and the mild difference between $\Gamma_{\rm b} \sim 2$ and $\Gamma_{\rm b} \sim 1.35$ (Kroupa-like) is likely not relevant for the present chapter. In terms of the dwarf-to-giant stellar ratio in the IMF (see La Barbera et al. 2013), up to $\sim$75% of the stellar mass in the centre of the massive galaxy NGC 4552 is accounted for by stars below M$<0.5$M$_{\odot}$, whereas for the outermost radial bin, this ratio decreases down to $\sim$ 50%. For the low-mass galaxy, NGC 4387, stars with M$<0.5$M$_{\odot}$ account for a roughly constant 56% of the total stellar mass at all radii.

The results of our analysis for NGC 4552 and NGC 4387 are summarized in Table 4.1, where we list the best-fitting age, [Z/H], and $\Gamma_{\rm b}$ for all radial distance bins, along with the typical signal-to-noise ratio of each spectrum. The table also lists the [$\alpha$/Fe] as inferred from the [$Z_{\rm Mg}/Z_{\rm Fe}$] proxy (see Sec. 4.2.3).

## 4.4 Robustness of inferred IMF gradients

To prove the robustness of our results, we have performed a battery of tests, varying the procedure to infer the IMF slope. These tests are described below.

Age estimate: This is one of the main uncertainties in the IMF determination, as most IMF-sensitive spectral indices are sensitive to age. In addition to including the Ca2 index in the analysis (which is sensitive to IMF, but not to age), we have addressed the age estimate issue as follows. (i) We have tested the effect of more complex star formation histories (than a single SSP), estimating the age from spectral fitting with two-SSP models.

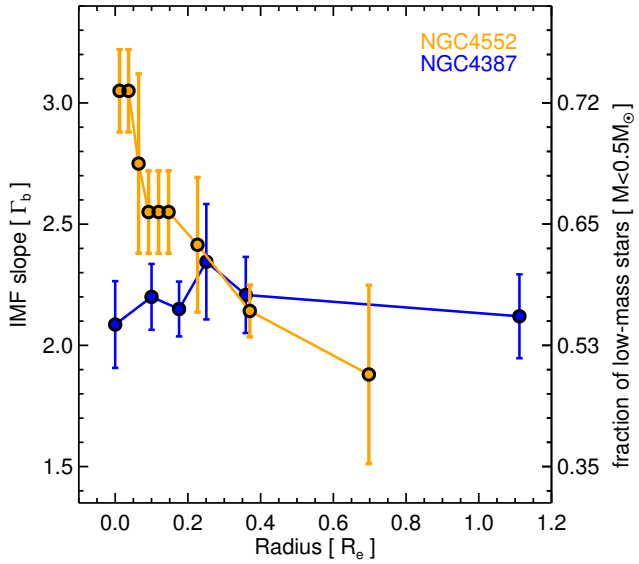


Figure 4.4: Radial IMF slope profiles for the low- and high-mass galaxies, NGC 4387 and NGC 4552, respectively. The IMF slope, $\Gamma_b$, is inferred via a detailed analysis of gravity-sensitive features in the galaxy spectra, at different galactocentric distances. The fraction of low-mass stars ($M<0.5M_\odot$) with respect to the total stellar mass is shown in the vertical axis on the right. The massive ETG (yellow) shows a significant IMF slope variation with radius. The less-massive system, NGC 4387, shows a rather flat IMF radial profile. Our measurements reveal that the enhanced population of dwarf stars (i.e. a higher $\Gamma_b$) in massive galaxies is confined to the central regions.

(ii) As a further *extreme* test, we have also calculated the radial IMF profiles by neglecting completely the age constraint from spectral fitting, i.e. repeating the fits by removing the first term in the right-hand side of Eq. 4.1. (iii) We have tested the impact of our assumption that residual $\delta$Ti correction affect only spectral indices, and not the age determination itself. To this aim, we have implemented an iterative approach, where spectral and index fitting are repeated, after dividing each input spectrum with the ratio of [Ti/Fe]-enhanced to solar-scale SSP theoretical models (Conroy & van Dokkum 2012a), the ratio being scaled to match the [Ti/Fe] residual abundance from the first minimisation of Eq. 4.1. In practise, the output best-fitting parameters from the first iteration are very similar (within a few percent) to those from the zero-order step, requiring no further iterations.

Temperature effects on the SSP modelling: We have varied (iv) the temperature scale of low-mass ($M < 0.5\,M_{\odot}$) dwarf stars in MILES models – which has a major impact on various IMF-sensitive indicators – according to a cooler prescription (Pols et al. 1995) than the MILES reference one (Vazdekis et al. 2012); (v) we have arbitrarily shifted the scale of RGB stars by ±50 K, as these changes affect significantly molecular bands (i.e. TiO features).

Flux calibration uncertainties: We have fitted the continuum of each observed spectrum, in the TiO spectral regions, with MILES SSPs multiplied by a low-order polynomial in each region (with degree $\delta(\lambda)/100$, where $\delta(\lambda)$ is the spectral range size, see Conroy & van Dokkum (2012a)). Fitting different models (e.g. varying slightly the IMF, age, metallicity of MILES SSPs, and/or the polynomial degree, and for different spectra) we estimated that the impact of flux calibration uncertainties may affect significantly $TiO_1$, and to less extent $TiO_2$. Even accounting for rotation, the net effect is to offset the observed line strengths (i.e. radial gradients

| Galaxy | $R$ ($R_e$) | $S/N$ | Age (Gyr) | [Z/H] (dex) | [$\alpha$/Fe] (dex) | $\Gamma_b$ |
|---|---|---|---|---|---|---|
| NGC 4552 | 0.01 | 1450 | $11.2 \pm 0.1$ | $+0.29 \pm 0.01$ | $0.41 \pm 0.01$ | $3.05 \pm 0.2$ |
| | 0.03 | 911 | $11.1 \pm 0.1$ | $+0.21 \pm 0.01$ | $0.30 \pm 0.01$ | $3.05 \pm 0.2$ |
| | 0.06 | 413 | $12.3 \pm 0.2$ | $+0.09 \pm 0.01$ | $0.30 \pm 0.01$ | $2.75 \pm 0.2$ |
| | 0.09 | 281 | $12.0 \pm 0.2$ | $+0.04 \pm 0.01$ | $0.29 \pm 0.02$ | $2.55 \pm 0.2$ |
| | 0.11 | 166 | $11.9 \pm 0.2$ | $-0.02 \pm 0.02$ | $0.27 \pm 0.02$ | $2.55 \pm 0.2$ |
| | 0.14 | 122 | $11.9 \pm 0.2$ | $-0.06 \pm 0.02$ | $0.23 \pm 0.02$ | $2.55 \pm 0.2$ |
| | 0.22 | 94 | $11.9 \pm 0.2$ | $-0.14 \pm 0.02$ | $0.21 \pm 0.02$ | $2.4 \pm 0.3$ |
| | 0.37 | 95 | $12.0 \pm 0.3$ | $-0.25 \pm 0.02$ | $0.18 \pm 0.03$ | $2.1 \pm 0.1$ |
| | 0.69 | 98 | $12.0 \pm 0.3$ | $-0.40 \pm 0.03$ | $0.08 \pm 0.04$ | $1.9 \pm 0.4$ |
| NGC 4387 | 0.00 | 529 | $8.7 \pm 0.3$ | $+0.06 \pm 0.01$ | $0.11 \pm 0.01$ | $2.1 \pm 0.2$ |
| | 0.10 | 349 | $7.5 \pm 0.6$ | $+0.05 \pm 0.02$ | $0.14 \pm 0.01$ | $2.2 \pm 0.2$ |
| | 0.17 | 187 | $8.0 \pm 0.6$ | $-0.02 \pm 0.02$ | $0.12 \pm 0.02$ | $2.1 \pm 0.1$ |
| | 0.25 | 143 | $8.1 \pm 0.6$ | $-0.05 \pm 0.03$ | $0.09 \pm 0.02$ | $2.3 \pm 0.3$ |
| | 0.35 | 110 | $7.9 \pm 0.7$ | $-0.09 \pm 0.03$ | $0.13 \pm 0.02$ | $2.2 \pm 0.2$ |
| | 1.11 | 93 | $7.8 \pm 0.6$ | $-0.16 \pm 0.03$ | $0.09 \pm 0.03$ | $2.1 \pm 0.2$ |

Table 4.1: Best-fitting parameters for the massive galaxy NGC 4552, and the low-mass galaxy NGC 4387. Uncertainties are quoted at the one sigma level.

are not affected at all). Thus, as a further test, (vi) we have repeated the analysis by shifting $TiO_1$ and $TiO_2$ line-strengths by the maximum shifts allowed by our continuum fits, i.e. +0.009 mag and +0.005 mag, respectively. The outcome of this test is that TiO flux calibration offsets can introduce a large shift in the derived $\delta$Ti, up to $\sim$0.6 dex, while IMF gradients remain unchanged. Hence, the absolute value of the $\delta$Ti does not reflect the actual [Ti/Fe] overabundance of the stellar population.

The results of the above tests (i–vi) are shown, – for our reference massive galaxy, NGC 4552 – in Fig. 4.5. The Figure plots IMF radial trends for all tests, proving that indeed our results are very robust. In particular, none of our experiments – changing the assumptions of fitting methodology, stellar population modelling, and exploring the impact of flux calibration issues in the data – alters the existence of a significant radial IMF gradient for NGC 4552.

## 4.5 Can we fit the observations with a constant IMF?

In the following, we elaborate on the tests presented in Section 4.4, discussing why a radial variation of the IMF seems to be the only possible explanation to the radial trends of IMF-sensitive indices in our massive galaxies. With this aim, we discuss several scenarios that might mimic the effect of a varying IMF with galacto-centric distance:

1. Varying the temperature scale of dwarf ($<0.5M_\odot$) stars. As mentioned in test (iv) of Section 5, we have constructed SSP models with a significantly cooler prescription (Pols et al. 1995) for low-mass dwarves than MILES SSPs (Vazdekis et al. 2012), by $\Delta T \sim 200$ K. This temperature variation turns out to affect mostly the TiO indices. For an IMF slope of $\Gamma_b = 3$, the $TiO_2$ decreases by $\sim 0.007$ mag (when using the cooler temperature scale). For $\Gamma_b = 1.35$ (i.e. Kroupa-like IMF), the $TiO_2$ changes only by $\sim -0.002$ mag. Since the metallicity proxy, [MgFe]$'$, is almost insensitive to the dwarf temperature scale, the net effect is to shrink the model $TiO_2$–[MgFe]$'$ grid in panel c of Fig. 4.3, along the "IMF axis" (y-axis). Hence, although a change in the temperature scale of low-mass dwarves affects the absolute values of the IMF slope in the galaxy centre, the IMF gradient cannot be removed, as shown in Fig. 4.5.

2. Varying the temperature scale of giant stars.

   We have constructed SSP models by shifting the temperature of RGB stars by $\delta(T_{\rm eff}) = -150$, $-100$, $-50$, 0, and +50 K, respectively (a shift

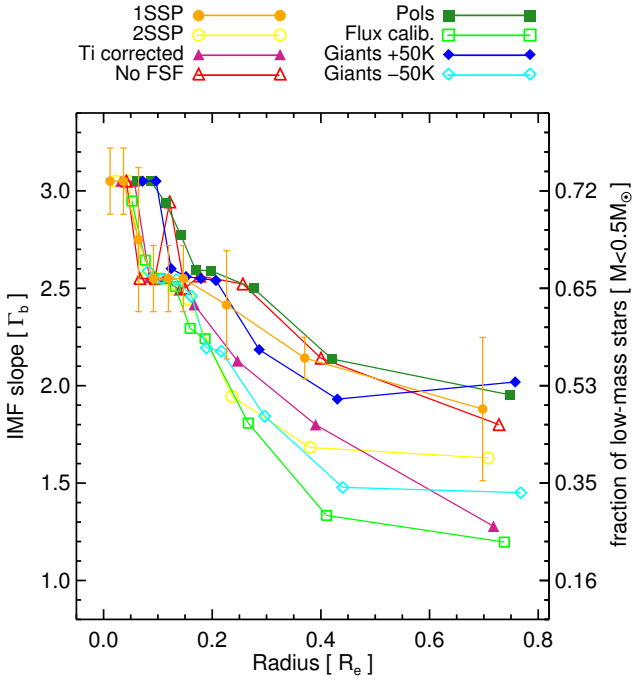


Figure 4.5: Different IMF radial profiles for NGC 4552, obtained by changing several assumptions in the modelling/fitting process. Profiles obtained with different assumptions are plotted with different colours and symbols, as labeled on the top of the figure. Remarkably, all radial profiles show a gradient in the IMF slope, from a bottom-heavy IMF in the galaxy centre to a more "standard" slope, closer to a Kroupa-like value of $\Gamma_b = 1.3$, at about one effective radius. Hence, our results are robust against all performed tests: age derived through one (*1SSP*) or two (*2SSP*) SSPs; considering the $\delta$Ti impact on the age estimation (*Ti corrected*); inferring the age with no information from full spectral fitting (*No FSF*); using a cooler prescription for the dwarf stars temperature (Pols); testing the flux calibration (*Flux calib.*) and changing the temperature scale of giant stars by plus 50 K (*Giants* $+50K$) and minus 50 K (*Giants* $-50K$).

of zero corresponding to our reference MILES models). For $\delta(T_{\rm eff}) = -150\,{\rm K}$, the model $TiO_2$ increases by $\sim$0.02 mag, i.e. a large variation, comparable to that between a bottom-heavy and standard IMFs. A similar result applies to Mg 4780 and $TiO_1$. Therefore, a radial gradient of $T_{\rm eff}$ might be able to explain, by itself, the TiO radial gradients. However,

this possibility is ruled out by our NIR spectral indices, as well as other gravity-sensitive features (CaH1 and CaH2, see App. C). In particular, for $\delta(T_{\rm eff}) = -150$ K, the model Ca2 index changes by only $\sim$0.03 Å, while the model NaI 8190 shows an opposite variation with respect to its observed radial gradient, *decreasing* by $\sim$0.2 Å. We notice that two of the main sources of opacity in a stellar population – total metallicity and [Mg/Fe], besides [Si/Fe] (VandenBerg et al. 2012) – are properly accounted for in our analysis, the former by the fact that we rely on models with varying total metallicity, and the latter by our [$\alpha$/Fe] correction procedure. This leaves very small leeway for residual $T_{\rm eff}$ variations. *Furthermore, as already mentioned, a positive radial gradient of $T_{\rm eff}$ cannot match simultaneously the observed radial trends of both TiO, Na, and Ca/CaH indices.* Since a change of $T_{\rm eff}$ also affects the shape of the TiO- [MgFe]$'$ index-index grid (see Fig. 4.3), we have also tested the impact of a fixed $\delta(T_{\rm eff})$ ($= +/- 50$ K) on our results. Since the change in the shape of the TiO1 vs. [MgFe]$'$ and TiO2 vs [MgFe]$'$ grids is very similar, no significant variation is found in the IMF trends (see Fig. 4.5).

3. Radial [$\alpha$/Fe] variation.

   As found in La Barbera et al. (2013), the [$\alpha$/Fe] correction of TiO indices is small (e.g. less than $\sim$0.005 mag for $TiO_2$). Therefore, radial gradients of [Mg/Fe] (and that of other $\alpha$ elements that closely follow Mg, such as [O/Fe]) can not explain the radial variation of TiO indices. Furthermore, the measured gradient in [$\alpha$/Fe] in both massive galaxies would imply a NaI 8190 gradient opposite to the observed one (i.e., in this scenario, NaI8190 should increase outwards).

4. Radial [Ti/Fe] abundance variation.

   A radial gradient of [Ti/Fe], as large as 2 dex, would be required to account for the observed gradient of the $TiO_2$ index. Because of the expected similar response of both TiO indices to Ti abundance, one cannot fit both $TiO_1$ and $TiO_2$ gradients with a radial variation of [Ti/Fe] alone. If we leave only age, metallicity, and [Ti/Fe] abundance as free parameters, for models with a fixed IMF, the best-fitting solution for the massive galaxy NGC 4552 deviates by more than $2\,\sigma$ ($3\,\sigma$) from the observed $TiO_1$ ($TiO_2$) values, as shown in Fig. 4.6. Thus, a radial variation of [Ti/Fe] cannot mimic the effect of a radially varying IMF.

5. Radial [Na/Fe] abundance variation.

In Appendix C.0.1, we analyze the radial behaviour of the Na features at 5900 Å (NaD) and 8200 Å (NaI8190), respectively. For a constant IMF, after subtracting off the expected variation due to the metallicity gradient of NGC 4552, one could explain the radial variation of NaI8190 with a gradient of about 1 dex in [Na/Fe] abundance (with an uncertainty of ±0.2 dex, depending on the data reduction procedure). Such a scenario would imply a change of about 3.3 Å in the NaD line strength. In contrast, a modest change is allowed by the observations (<1 Å, after removing the effect of metallicity; see bottom panel of Fig. C.2 and Appendix C.0.1). Hence, similarly to TiO indices, we cannot explain multiple indices (in this case, the NaD and NaI8190 radial gradients) by invoking a variation of [Na/Fe] alone, with the assumption of a fixed IMF.

Finally, we want to emphasize that the agreement in the radial behaviour of a wide set of spectral features (from different chemical species and covering a large wavelength range) as that considered in this chapter (i.e. TiO1, TiO2, Ca2, Mg 4780 plus aTiO, CaH2, NaD, NaI 8190) breaks the degeneracy between IMF and elemental abundances and/or $T_{eff}$ (see App. C and Sec. 4.4), proving the robustness of our result, i.e. the IMF radial variation in the two massive ETGs studied here, namely NGC 4552 and NGC 5557.

## 4.6 Discussion

We have found that the massive ETG NGC 4552 shows a radial variation of gravity-sensitive indices that can only be explained if an IMF radial gradient is invoked, from a bottom-heavy slope (i.e., an enhanced dwarf-to-giant ratio) in the centre, to a significantly flatter distribution, closer to the standard (Kroupa-like) IMF, at a galacto-centric distance of about one effective radius. Evidence for a decrement in IMF slope are also found for the additional high-mass galaxy NGC 5557, whose IMF slope is fully consistent with a Kroupa-like IMF in the outermost radial bin. On the contrary, a low mass ETG, NGC 4387, presents a flat radial trend of IMF slope.

Hence, although previous studies suggested a trend with galaxy mass on a global sense (Cenarro et al. 2003; van Dokkum & Conroy 2010; Ferreras et al. 2013; La Barbera et al. 2013), our findings imply that *it is in the cores of massive galaxies* where star formation processes are fundamentally different, leading to a bottom-heavy IMF. The $\Gamma_b$ profiles of Fig. 4.4 imply that the correlation of IMF slope and galaxy mass found in previous studies (Cenarro et al. 2003; van Dokkum & Conroy 2010; Cappellari et al. 2012; Ferreras et al. 2013; La

Barbera et al. 2013) likely arises because of an enhanced fraction of low-mass stars in the central regions ($R \lesssim 0.3 - 0.5\,R_e$) of the most massive ETGs. The $\Gamma_b$-mass relation (Ferreras et al. 2013; La Barbera et al. 2013) predicts $\Gamma_b \sim 3$ for $\sigma \sim 300\,\mathrm{km\,s^{-1}}$ , a value fully consistent with the innermost radial bins of NGC 4552. It is therefore the central region that drives the observed correlation between IMF slope and velocity dispersion among galaxies.

Our results suggest that the IMF in ETGs is driven by the local conditions of the interstellar medium during the process of formation. At present, there is no complete theory of star formation that could address in a comprehensive way the connection between the initial stages of star formation and the properties of the IMF, especially the characteristic stellar mass and the location of the turnover in the power law at low masses. The fragmentation scales are driven by complex physics involving thermal properties of the gas; the contribution of dust to cooling; magnetic fields; turbulence; the effect of supersonic motions in the turbulent gas; and the transition from pre-stellar cores to stars, among others (Padoan & Nordlund 2002; Larson 2005; Bonnell et al. 2008; Hopkins 2013). In addition, constraints based on observations of unresolved stellar populations can only provide an effective IMF integrated with respect to the past star formation history of the galaxy (i.e. the integrated galactic IMF, Kroupa & Weidner 2003, IGIMF). For instance, a naïve assumption of a bottom-heavy IMF in the cores of massive galaxies would lead to a significant paucity of metals, in conflict with the observed metal-rich populations in these regions. It is by assuming that the IMF is time-dependent, and coupled to the star formation rate, that one can obtain results that are compatible with the observations (Vazdekis et al. 1997; Elmegreen & Scalo 2006; Weidner et al. 2013). Nevertheless, it is not clear at present how the most developed theoretical mechanisms describing variations in the IGIMF over galactic scales (Weidner & Kroupa 2005) can also explain local variations. Therefore, observational constraints such as the one presented in this chapter provide essential information towards a complete theory of star formation.

Furthermore, the observed radial difference in the IMF of massive galaxies can be understood as the imprint from two different modes of galaxy formation (Oser et al. 2010): a quick and efficient one, building up the cores of massive ETGs at high redshift, during an early epoch (Eggen et al. 1962) – leading to a system with high velocity dispersion and a bottom-heavy IMF – followed by a more gradual growth of the outermost regions (Navarro-González et al. 2013), perhaps either by the accretion of smaller structures (Naab et al. 2009), or via a quiet, prolonged, star-formation rate, where the lower velocity dispersion of the interstellar medium leads to a standard IMF. Studies of massive ETGs with uncorrelated radial gradients of the IMF distribution and [$\alpha$/Fe] enhancement

are crucial to determine the local parameter driving the IMF in these galaxies. This two-phase formation scenario is in sharp contrast with a naïve interpretation of the hierarchical buildup paradigm of galaxy formation, where high-mass systems form through the mere assembly of smaller units, and calls for further observational and theoretical advances.

## 4.7 Conclusions

We have analysed the spectra of two nearby ETGs: a massive galaxy, NGC 4552, and a low-mass counterpart, NGC 4387. Results for an additional high-mass galaxy, NGC 5557 (with lower quality data), are also discussed. Comparing observed line-strengths to predictions of state-of-art stellar population models, we have found that:

1. Massive galaxies show a steep radial variation of the IMF slope, with an enhanced fraction of low-mass stars in the centre and a standard Kroupa-like distribution at the effective radius (Fig. 4.4).

2. The IMF gradient of the low-mass galaxy is rather flat, mildly steeper than that for a Kroupa-like IMF throughout (Fig. 4.4).

3. Our result naturally explains the IMF-slope vs central velocity dispersion relation of ETGs, as a luminosity-weighted average of the underlying IMF radial gradient,

We therefore suggest that the IMF of nearby ETGs should be regarded as a "local" property, with an excess of low-mass stars being produced by processes driving the formation of their cores – during the early phases of star formation.

Although simple, phenomenological models provide explanations to this scenario (Hopkins 2013; Weidner et al. 2013), detailed ab initio numerical simulations are required to understand this fundamental link between the growth of structures and the "baryon" physics of galaxy formation.

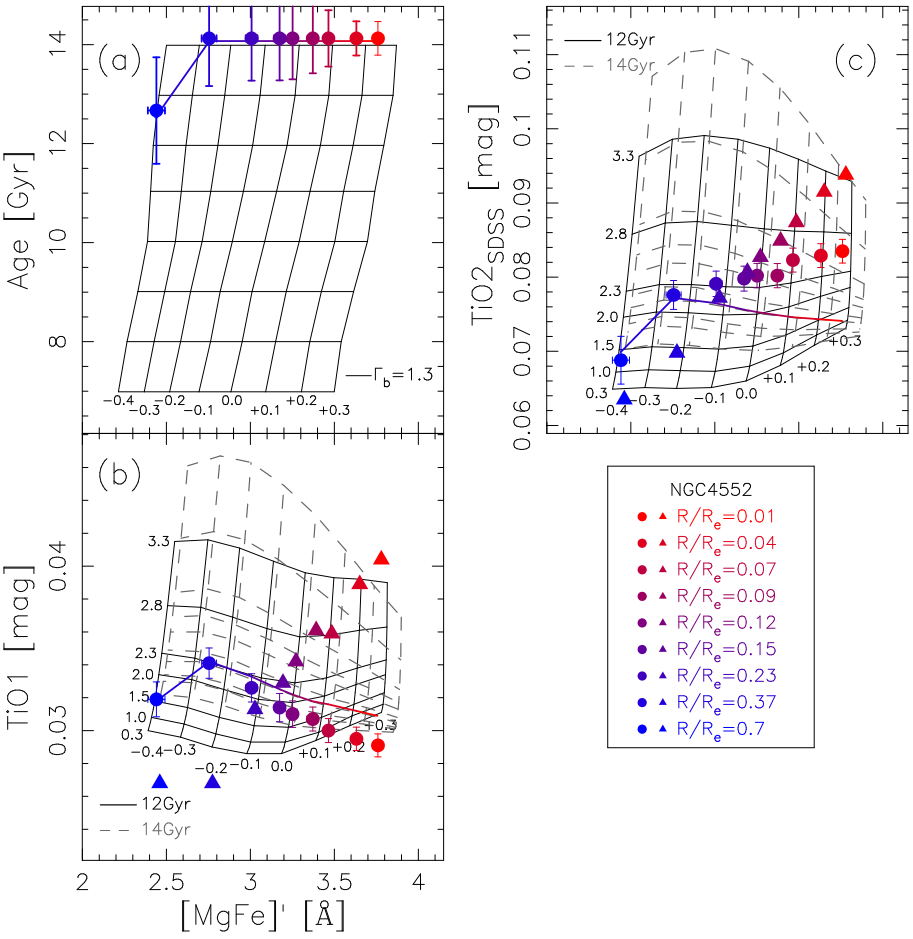


Figure 4.6: Fitting results for our reference high-mass galaxy, NGC 4552, obtained by leaving age, metallicity, and $\delta$Ti as free parameters, but assuming a fixed, standard (Kroupa-like), IMF. Panel (a): coloured dots, with error bars, are age estimates from spectral fitting, for a Kroupa IMF. The grid shows the effect of varying metallicity on the [MgFe]$'$ index, for SSPs with a Kroupa-like IMF ($\Gamma_b = 1.35$) and different ages. Panels (b-c): solid and dashed grids show line strengths for SSP models with varying $\Gamma_b$ and [Z/H], for two representative ages of 12 (outermost radial bin; see panel a) and 14 Gyr (innermost bins), respectively. Filled circles, with error bars, are the [$\alpha$/Fe]-corrected and $\delta$Ti shifted line strengths, while triangles plot raw line strengths (as measured on the spectra). Notice that triangles are the same as in panels (b-c) of Fig. 4.3. Since $\delta$Ti is a free fitting parameter, the $\delta$Ti values are not the same when assuming a fixed, relative to a varying, IMF. Hence, coloured dots in panels (b-c) are not the same as those in Fig. 4.3. In all panels, solid-coloured curves show the best-fit solutions, with colour varying from red, in the galaxy centre, through blue, at larger galactocentric distances. The same colour coding applies to dots and triangles (see the legend in the lower–right corner of the plot). For the two outermost bins, the best-fit Kroupa-like models (coloured curves) match the [$\alpha$/Fe]-corrected and $\delta$Ti shifted line strengths (filled circles). On the contrary, in the five innermost bins, the model $TiO_2$ deviates by more than $3\,\sigma$ from the observations, while significant deviations (at $2\,\sigma$) are also seen for $TiO_1$.

# 5

# The stellar initial mass function at 0.9<z<1.5

This chapter has been published as *Martín-Navarro et al. 2015, ApJL, 798, 4*

To have a consistent picture of galaxy evolution, it is absolutely necessary to investigate the IMF at different redshifts. So far, the IMF of $z \lesssim 1$ galaxies has been studied indirectly using virial masses (Renzini 2006; van de Sande et al. 2013) or elaborated dynamical models (Shetty & Cappellari 2014). These works point to a Salpeter (1955) IMF for massive galaxies at intermediate redshift. Other indirect IMF-sensitive observables have also been used in the topic. For instance, the consistency between the cosmic stellar mass and star formation rate densities (Davé 2008; Pérez-González et al. 2008) and the luminosity evolution of massive ETGs (van Dokkum 2008) are better described by a flatter (i.e., with a relatively larger number of massive stars) IMF at higher look-back times. Even in star-forming galaxies, the constancy of the IMF is in tension with observations (Hoversten & Glazebrook 2008; Meurer et al. 2009)

Here we explore, for the first time, the IMF slope at $z \gtrsim 1$ using stellar populations synthesis models in massive quiescent galaxies (MQGs). To achieve this goal, we study the $TiO_2$ IMF-sensitive spectral feature (Mould 1976). In Section 5.1, we describe the data. The IMF inference is explained in Section 5.2. In Section 5.3, we discuss our results. We adopt a standard cosmology: $H_0$= 70 km $s^{-1}$ $Mpc^{-1}$, $\Omega_m$= 0.3, and $\Omega_\Lambda$=0.7.

## 5.1 Sample and data description

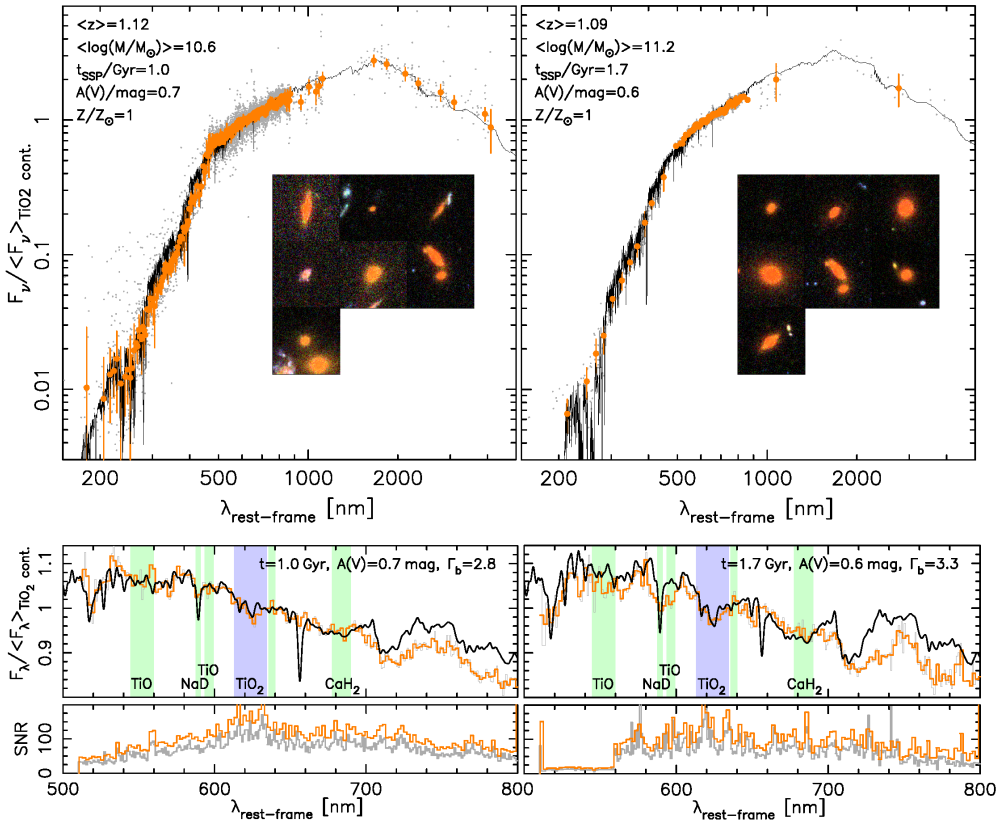


Figure 5.1: Stacked SEDs (normalized to the average $TiO_2$ continuum flux) for MQGs at 0.9<z<1.5 in GOODS-N for the low-mass (left) and high (right) samples. We show the complete UV-to-NIR stack on *top*, with data for individual galaxies (gray dots) and average fluxes in bins of 20 photometric data points (orange), including $2\sigma$ bars. The black line shows best-fitting BC03/XMILES SSP models with a Kroupa IMF, and assuming a Calzetti et al. (2000) law for the dust attenuation. We provide 5"×5" RGB postage stamps for representative examples of the sample. At the *bottom*, we show the WFC3/G141 grism data including stacked (gray) and smoothed (orange) spectra (using 10 and 20 Å bins, respectively), and their SNR. The black line shows best-fitting MIUSCAT SSP models. Shaded regions mark the $TiO_2$ absorption (blue), and other IMF-sensitive indices (green). Deviations from an SSP appear beyond 700nm, where a small fraction ($\sim$ 10%) of a younger population can significantly affect the continuum, but barely changes (0.004 mag) the $TiO_2$ value.

To facilitate the determination of the IMF slope at high-z, we study galaxies

with no signs of recent star formation (quiescent galaxies). These objects have simpler Star Formation Histories (SFHs) than star-forming galaxies and are sufficiently well represented by a single stellar population (SSP) model (e.g., Whitaker et al. 2013).

MQGs at 0.9<z<1.5 were selected with two criteria: (1) the $UVJ$ diagram with no MIR/FIR detections; and (2) a sSFR vs. stellar mass plot. We worked with the mass selected sample presented in Pérez-González et al. (2008). From this work, we took the spectral energy distributions (SEDs), stellar population and dust emission models for all IRAC sources in GOODS-N. Those SEDs were complemented with medium-band optical photometry from the Survey for High-z Absorption Red and Dead Sources, SHARDS (Pérez-González et al. 2013). The broad- and medium-band photometry was fitted with a variety of stellar population models to obtain photometric redshifts, stellar masses, SFRs, and rest-frame synthetic colors (see Barro et al. 2011a,b). Thanks to the ultra-deep medium-band data from SHARDS, the quality of our photometric redshifts is excellent: the median $\Delta z/(1+z)$ is 0.0067 for the 2650 sources with $I$<25 (Pérez-González *et al.* 2014, in prep; Ferreras et al. 2014). SFRs were calculated for all galaxies using various dust emission templates and the *Spitzer*-MIPS and *Herschel*-PACS/SPIRE fluxes, jointly with UV-based measurements for non-detections in the MIR/FIR. The UV-based SFRs were corrected for extinction with the UV slope $\beta$ and an extrapolation of the IR-$\beta$ (IRX) relationship (Meurer et al. 1999). The extrapolation technique was developed to recalibrate the IRX-$\beta$ relation using faint IR emitters (more similar to MIR-undetected galaxies) at the same redshifts. Details about the selection will be given in Domínguez Sánchez *et al.* (2014, in prep.).

Using this dataset, we selected galaxies at 0.9<z<1.5 having stellar masses M> $2\times10^{10}$ $M_\odot$(Kroupa 2001 IMF), and rest-frame $UVJ$ colors within the quiescent galaxy wedge ($U-V>1.3$, $V-J<1.6$, $U-V>0.88\times(V-J)+0.59$; Whitaker et al. 2011). The mass cut was chosen to allow measuring the $TiO_2$ absorption in the grism spectra described below. The $UVJ$-selected sample was complemented with galaxies with sSFR<0.2 $Gyr^{-1}$, our limit for quiescence. Galaxies with MIPS detections were removed from the sample, as the MIR emission indicates active/residual star formation or nuclear activity, which would complicate the stellar population analysis. Using these two criteria, we selected 124 sources in the 112 $arcmin^2$ covered simultaneously by GOODS, SHARDS, CANDELS, and *Herschel*-GOODS.

The $TiO_2$ spectral index was measured in stacked WFC3/G141 grism data (covering $1.1\lesssim\lambda\lesssim1.6$ $\mu$m) from the AGHAST survey (PI: Weiner). We selected all galaxies with $H$<25.5 mag from the F160W imaging in CANDELS (Grogin et al. 2011; Koekemoer et al. 2011) and reduced the grism data to extract 2D

spectra using the aXe software (version 2.3). Then we collapsed the data to obtain 1D spectra using our own dedicated software. The reduction used 0.064 arcsec/pixel and 23.5 Å/pixel. The 1D extractions were optimized for each galaxy using its effective radius, position angle, and the contamination map provided by aXe. Visual inspection helped to remove spectra with significant contamination and/or artifacts, leaving 97 galaxies with usable G141 spectra. We kept the spectra with SNR>5 per pixel. Our final sample is composed by 57 galaxies with $2\times10^{10}<M/M_{\odot}<10^{11.5}$ ($<M>=10^{10.6}$ $M_{\odot}$) and 0.9<z<1.5 (<z>=1.1). Reliable spectroscopic redshifts were available for 33 galaxies; the median quality of the photo-redshifts for $M>10^{10.5}$ $M_{\odot}$galaxies is $\Delta z/(1+z)$ =0.0047.

Measurements were carried out in stacked spectra of these 57 z∼1 MQGs. We dissected the sample to probe the lowest and highest mass regimes with two stacked spectra of similar SNR (Figure 5.1). The high-mass sample was composed by 7 galaxies with $M>10^{11}$ $M_{\odot}$($H$=19.7-21.3 mag), and the low-mass spectra by 50 galaxies with $M< 2\times10^{10}$ $M_{\odot}$($H$=20.3-22.4 mag). To build the stacks, we first de-redshifted all individual observed spectra, then normalizing them to the $TiO_2$ continuum (see next section). We calculated flux averages and errors in rest-frame wavelength bins of 10 Å. Finally, we smoothed the stacks with a 20 Åboxcar kernel. The average SNR per resolution element of the final stacked (smoothed) spectra is 70 (100), 100 (140) around the $TiO_2$ absorption.

## 5.2 SED analysis: ages and IMF slope

The integrated spectral properties of a SSP are defined by four parameters: age, metallicity ([Z/H]), IMF and $\alpha$-elements over-abundance ([$\alpha$/Fe]). In this Letter, we analyze the $TiO_2$ absorption, an IMF-sensitive feature which depends very weakly on [Z/H] and [$\alpha$/Fe] (Thomas et al. 2011a; La Barbera et al. 2013). We present the age and IMF constraints for z∼1 MQGs based on this $TiO_2$ spectral index as well as on the ultraviolet to near-infrared SEDs. In Section 5.3, we discuss the impact of the unknown values of [Z/H] and [$\alpha$/Fe] on our results. The $TiO_2$ absorption is wide and deep enough to be measured with WFC3 grism data. Measurements for other IMF-sensitive features (see Figure 5.1) would be compromised by low SNR at $\lambda_{rf}$<500 nm, the low spectral resolution in the case of NaD, or the proximity to emission features in the case of $CaH_2$. Thus, we concentrate our IMF analysis on $TiO_2$ measurements.

### 5.2.1 Age determination

To constrain the age of the stellar population, we used three different methods. First, we fitted the G141 grism stacked spectra constrained to the rest-frame wavelength range $500<\lambda_{\rm rf}<800$ nm (Figure 5.1). We used the Bruzual & Charlot (2003, hereafter BC03) models fed with the XMILES library (Charlot & Bruzual, private communication). We assumed a SSP with solar and super-solar metallicities, and a Calzetti et al. (2000) attenuation law, and fitted the data to obtain ages, extinctions, and metallicities. We tested how the results were affected by: (1) using Salpeter (1955), Kroupa (2001), and Chabrier (2003) IMFs; (2) different attenuation recipes, namely, Calzetti et al. (2000), appropriate for starburst galaxies, and the more general law from Charlot & Fall (2000); and (3) different stellar population synthesis libraries and codes, namely, BC03 using XMILES and STELIB(Le Borgne et al. 2003) libraries, and MIUSCAT (Vazdekis et al. 2010). In all cases, we found negligible differences in the estimated ages (<0.1 Gyr) and extinctions (0.1 mag). Our fitting method included a Montecarlo algorithm to analyze uncertainties and degeneracies (see Pérez-González et al. 2013). Given the short wavelength range probed by the grism data, the dust extinction was not well constrained. Indeed, we found a strong age-extinction degeneracy. For example, for the high-mass stack, equally good fits were obtained for stellar populations with relatively young ages ($\sim$1 Gyr) and large extinctions (A(V)>1.5 mag) and for older ages and lower extinctions (1–2 Gyr and A(V)<1 mag). Constraining the extinction to A(V)<1 mag, we found that the stacked high-mass spectrum was best fitted by a SSP with solar metallicity, t=1.6$\pm$0.2 Gyr, and A(V)=0.5$\pm$0.3 mag. The low-mass stack was best fitted with solar metallicity, t=1.0$\pm$0.2 Gyr, and A(V)=0.7$\pm$0.3 mag.

Our second age determination method used the whole UV-to-NIR stacked SED (Figure 5.1). The SHARDS medium-band and grism data allow accurate measurements of both the 4000 Å break and the $\rm Mg_{UV}$ absorption, two very good age estimators (see Pérez-González et al. 2013; Hernán-Caballero et al. 2013; Ferreras et al. 2014, and references therein). The wider spectral range resulted in better constraints on the age and the extinction. The best-fitting BC03/XMILES SSP model provided $t$=1.77$\pm$0.17 Gyr, A(V)=0.60$\pm$0.06, and $t$=1.02$\pm$0.15 Gyr and A(V)=0.70$\pm$0.06 for the high-mass and low-mass samples, respectively (solar metallicity in both cases). Again, very similar results were obtained with other IMFs, extinction recipes, and stellar population libraries. Under an unrealistic assumption of A(V)=0, the best-fitting ages were $t$=1.5 Gyr and $t$=2.6 Gyr for the low- and high-mass stacks, respectively. These solutions provide, based on the $\chi^2$ values, worse fits, and do not affect our main conclusions, which will also stand if the actual extinction is more severe than

our estimations (cf. Section 5.3).

Finally, we measured the stellar population ages fitting the whole UV-to-NIR SED for each individual galaxy also using the Montecarlo method, and calculating average properties for the low and high-mass sub-samples. These were remarkably and reassuringly similar (within the uncertainties) to the ones obtained with the other methods: t=1.0±0.2 Gyr with A(V)=0.9±0.2 mag and t=1.5±0.3 Gyr with A(V)=0.9±0.3 mag for the low-mass and high-mass samples, respectively.

Our age estimations are completely consistent with those obtained by Whitaker et al. (2013) using a stacked G141 grism spectrum around the H$\beta$ absorption also for $UVJ$-selected MQGs, but at 1.4<z<2.2. They find ages between 0.9 Gyr and 1.6 Gyr for blue and red massive galaxies, very similar to the ranges we find for the our two sub-samples. Consistent ages are also found for MQGs at z>1 (selected in a variety of ways and counting with heterogeneous data) by Onodera et al. (2012), van de Sande et al. (2013), Bedregal et al. (2013), and Marchesini et al. (2014). In summary, the ages of the $UVJ$- and sSFR-selected z∼1 MQGs are confidently constrained to be <2 Gyr.

### 5.2.2 IMF estimation

Once average ages were determined, we proceeded to the IMF analysis based on the $TiO_2$ absorption. Given that this molecular band dominates the spectrum of cool-dwarf stars between 600 and 640 nm, it has been widely used to infer the IMF slope in unresolved stellar systems (Ferreras et al. 2013; La Barbera et al. 2013; Spiniello et al. 2014).

We used the MILES SSP models (Vazdekis et al. 2010), where the IMF is parametrized as a single power law, truncated (i.e., flatted out) for stellar masses below M<0.6 $M_\odot$. This bimodal IMF is completely described by a single parameter, $\Gamma_b$ (see Vazdekis et al. 1996). Under this parametrization, the Kroupa (2001) IMF is recovered for $\Gamma_b$=1.3. The main advantage of the bimodal IMF, compared to a regular single power law (Salpeter-like) IMF, is the fact that, even when dealing with very high $\Gamma_b$ values, the $M/L$ ratio remains within the observational limits suggested by dynamical studies (Ferreras et al. 2013). From the point of view of the stellar population properties, both bimodal and uni-modal IMF parametrizations are indistinguishable.

MILES models cover a range from −2.32 dex to +0.22 dex in metallicity, 0.06 Gyr to 17 Gyr in age, and $\Gamma_b$=0.3–3.3 in IMF slopes. Given the weak dependence of the $TiO_2$ index with metallicity, we fixed it to solar (as suggested by the SED fitting).

The classical definition for the $TiO_2$ spectral index expands along ∼400 Å,

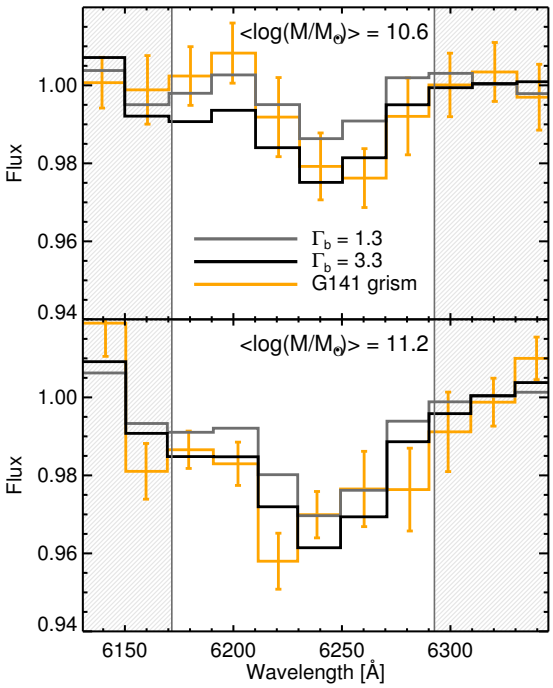


Figure 5.2: The $TiO_2$ spectral region of the low- (top) and high-mass (bottom) stacks, as observed through the WFC3 G141 grism (orange solid line). Data points are compared to models (smoothed to the same resolution) with a bottom-heavy (black histogram) and a standard Kroupa-like IMFs (gray). The observed spectra and models were normalized to the flux in the continuum bands (gray shaded regions). Ages were fixed to the results discussed in Section 5.2.1.

making it extremely sensitive to the adopted flux calibration (see Section 5 in Martín-Navarro et al. 2015a). To improve the signal, we redefined the blue and red $TiO_2$ pseudo-continua, making them contiguous to the central bandpass. The adopted blue and red pseudo-continua are 613.0–617.2 nm and 629.3–634.5 nm, respectively. Figure 5.2 presents, for both stacks, the data and fits to the $TiO_2$ spectral region.

The analysis of the $TiO_2$ absorption was based on fits to the six spectral elements ($P_{obs}(\lambda)$) within the central band of our $TiO_2$ index definition, after removing the continuum. The models were degraded to the same spectral resolution ($P_{SSP}(\lambda)$). The goodness of the fit was estimated with a $\chi^2$ function:

$$\chi^2(\Gamma_{\rm b}, {\rm age}) = \sum_{\lambda} \frac{[{\rm P_{obs}}(\lambda) - {\rm P_{SSP}}(\lambda)]^2}{\sigma^2_{\rm obs}(\lambda)} \quad (5.1)$$

where $\sigma_{\rm obs}(\lambda)$ represents the estimated error of the flux in each spectral bin. The $\chi^2$ maps in the age-IMF slope plane for the low- and high-mass samples are shown in Figure 5.3.

## 5.3 Discussion

Figure 5.3 shows our constraints on the stellar population age and IMF slope for MQGs at z∼1. As expected, there is a clear IMF/age degeneracy: similar $TiO_2$ values are obtained by either an old population with a standard Kroupa-like IMF or with a steeper IMF and younger ages. To further constrain the IMF, we use the age determinations from the SED fitting.

For the high-mass sample, Figure 5.3 shows that our age determination of 1.7±0.3 Gyr combined with the $TiO_2$ index measurements strongly suggest that the IMF of $M \gtrsim 10^{11}$ $M_\odot$MQGs at z∼1 is bottom-heavy. The IMF slope is $\Gamma_b$=3.2±0.2, very similar to that measured for present-day early-type galaxies (La Barbera et al. 2013; Spiniello et al. 2014). For the low-mass stack, considering a typical age of 1.0±0.2 Gyr, we find that the IMF is flatter: $\Gamma_b = 2.7^{+0.3}_{-0.4}$. The uncertainty in this case is larger, mainly because the degeneracies between age and IMF increase for younger ages and flatter IMFs. Using these IMF values, and assuming a bimodal parametrization, the mass-limits of our stacks change to $M>10^{11.5} M_\odot$and $10^{10.7}<M<10^{11.5}$ $M_\odot$for the high- and low-mass stacks, respectively. Although our age constraints are rather conservative (see Section 4.2.3), an offset of +0.5 Gyr in the lighter stack would leave the IMF slope unconstrained below $\Gamma_b \sim 3$. Such a large error in a 1 Gyr old population is not expected, but the IMF determination of this lighter stack should be considered more tentative than that for the massive stack. Furthermore, low-mass galaxies tend to have more extended SFHs (Thomas et al. 2005) and therefore, their SED may be less well represented by a single SSP. Note also that the departure from a SSP is expected to become larger if galaxies are observed closer to their formation age. This slightly extended star formation history in the lighter stack increases the scatter in the UV region, as shown in the upper left panel of Figure 5.1. In addition, at lower stellar masses the nature of galaxies becomes more heterogeneous, increasing the likelihood of having systems following different evolutionary tracks (e.g., disks and spheroids with different assembly histories maybe affecting the IMF).

Two main caveats should be considered before further interpreting our data:

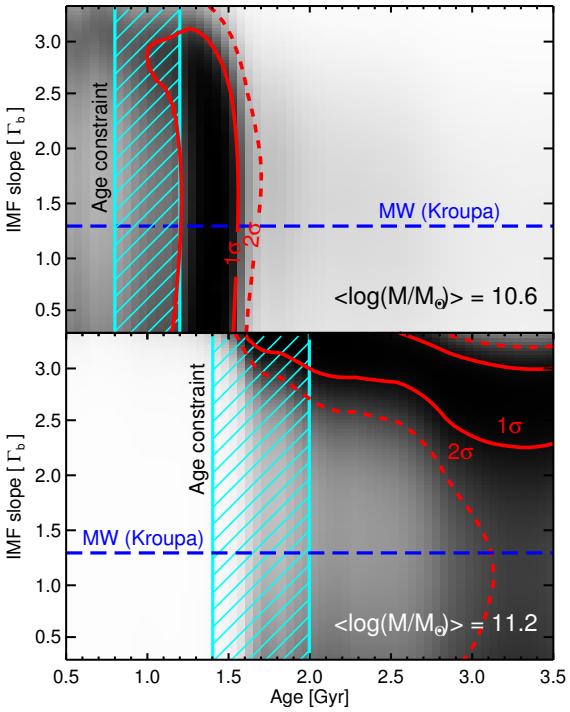


Figure 5.3: $\chi^2$ values in the IMF slope vs. age plane for the low-mass (top) and the high-mass (bottom) samples. Darker tones indicate more probable SSP solutions. The solid and dashed red lines enclose the 1- and 2-$\sigma$ probability contours. Dashed cyan regions mark the age range inferred from SED fitting. The combination of the $TiO_2$ index measurements and the stellar ages indicates that the IMF of massive quiescent galaxies at z$\sim$1 is bottom-heavy. For the low-mass galaxies, degeneracies are larger and the IMF slope determination is significantly more uncertain.

the effect of $\alpha$-element enhancement and metallicity. Our fits do not account for non-solar $\alpha$-elements abundances. Massive galaxies exhibit an enhanced fraction of $\alpha$-elements compared to the solar neighborhood, commonly interpreted as an imprint of a fast formation process (Thomas et al. 2005). For a 1-2 Gyr old population, an overabundance of $\sim$1 dex in [Ti/Fe] would be needed to mimic the effect of a $\Gamma_b$=3.2 IMF (Thomas et al. 2011a). However, La Barbera et al. (2013) found an excess of only $\sim$0.2 dex in [Ti/Fe] for massive galaxies at $z \sim 0$. Therefore, unless the situation is totally different at high-z (but see Choi et al. 2014), our $TiO_2$ measurement is unlikely to be explained with a standard IMF plus a non-solar [Ti/Fe] abundance. The second caveat relates to the fact that we have used models with fixed solar metallicity. The effect

of the metallicity on the $TiO_2$ line is very weak but not null. In this sense, we find steeper IMFs when assuming larger metallicities. However, neither our SED fits, nor z∼0 massive galaxies (La Barbera et al. 2013) suggest a strong departure from solar metallicity. On the contrary, an overestimation of the actual metallicity would weakly mimic the effect of a step IMF slope on the $TiO_2$ feature. However, sub-solar metallicities can be ruled out considering that galaxies as massive as those in our sample, show almost no metallicity evolution since $z \sim 1$ (Choi et al. 2014), being metal-rich at $z \sim 0$ (La Barbera et al. 2013). Thus, our results are robust against a poor metallicity determination.

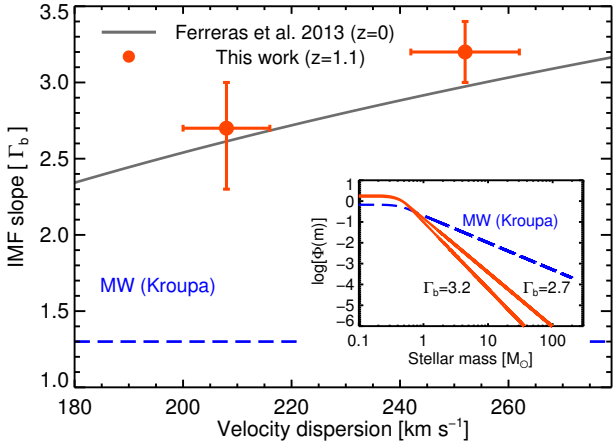


Figure 5.4: IMF slope vs. velocity dispersion for MQGs at z∼1, compared to the relation found for present-day ETGs (Ferreras et al. 2013) and a Kroupa (2001) IMF. The inset explicitly shows the differences among all these IMFs.

In a more qualitative way, in Figure 5.4 we compare our results with the IMF slope vs. velocity dispersion relation found in the nearby Universe (Ferreras et al. 2013). We have translated our stellar mass scale to velocity dispersion using individual measurements for our galaxies and statistical properties for samples at the same redshift and selected in similar way. Based on measurements found in the literature (mainly in van de Sande et al. 2013; Belli et al. 2014) for galaxies with similar masses at similar redshifts, we obtain an average velocity dispersion of 252±10 km s$^{-1}$ and 208±8 km s$^{-1}$ for our high- and low-mass stacks, respectively. In addition, individual velocity dispersions have been measured for two galaxies contributing to our low-mass stacked spectrum (Newman et al. 2010). The mass of one of these galaxies is M=$10^{10.6}$ $M_{\odot}$and its velocity

dispersion $\sigma$=206 km s$^{-1}$, and for the other M=$10^{10.9}$ M$_{\odot}$and $\sigma$=239 km s$^{-1}$. According to Figure 5.4, our z$\sim$1 IMF estimations are in good agreement with the IMF slope in early-type galaxies of similar mass in the present-day Universe. This suggests a direct evolutionary link between both populations and that the IMF, a key characteristic of the stellar populations in galaxies, have remained unchanged in the last $\sim$8 Gyr.

# 6

# The initial mass function of a massive relic galaxy

This chapter has been published as *Martín-Navarro et al. 2015, MNRAS, 451, 1081*

A combination of major and minor dry mergers are the favoured explanation for the evolution of the scaling relations of massive galaxies since $z \sim 2$ (e.g. Naab et al. 2009; Trujillo et al. 2011; Ferreras et al. 2014; Ruiz et al. 2014). Being a stochastic process, a natural prediction of this evolutionary channel is the presence, in the local volume, of a number of massive galaxies which have experienced few if any significant merger events since they were formed (Quilis & Trujillo 2013). These putative *relic galaxies* present a unique opportunity to study in detail the properties of massive, $z \sim 2$ galaxy analogues in the nearby Universe.

The Perseus cluster galaxy NGC 1277 fulfills all the characteristics to be considered a relic massive galaxy (Trujillo et al. 2014). The galaxy exhibits an unusually high central velocity dispersion (above 400 $\mathrm{km\,s^{-1}}$) and is physically compact, with an effective circularized radius of 1.2 kpc (Trujillo et al. 2014). The bulk of its stars are old (age $>$ 10 Gyr) and $\alpha$-enhanced ([Mg/Fe] $\sim$ 0.3 dex), which suggests a short ($\tau \sim 100$ Myr) and intense (SFR $\gtrsim 10^3$ $\mathrm{M_\odot/yr}$) star formation burst at $z \sim 2$, followed by subsequent quiescent evolution (Trujillo et al. 2014). In addition, NGC 1277 hosts the most massive (compared to the total galaxy mass) black hole found to date (van den Bosch et al. 2012, but see Emsellem 2013).

Trujillo et al. (2014) studied the stellar population properties of NGC 1277 assuming that its stellar initial mass function (IMF) follows that seen in the Milky Way (Kroupa 2002; Chabrier 2003). Although this approach has been extensively used in the literature, many studies (Cenarro et al. 2003; van Dokkum & Conroy 2010; Cappellari et al. 2012; Ferreras et al. 2013; La Barbera et al. 2013; Spiniello et al. 2014) have shown that the shape and the normalization of the IMF correlate with galaxy mass. Moreover, Martín-Navarro et al. (2015a) have found that the IMF slope of some representative massive galaxies depends on galactocentric distance. Since the inferred properties of a stellar population strongly depend on the adopted IMF (Ferré-Mateu et al. 2013), it is important to investigate the stellar populations of massive systems such as NGC 1277 while relaxing the assumption of a universal IMF.

The importance of measuring the behaviour of the IMF as a function of radius in NGC 1277 is two-fold. On the one hand, it provides a route to understanding the physical conditions of massive galaxies when the majority of their stars were formed, with no influence from later accretion events. On the other hand, NGC 1277 shows an atypical combination of kinematical and stellar population properties (van den Bosch et al. 2012; Trujillo et al. 2014), which can be used to investigate the main driver behind these IMF variations.

By studying the radial variation of IMF-sensitive spectral indices, we have been able to derive its IMF radial profile, which remains bottom-heavy up to $\sim 1.5\mathrm{R_e}$. We have simultaneously inferred, in a self-consistent manner (i.e., by adopting the best-fitting IMF value at each radius), its age, metallicity and [Mg/Fe] gradients. Here we find that the claims made by Trujillo et al. (2014) regarding NGC 1277 as being a relic object are also supported under the assumption of a steep IMF.

This chapter is structured as follows: in Section 2 we present our data; Section 3 contains the analysis and the main results, which are finally discussed in Section 4. We adopt a standard cosmology: $\mathrm{H_0}$= 70 km $\mathrm{s^{-1}}$ $\mathrm{Mpc^{-1}}$, $\Omega_m$= 0.3, and $\Omega_\Lambda$=0.7.

## 6.1 Data and data reduction

Our data consist of two sets of long-slit spectroscopic observations of NGC 1277 carried out at the 4.2m William Hershel Telescope (WHT) and at the 10.4m Gran Telescopio Canarias (GTC), located at the Spanish Observatorio del Roque de los Muchachos on La Palma. The WHT spectra were acquired with the Intermediate dispersion Spectrograph and Imaging System (ISIS), using the R300B grating and a 1 arcsec slit, placed along the major axis of the galaxy (see Trujillo et al. 2014, for details). The total on-source integration time for these

observations was 3 hours, with 1 arcsec seeing. The spectra cover the wavelength range from $\sim 3700$ to $\sim 6000$ Å, with 3.4 Å spectral resolution (FWHM). In a second run of observations, we again targeted the NGC 1277 major axis with the GTC Optical System for Imaging and low-Intermediate-Resolution Integrated Spectroscopy (OSIRIS) in order to increase the wavelength coverage up to 10000 Å, allowing us to include near-infrared IMF-sensitive features such as Na 8190 (Schiavon et al. 2000) and the Calcium triplet (Cenarro et al. 2001). These data have a (wavelength-dependent) resolution ranging from 6 Å at $\lambda \sim 5000$ Å to 8 Å at $\lambda \sim 10000$ Å. The total exposure time was 1.5 hours on source with a typical 0.8 arcsec seeing. In both datasets, the pixel size was 0.25 arcsec. In this chapter, all measurements (i.e. line-strengths indices) blueward and redward of 5700 Å come from WHT and GTC data, respectively.

Data reduction was performed using the REDUCEME package (Cardiel 1999), which allows for the careful treatment of error propagation. The reduction process included the standard bias subtraction, flat-fielding, cosmic ray cleaning, distortion (C and S) correction, wavelength calibration, sky subtraction and flux calibration.

Note that, for our purposes, sky removal is a critical step of the reduction, as both airglow emission and telluric absorption have a prominent role in the raw spectra above $\lambda \sim 7000$ Å. To ensure an accurate sky subtraction, an *on-and-off* observational strategy was followed, where the galaxy was offset in the CCD plane during the observations. This allowed for a clean sky emission removal by subtracting consecutive exposures. The second crucial aspect was that of correcting the spectra for telluric absorption features. In order to investigate the impact of such correction on the derived stellar population parameters, we adopted two independent approaches. The spectrophotometric standard star (Hiltner 600, B1) was targeted at the end of the observations. Using the IRAF task *telluric*, the derived atmospheric transmission spectrum was scaled to correct the NGC 1277 data. In addition, we made use of the ESO tool MOLECFIT (Kausch et al. 2014). The latter does not require any extra calibration data (i.e. a spectrophotometric standard star) as it constructs a synthetic atmospheric absorption model for a given spectrum, by fitting spectral regions dominated by telluric absorption in the spectrum itself[1]. To this effect, molecfit relies on the radiative transfer code LBLRTM (Clough et al. 2005), allowing for a simultaneous fit of both the telluric model and the line

[1]In particular, we run MOLECFIT by fitting the spectral regions $\lambda\lambda$ 8130,8300 Å; $\lambda\lambda$ 7585,7698 Å; $\lambda\lambda$ 7235,7326 Å and $\lambda\lambda$ 6861,6924 Å, where strong $H_2O$ and $O_2$ telluric features are found.

spread function to the data. The differences in the inferred stellar population properties among the two approaches are described in Appendix A.

Since the analysis of stellar populations requires a higher signal-to-noise (SN) than kinematics, we performed a first radial binning by imposing a SN threshold of 20. The radial velocity and velocity dispersion gradients, derived using the public available software pPXF (Cappellari & Emsellem 2004), are shown in Fig. 6.1. Our measurements are in good agreement with those published by van den Bosch et al. (2012), showing that NGC 1277 is pressure-supported in the central regions ($\sigma_c \sim 400$ km s$^{-1}$ ), whereas ordered motions dominate beyond $\sim 0.5$R$_e$. We used the inferred kinematics (radial velocity and velocity dispersion) to correct every row (spectrum) in the image to the rest-frame via linear interpolation of our measurements. Once all the spectra were at rest-frame, we calculated a representative spectrum at each radius of the galaxy with a minimum SN per Å (at $\lambda\lambda$ 6000,6200 Å) of 80 in the outskirts, achieving over 700 in the central bin.

Throughout this chapter, we assume a circularized effective radius of R$_e$ = 1.2 kpc for NGC 1277, with a 0.344 kpc arcsec$^{-1}$ scale (Trujillo et al. 2014). Fig. 6.2 shows three representative spectra at 0, 0.5, and 1 R$_e$, respectively. The change in spectral resolution from the WHT to the OSIRIS data appears at $\lambda = 5700$ Å. Note also how the intrinsic (associated with the velocity dispersion) resolution varies from the central (in red, $\sigma \sim 400$ km s$^{-1}$ ) to the outermost bin (in orange, $\sigma \sim 200$ km s$^{-1}$ ). A zoom around the H$\beta$ feature is shown as an inset, suggesting no significant contamination of the line from nebular emission (see § 6.2).

## 6.2 Analysis and results

We based our stellar population analysis on the extended version of the MILES models (Vazdekis et al. 2010, 2012). The MILES models cover a range from $-2.32$ dex to $+0.22$ dex in total metallicity, and from 0.06 Gyr to 17 Gyr in age. We allowed for a variation in the IMF slope, $\Gamma_b$, from 0.8 (bottom-light) to 3.3 (bottom-heavy). Note that $\Gamma_b$ varies the slope of the high-mass end of the (bimodal) IMF, in contrast to other studies where the high-mass end of the IMF is kept fixed, while the low-mass end is varied (e.g. Conroy & van Dokkum 2012b). Since the (bimodal) IMF is normalized to have a total mass of 1 $M_\odot$, changing $\Gamma_b$ does actually vary the mass fraction of low- to high-mass stars. Hence, for the present study, $\Gamma_b$ should not be regarded as the high-mass end slope of the IMF, but rather as a proxy for the fraction of low-mass stars.

To determine the stellar population parameters we followed the same approach as in La Barbera et al. (2013). Age, metallicity, and IMF slope were

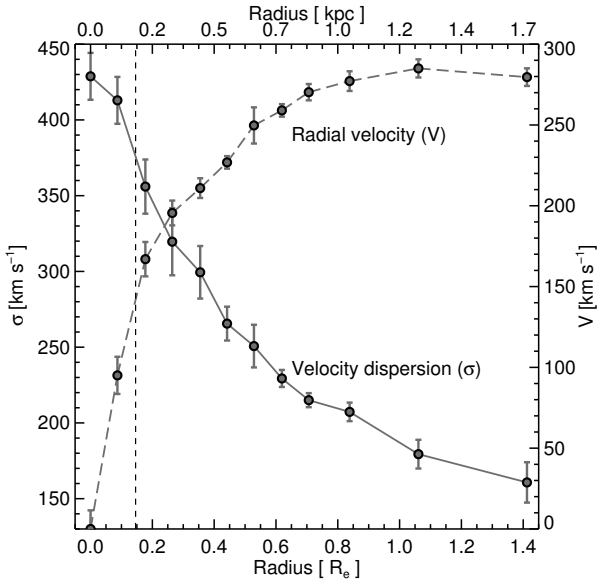


Figure 6.1: Velocity dispersion (solid line, left vertical axis) and radial velocity (dashed line, right vertical axis) profiles as a function of the major-axis radial distance, normalized to the (circularized) effective radius $R_e$. Dashed vertical line indicates the seeing radius, measured by its average half width at half maximum (HWHM) value (0.4 arcsec).

obtained by minimising the following equation:

$$\chi^2(\Gamma_b, \mathrm{age}, [\mathrm{Z/H}]) = \sum_i \left[ \frac{(EW_i - \Delta_{\alpha,i}) - EW_{M,i}}{\sigma_{EW_i}} \right]^2, \qquad (6.1)$$

where the sum expands over the $i$th observed and predicted line-strength indices included in the analysis. $EW_i$ are the measured line-strengths, $EW_{M,i}$ the predictions from MILES models, and $\Delta_{\alpha,i}$ is a correction applied to each index to account for deviations from a non-solar abundance scale, and the effect of "residual" abundance ratios on line strengths (see La Barbera et al. 2013 and Appendix A, for details). To derive [Mg/Fe], for each radial bin we estimated separately the Magnesium and the Iron metallicities ($Z_{Mg}$ and $Z_{Fe}$, respectively) through index-index fitting of the $H_{\beta_o}$ vs. Mgb and $\langle$Fe$\rangle$ line-strengths, respectively. We then subtracted one metallicity from the other to calculate the $[Z_{Mg}/Z_{Fe}]$ proxy, which tightly correlates with the "true" [Mg/Fe] (see Fig.6 in La Barbera et al. 2013). In Fig. 6.3 we show the measured radial profiles of all indices considered in the fitting process, along with the best-fitting SSP

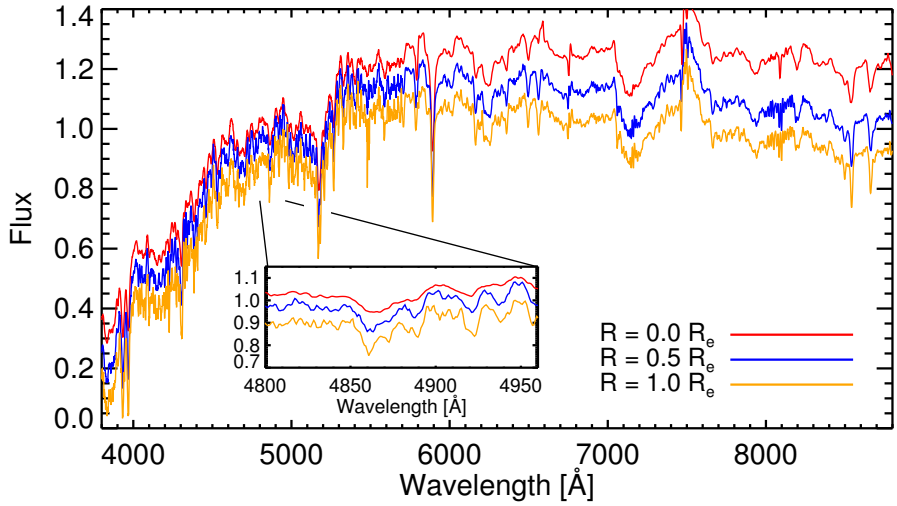


Figure 6.2: Averaged spectra at 0.0 (red), 0.5 (blue) and 1.0 (yellow) $R_e$, arbitrarily scaled in the vertical direction. Note the different spectral resolution between the GTC-OSIRIS ($\lambda > 5700$ Å) and the WHT ($\lambda < 5700$ Å) data. Note also the large variation in the velocity dispersion, reflected in a gradual smoothing when moving from the outer $1.0R_e$ spectrum to the central radial bin. The inset panel shows a zoom in of the H$\beta$ line.

solution at each radius. Notice that the $H_{\beta_o}$ line has been corrected for nebular emission contamination, as detailed in Appendix A.

The derived age, metallicity and [Mg/Fe] radial profiles are shown in Fig. 6.4. NGC 1277 exhibits a flat age profile, always above 10 Gyrs. The metallicity, on the contrary, decreases with increasing radius. Notice that the metallicity in the central bin (+0.41 dex) exceeds the maximum value of MILES models (+0.22). Hence, for this specific bin, we extrapolated the models (in the same way as in La Barbera et al. 2013) to match the observed indices (in particular, the total metallicity indicator [MgFe]′). Although in general there is a good agreement between the observed and best-fitting line strengths in Fig. 6.3, some discrepancies exist. In particular, the mismatch between observed and model indices in the most central bins (see, e.g., panels (f) and (i)), can be at least partly understood as a limitation of the stellar population models to describe very metal-rich ($\gtrsim 0.2$ dex) populations and/or uncertainties in the age estimate. However, none of these issues significantly affect the results of our work, as discussed in Appendix A. Fig. 6.4 also shows that the [Mg/Fe] gradient of NGC 1277 is flat, with [Mg/Fe]$\sim 0.3$ dex at all radii. This flat [Mg/Fe] radial profile can be also directly inferred from the fact that both the Mgb and $\langle$Fe$\rangle$

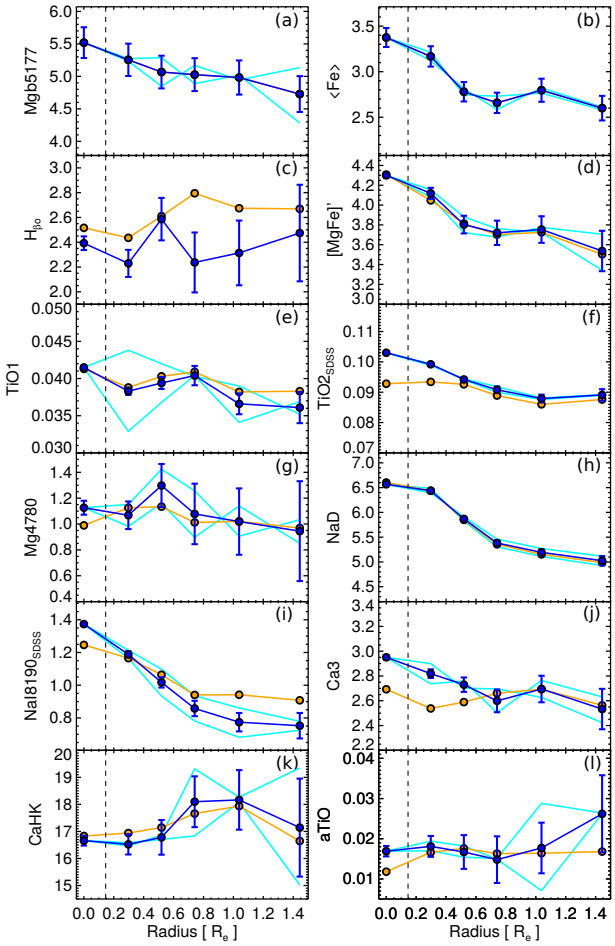


Figure 6.3: Observed gradients of the age-, metallicity- and IMF-sensitive indices considered in the fitting process (blue symbols). Dark blue represents the mean radial profile, whereas in light blue we show the radial gradient at each side of the galaxy. The $1\sigma$ error bars are also shown for the mean profile. The best-fitting solution is overplotted in orange. The definition of all spectral indices are given in La Barbera et al. (2013), while aTiO has been computed according to the definition of Spiniello et al. (2014). Although not individually included in the fitting process, panels (a) and (b) show the Mgb and $\langle$Fe$\rangle$ line-strength profiles. Note that, according to the MILES models, both indices have quite similar sensitivities to a variation in total metallicity. Since they also exhibit the same radial variation ($\sim 0.8$Å), a flat [Mg/Fe] gradient is expected, consistent with Fig. 6.4. In all panels, dashed vertical lines mark the seeing radius.

spectral indices (see panels (a) and (b) of Fig. 6.3) show a similar amount of ra-

dial variation [2]. Note that the large error bars on [Mg/Fe] in the central regions reflect the uncertainties on the [Fe/H] and [Mg/H] determination/extrapolation used to derive the [Mg/Fe] proxy. The gradients shown in Fig. 6.4 are in agreement with those published by Trujillo et al. (2014, Fig. 4 in their paper). This is not a trivial result, since here we have allowed for possible radial variations of the IMF.

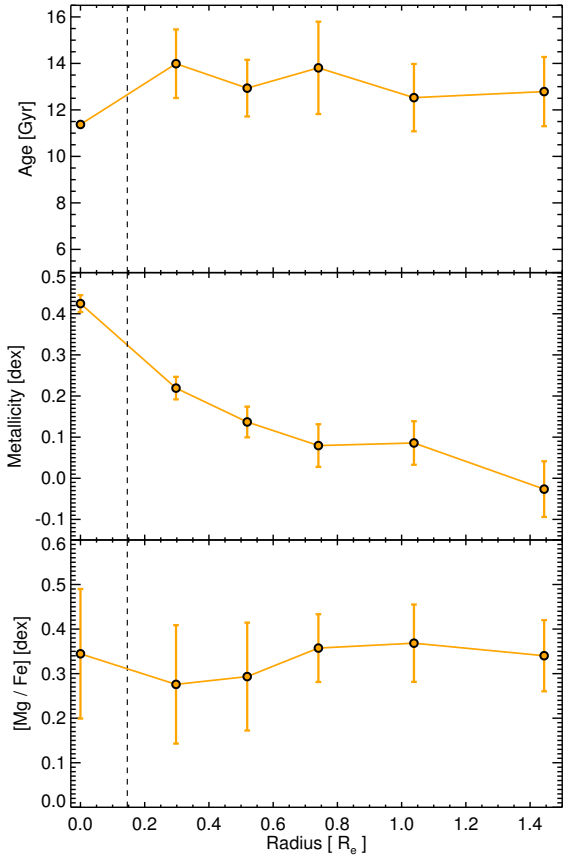


Figure 6.4: Best-fitting age (top), metallicity (middle) and [Mg/Fe] (bottom) gradients. Both age and [Mg/Fe] show a fairly flat radial behaviour, whereas metallicity decreases by 0.4 dex from the centre outwards to $1.5R_e$. An extrapolation of stellar population models is required to account for line-strength values in the central region. In all panels, dashed vertical lines mark the seeing radius.

[2]Notice, in fact, that in MILES models, both Mgb and ⟨Fe⟩ have a similar sensitivity to total metallicity, hence a similar radial gradient for the two indices implies a flat trend of the $[Z_{Mg}/Z_{Fe}]$ proxy.

The IMF radial profile of NGC 1277 is shown in Fig. 6.5, where the shaded region accounts for the scatter among $\Delta\Gamma_b$ values from different tests, where the fitting process has been repeated with different sets of spectral indices and different methods to remove telluric lines as detailed in Appendix A. Regarding the discrepancies between the observed and best-fitting line strengths (see Fig. 6.3), note that the $TiO_2$ and NaI 8190 lines can be potentially affected by errors in the flux calibration (the former) and telluric residuals (both). Although the central $TiO_2$ value might suggest a slightly steeper IMF profile, our best-fitting solution points to a mild radial variation of IMF slope ($\Gamma_b \sim -0.5$), i.e. a bottom-heavy IMF at all radii. Notice that in the present analysis we have not included the CaH1[3] and CaH2 IMF-sensitive features of Spiniello et al. (2015), as (1) CaH1 has been shown to be not matched by extended MILES models (regardless of the IMF, see La Barbera et al. 2013), while (2) CaH2 is strongly affected by the $O_2$ ($B$-band) atmospheric absorption at $\lambda \sim 6900$ Å in our data. Concerning Ca3, the (observed) index tends to decrease with radius, while our best-fitting solutions favour a flat radial behaviour for Ca3. This discrepancy might be related to some radial variation of the [Ca/Fe] abundance ratio which is not well captured by our fitting approach. In fact, although we have included [Ca/Fe] as a free fitting parameter (see Appendix A), the [Ca/Fe] is mainly constrained, in this chapter, from the CaHK line, which is strongly affected by the abundance pattern of other alpha elements (e.g. Vazdekis et al. 2015). Nevertheless, a decreasing trend of Ca3 with radius is the opposite behaviour to what one would expect for a less bottom-heavy IMF at larger radii (as Ca3 decreases with $\Gamma_b$). This is consistent with our conclusion that the IMF of NGC1277 shows only a mild radial variation. In fact, as shown in Appendix A, removing this index altogether from the fits does not significantly change the radial trend of $\Gamma_b$. Regarding aTiO, the only point that deviates significantly from the best-fits is the innermost one. This could be related to some issue in the extrapolation of the models at high metallicity, and/or some peculiar abundance ratio for $R=0\,R_e$. However, as the deviation affects only one single point, it does not change our general conclusions about the radial behaviour of $\Gamma_b$ for NGC1277.

The robustness of the IMF profile, against all issues mentioned so far, is demonstrated in Appendix A, where we show how the mildly decreasing behaviour of $\Gamma_b$ persists under different telluric correction procedures (see § 6.1), as well as different combinations of indices included in the fits, and changes in the modelling assumptions.

[3]Although not used in our analysis, the radial variation of the CaH1 index is mild (0.002 mag) and further supports a rather flat IMF profile.

Ultimately, gravity-sensitive indices trace the dwarf-to-giant star ratio in the IMF, regardless of the adopted IMF parametrization (La Barbera et al. 2013). This is explicitly shown in the right vertical axis of Fig. 6.5, where we represent the fraction (in mass) of stars below $0.5M_{\odot}$ for each IMF slope. The inferred dwarf-to-giant ratio in NGC 1277 is, at all radii, at least a factor of 2 larger than in the Milky Way (horizontal dashed line).

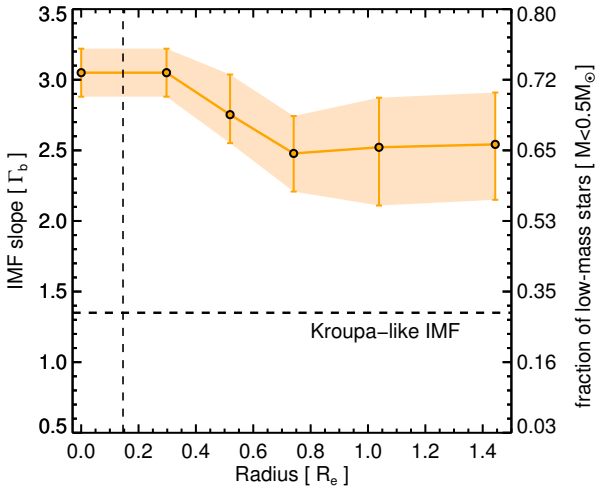


Figure 6.5: Radial IMF-slope gradient for the relic massive galaxy NGC 1277. The left vertical axis indicates the slope of the IMF in the bimodal case ($\Gamma_b$), i.e., the slope of the IMF for stars with masses larger than $0.5M_{\odot}$. This $\Gamma_b$ parameter can be transformed into a dwarf-to-giant ratio (right vertical axis), which is what the line-strength indices are actually tracing (La Barbera et al. 2013). For reference, the Milky-Way IMF value is shown as a horizontal dashed line. The inferred IMF gradient is mildly decreasing and it is very bottom-heavy up to $1.5R_e$. Uncertainties (the orange shaded region) are obtained by removing line-strength indices from the fitting process which might be potentially affected by flux calibration, telluric correction or modelling uncertainties. Dashed vertical line indicates the extent of the seeing disc.

The inferred stellar population properties of NGC 1277 (ages, metallicities, and IMF slopes; as shown in Figs. 6.4 and 6.5) can be used to estimate the stellar M/L radial profile. Notice, however, that for old stellar systems ($\gtrsim 10$ Gyr), stellar population analysis cannot provide fully reliable mass-to-light ratios, as it relies on the assumption of a given parametrisation for the IMF(Ferreras et al. 2014). In this sense, our favoured bimodal distribution seems to better match the dynamical M/L estimates (La Barbera et al. 2013; Spiniello et al. 2014), while a single power-law distribution provides unrealistically high M/L's. For

a bimodal IMF parametrisation, the expected M/L radial profile of NGC 1277 is shown in Fig. 6.6.

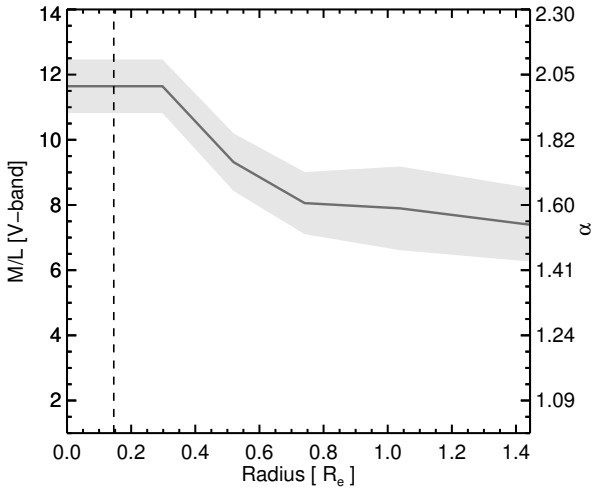


Figure 6.6: Radial M/L ratio ($V$-band) gradient for the massive compact galaxy NGC 1277, under the assumption of a bimodal IMF. At each radius, the best-fitting age, metallicity and IMF slope shown in Figs. 6.4 and 6.5 translate into a $V$-band M/L ratio. The right-hand axis represents the "mismatch parameter", $\alpha$, defined as the ratio between the inferred M/L and that expected from a stellar population with the same age and metallicity as observed, but with a Milky Way-like IMF slope. Notice that the absolute values of the M/L gradients heavily depend on the parametrisation adopted for the IMF (Ferreras et al. 2014). The light shaded region accounts for the uncertainties in all the stellar population parameters (e.g., error bars in Fig. 6.4 and shaded region in Fig. 6.5). Dashed vertical lines mark the seeing radius.

## 6.3 Discussion

### 6.3.1 The excess of low-mass stars in ETGs

What drives the excess of low-mass stars in ETGs remains unknown, however there are presently two distinct candidates, namely [Mg/Fe] and $\sigma$. The latter may be viewed as a dynamical controlling parameter, whereas the former is a stellar population parameter.

Dynamical studies (Treu et al. 2010; Cappellari et al. 2012) suggest that the galaxy central velocity dispersion correlates strongly with the IMF slope - with more massive galaxies having steeper IMF slopes than less massive galaxies. This result has found support from several groups using different methodologies

(Ferreras et al. 2013; La Barbera et al. 2013; Spiniello et al. 2014). However, based on our analysis, we *reject the hypothesis that local velocity dispersion is the principal agent driving IMF variations*. Given the velocity dispersion gradient observed in NGC 1277 (from $\sim$ 420 km s$^{-1}$ to 150 km s$^{-1}$ ), if the correlation between IMF slope and central velocity dispersion holds also for local velocity dispersion, we would expect a typical radial change in the IMF slope of $\Delta\Gamma_{\rm b} = -2.4$. This value is incompatible with our inferred IMF gradient ($\Delta\Gamma_{\rm b} \sim -0.5$). Note, however, that our conclusions apply to the local velocity dispersion, not to the effective central velocity dispersion. To investigate the relation between IMF slope and local kinematical properties of NGC 1277, we show in Fig. 6.7 its $V_{\rm rms}$ radial profile, defined as:

$$V_{\rm rms} = \sqrt{V_{\rm rot}^2 + \sigma^2}$$

Note that the effective velocity dispersion analysed in La Barbera et al. (2013) and in Spiniello et al. (2014), which was estimated using a 3 arcsec wide fibre, is better represented by $V_{\rm rms}$ rather than by the local sigma, since the latter does not include the line broadening associated with the rotational velocity profile. Both $\Gamma_{\rm b}$ and $V_{\rm rms}$ decrease with radius; $V_{\rm rms}$ is greater than 300km s$^{-1}$, and $\Gamma_{\rm b}$ is steeper than the Milky Way value at all radii in NGC 1277. This is consistent with previous works reporting a bottom-heavy IMF at high *effective* velocity dispersion.

As an alternative explanation for the IMF variations, based on stellar population analysis, Conroy & van Dokkum (2012b) found that the IMF slope also correlates with the overabundance of $\alpha$-elements, in particular with the [Mg/Fe] ratio, in the sense that galaxies more enhanced in [Mg/Fe] have steeper IMF slopes. As we mentioned in §6.2, our [Mg/Fe] measurements are heavily dependent on the interpolation scheme we use, and we find that our data can entertain either slightly decreasing or increasing [Mg/Fe] radial gradients. Therefore, from the present study we cannot assess the relation between IMF slope and [Mg/Fe] (but see La Barbera et al. 2015).

To understand the differences among the aforementioned studies, Smith (2014) has independently reviewed the dynamical results from Cappellari et al. (2012) and those based on stellar population analysis of Conroy & van Dokkum (2012b). Although he found an overall agreement between both studies, the galaxy-by-galaxy comparison shows that the correlation between IMF slope and velocity dispersion does not agree with that found when comparing the IMF and [Mg/Fe].

The rapidly growing observational evidence of a variable IMF slope may be

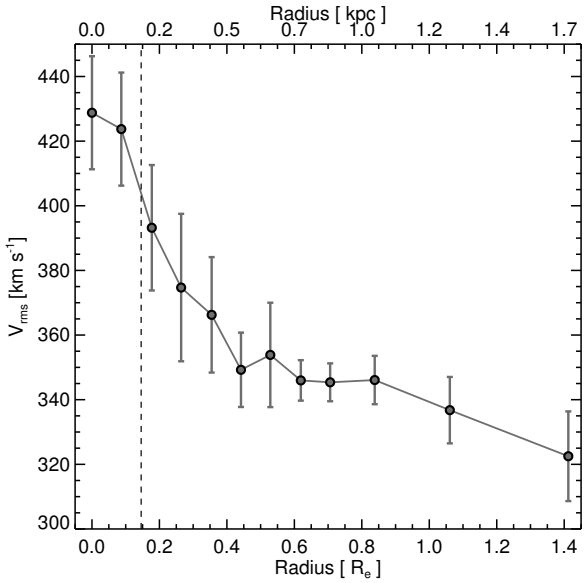


Figure 6.7: Radial $V_{rms}$ profile of NGC 1277. This quantity, accounting for the total kinetical energy, is more closely related to the effective velocity dispersion, which has been found to tightly correlate with the observed IMF variations. The radial $V_{rms}$ variation is significant, albeit milder, than the $\sigma$ variation. Dashed vertical lines mark the seeing radius.

in tension with other well-established properties of ETGs in the local Universe. In particular, chemical evolution models assuming a bottom-heavy IMF are unable to reproduce the observed metallicities and abundance ratios of ETGs (Arrigoni et al. 2010). This idea has been recently revisited in a series of articles by Weidner et al. (2013) and Ferreras et al. (2015) (see also Vazdekis et al. 1997; Larson 1998) who found that a time-dependent IMF is necessary to explain the stellar population properties of massive ETGs at $z \sim 0$. Note that, according to Ferreras et al. (2015), a constant-in-time IMF can be ruled out, not only for a bimodal IMF shape, but also for a two-segment IMF parametrization (e.g. as defined in Conroy & van Dokkum 2012b), and even for a V-shaped IMF (characterized by an enhanced fraction of both low- and high-mass stars).

### 6.3.2 The emerging picture

Our analysis of the stellar population properties of NGC 1277 is summarized in Figs. 6.4 and 6.5. The radial age profile of this galaxy, even allowing for possible IMF variations, indicates that the underlying stellar population is very

old ($\gtrsim 10$ Gyr) at all radii, with no evidence of recent star formation (Trujillo et al. 2014). This result suggests that the stellar component of NGC 1277 was formed at high redshift ($z \gtrsim 2$), and that solving for the IMF at each radius does not convert NGC 1277 into a young, massive and compact system, as those identified in the local Universe (Trujillo et al. 2009; Ferré-Mateu et al. 2012, 2013).

In terms of kinematics, NGC 1277 shows an extreme radial velocity dispersion gradient, ranging from more than 400 km s$^{-1}$ in the centre to $\sigma \sim 150$ km s$^{-1}$ beyond 1 $R_e$. The rotation in this galaxy shows the opposite behaviour, rising to $V_{rot} \sim 280$ km s$^{-1}$ at 1 $R_e$. Interestingly, these differences in the kinematical properties between the centre and the outskirts of NGC 1277 are not reflected in the properties of its stellar populations. The radial variation of $\alpha$-element overabundance, age and IMF slope are mild, whereas the total metallicity decreases by $\sim 0.4$ dex from the centre to 1 $R_e$. These gradients are consistent with a *fast, monolithic-like formation process* (Sánchez-Blázquez et al. 2007). In this sense, in terms of its stellar population properties, NGC 1277 does not differ from typical massive ETGs in the Local Universe. However, its extreme dynamics and compact morphology set it apart from the vast majority of local ETGs.

The IMF radial profile of NGC 1277 further constrains the formation process of massive ETGs. NGC 1277 shows much weaker radial variations of the IMF slope ($\Delta\Gamma_b = -0.5$) when compared to the IMF gradient of the two massive galaxies analysed by Martín-Navarro et al. (2015a) ($\Delta\Gamma_b = -1.5$ ). Our suggestion is that NGC 1277 represents the monolithic-like formation phase of massive ETGs. In this picture the later accretion of less massive satellites (with "standard" Kroupa-like IMF slopes), which would settle preferentially in the galaxy periphery due to their lower densities, would steepen the pristine IMF gradient making it more similar to that found in nearby massive galaxies Martín-Navarro et al. (2015a) .

Indeed, we hypothesize that relic galaxies, such as NGC 1277, will evolve to become the cores of massive ellipticals in the nearby Universe (Trujillo et al. 2014). The bulk of the stellar mass of this galaxy was formed in a short ($\tau \sim 100$ Myr) and intense (SFR $\gtrsim 10^3$ $M_\odot$/yr) burst at redshift $z \gtrsim 2$, but remained concentrated within a few kpcs in the centre of the dark matter halo. Afterwards, through dry merging (van Dokkum et al. 2010; Trujillo et al. 2011; Ferreras et al. 2014), the system would typically evolve to the characteristic sizes and stellar masses that are observed at $z \sim 0$. This interpretation is supported by numerical simulations (e.e. Oser et al. 2010; Navarro-González et al. 2013), and also by stellar population studies of the outskirts of nearby ETGs (Coccato et al. 2010; La Barbera et al. 2012; Pastorello et al. 2014;

Montes et al. 2014). Since dry mergers cannot significantly alter the properties of the stellar populations, a relic massive galaxy should present the same stellar population properties as the core of a typical $z \sim 0$, massive ETG, but with the latter's morphology and kinematics shaped by successive mergers.

It may seem surprising, at face value, that such a relic system should be identified in such a dense and dynamic environment such as that represented by the Perseus cluster ($M_{200} = 7.74 \times 10^{14} \mathrm{M}_{\odot}$, Aleksić et al. 2010). However, this is in fact a natural expectation in the hierarchical clustering paradigm since overdensities in what are now galaxy clusters were the first structures to collapse and to form massive galaxies (Mo & White 1996). In addition, the active intracluster environment may have inhibited the subsequent formation of younger stellar populations within NGC 1277 either via the stripping or heating of cold gas (Edge et al. 1992; O'Dea et al. 2008). In this sense, Stringer et al. (2015) have recently shown that in the BOLSHOI numerical simulation (Klypin et al. 2011), dark matter haloes similar to those hosting NGC 1277-like objects have experienced below-average mass accretion, or even mass loss, since $z = 2$.

Finally, we find that the radial IMF behaviour seen in NGC 1277 is not driven by the local velocity dispersion, and therefore, it cannot explain the IMF variations seen in ETGs. The fact that the IMF slope can vary radially within galaxies (Martín-Navarro et al. 2015a) suggests a complex galaxy formation scenario, with significantly different enrichment and supernovae-feedback rates when comparing the centre and the outskirts of ETGs. Thus, more observational efforts are needed to better understand the IMF behaviour in nearby galaxies, investigating what stellar population properties can explain the observed IMF variations. In this sense, large resolved spectroscopic surveys such as CALIFA (Sánchez et al. 2012) and MaNGA will provide statistically significant samples. In addition, the joint analysis of the IMF inferred from dynamical modelling and from stellar population analysis can reveal important information about the interplay between galaxy stellar population properties and dynamics. The intrinsic degeneracies of these methods ($M/L$ ratios, dark matter content, stellar remnants and central black-hole mass) may be broken if both approaches are combined.

# 7

# IMF – metallicity: a tight local relation revealed by the CALIFA survey

This chapter has been published as *Martín-Navarro et al. 2015, ApJL, 806, 31*

Assuming that the answer to all the observational results described in the previous chapters is indeed a non-universal IMF, two main parameters have been proposed. On the one hand, the integrated stellar velocity dispersion is found to correlate with the IMF slope as inferred from both dynamical models (e.g. Cappellari et al. 2012) and stellar population analysis (e.g. La Barbera et al. 2013). On the other hand, Conroy & van Dokkum (2012b) claimed a stronger correlation when comparing the [Mg/Fe] pattern to the IMF slope. Nevertheless, these trends have to be carefully interpreted because they are based on the spatially-integrated light of early-type galaxies (ETGs). Thus, the inferred properties are luminosity weighted quantities, convolved by the radial light distribution, which depends itself on the stellar velocity dispersion (Graham et al. 2001), and is highly peaked towards the centre.

We showed in Martín-Navarro et al. (2015a,b, see also Pastorello et al. 2014) that the IMF is a local property, not only varying among but also within galaxies. The lack of a large statistical sample, however, limited further interpretations of our data, and the question about which is the main driver of IMF variations remains open. In this chapter, we use the 2D spatially-resolved IFS

data from the CALIFA survey (Sánchez et al. 2012) to address this problem by analyzing the radial IMF profiles of a sample of 24 ETGs.

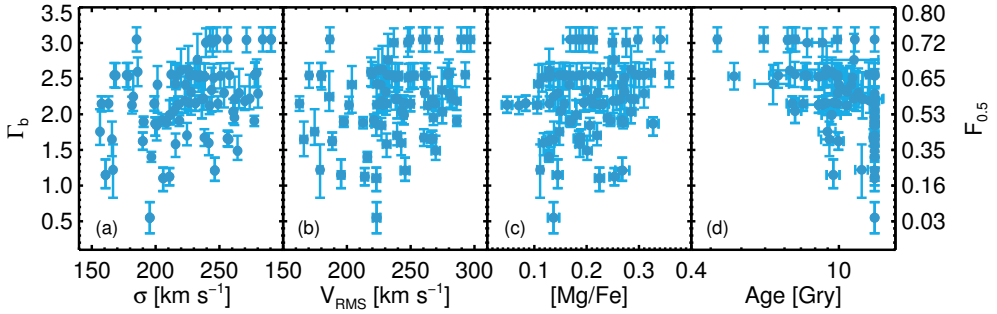


Figure 7.1: The best-fitting IMF slope $\Gamma_b$ is compared to the local $\sigma$ (a), $V_{rms}$ (b), [Mg/Fe] (c) and age (b). Neither the kinematics properties nor the [Mg/Fe] or the age follow the measured IMF variations ($\rho_\sigma = 0.35$, $\rho_{V_{rms}} = 0.30$, $\rho_{[Mg/Fe]} = 0.21$, $\rho_{age} = -0.50$, with $\rho$ being the Spearman correlation coefficient). The right vertical axis represents the IMF slope in terms of $F_{0.5}$, defined as the fraction (with respect to the total mass) of stars with masses below 0.5 $M_\odot$.

## 7.1 Data

We selected the sub-sample of 24 ETGs with redshift $0.018 < z < 0.030$ among the observed CALIFA galaxies (for sample properties see Walcher et al. 2014). In the local Universe, the strong IMF sensitive index $TiO_2$ is potentially affected by a telluric absorption feature at ∼6280Å. The selected redshift window maximizes the number of ETGs unaffected by this feature. Technical details of the data are fully described in Sánchez et al. (2012); García-Benito et al. (2014). The central velocity dispersion in our galaxy sample ranges from ∼160 to ∼310 $km\,s^{-1}$, although the bulk of them (21 galaxies) have velocity dispersions greater than 200 $km\,s^{-1}$. The mean stellar mass in our sample is $\overline{M_\star} = 10^{11.54} M_\odot$ according to González Delgado et al. (2014).

We derived the line-of-sight mean stellar velocity (V) and velocity dispersion ($\sigma$) following Falcón-Barroso et al. (2015, *in prep.*) Using these measurements, each IFU spaxel was then corrected to the rest-frame. Finally, we radially binned each galaxy using elliptical apertures. The size of the apertures was set to reach a signal-to-noise of, at least, 125 per Å at $\lambda\lambda = 6000, 6200$Å. All the quantities discussed in this chapter are averaged spaxel-values over these elliptical annuli.

## 7.2 Analysis

### 7.2.1 Stellar populations

For this work, we made use of the extended MILES (MIUSCAT) stellar population models (Vazdekis et al. 2010, 2012). We assume a bimodal, low-mass tapered, IMF, whose only free parameter, $\Gamma_{\rm b}$, is the slope of the high-mass end (above $0.6 M_{\odot}$) of the distribution. This parametrization, first introduced by Vazdekis et al. (1996), generalizes the Kroupa IMF, which is recovered for $\Gamma_{\rm b} = 1.35$. Note that the current version of the extended MILES models cover from $\Gamma_{\rm b} = 0.3$ to $\Gamma_{\rm b} = 3.3$, which can lead to some saturation for high IMF values.

Given the CALIFA wavelength range ($\lambda\lambda$ 3700, 7500 Å), we focused on five prominent spectral indices: $H_{\beta_{\rm O}}$, [MgFe]′, Mg2Fe (Bruzual & Charlot 2003), NaD, $TiO2_{\rm CALIFA}$ and $TiO_1$. The last three are IMF-sensitive features, whereas [MgFe]′ and Mg2Fe depend on metallicity and $H_{\beta_{\rm O}}$ on age. The $TiO2_{\rm CALIFA}$ index follows the standard $TiO_2$ definition (Trager et al. 1998) but with a narrower blue pseudo-continuum ($\lambda\lambda$ 6060.625, 6080.625 Å) to avoid any telluric contamination. The correction of $H_{\beta_{\rm O}}$ from nebular emission was done in the same way as in La Barbera et al. (2013). For each spectrum (i.e. each galaxy and radial bin), we inferred stellar population properties with three different approaches:

i) Following La Barbera et al. (2013), we minimized:

$$\chi^2(\Gamma_{\rm b}, {\rm age}, [{\rm M/H}]) = \sum_i \left[ \frac{(EW_i - \Delta_{\alpha,i}) - EW_{M,i}}{\sigma_{EW_i}} \right]^2 , \qquad (7.1)$$

where our index measurements ($EW_i$), after being corrected for non-solar abundances ($\Delta_{\alpha,i}$), are compared to the model predictions ($EW_{M,i}$). The fitting process was repeated by considering different combinations of IMF sensitive indices, leading to consistent results.

ii) We implemented an iterative fitting scheme where age and metallicity were calculated first using an index-index ($H_{\beta_{\rm O}}$-[MgFe]′) diagram, assuming a standard IMF. The age estimate coming from this first step was then used to derive the metallicity and the IMF in a second index-index ($TiO2_{\rm CALIFA}$[MgFe]′) diagram. These two steps were repeated, re-deriving age and metallicity from the $H_{\beta_{\rm O}}$-[MgFe]′ diagram with an updated IMF, until the solution converged.

iii) Alternatively, we also fit our data following Eq. 7.1 but neglecting individual [$\alpha$/Fe] corrections.

The three approaches show a good agreement, with small differences only for low IMF-slope values, where IMF effects can be mimicked by changes in other

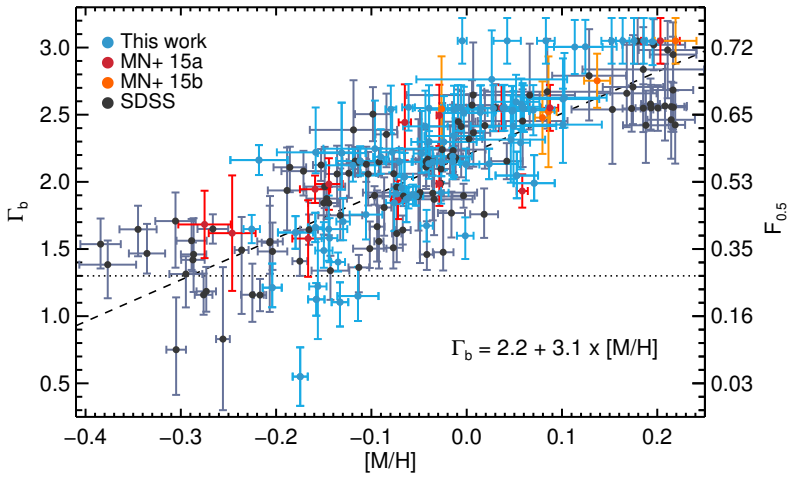


Figure 7.2: IMF–metallicity relation obtained from CALIFA local measurements (blue). We also show the local IMF and metallicities measurements derived by Martín-Navarro et al. (2015a,b) (red, orange) for three of nearby ETGs, as well as global SDSS measurements (black). We found it to be the strongest correlation ($\rho_{[M/H]} = 0.82$). As in Fig. 7.1, the right vertical axis indicates the $F_{0.5}$ ratio. For reference, the standard Kroupa IMF value is shown as a horizontal dotted line. Dashed line correspond to the best-fitting linear relation to all the datasets.

stellar population parameters. For simplicity, we will refer through this chapter to the best-fitting values derived from the simultaneous fit (Eq. 7.1) of the $H_{\beta_O}$, $[MgFe]'$ and $TiO2_{CALIFA}$ indices. Note that the latter, compared to the $TiO_1$, exhibits a milder dependence on both abundance ratios and total metallicity (La Barbera et al. 2013). However, the absolute $TiO_2$ sensitivity to these parameters depends on the adopted stellar population synthesis model (Bruzual & Charlot 2003; Thomas et al. 2011b). Moreover, $TiO_2$ is less sensitive to variations in the temperature scale of giant stars. Spiniello et al. (2015) showed that, after accounting for metallicity, no variation in the effective temperature is needed to fit the strength of gravity-sensitive features in massive ETGs, and that a similar result would be recovered with other stellar population models if the same IMF parameterization were used. Although our fitting scheme does not account for the residual impact of non-solar abundances on the temperature scale of the (solar-scaled) isochrones, the [$\alpha$/Fe] effect on the isochrones is significantly milder than that on the stellar atmospheres (Vazdekis et al. 2015). The latter is corrected in our approach ($\Delta_{\alpha,i}$ in Eq. 7.1).

In addition to the IMF, age and metalliciy, the [Mg/Fe] of each radial bin

was derived by means of the $[Z_{Mg}/Z_{Fe}]$ proxy (La Barbera et al. 2013), i.e., using the metallicity difference between two index-index diagrams, where $H_{\beta_O}$ is plotted against a Mg and Fe metallicity indicator, respectively.

### 7.2.2 Stellar kinematics

To understand the IMF variations, we also compared our best-fitting IMF values to two kinematics parameters: the local $\sigma$ and the local $V_{\rm rms}$ defined as $V_{\rm rms} \equiv \sqrt{V^2 + \sigma^2}$ . Whereas $\sigma$ has been claimed to be the main driver of the IMF variations (Treu et al. 2010; Ferreras et al. 2013), in spatially resolved studies $V_{\rm rms}$ accounts for both random and ordered motions.

## 7.3 Results

In Fig. 7.1 we present the correlation between the best-fitting IMF slope, $\Gamma_{\rm b}$, and the local values of [Mg/Fe], age, $\sigma$ and $V_{\rm rms}$. None of them show a tight correlation with $\Gamma_{\rm b}$. The mild relation between age and $\Gamma_{\rm b}$ can be understood either as a residual degeneracy between both parameters or as a consequence of the IMF-metallicity relation, since young stars within massive ETGs are likely formed from metal-enriched material.

### 7.3.1 The IMF–metallicity relation

Among all the explored relations, the IMF slope–local metallicity relation emerges as the most fundamental. This is shown in Fig. 7.2, where the local $\Gamma_{\rm b}$–[M/H] relation derived from the CALIFA survey (blue) is combined with local IMF estimates, obtained at different galactocentric distances, for three nearby ETGs by Martín-Navarro et al. (2015a,b) (red and orange symbols). In addition, we also show (black) the best-fitting IMF and metallicity inferred from SDSS stacked spectra. To construct these spectra, we followed La Barbera et al. (2013), but binning according to both $\sigma$ and [M/H] of the individual galaxies. The broad wavelength range of the SDSS data set allows us to infer the IMF, not only using those features within the CALIFA spectral range, but also prominent near-IR IMF sensitive features such as the NaI 8189 and the CaII triplet (see §4.1 in La Barbera et al. 2013, for a detailed description of gravity-sensitive features in SDSS spectra).

The fact that the three datasets included, although based on different sets of line-strengths, lie on the same relation, supports a tight connection between IMF slope and metallicity, regardless of the details in the determination of the stellar population parameters. Moreover, the agreement between integrated

measurements from the SDSS spectra and spatially-resolved values, suggests that the mechanism behind the local IMF variations ultimately shapes the global galaxy mass–IMF relation.

A linear fit to all the measurements shown in Fig. 7.2 leads to the following relation between IMF slope and metallicity in ETGs

$$\Gamma_{\rm b} = 2.2(\pm0.1) + 3.1(\pm0.5) \times [{\rm M/H}] \tag{7.2}$$

Since IMF-sensitive features ultimately trace the dwarf-to-giant ratio $F_{0.5}$, as defined in La Barbera et al. (2013), the above equation can be expressed in terms of a single power law IMF as

$$\Gamma = 1.50(\pm0.05) + 2.1(\pm0.2) \times [{\rm M/H}] \tag{7.3}$$

Apart from the measurement errors, the scatter in the relation comes from two sources: the IMF–[$\alpha$/Fe] degeneracy when fitting gravity-sensitive features around the Kroupa-like IMF regime (La Barbera et al. 2013) and the dependence of the IMF on the minimized set of indices[1] (Spiniello et al. 2014). In this sense, the fact that the $TiO_2$-based CALIFA measurements show a steeper IMF-metallicity trend is consistent with a stronger metallicity dependence of this index than predicted in the MILES models. On the other hand, the consistency among different data-sets ($\rho = 0.82$ when CALIFA, SDSS and Martín-Navarro et al. (2015a,b) are considered) points to a genuine IMF-[M/H] trend, as shown in Fig. 7.2.

### 7.3.2 The [MgFe]′–$TiO_{2_{\rm CALIFA}}$ empirical relation

To strengthen the validity of our result, we adopted an empirical approach. In Fig. 7.3 we compare the [MgFe]′ to the $TiO_{2_{\rm CALIFA}}$ individual measurements for all radial bins in our sample, at a common 200 km s$^{-1}$ resolution. Each point is color-coded by its $H_{\beta_{\rm O}}$ value, representing an age segregation. The [MgFe]′ index is independent of the IMF, depending almost entirely on the total metallicity. On the contrary, the $TiO_{2_{\rm CALIFA}}$ is a strong IMF indicator, that increases with age (La Barbera et al. 2013). Since MILES stellar population models predict the $TiO_{2_{\rm CALIFA}}$ feature to be, in the explored metallicity and age regime, almost independent of total metallicity, the strong (correlation coefficient $\rho = 0.86$) correlation shown in Fig. 7.3 can be interpreted as a metallicity–IMF trend. A similar relation was found by Trager et al. (1998)

[1] Uncertainties in Eq. 7.2-7.3 account for this effect, by repeating the fit using only CALIFA data.

while comparing the $Mg_2$ and the $TiO_2$ indices. Note that if the $TiO_2$ sensitivity to total metallicity is larger than predicted by MILES models, a certain correlation between these two indices would also be expected.

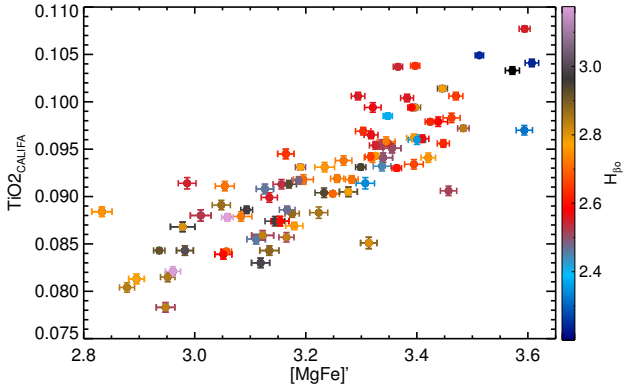


Figure 7.3: Empirical relation between the metallicity-sensitive [MgFe]′ and the IMF-sensitive $TiO_{2_{CALIFA}}$ features. Index measurements (at a resolution of 200 $km\,s^{-1}$) are color-coded by their $H_{\beta_O}$ value, as an age proxy. An IMF–metallicity relation is needed to explain the observed trend, since the $TiO_{2_{CALIFA}}$ weakly depends on the total metallicity and [MgFe]′ is almost independent of the IMF.

## 7.4 Discussion

ETGs are characterized by old stellar populations and thus, only stars with masses $M \lesssim 1M_\odot$ remain alive. Therefore, the analysis of gravity-sensitive features in the integrated light of unresolved ETGs can only constraint the dwarf-to-giant ratio. We vary this ratio by changing the slope ($\Gamma_b$) of the high-mass end of the IMF, while it was kept constant for stars with masses below $0.5M_\odot$. Notice that our results, restricted to inference of the dwarf-to-giant ratio, barely depend on the detailed IMF shape, but it must be considered when exploring, for example, the chemical evolution and the expected mass-to-light ratios of ETGs.

### 7.4.1 The underlying parameters behind the varying dwarf-to-giant ratio in ETGs

Two competing candidates have been proposed to explain the observed dwarf-to-giant ratio variations in ETGs: $\sigma$ and [Mg/Fe]. Smith (2014) investigated these two parameters over the same sample of galaxies (Cappellari et al. 2011;

Conroy & van Dokkum 2012b), pointing out that the stellar population analysis favors the stellar population property ([Mg/Fe]), whereas a dynamical analysis supports the dynamical-related quantity ($\sigma$). The work of Smith opened the question of whether IMF studies are actually probing the IMF or whether they are, at least partially, dominated by confounding factors. However, stellar population analyses of SDSS stacked spectra (La Barbera et al. 2013; Spiniello et al. 2014) have shown a strong correlation between $\sigma$ and the dwarf-to-giant ratio. Moreover, La Barbera et al. (2015), using also SDSS stacked spectra, showed that [Mg/Fe] is loosely (or un-) correlated with the IMF slope. The latter result is in agreement with panel (c) in Fig. 7.1, where we show that the local [Mg/Fe] is decoupled from the dwarf-to-giant ratio variations.

Regarding $\sigma$, in Martín-Navarro et al. (2015b) we showed that its local value was not the main driver behind the dwarf-to-giant ratio variations of the massive relic galaxy NGC 1277. In the present work we confirm this result using a statistically significant sample of ETGs (panel (a) in Fig. 7.1). Notice that previous studies suggesting a connection between $\sigma$ and the IMF slope were based on spatially unresolved spectra. Thus, their velocity dispersions trace the overall galaxy potential (mass) rather than the detailed kinematics. Thanks to the CALIFA data, we propose that this connection between galaxy mass and IMF slope arises from considering simultaneously both the galaxy mass–metallicity and the metallicity–IMF slope relations. In this sense, the dwarf-to-giant ratio gradients observed in ETGs (Martín-Navarro et al. 2015a,b) can be also accounted for the radial metallicity variation within these galaxies. To illustrate the suggested metallicity-driven galaxy mass–IMF slope relation, we used the above described Sloan data (black dots in Fig. 7.2) to calculate the mean global metallicity per galaxy mass ($\sigma$) bin. Then, we transformed this metallicity into the expected IMF slope according to Eq. 7.2. The result is summarized in Fig. 7.4. Although it can not be directly compared with previous works, we qualitatively recover the observed relation between galaxy mass and IMF slope, with more massive galaxies being bottom-heavier.

### 7.4.2 Metallicity as a driver of IMF variations

Metallicity-driven dwarf-to-giant ratio variations can be explained if molecular clouds collapse following a Jeans spectrum. Such a scenario is expected if thermal pressure dominates the process, although a turbulent medium can yield similar results if dust cooling is significant (Larson 2005). Perhaps, a realistic scenario would couple a Jeans-driven mechanism with turbulence-induced fragmentation (e.g. Padoan & Nordlund 2002). Nevertheless, this chapter shows the importance that metallicity plays in determining the stellar mass spectrum.

Such a scenario is consistent with studies of nearby resolved galaxies (Geha et al. 2013), line-strength indices (Cenarro et al. 2003) and optical colors (Ricciardelli et al. 2012). In low-metallicity regions, it is found that molecular clouds are very efficient in forming massive stars, leading to top-heavy IMFs. This is supported by observations of metal-poor systems showing evidence of an IMF dominated by massive stars (Marks et al. 2012).

If metallicity is one of the main drivers behind the IMF variations, a number of fundamental aspects of galaxy evolution must be revisited. Because the stellar feedback regulates the chemical enrichment of galaxies, IMF, star formation and chemical composition will be tightly related during the time evolution. In particular, massive galaxies are expected to increase their metallicity during the formation of their stellar populations, and therefore, the dwarf-to-giant ratio should have been smaller at higher redshifts, such that there were fewer low-mass stars per high-mass star. Such a time-dependent IMF scenario (Arnaud et al. 1992; Vazdekis et al. 1997; Larson 1998; Weidner et al. 2013; Ferreras et al. 2015) would explain the observations of nearby massive ETGs, which are inconsistent with a time-invariant, steep (or even Milky-Way like) IMF slope (Arrigoni et al. 2010).

Moreover, the [Mg/Fe] has been extensively used as a proxy for the formation time-scale (e.g. Thomas et al. 2005): rapid formation events lead to high [Mg/Fe] values. However, an IMF dominated at early times by high-mass stars would also produce an enhanced [Mg/Fe], relaxing the typical ($\sim$ 1Gyr) constraint on the rapid formation time-scale. Thus, to safely interpret $z \sim 0$ observations, it is crucial to understand the chemical evolution of galaxies since they were formed, and in particular, during the build-up of their chemical properties (Vazdekis et al. 1996). In this sense, it has been shown (e.g. Ferreras et al. 2009; Choi et al. 2014; Ferré-Mateu et al. 2014) that the chemical composition of massive galaxies has remained constant over the last $\sim$ 7 Gyr. If metallicity actually regulates the dwarf-to-giant ratio variations, it would imply that the IMF of massive objects was bottom-heavy at $z \sim 1$, as recently suggested by observations (Shetty & Cappellari 2014; Martín-Navarro et al. 2015c), since no chemical evolution has happened since then.

Finally, we want to emphasize that the present study is restricted to the analysis of ETGs. The local conditions (e.g. turbulence, pressure, density, radiation, and magnetic fields) of the interstellar medium at high-$z$, or even in nearby disk galaxies, are expected to differ from the local environment within ETGs. Thus, more observational efforts are still needed to fully characterize the IMF behavior with varying star-forming conditions. In fact, for very metal-poor systems, Geha et al. (2013) found a slightly top-heavy IMF, but steeper than expected from a crude extrapolation of Eq. 7.2. The trend in Fig. 7.2 seems to

actually flatten at lowest and highest metallicity, pointing to a non-linearity of the IMF–metallicity relation.

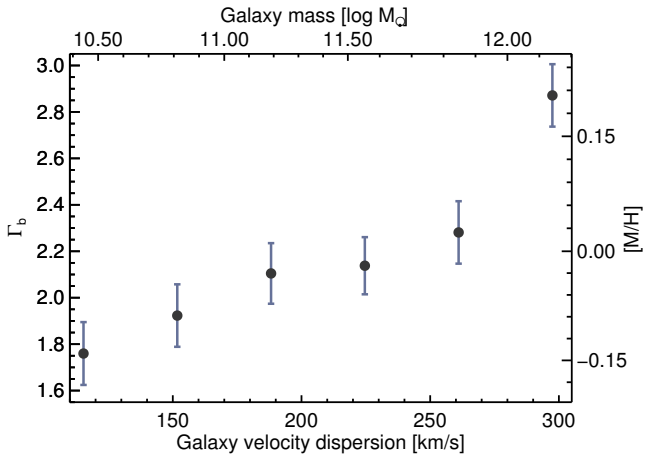


Figure 7.4: Predicted IMF slope – galaxy velocity dispersion relation. The best-fitting metallicity of the global SDSS measurements (right vertical axis) was transformed, following Eq. 7.2, into an *expected* IMF-slope value $\Gamma_b$. The upper horizontal axis represents the galaxy mass, estimated from the velocity dispersion (Cappellari et al. 2013). We suggest that the relation found between IMF slope and galaxy mass can be understood as the combination of the mass – metallicity and the metallicity – IMF slope relations.

## 7.5 Summary

Although deviations from the standard Milky-Way IMF have been extensively reported in the literature over the last years, the mechanism responsible for these variations remains unknown. We have analysed the radial gradients of IMF-sensitive features in a sample of 24 ETGs observed by the CALIFA survey, finding that *the local IMF is tightly related to the local metallicity*. Our result agrees with previous works reporting local and global IMF variations, and it explains the observed galaxy mass–IMF relation. We speculate about the implications of metallicity-driven IMF variations in the context of galaxy formation and evolution.

The intimate connection between IMF and metallicity described in our work suggests a complex massive galaxy formation process, departing from the classical picture where these objects formed under nearly stationary conditions. Thus, to safely understand and interpret $z \sim 0$ observations, it is necessary to untangle the early life of massive galaxies at high-$z$. The combination of

more sophisticated stellar population synthesis models (Conroy & van Dokkum 2012b; Vazdekis et al. 2015) and high-$z$ spectroscopic surveys (Brammer et al. 2012; Kriek et al. 2014) will provide valuable insights.

# 8

# Conclusions

*Mas no sabía el doctor*
*que hoy es siempre todavía*
A. Machado

This thesis aimed to investigate the formation and evolution of galaxies in a comprehensive manner, studying the two most relevant morphological types: spirals and early-type galaxies. To this end, we combined photometric and spectroscopic observations, focusing on the analysis of the stellar populations properties, and in particular of their radial variations. We studied the radial light distributions of nearby edge-on spirals and we use extremely deep spectroscopic data to derive the stellar population parameters in a sample of local ETGs. Moreover, we investigated *in situ* the stellar population content of massive galaxies at $z \sim 1$. We paid special attention to the analysis of the IMF variations, locally in the nearby Universe and globally at higher redshift, trying to understand why the IMF in massive galaxies departs from what it is measured in nearby resolved systems. In summary, the main conclusions of this thesis are as follows:

On spiral galaxies:

- *Breaks & truncations:* studying the radial light distributions of a sample of 34 nearby edge-on galaxies we find that breaks, usually detected in face-on galaxies, and truncations, measured in edge-on spirals, are different phenomena. Whereas the first might be related to baryonic processes, and in particular to a threshold in the star formation, the latter seem to be associated with a real drop in the stellar mass density, probably

tracing the pristine angular momentum imprinted during the formation of the stellar disk.

- *Truncations in face-on galaxies:* the absence of truncations in face-on spirals is due to a projection effect. Under this projection, the brightness of the stellar halo, combined with the point spread function effect, competes with the brightness of the spiral disk at the truncation distance, making it undetectable. In edge-on galaxies, the integration along the LOS increases the overall surface brightness, and truncations can be measured.

On early-type galaxies:

- *Radial IMF variations:* the detailed analysis of the stellar populations properties of two massive (NGC 4552 and NCG 5557) and a low-mass (NGC 4387) ETG suggests that the IMF varies radially within galaxies, and therefore, it is a local property. In massive systems, the number ratio of low-mass stars (M$\sim 0.5\mathrm{M}_{\odot}$) decreases when moving from the centre to the effective radius, where it reaches a value similar to what is observed in spiral galaxies. This might indicate that the star formation process in the central regions was different from the outskirts.

- *IMF and local velocity dispersion:* local IMF variations observed in nearby ETGs are decoupled from the local velocity dispersion, which apparently contrasts with the relation between global IMF and effective velocity dispersion.

- *The IMF of a massive relic galaxy:* the stellar population properties and kinematics of NGC 1277 suggest that this object is a massive relic galaxy, formed at high redshift ($z \gtrsim 2$) and with no later major merger events. This conclusion stands even if the IMF is allowed to vary, and supports a formation scenario where the core of present-day massive ETGs formed early in the Universe in fast, dissipational collapses. Afterwards, the accretion of material with distinct stellar population properties (e.g. dwarf and spiral galaxies) created an envelope in the outer regions of the initial cores. These two stages might have shaped the observed scaling relations in the local Universe.

- *IMF at $z \sim 1$:* by analysing the spectrophotometric properties of a sample of massive quiescent galaxies at redshift $z \sim 1$, we find that the relation between IMF and galaxy mass is at place at that redshift ($z \sim 1$). This is consistent with passively evolving stellar populations in ETGs over the last 10 Gyr, as suggested by observations. Moreover, it sets an upper limit

for the invoked temporal IMF variations, which, if happened, should have occurred during the first Myr of formation.

- *IMF slope–metallicity relation:* the radial IMF gradients derived for a sample of 24 ETGs in the CALIFA survey reveals that there is a tight relation between IMF slope and total metallicity. So far, this is the only reported relation that stands both for local and global measurements and thus, it seems to be a fundamental relation between both quantities. This IMF–metallicity relation suggests that the local conditions of the ISM from which the observed generations of stars were formed have a significant impact on the subsequent star formation. In addition, the IMF–metallicity relation could explain the galaxy mass (velocity dispersion)–IMF relation, although other parameters (e.g. density or star formation efficiency) might also be important for the observed IMF variations.

Two competing views of galaxy evolution have been challenged in this thesis. Are galaxies in the local Universe the result of a pure monolithic formation scenario, as suggested by the passively evolving stellar population properties of nearby massive ETGs, or are they the product of a hierarchical assembly of smaller structures, in agreement with numerical simulations? We have shown that the radial gradients in the stellar populations properties of nearby galaxies suggest distinct star formation processes between central and outer regions. Moreover, strong differences were found in the stellar population gradients between regular and relic galaxies. We hypothesise that these differences result from two distinct evolutionary phases of galaxy evolution. In an early stage, the core of present-day massive ETGs was formed in intense starburst events, where the bulk of the stellar mass was built up. This would lead to $\alpha$-enhanced stellar populations that follow tight scaling relations driven by galaxy mass. Later on, the accretion of smaller structures, with lower masses, metallicities, and presumably also flatter IMF slopes, shaped the stellar population gradients that we observe locally. Therefore, as supported by the results of this thesis, *an early monolithic-like collapse followed by the accretion of smaller structures, mostly located in the outskirts, stands as the most promising scenario to explain the formation and evolution of massive galaxies.*

# 9

# Future work

*What's past is prologue*
W. Shakespeare (The Tempest)

The natural step forward in the investigation of breaks and truncations is to carry out a detailed stellar population analysis of these features in nearby edge-on galaxies. If breaks are actually associated to thresholds in the star formation, a minimum in the radial age gradient is expected at the break distance, as suggested by the color profiles (Bakos et al. 2008). Around the truncation however, no change in the stellar population properties is expected, but kinematic measurements will be crucial to discriminate among the different scenarios. For this purpose, we already targeted NGC 4565, a nearby edge-on galaxy, with the GTC telescope. With a total on-source time of 15 hours, we expect to probe with these data surface brightnesses around $\mu \sim 26$ mag arcsec$^{-2}$, one magnitude dimmer than the truncation. Thus, this pioneer work will allow us to spectroscopically investigate for the first time the origin of these faint features.

Presumably, because of the lower level of star formation, the outskirts of NGC 4565, and in general of spiral galaxies, share some similarities with the outskirts of ETGs. In fact, if the envelope of present-day massive ETGs was actually formed via accretion of satellites, low-mass spirals might have contributed to create these outer regions. In this sense, dwarf galaxies have been proposed as building blocks of more massive ETGs. Ryś et al. (2015) have recently shown that dwarf ellipticals did not significantly contribute to the mass assembly of the central regions in massive ETGs. However, it is beyond the ef-

fective radius where dwarf galaxies are supposed to become an important agent. Making use of the new $\alpha$-enhanced MILES models (Vazdekis et al. 2015), we plan to investigate whether the stellar population properties of nearby dwarf ellipticals are consistent with the observed properties of ETGs at large radii.

Radial gradients in the stellar populations still retain useful information to test and constraint the standard $\Lambda$-CDM. In the local Universe, the CALIFA survey (Sánchez et al. 2012) will be used to provide detailed measurements up to two effective radii. At larger radial distances, the SLUGGS survey (Brodie et al. 2014) will provide, not only stellar populations, but also kinematical insights. This combination is crucial to complement the weaknesses of both approaches.

Combining stellar populations and dynamical analysis is also mandatory to fully understand the physics behind the IMF. Apart from exploring other parameters that might contribute to the observed IMF variations, we will combine the kinematical and stellar populations analysis within the CALIFA collaboration to perform a comprehensive study of these IMF variations. Finally, our current understanding of galaxy formation requires the investigation of a completely unknown observational evidence: the IMF during the formation of massive galaxies. This challenging task will need from completely different approaches that we used to employ in the local Universe, but it is key to safely interpret $z \sim 0$ observations and to understand the formation of the most massive galaxies in the Universe.

# Bibliography


Abazajian, K. N., Adelman-McCarthy, J. K., Agüeros, M. A., et al. 2009, ApJS, 182, 543

Aleksić, J., Antonelli, L. A., Antoranz, P., et al. 2010, ApJ, 710, 634

Arnaud, M., Rothenflug, R., Boulade, O., Vigroux, L., & Vangioni-Flam, E. 1992, A&A, 254, 49

Arrigoni, M., Trager, S. C., Somerville, R. S., & Gibson, B. K. 2010, MNRAS, 402, 173

Auger, M. W., Treu, T., Gavazzi, R., et al. 2010, ApJ, 721, L163

Azzollini, R., Trujillo, I., & Beckman, J. E. 2008, ApJ, 684, 1026

Bakos, J., & Trujillo, I. 2012, ArXiv e-prints:1204.3082, arXiv:1204.3082

Bakos, J., Trujillo, I., & Pohlen, M. 2008, ApJ, 683, L103

Barker, M. K., Ferguson, A. M. N., Cole, A. A., et al. 2011, MNRAS, 410, 504

Barker, M. K., Ferguson, A. M. N., Irwin, M. J., Arimoto, N., & Jablonka, P. 2012, MNRAS, 419, 1489

Barro, G., Pérez-González, P. G., Gallego, J., et al. 2011a, ApJS, 193, 13

—. 2011b, ApJS, 193, 30

Barteldrees, A., & Dettmar, R.-J. 1994, A&AS, 103, 475

Bastian, N., Covey, K. R., & Meyer, M. R. 2010, ARA&A, 48, 339

Bedregal, A. G., Scarlata, C., Henry, A. L., et al. 2013, ApJ, 778, 126

Bekki, K., & Shioya, Y. 1998, ApJ, 497, 108

Bell, E. F., McIntosh, D. H., Katz, N., & Weinberg, M. D. 2003, ApJS, 149, 289

Belli, S., Newman, A. B., & Ellis, R. S. 2014, ApJ, 783, 117

Bender, R., Burstein, D., & Faber, S. M. 1992, ApJ, 399, 462

—. 1993, ApJ, 411, 153

Bensby, T., Feltzing, S., & Lundström, I. 2004, A&A, 415, 155

Bertin, E., & Arnouts, S. 1996, A&AS, 117, 393

Bertin, E., Mellier, Y., Radovich, M., et al. 2002, in Astronomical Society of the Pacific Conference Series, Vol. 281, Astronomical Data Analysis Software and Systems XI, ed. D. A. Bohlender, D. Durand, & T. H. Handley, 228

Blakeslee, J. P., Franx, M., Postman, M., et al. 2003, ApJ, 596, L143

Bland-Hawthorn, J., Vlajić, M., Freeman, K. C., & Draine, B. T. 2005, ApJ, 629, 239

Bonnell, I. A., Clark, P., & Bate, M. R. 2008, MNRAS, 389, 1556

Bower, R. G., Lucey, J. R., & Ellis, R. S. 1992, MNRAS, 254, 589

Brammer, G. B., van Dokkum, P. G., Franx, M., et al. 2012, ApJS, 200, 13

Brodie, J. P., Romanowsky, A. J., Strader, J., et al. 2014, ApJ, 796, 52

Bruzual, G., & Charlot, S. 2003, MNRAS, 344, 1000

Bush, S. J., Cox, T. J., Hayward, C. C., et al. 2010, ApJ, 713, 780

Calzetti, D., Armus, L., Bohlin, R. C., et al. 2000, ApJ, 533, 682

Cappellari, M., & Emsellem, E. 2004, PASP, 116, 138

Cappellari, M., Emsellem, E., Krajnović, D., et al. 2011, MNRAS, 413, 813

Cappellari, M., McDermid, R. M., Alatalo, K., et al. 2012, Nature, 484, 485

—. 2013, MNRAS, 432, 1862

Cardiel, N. 1999

Carter, D., Visvanathan, N., & Pickles, A. J. 1986, ApJ, 311, 637

Cenarro, A. J., Cardiel, N., Gorgas, J., et al. 2001, MNRAS, 326, 959

Cenarro, A. J., Gorgas, J., Vazdekis, A., Cardiel, N., & Peletier, R. F. 2003, MNRAS, 339, L12

Cepa, J., Aguiar, M., Escalera, V. G., et al. 2000, in Society of Photo-Optical Instrumentation Engineers (SPIE) Conference Series, Vol. 4008, Optical and IR Telescope Instrumentation and Detectors, ed. M. Iye & A. F. Moorwood, 623–631

Chabrier, G. 2003, PASP, 115, 763

Charlot, S., & Fall, S. M. 2000, ApJ, 539, 718

Choi, J., Conroy, C., Moustakas, J., et al. 2014, ApJ, 792, 95

Clough, S. A., Shephard, M. W., Mlawer, E. J., et al. 2005, J. Quant. Spec. Radiat. Transf., 91, 233

Coccato, L., Gerhard, O., & Arnaboldi, M. 2010, MNRAS, 407, L26

Cohen, J. G. 1979, ApJ, 228, 405

Cole, S., Aragon-Salamanca, A., Frenk, C. S., Navarro, J. F., & Zepf, S. E. 1994, MNRAS, 271, 781

Comerón, S., Knapen, J. H., Sheth, K., et al. 2011, ApJ, 729, 18

Comerón, S., Elmegreen, B. G., Salo, H., et al. 2012, ApJ, 759, 98

Conroy, C. 2013, ARA&A, 51, 393

Conroy, C., Graves, G. J., & van Dokkum, P. G. 2014, ApJ, 780, 33

Conroy, C., & van Dokkum, P. 2012a, ApJ, 747, 69

Conroy, C., & van Dokkum, P. G. 2012b, ApJ, 760, 71

Conroy, C., van Dokkum, P. G., & Kravtsov, A. 2015, ApJ, 803, 77

Conselice, C. J., Grogin, N. A., Jogee, S., et al. 2004, ApJ, 600, L139

Cortese, L., Fogarty, L. M. R., Ho, I.-T., et al. 2014, ApJ, 795, L37

Courteau, S., Widrow, L. M., McDonald, M., et al. 2011, ApJ, 739, 20

Davé, R. 2008, MNRAS, 385, 147

de Grijs, R., Kregel, M., & Wesson, K. H. 2001, MNRAS, 324, 1074

de Grijs, R., & Peletier, R. F. 1997, A&A, 320, L21

de Grijs, R., Peletier, R. F., & van der Kruit, P. C. 1997, A&A, 327, 966

de Grijs, R., & van der Kruit, P. C. 1996, A&AS, 117, 19

de Jong, R. S. 2008, MNRAS, 388, 1521

de Jong, R. S., Seth, A. C., Radburn-Smith, D. J., et al. 2007, ApJ, 667, L49

De Lucia, G., Springel, V., White, S. D. M., Croton, D., & Kauffmann, G. 2006, MNRAS, 366, 499

de Vaucouleurs, G. 1948, Annales d'Astrophysique, 11, 247

—. 1958, ApJ, 128, 465

de Zeeuw, P. T., Bureau, M., Emsellem, E., et al. 2002, MNRAS, 329, 513

Debattista, V. P., Mayer, L., Carollo, C. M., et al. 2006, ApJ, 645, 209

Delisle, S., & Hardy, E. 1992, AJ, 103, 711

Di Matteo, T., Springel, V., & Hernquist, L. 2005, Nature, 433, 604

Dutton, A. A., Macciò, A. V., Mendel, J. T., & Simard, L. 2013, MNRAS, 432, 2496

Edge, A. C., Stewart, G. C., & Fabian, A. C. 1992, MNRAS, 258, 177

Eggen, O. J., Lynden-Bell, D., & Sandage, A. R. 1962, ApJ, 136, 748

Elmegreen, B. G., & Hunter, D. A. 2006, ApJ, 636, 712

Elmegreen, B. G., & Parravano, A. 1994, ApJ, 435, L121

Elmegreen, B. G., & Scalo, J. 2006, ApJ, 636, 149

Emsellem, E. 2013, MNRAS, 433, 1862

Emsellem, E., Cappellari, M., Peletier, R. F., et al. 2004, MNRAS, 352, 721

Emsellem, E., Cappellari, M., Krajnović, D., et al. 2011, MNRAS, 414, 888

Erwin, P., Beckman, J. E., & Pohlen, M. 2005, ApJ, 626, L81

Erwin, P., Pohlen, M., & Beckman, J. E. 2008, AJ, 135, 20

Falcón-Barroso, J., Peletier, R. F., Vazdekis, A., & Balcells, M. 2003, ApJ, 588, L17

Fall, S. M., & Efstathiou, G. 1980, MNRAS, 193, 189

Fazio, G. G., Hora, J. L., Allen, L. E., et al. 2004, ApJS, 154, 10

Ferguson, A., Irwin, M., Chapman, S., et al. 2007, Resolving the Stellar Outskirts of M31 and M33, ed. R. S. de Jong, 239

Ferguson, A. M. N., Irwin, M. J., Ibata, R. A., Lewis, G. F., & Tanvir, N. R. 2002, AJ, 124, 1452

Ferré-Mateu, A., Sánchez-Blázquez, P., Vazdekis, A., & de la Rosa, I. G. 2014, ApJ, 797, 136

Ferré-Mateu, A., Vazdekis, A., & de la Rosa, I. G. 2013, MNRAS, 431, 440

Ferré-Mateu, A., Vazdekis, A., Trujillo, I., et al. 2012, MNRAS, 423, 632

Ferreras, I., La Barbera, F., de la Rosa, I. G., et al. 2013, MNRAS, 429, L15

Ferreras, I., Weidner, C., Vazdekis, A., & La Barbera, F. 2015, ArXiv e-prints, arXiv:1501.01636

Ferreras, I., Pasquali, A., Malhotra, S., et al. 2009, ApJ, 706, 158

Ferreras, I., Trujillo, I., Mármol-Queraltó, E., et al. 2014, MNRAS, 444, 906

Freeman, K. C. 1970, ApJ, 160, 811

Fry, A. M., Morrison, H. L., Harding, P., & Boroson, T. A. 1999, AJ, 118, 1209

Gadotti, D. A. 2012, Astronomical and Astrophysical Transactions, 27, 221

García-Benito, R., Zibetti, S., Sánchez, S. F., et al. 2014, ArXiv e-prints, arXiv:1409.8302

Geha, M., Brown, T. M., Tumlinson, J., et al. 2013, ApJ, 771, 29

Genel, S., Vogelsberger, M., Springel, V., et al. 2014, MNRAS, 445, 175

González Delgado, R. M., Pérez, E., Cid Fernandes, R., et al. 2014, A&A, 562, A47

Governato, F., Willman, B., Mayer, L., et al. 2007, MNRAS, 374, 1479

Graham, A. W., Trujillo, I., & Caon, N. 2001, AJ, 122, 1707

Grogin, N. A., Kocevski, D. D., Faber, S. M., et al. 2011, ApJS, 197, 35

Grossi, M., Hwang, N., Corbelli, E., et al. 2011, A&A, 533, A91

Gutiérrez, L., Erwin, P., Aladro, R., & Beckman, J. E. 2011, AJ, 142, 145

Hardy, E., & Couture, J. 1988, ApJ, 325, L29

Helou, G., Madore, B. F., Schmitz, M., et al. 1991, in Astrophysics and Space Science Library, Vol. 171, Databases and On-line Data in Astronomy, ed. M. A. Albrecht & D. Egret, 89–106

Hernán-Caballero, A., Alonso-Herrero, A., Pérez-González, P. G., et al. 2013, MNRAS, 434, 2136

Holwerda, B. W., Bianchi, S., Böker, T., et al. 2012, A&A, 541, L5

Hopkins, P. F. 2013, MNRAS, 433, 170

Hoversten, E. A., & Glazebrook, K. 2008, ApJ, 675, 163

Ibata, R., Martin, N. F., Irwin, M., et al. 2007, ApJ, 671, 1591

Ibata, R., Mouhcine, M., & Rejkuba, M. 2009, MNRAS, 395, 126

Irwin, M. J., Ferguson, A. M. N., Ibata, R. A., Lewis, G. F., & Tanvir, N. R. 2005, ApJ, 628, L105

Jablonka, P., Tafelmeyer, M., Courbin, F., & Ferguson, A. M. N. 2010, A&A, 513, A78

Jeong, H., Yi, S. K., Kyeong, J., et al. 2013, ApJS, 208, 7

Johansson, J., Thomas, D., & Maraston, C. 2012, MNRAS, 421, 1908

Kausch, W., Noll, S., Smette, A., et al. 2014, in Astronomical Society of the Pacific Conference Series, Vol. 485, Astronomical Data Analysis Software and Systems XXIII, ed. N. Manset & P. Forshay, 403

Kennicutt, Jr., R. C. 1989, ApJ, 344, 685

Klypin, A. A., Trujillo-Gomez, S., & Primack, J. 2011, ApJ, 740, 102

Kobayashi, C. 2004, MNRAS, 347, 740

Koekemoer, A. M., Faber, S. M., Ferguson, H. C., et al. 2011, ApJS, 197, 36

Kormendy, J., & Bender, R. 2012, ApJS, 198, 2

Kregel, M., van der Kruit, P. C., & de Grijs, R. 2002, MNRAS, 334, 646

Kriek, M., Shapley, A. E., Reddy, N. A., et al. 2014, ArXiv e-prints, arXiv:1412.1835

Kroupa, P. 2001, MNRAS, 322, 231

—. 2002, Science, 295, 82

Kroupa, P., & Weidner, C. 2003, ApJ, 598, 1076

Kroupa, P., Weidner, C., Pflamm-Altenburg, J., et al. 2013, 115

La Barbera, F., Ferreras, I., de Carvalho, R. R., et al. 2012, MNRAS, 426, 2300

La Barbera, F., Ferreras, I., & Vazdekis, A. 2015, submitted

La Barbera, F., Ferreras, I., Vazdekis, A., et al. 2013, MNRAS, 433, 3017

Larson, R. B. 1974, MNRAS, 166, 585

—. 1998, MNRAS, 301, 569

—. 2005, MNRAS, 359, 211

Le Borgne, J.-F., Bruzual, G., Pelló, R., et al. 2003, A&A, 402, 433

Marchesini, D., Muzzin, A., Stefanon, M., et al. 2014, ArXiv e-prints, arXiv:1402.0003

Marks, M., Kroupa, P., Dabringhausen, J., & Pawlowski, M. S. 2012, MNRAS, 422, 2246

Martín-Navarro, I., Barbera, F. L., Vazdekis, A., Falcón-Barroso, J., & Ferreras, I. 2015a, MNRAS, 447, 1033

Martín-Navarro, I., La Barbera, F., Vazdekis, A., Falcón-Barroso, J., & Ferreras, I. 2015b

Martín-Navarro, I., Bakos, J., Trujillo, I., et al. 2012, MNRAS, 427, 1102

Martín-Navarro, I., Pérez-González, P. G., Trujillo, I., et al. 2015c, ApJ, 798, L4

Martínez-Serrano, F. J., Serna, A., Doménech-Moral, M., & Domínguez-Tenreiro, R. 2009, ApJ, 705, L133

Meurer, G. R., Heckman, T. M., & Calzetti, D. 1999, ApJ, 521, 64

Meurer, G. R., Wong, O. I., Kim, J. H., et al. 2009, ApJ, 695, 765

Misiriotis, A., Popescu, C. C., Tuffs, R., & Kylafis, N. D. 2001, A&A, 372, 775

Mo, H. J., & White, S. D. M. 1996, MNRAS, 282, 347

Montes, M., Trujillo, I., Prieto, M. A., & Acosta-Pulido, J. A. 2014, MNRAS, 439, 990

Mouhcine, M., Ferguson, H. C., Rich, R. M., Brown, T. M., & Smith, T. E. 2005, ApJ, 633, 810

Mould, J. R. 1976, A&A, 48, 443

Naab, T., Johansson, P. H., & Ostriker, J. P. 2009, ApJ, 699, L178

Navarro, J. F., Frenk, C. S., & White, S. D. M. 1997, ApJ, 490, 493

Navarro, J. F., & Steinmetz, M. 2000, ApJ, 538, 477

Navarro-González, J., Ricciardelli, E., Quilis, V., & Vazdekis, A. 2013, MNRAS, 436, 3507

Newman, A. B., Ellis, R. S., Treu, T., & Bundy, K. 2010, ApJ, 717, L103

O'Connell, R. W. 1986, in Stellar Populations, ed. C. A. Norman, A. Renzini, & M. Tosi, 167–189

O'Dea, C. P., Baum, S. A., Privon, G., et al. 2008, ApJ, 681, 1035

Onodera, M., Renzini, A., Carollo, M., et al. 2012, ApJ, 755, 26

Oser, L., Ostriker, J. P., Naab, T., Johansson, P. H., & Burkert, A. 2010, ApJ, 725, 2312

Padoan, P., & Nordlund, Å. 2002, ApJ, 576, 870

Pastorello, N., Forbes, D. A., Foster, C., et al. 2014, ArXiv e-prints, arXiv:1405.2338

Patterson, F. S. 1940, Harvard College Observatory Bulletin, 914, 9

Paturel, G., Petit, C., Prugniel, P., et al. 2003, A&A, 412, 45

Peletier, R. F. 1989, PhD thesis, , University of Groningen, The Netherlands, (1989)

—. 2013, Stellar Populations, ed. J. Falcón-Barroso & J. H. Knapen, 353

Pérez, I. 2004, A&A, 427, L17

Pérez-González, P. G., Rieke, G. H., Villar, V., et al. 2008, ApJ, 675, 234

Pérez-González, P. G., Cava, A., Barro, G., et al. 2013, ApJ, 762, 46

Peters, S., Hinz, J. L., Gil de Paz, A., et al. 2014, in prep

Pipino, A., & Matteucci, F. 2004, MNRAS, 347, 968

Pohlen, M., Balcells, M., Lütticke, R., & Dettmar, R.-J. 2004, A&A, 422, 465

Pohlen, M., Dettmar, R.-J., & Lütticke, R. 2000, A&A, 357, L1

Pohlen, M., & Trujillo, I. 2006, A&A, 454, 759

Pohlen, M., Zaroubi, S., Peletier, R. F., & Dettmar, R.-J. 2007, MNRAS, 378, 594

Pols, O. R., Tout, C. A., Eggleton, P. P., & Han, Z. 1995, MNRAS, 274, 964

Popescu, C. C., Tuffs, R. J., Dopita, M. A., et al. 2011, A&A, 527, A109

Quilis, V., & Trujillo, I. 2013, ApJ, 773, L8

Radburn-Smith, D. J., Roškar, R., Debattista, V. P., et al. 2012a, ApJ, 753, 138

—. 2012b, ApJ, 753, 138

Renzini, A. 2006, ARA&A, 44, 141

Ricciardelli, E., Vazdekis, A., Cenarro, A. J., & Falcón-Barroso, J. 2012, MNRAS, 424, 172

Richardson, J. C., Ferguson, A. M. N., Johnson, R. A., et al. 2008, AJ, 135, 1998

Roediger, J. C., Courteau, S., Sánchez-Blázquez, P., & McDonald, M. 2012, ApJ, 758, 41

Roškar, R., Debattista, V. P., Stinson, G. S., et al. 2008, ApJ, 675, L65

Ruiz, P., Trujillo, I., & Mármol-Queraltó, E. 2014, MNRAS, 442, 347

Ryś, A., Koleva, M., Falcón-Barroso, J., et al. 2015, MNRAS, 452, 1888

Saglia, R. P., Maraston, C., Thomas, D., Bender, R., & Colless, M. 2002, ApJ, 579, L13

Saha, A., Olszewski, E. W., Brondel, B., et al. 2010, AJ, 140, 1719

Salpeter, E. E. 1955, ApJ, 121, 161

Sánchez, S. F., Kennicutt, R. C., Gil de Paz, A., et al. 2012, A&A, 538, A8

Sánchez-Blázquez, P., Courty, S., Gibson, B. K., & Brook, C. B. 2009, MNRAS, 398, 591

Sánchez-Blázquez, P., Forbes, D. A., Strader, J., Brodie, J., & Proctor, R. 2007, MNRAS, 377, 759

Sánchez-Blázquez, P., Ocvirk, P., Gibson, B. K., Pérez, I., & Peletier, R. F. 2011, MNRAS, 415, 709

Sánchez-Blázquez, P., Peletier, R. F., Jiménez-Vicente, J., et al. 2006, MNRAS, 371, 703

Sarzi, M., Falcón-Barroso, J., Davies, R. L., et al. 2006, MNRAS, 366, 1151

Schaye, J. 2004, ApJ, 609, 667

Schaye, J., Crain, R. A., Bower, R. G., et al. 2015, MNRAS, 446, 521

Schiavon, R. P., Barbuy, B., & Bruzual A., G. 2000, ApJ, 532, 453

Sersic, J. L. 1968, Atlas de galaxias australes

Serven, J., Worthey, G., & Briley, M. M. 2005, ApJ, 627, 754

Shaw, M. A., & Gilmore, G. 1990, MNRAS, 242, 59

Sheth, K., Regan, M., Hinz, J. L., et al. 2010, PASP, 122, 1397

Shetty, S., & Cappellari, M. 2014, ApJ, 786, L10

Silk, J. 1977, ApJ, 211, 638

Smith, R. J. 2014, MNRAS, 443, L69

Smith, R. J., & Lucey, J. R. 2013, MNRAS, 434, 1964

Somerville, R. S., Primack, J. R., & Faber, S. M. 2001, MNRAS, 320, 504

Spiniello, C., Trager, S., Koopmans, L. V. E., & Conroy, C. 2014, MNRAS, 438, 1483

Spiniello, C., Trager, S. C., & Koopmans, L. V. E. 2015, ApJ, 803, 87

Spiniello, C., Trager, S. C., Koopmans, L. V. E., & Chen, Y. P. 2012, ApJ, 753, L32

Springel, V., White, S. D. M., Jenkins, A., et al. 2005, Nature, 435, 629

Stringer, M., Trujillo, I., Dalla Vecchia, C., & Martinez-Valpuesta, I. 2015, ArXiv e-prints, arXiv:1503.03078

Tanaka, M., Chiba, M., Komiyama, Y., et al. 2010, ApJ, 708, 1168

Thomas, D., Greggio, L., & Bender, R. 1999, MNRAS, 302, 537

Thomas, D., Maraston, C., & Bender, R. 2003, MNRAS, 339, 897

Thomas, D., Maraston, C., Bender, R., & Mendes de Oliveira, C. 2005, ApJ, 621, 673

Thomas, D., Maraston, C., & Johansson, J. 2011a, MNRAS, 412, 2183

Thomas, J., Saglia, R. P., Bender, R., et al. 2011b, MNRAS, 415, 545

Tortora, C., Pipino, A., D'Ercole, A., Napolitano, N. R., & Matteucci, F. 2013, ArXiv e-prints, arXiv:1307.4079

Trager, S. C., Worthey, G., Faber, S. M., Burstein, D., & Gonzalez, J. J. 1998, ApJS, 116, 1

Treu, T., Auger, M. W., Koopmans, L. V. E., et al. 2010, ApJ, 709, 1195

Trujillo, I., & Bakos, J. 2013, MNRAS, 431, 1121

Trujillo, I., Cenarro, A. J., de Lorenzo-Cáceres, A., et al. 2009, ApJ, 692, L118

Trujillo, I., Ferré-Mateu, A., Balcells, M., Vazdekis, A., & Sánchez-Blázquez, P. 2014, ApJ, 780, L20

Trujillo, I., Ferreras, I., & de La Rosa, I. G. 2011, MNRAS, 415, 3903

Trujillo, I., Graham, A. W., & Caon, N. 2001, MNRAS, 326, 869

Trujillo, I., & Pohlen, M. 2005, ApJ, 630, L17

van de Sande, J., Kriek, M., Franx, M., et al. 2013, ApJ, 771, 85

van den Bosch, R. C. E., Gebhardt, K., Gültekin, K., et al. 2012, Nature, 491, 729

van der Kruit, P. C. 1987, A&A, 173, 59

—. 1988, A&A, 192, 117

—. 2007, A&A, 466, 883

van der Kruit, P. C., & Freeman, K. C. 2011, ARA&A, 49, 301

van der Kruit, P. C., & Searle, L. 1981, A&A, 95, 105

—. 1982, A&A, 110, 61

van Dokkum, P. G. 2008, ApJ, 674, 29

van Dokkum, P. G., & Conroy, C. 2010, Nature, 468, 940

van Dokkum, P. G., Whitaker, K. E., Brammer, G., et al. 2010, ApJ, 709, 1018

VandenBerg, D. A., Bergbusch, P. A., Dotter, A., et al. 2012, ApJ, 755, 15

Vazdekis, A., Casuso, E., Peletier, R. F., & Beckman, J. E. 1996, ApJS, 106, 307

Vazdekis, A., Cenarro, A. J., Gorgas, J., Cardiel, N., & Peletier, R. F. 2003, MNRAS, 340, 1317

Vazdekis, A., Peletier, R. F., Beckman, J. E., & Casuso, E. 1997, ApJS, 111, 203

Vazdekis, A., Ricciardelli, E., Cenarro, A. J., et al. 2012, MNRAS, 424, 157

Vazdekis, A., Sánchez-Blázquez, P., Falcón-Barroso, J., et al. 2010, MNRAS, 404, 1639

Vazdekis, A., Coelho, P., Cassisi, S., et al. 2015, MNRAS, 449, 1177

Vlajić, M., Bland-Hawthorn, J., & Freeman, K. C. 2009, ApJ, 697, 361

—. 2011, ApJ, 732, 7

Wainscoat, R. J., Freeman, K. C., & Hyland, A. R. 1989, ApJ, 337, 163

Walcher, C. J., Wisotzki, L., Bekeraité, S., et al. 2014, A&A, 569, A1

Wegner, G. A., Corsini, E. M., Thomas, J., et al. 2012, AJ, 144, 78

Weidner, C., Ferreras, I., Vazdekis, A., & La Barbera, F. 2013, MNRAS, 435, 2274

Weidner, C., & Kroupa, P. 2005, ApJ, 625, 754

Whitaker, K. E., Labbé, I., van Dokkum, P. G., et al. 2011, ApJ, 735, 86

Whitaker, K. E., van Dokkum, P. G., Brammer, G., et al. 2013, ApJ, 770, L39

White, S. D. M., & Rees, M. J. 1978, MNRAS, 183, 341

Worthey, G. 1994, ApJS, 95, 107

Worthey, G., & Collobert, M. 2003, ApJ, 586, 17

Worthey, G., Faber, S. M., & Gonzalez, J. J. 1992, ApJ, 398, 69

Wu, H., Burstein, D., Deng, Z., et al. 2002, AJ, 123, 1364

Xilouris, E. M., Alton, P. B., Davies, J. I., et al. 1998, A&A, 331, 894

Xilouris, E. M., Byun, Y. I., Kylafis, N. D., Paleologou, E. V., & Papamastorakis, J. 1999, A&A, 344, 868

Xilouris, E. M., Kylafis, N. D., Papamastorakis, J., Paleologou, E. V., & Haerendel, G. 1997, A&A, 325, 135

Yoachim, P., Roškar, R., & Debattista, V. P. 2012, ApJ, 752, 97

Zackrisson, E., de Jong, R. S., & Micheva, G. 2012, MNRAS, 421, 190

Zibetti, S., & Ferguson, A. M. N. 2004, MNRAS, 352, L6

Zibetti, S., White, S. D. M., & Brinkmann, J. 2004, MNRAS, 347, 556

# A

# Sample of nearby edge-on galaxies (see Chapter 1)

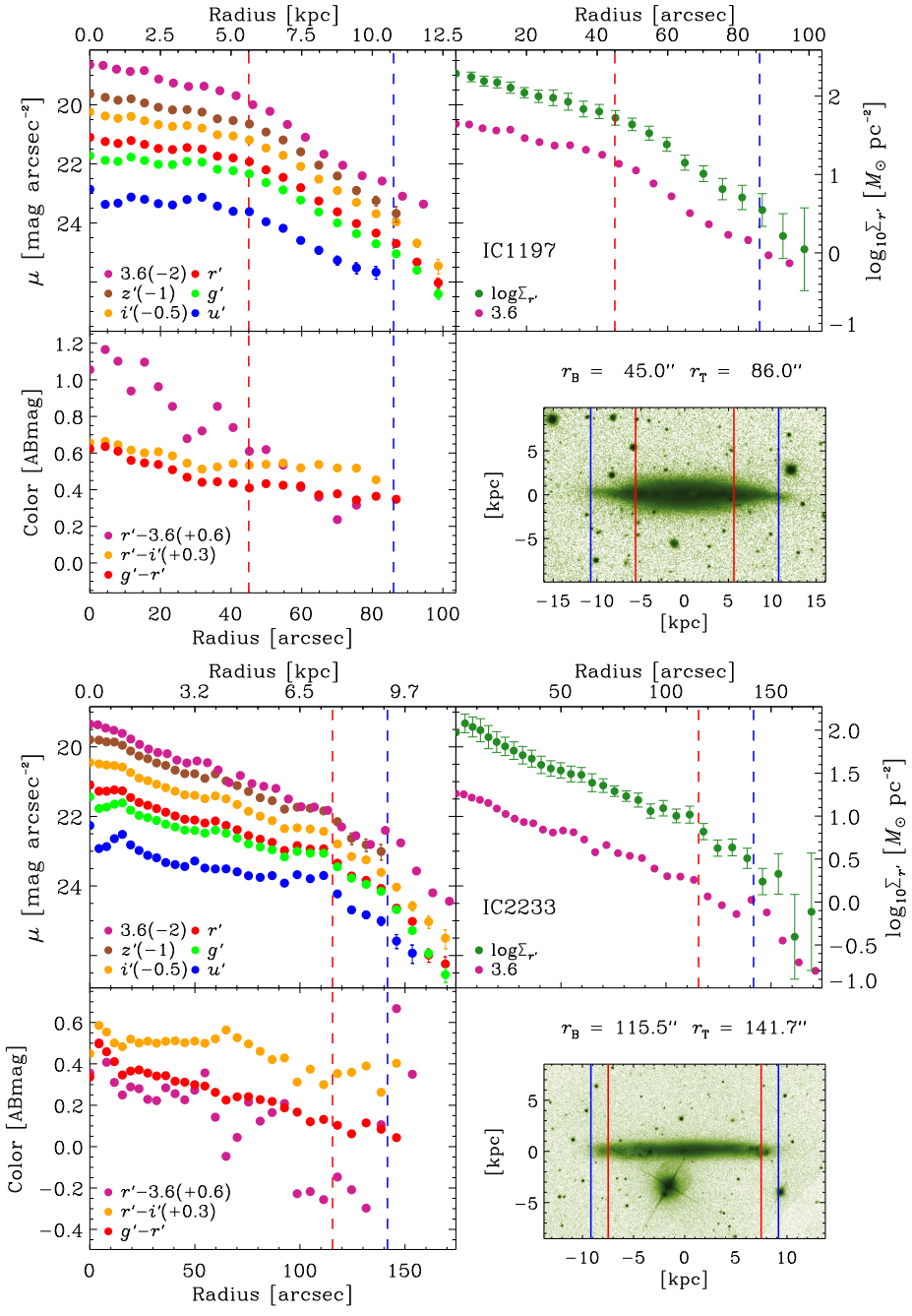
Radius [kpc]
Radius [arcsec]
μ [mag arcsec⁻²]
log10Σr' [M⊙ pc⁻²]
IC1197
3.6(−2) r'
z'(−1) g'
i'(−0.5) u'
logΣr'
3.6
Color [ABmag]
r'−3.6(+0.6)
r'−i'(+0.3)
g'−r'
rB = 45.0'' rT = 86.0''
[kpc]
IC2233
rB = 115.5'' rT = 141.7''

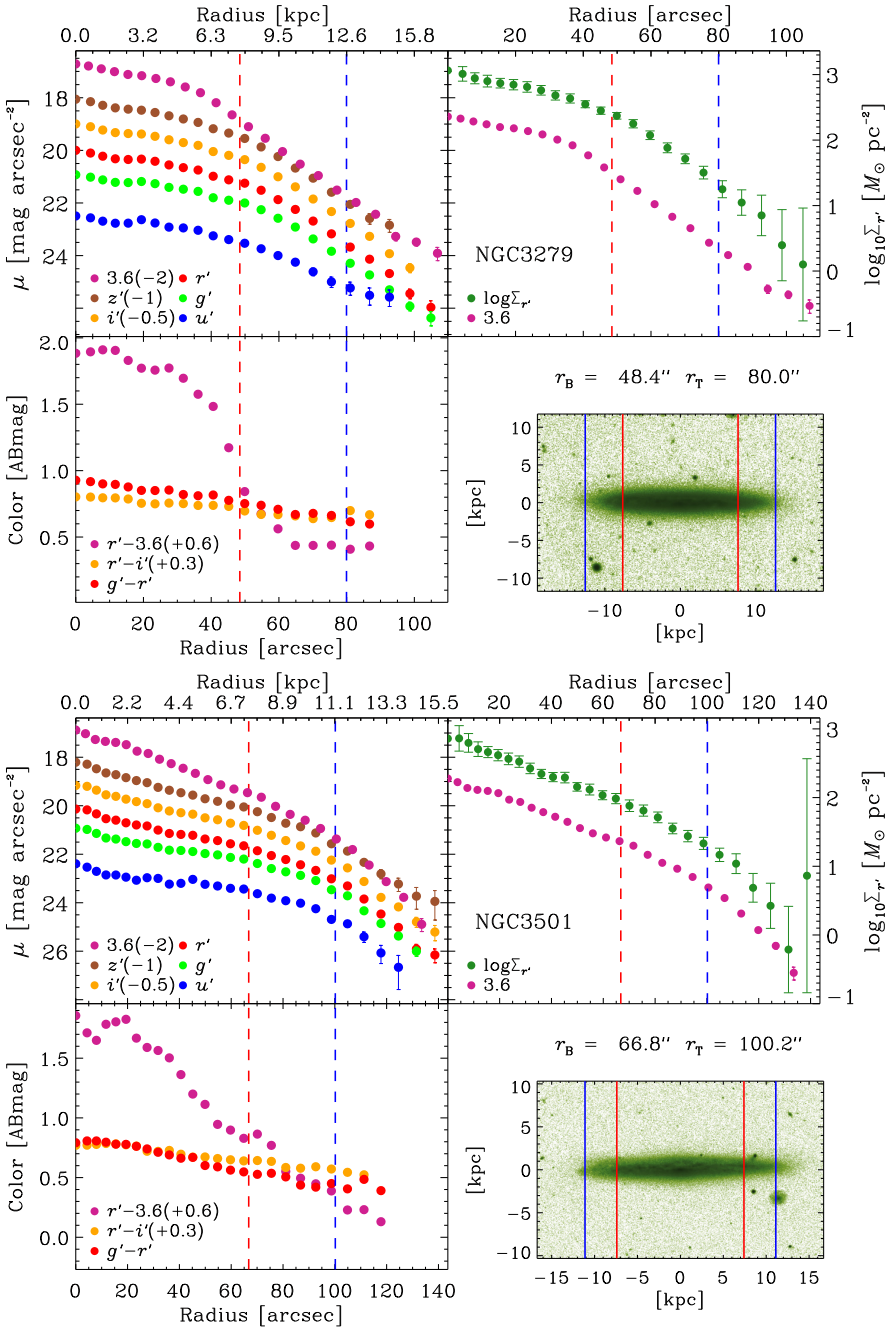
Radius [kpc]
Radius [arcsec]
μ [mag arcsec⁻²]
log10Σr' [M⊙ pc⁻²]
3.6(−2) r'
z'(−1) g'
i'(−0.5) u'
NGC3279
logΣr'
3.6
Color [ABmag]
r'−3.6(+0.6)
r'−i'(+0.3)
g'−r'
rB = 48.4'' rT = 80.0''
[kpc]
NGC3501
rB = 66.8'' rT = 100.2''

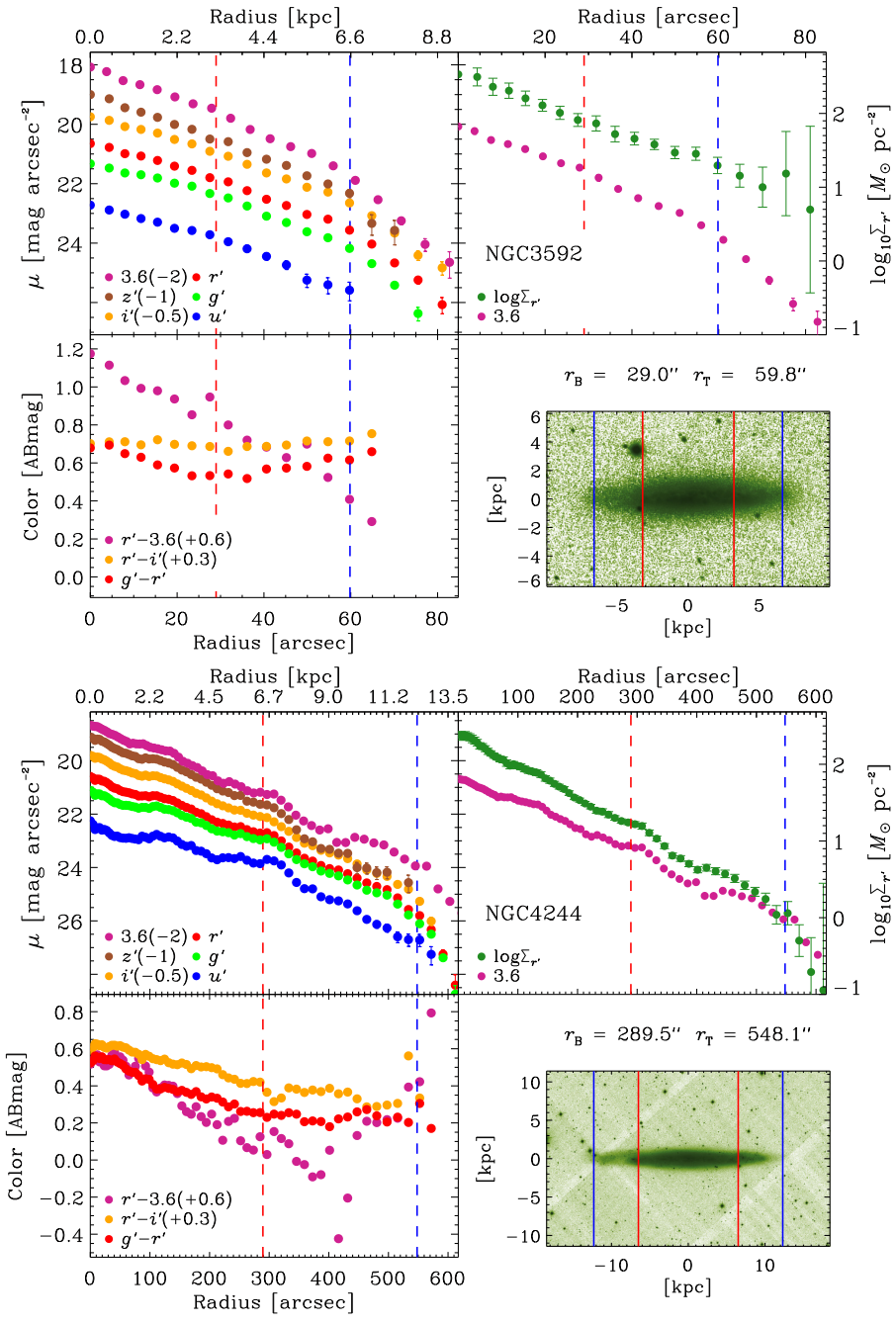
Radius [kpc]
Radius [arcsec]
μ [mag arcsec⁻²]
log10Σr' [M⊙ pc⁻²]
NGC3592
3.6(−2) r'
z'(−1) g'
i'(−0.5) u'
logΣr'
3.6
rB = 29.0'' rT = 59.8''
Color [ABmag]
r'−3.6(+0.6)
r'−i'(+0.3)
g'−r'
[kpc]
NGC4244
rB = 289.5'' rT = 548.1''

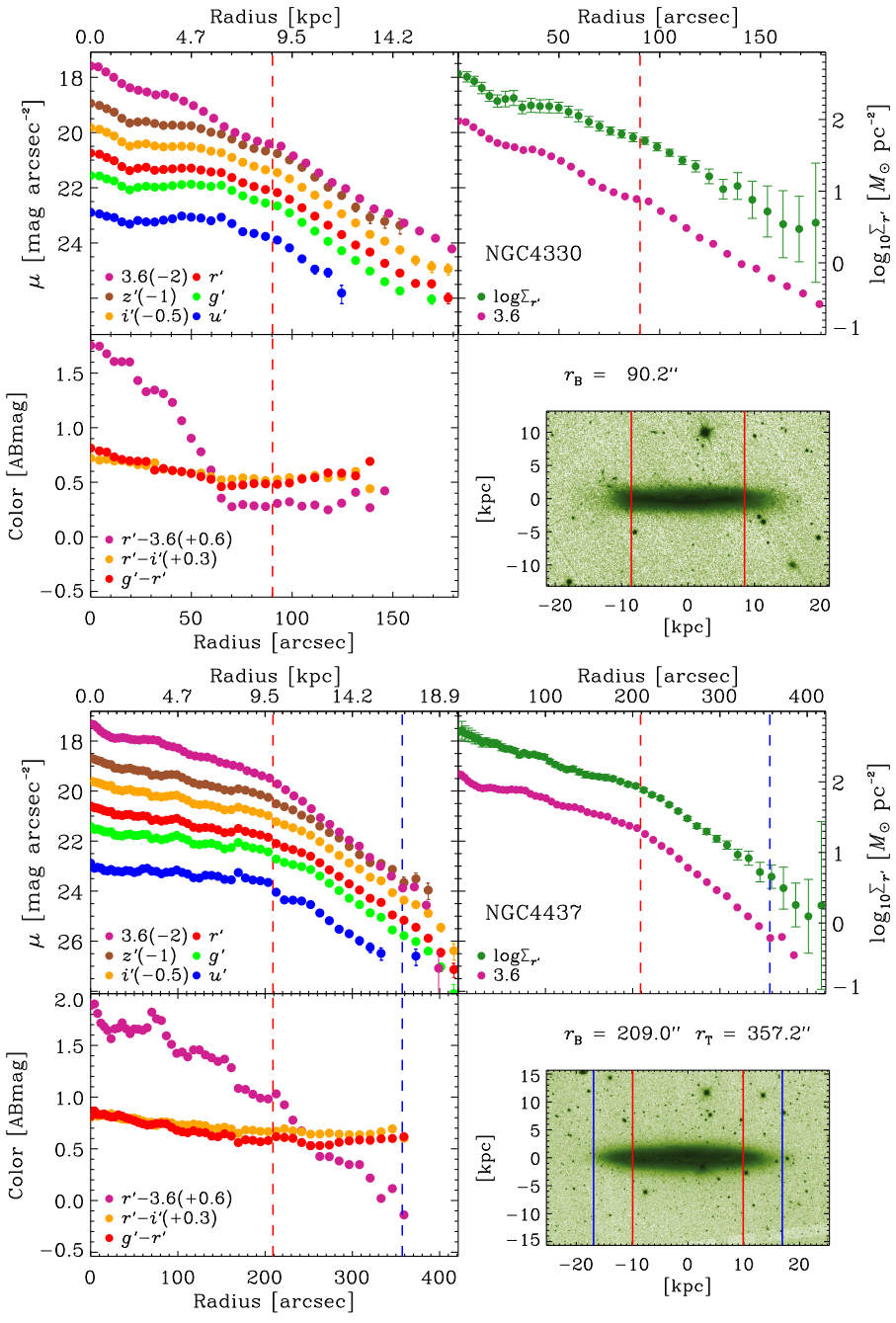
Radius [kpc]
Radius [arcsec]
μ [mag arcsec⁻²]
log10Σr' [M⊙ pc⁻²]
NGC4330
3.6(−2) r'
z'(−1) g'
i'(−0.5) u'
logΣr'
3.6
Color [ABmag]
r'−3.6(+0.6)
r'−i'(+0.3)
g'−r'
rB = 90.2''
[kpc]
NGC4437
rB = 209.0'' rT = 357.2''

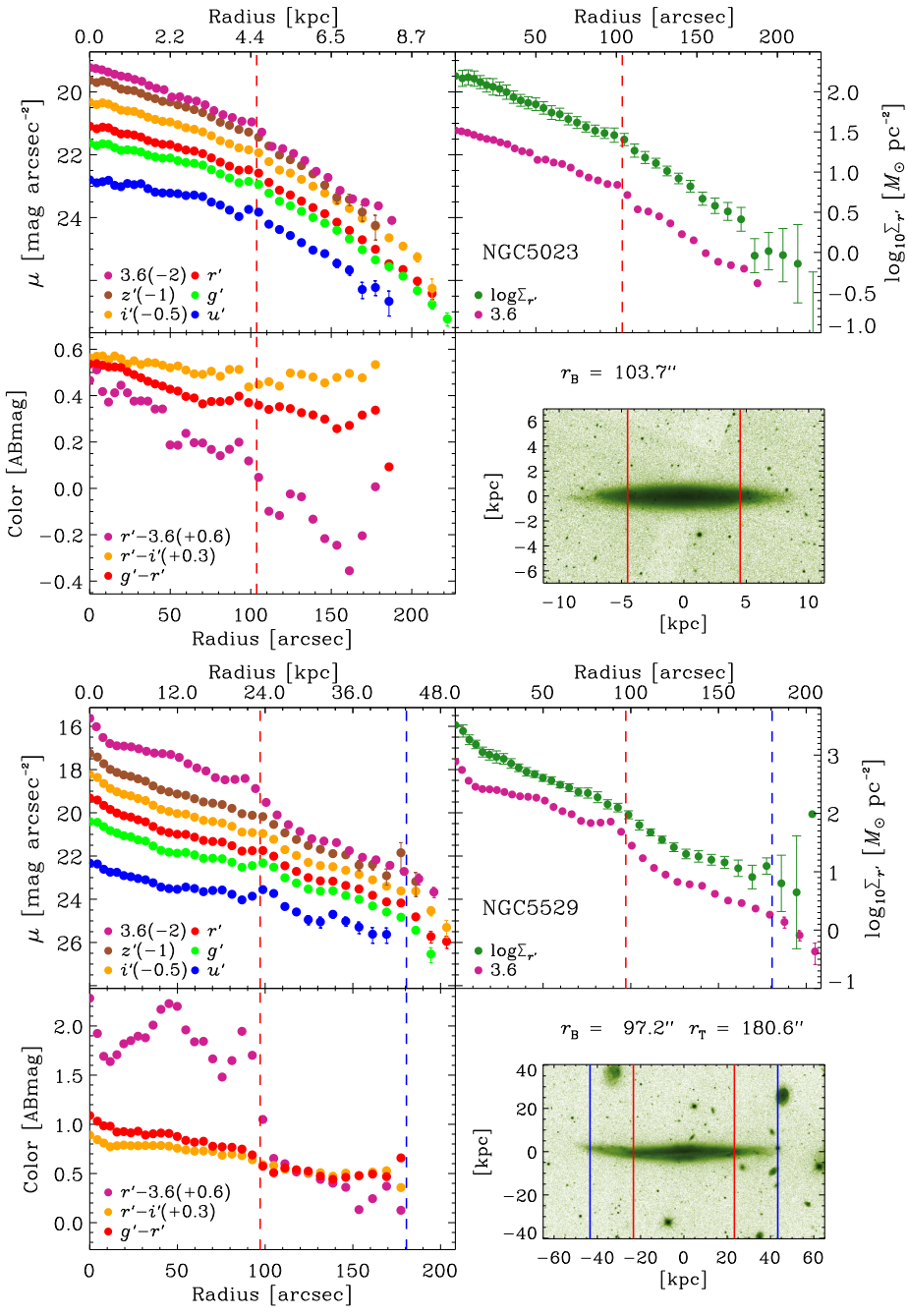
Radius [kpc]
Radius [arcsec]
μ [mag arcsec⁻²]
log10Σr' [M⊙ pc⁻²]
3.6(−2) r'
z'(−1) g'
i'(−0.5) u'
NGC5023
logΣr'
3.6
rB = 103.7''
Color [ABmag]
r'−3.6(+0.6)
r'−i'(+0.3)
g'−r'
[kpc]
NGC5529
rB = 97.2'' rT = 180.6''

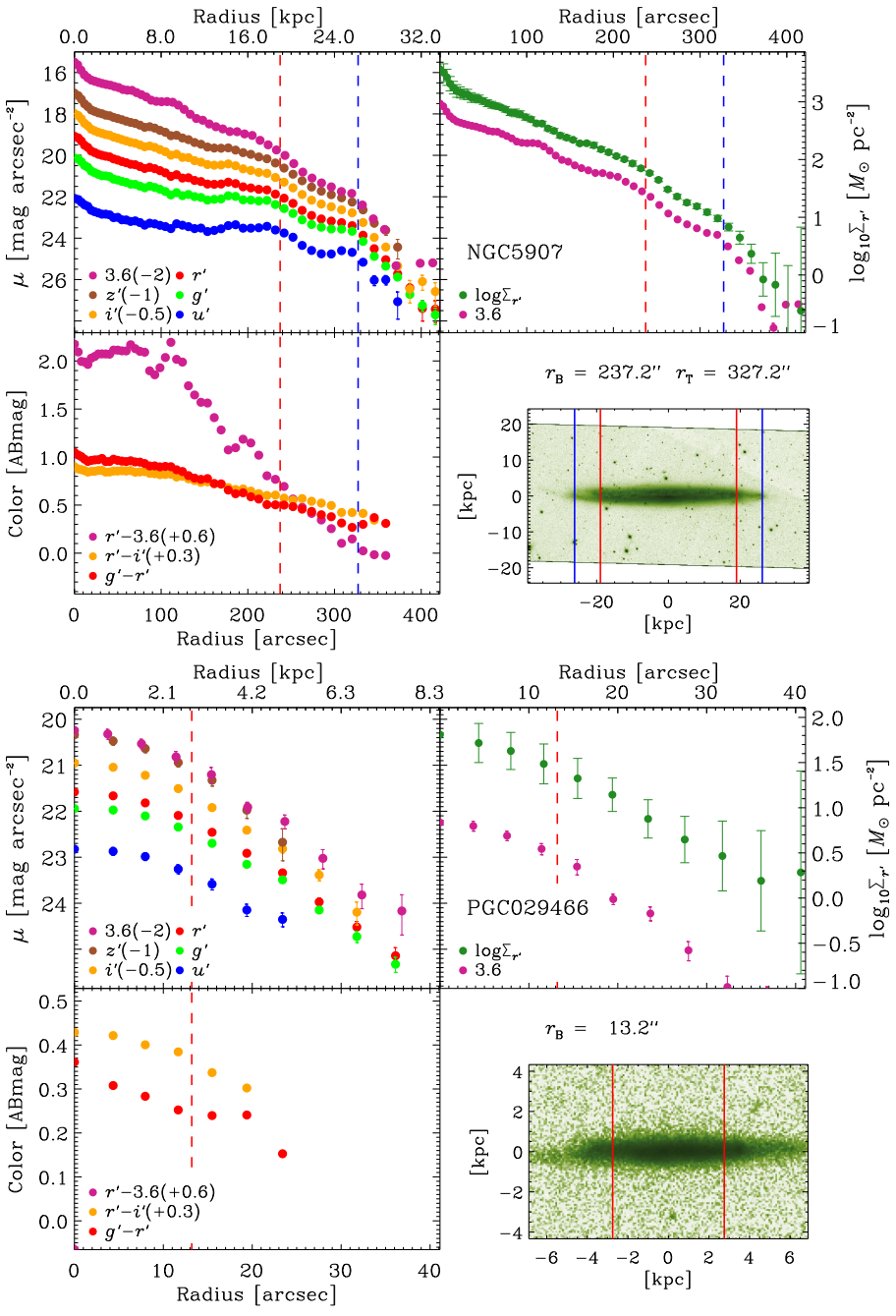
Radius [kpc]
Radius [arcsec]
μ [mag arcsec⁻²]
log10Σr′ [M⊙ pc⁻²]
3.6(−2) r′
z′(−1) g′
i′(−0.5) u′
NGC5907
logΣr′
3.6
Color [ABmag]
r′−3.6(+0.6)
r′−i′(+0.3)
g′−r′
rB = 237.2″ rT = 327.2″
[kpc]
PGC029466
rB = 13.2″

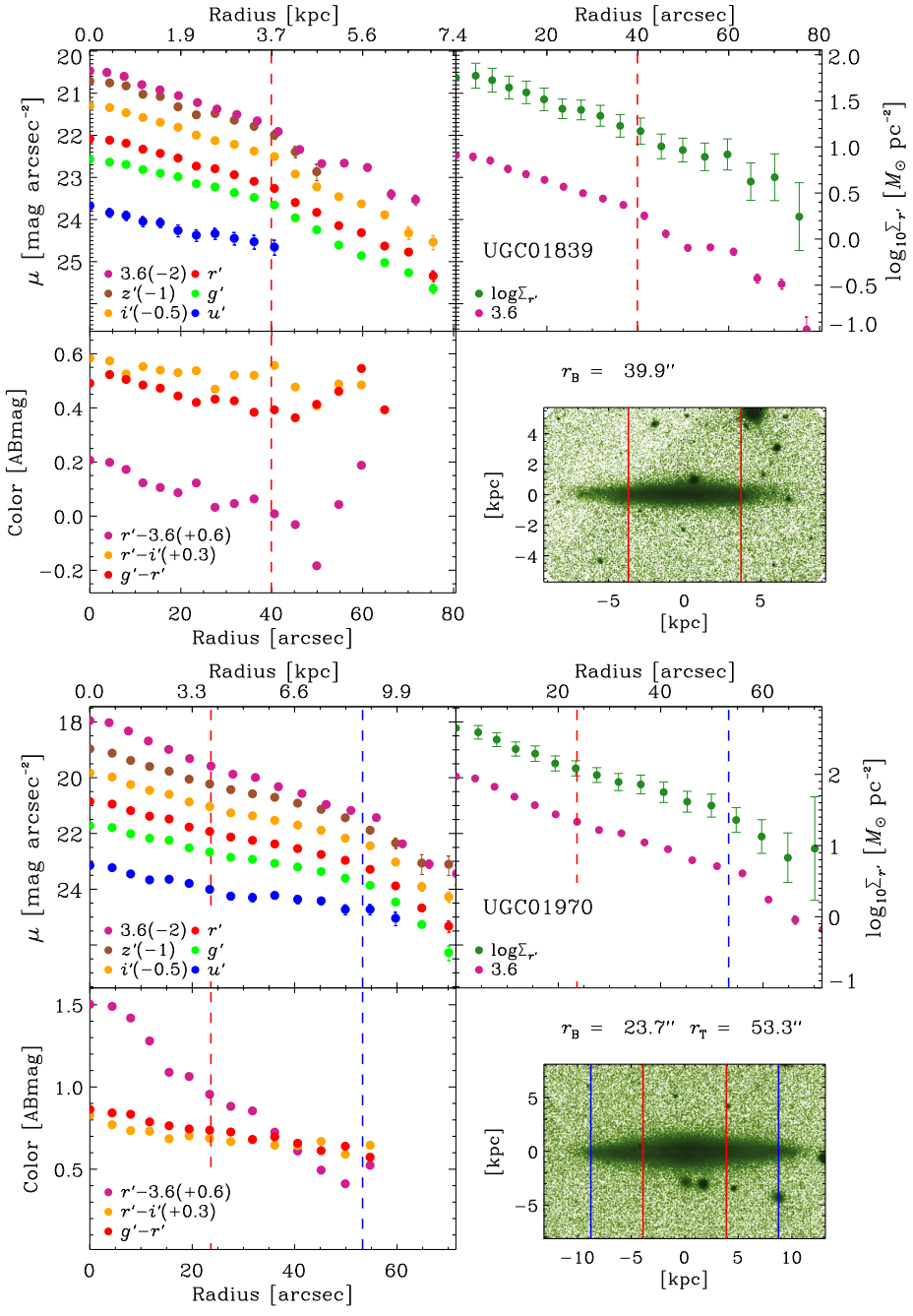
Radius [kpc]
Radius [arcsec]
μ [mag arcsec⁻²]
log10Σr' [M⊙ pc⁻²]
3.6(−2) r'
z'(−1) g'
i'(−0.5) u'
UGC01839
logΣr'
3.6
rB = 39.9''
Color [ABmag]
r'−3.6(+0.6)
r'−i'(+0.3)
g'−r'
[kpc]
UGC01970
rB = 23.7'' rT = 53.3''

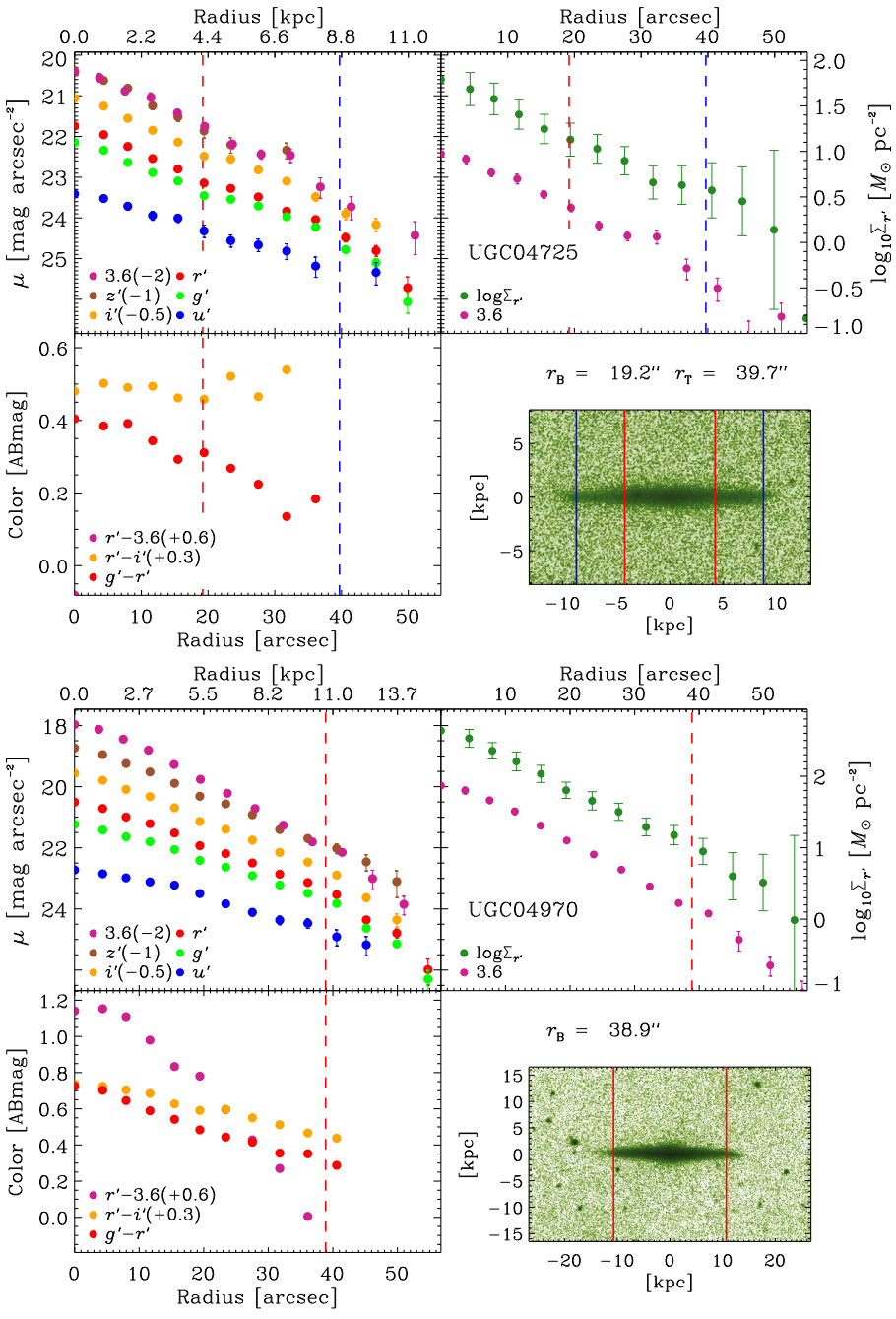
Radius [kpc]
Radius [arcsec]
μ [mag arcsec⁻²]
log₁₀Σ_r' [M⊙ pc⁻²]
3.6(−2) r'
z'(−1) g'
i'(−0.5) u'
UGC04725
logΣ_r'
3.6
Color [ABmag]
r'−3.6(+0.6)
r'−i'(+0.3)
g'−r'
r_B = 19.2'' r_T = 39.7''
[kpc]
UGC04970
r_B = 38.9''

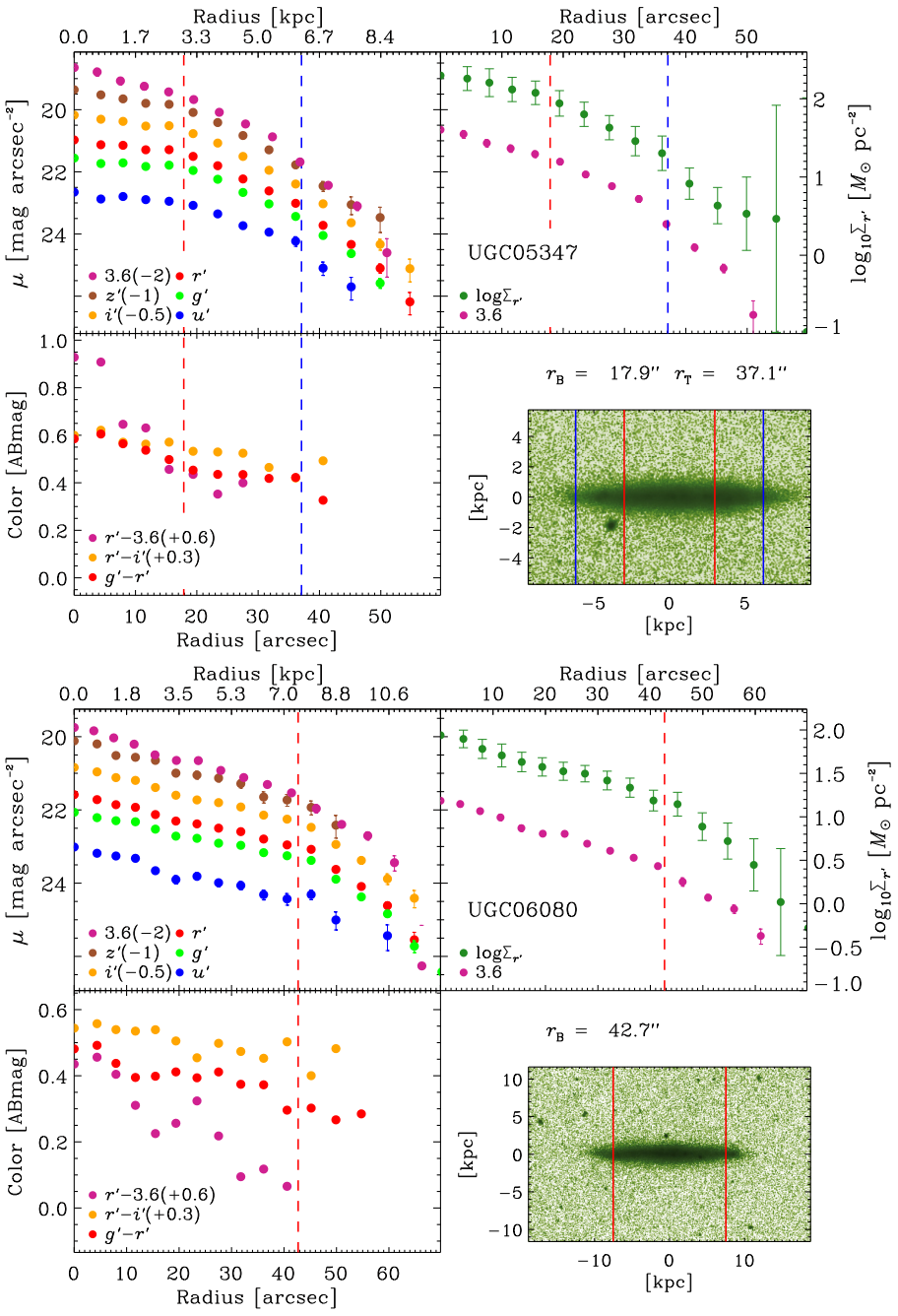
Radius [kpc]
Radius [arcsec]
μ [mag arcsec⁻²]
log10Σr' [M⊙ pc⁻²]
UGC05347
3.6(−2) r'
z'(−1) g'
i'(−0.5) u'
logΣr'
3.6
rB = 17.9'' rT = 37.1''
Color [ABmag]
r'−3.6(+0.6)
r'−i'(+0.3)
g'−r'
[kpc]
UGC06080
rB = 42.7''

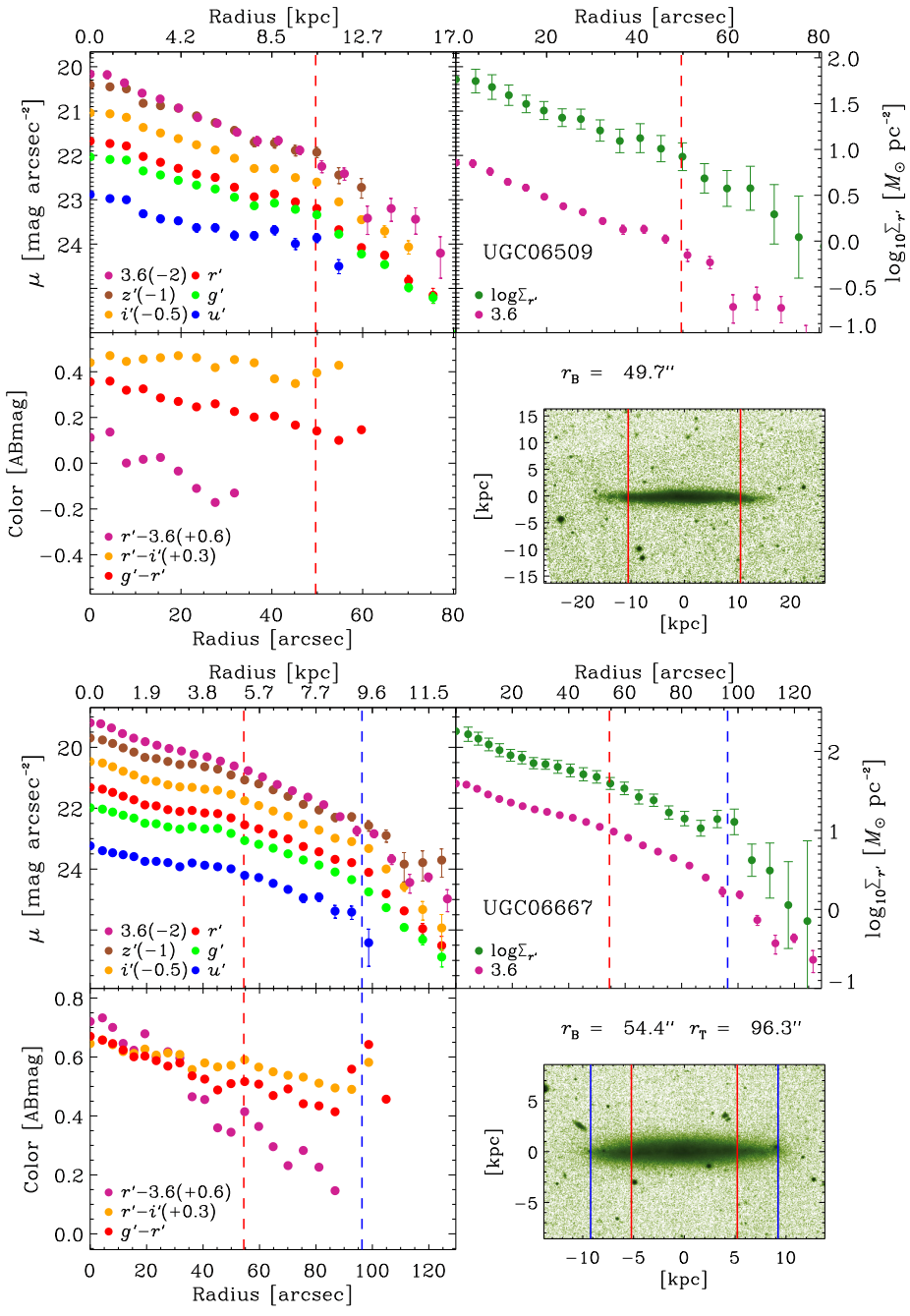
Radius [kpc]
Radius [arcsec]
μ [mag arcsec⁻²]
log₁₀Σ_r' [M⊙ pc⁻²]
3.6(−2) r'
z'(−1) g'
i'(−0.5) u'
UGC06509
logΣ_r'
3.6
Color [ABmag]
r'−3.6(+0.6)
r'−i'(+0.3)
g'−r'
r_B = 49.7''
[kpc]
Radius [kpc]
Radius [arcsec]
μ [mag arcsec⁻²]
log₁₀Σ_r' [M⊙ pc⁻²]
3.6(−2) r'
z'(−1) g'
i'(−0.5) u'
UGC06667
logΣ_r'
3.6
Color [ABmag]
r'−3.6(+0.6)
r'−i'(+0.3)
g'−r'
r_B = 54.4'' r_T = 96.3''
[kpc]

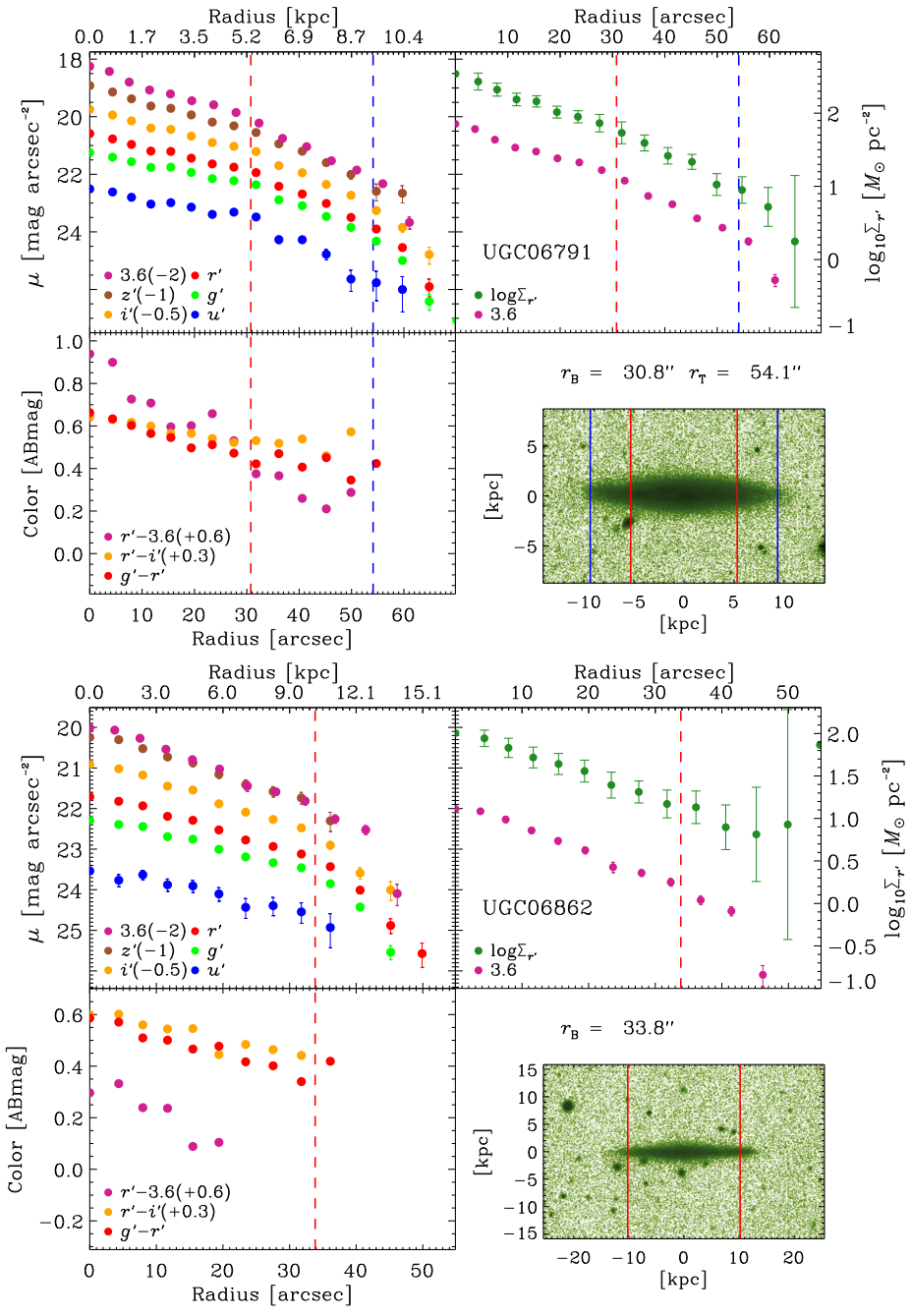
Radius [kpc]
Radius [arcsec]
μ [mag arcsec⁻²]
log10Σr' [M⊙ pc⁻²]
UGC06791
3.6(−2) r'
z'(−1) g'
i'(−0.5) u'
logΣr'
3.6
Color [ABmag]
r'−3.6(+0.6)
r'−i'(+0.3)
g'−r'
rB = 30.8'' rT = 54.1''
[kpc]
UGC06862
rB = 33.8''

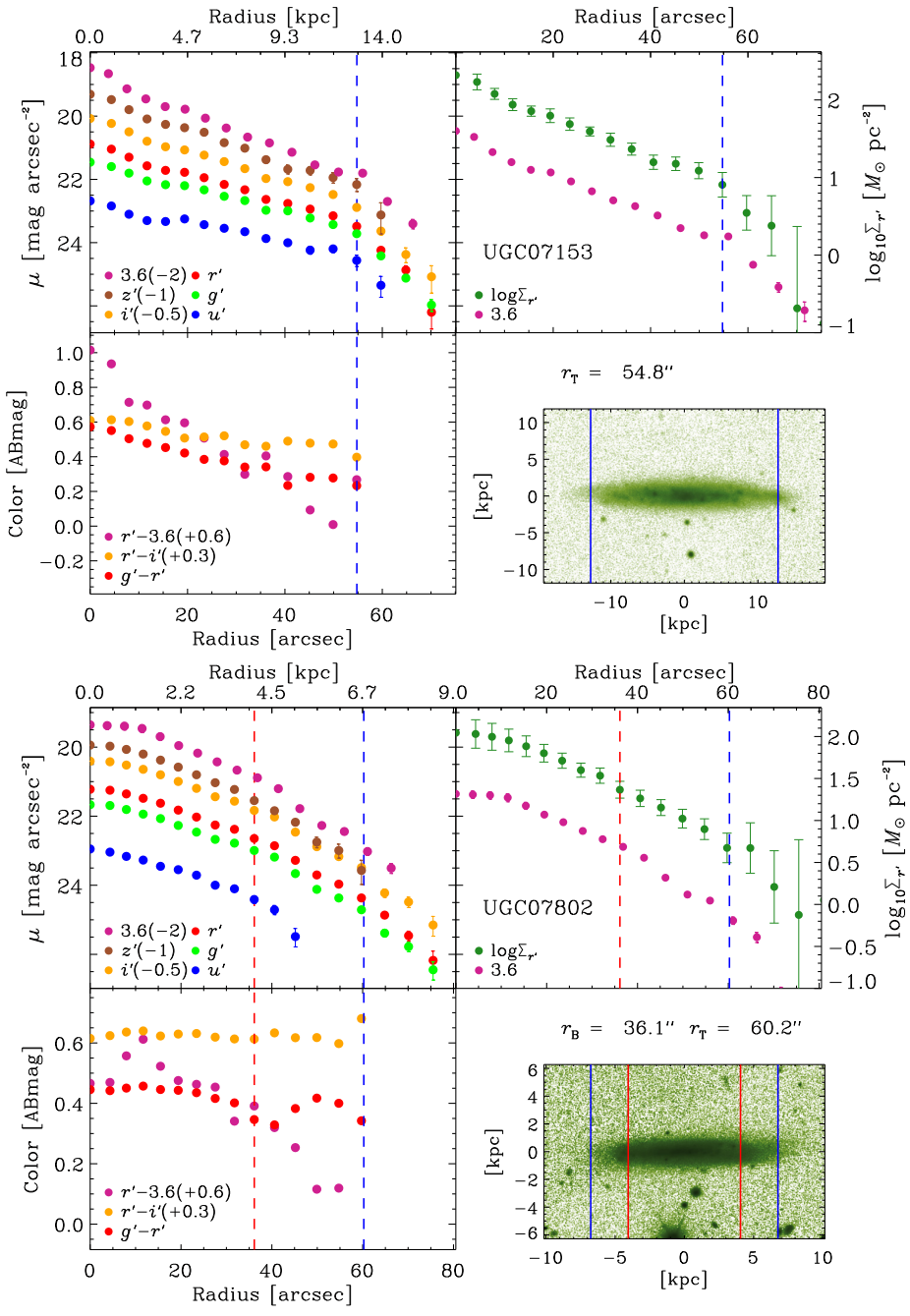
Radius [kpc]
Radius [arcsec]
μ [mag arcsec⁻²]
log10Σr' [M⊙ pc⁻²]
UGC07153
3.6(−2) r'
z'(−1) g'
i'(−0.5) u'
logΣr'
3.6
Color [ABmag]
r'−3.6(+0.6)
r'−i'(+0.3)
g'−r'
rT = 54.8''
[kpc]
UGC07802
rB = 36.1'' rT = 60.2''

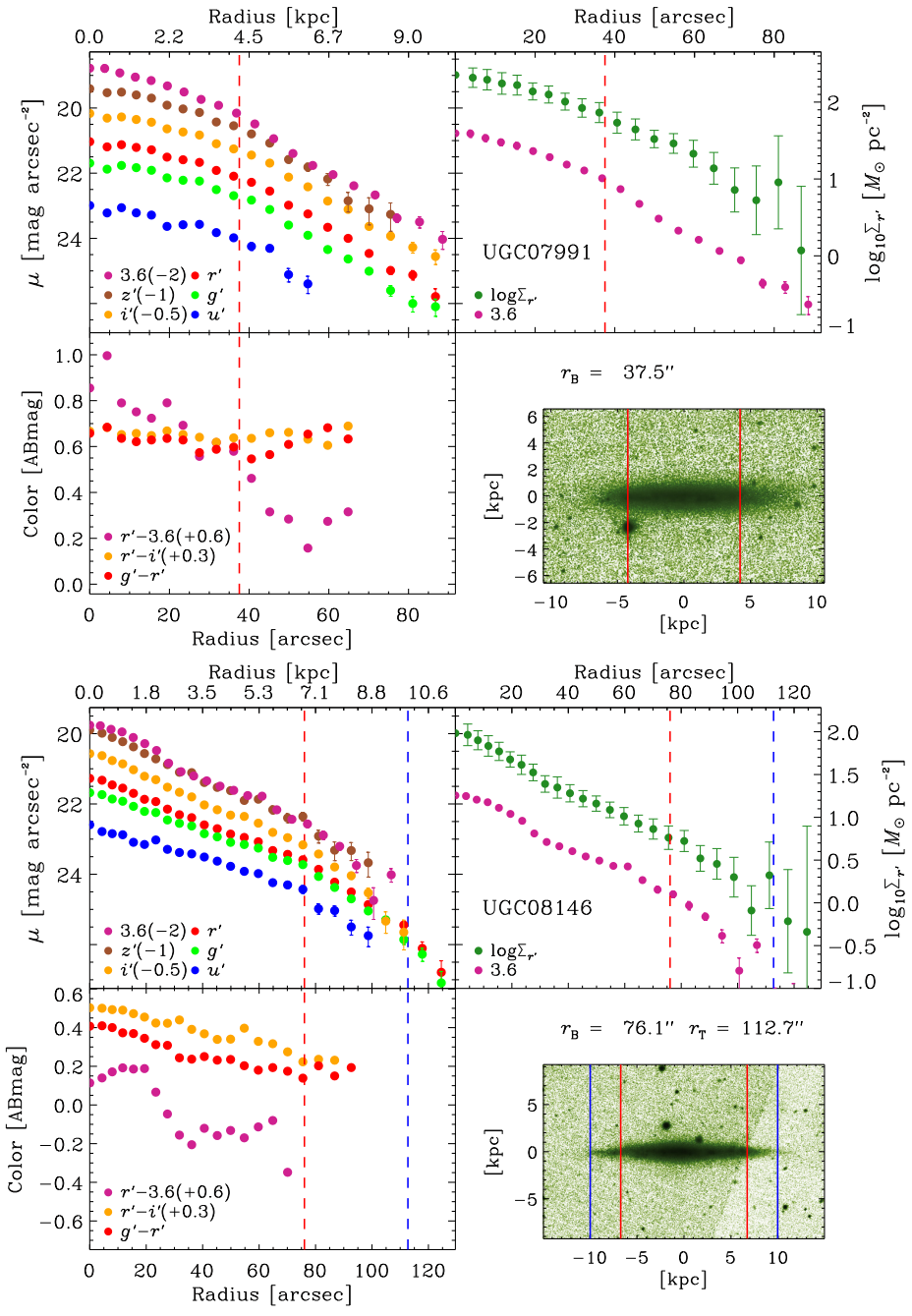
Radius [kpc]
Radius [arcsec]
μ [mag arcsec⁻²]
log10Σr' [M⊙ pc⁻²]
UGC07991
3.6(−2) r'
z'(−1) g'
i'(−0.5) u'
logΣr'
3.6
rB = 37.5″
Color [ABmag]
r'−3.6(+0.6)
r'−i'(+0.3)
g'−r'
[kpc]
UGC08146
rB = 76.1″ rT = 112.7″

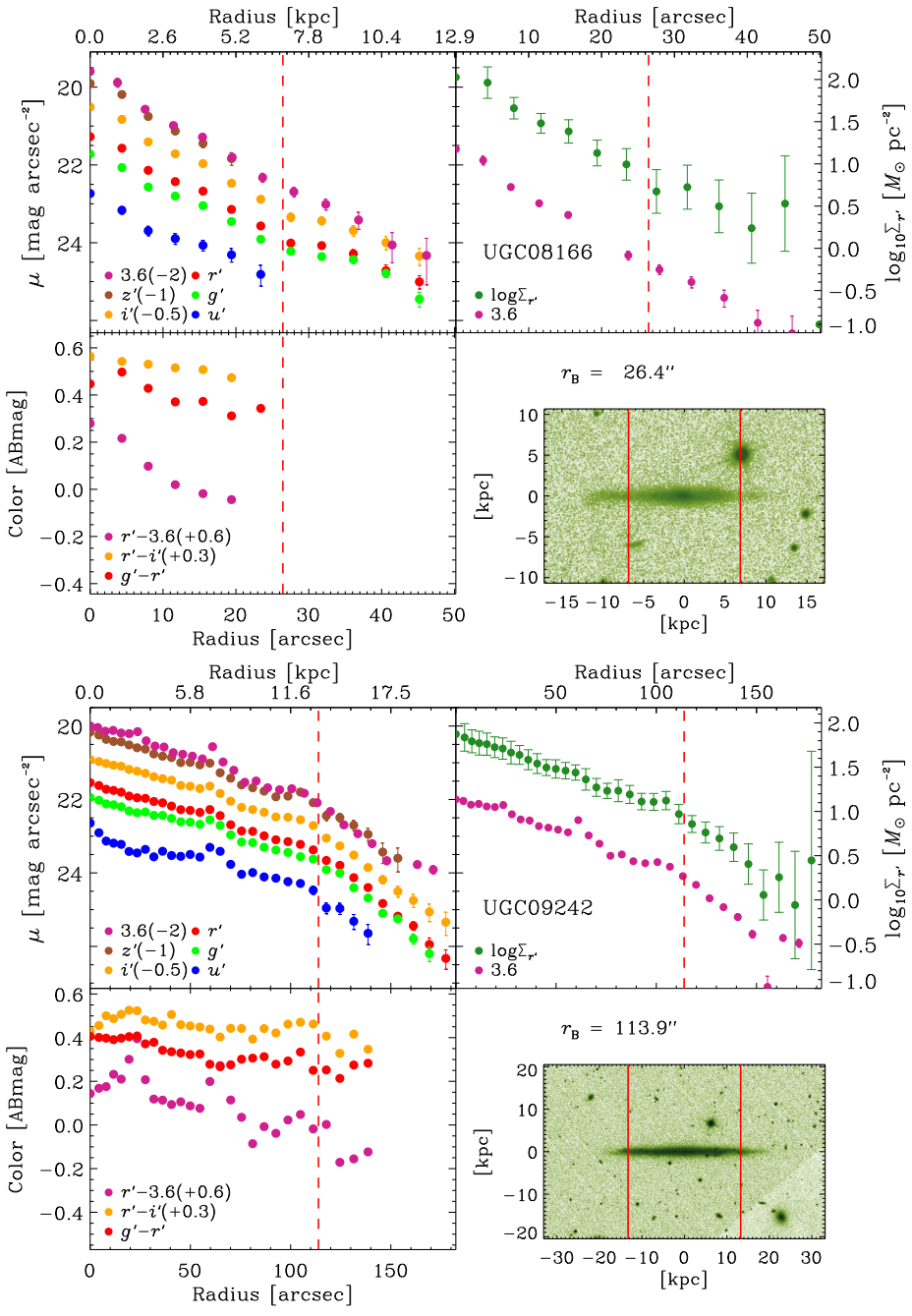
Radius [kpc]
Radius [arcsec]
μ [mag arcsec⁻²]
log10Σr′ [M⊙ pc⁻²]
3.6(−2) r′
z′(−1) g′
i′(−0.5) u′
UGC08166
logΣr′
3.6
Color [ABmag]
r′−3.6(+0.6)
r′−i′(+0.3)
g′−r′
rB = 26.4″
[kpc]
UGC09242
rB = 113.9″

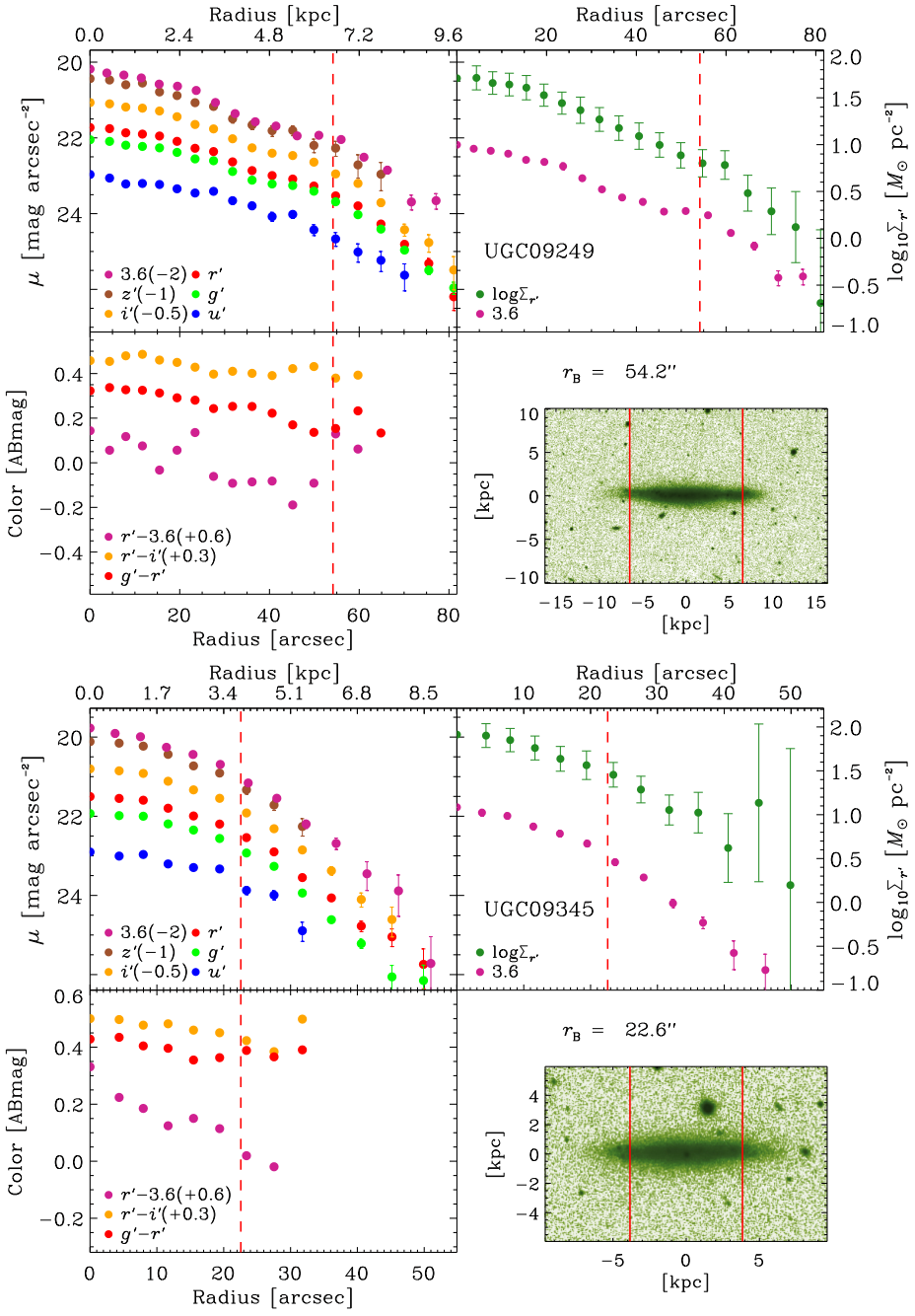
Radius [kpc]
Radius [arcsec]
μ [mag arcsec⁻²]
log10Σr' [M⊙ pc⁻²]
UGC09249
3.6(−2) r'
z'(−1) g'
i'(−0.5) u'
logΣr'
3.6
rB = 54.2''
Color [ABmag]
r'−3.6(+0.6)
r'−i'(+0.3)
g'−r'
[kpc]
UGC09345
rB = 22.6''

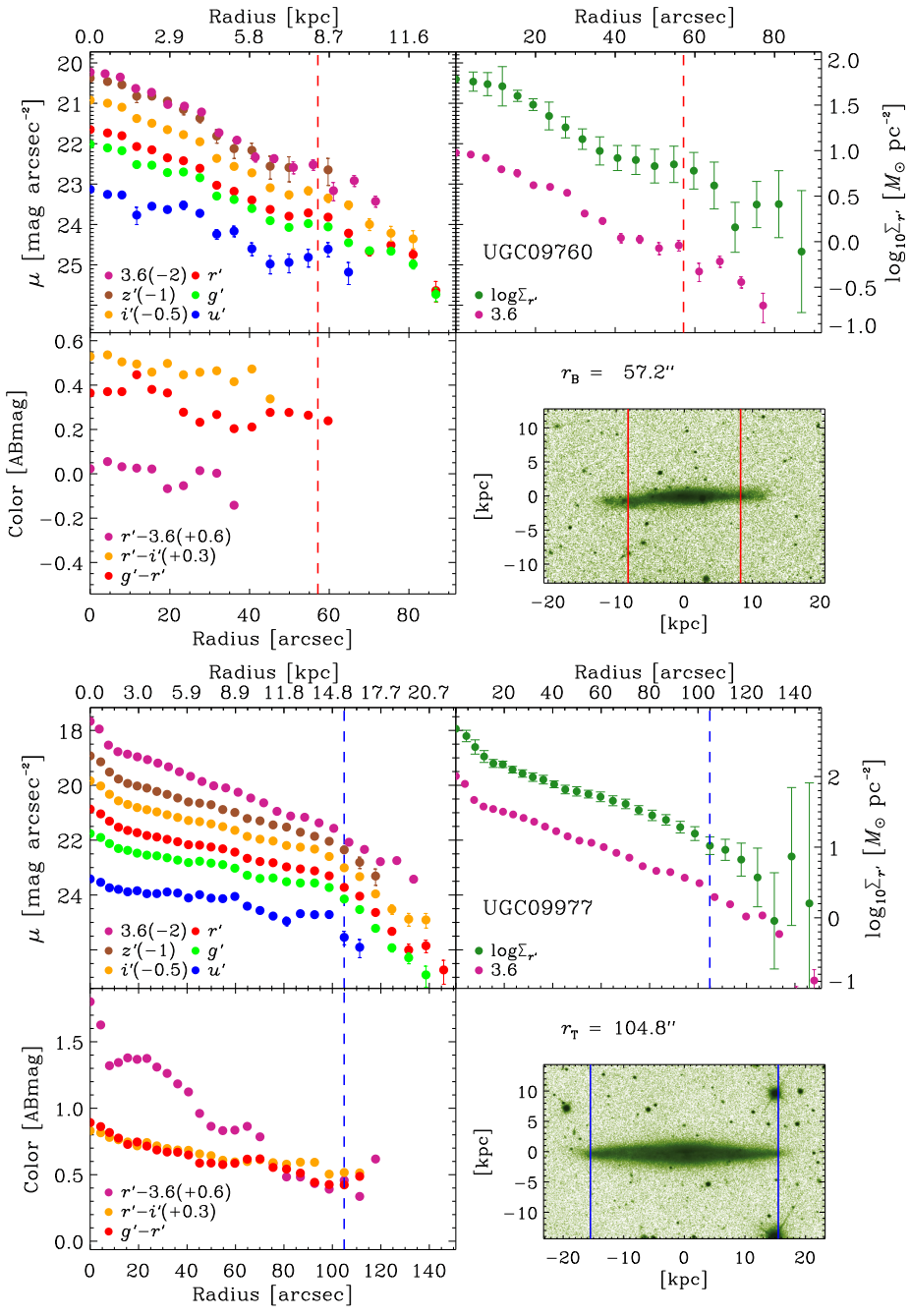
Radius [kpc]
Radius [arcsec]
μ [mag arcsec⁻²]
log₁₀Σ_r' [M⊙ pc⁻²]
UGC09760
3.6(−2) r'
z'(−1) g'
i'(−0.5) u'
logΣ_r'
3.6
Color [ABmag]
r'−3.6(+0.6)
r'−i'(+0.3)
g'−r'
r_B = 57.2''
[kpc]
UGC09977
r_T = 104.8''

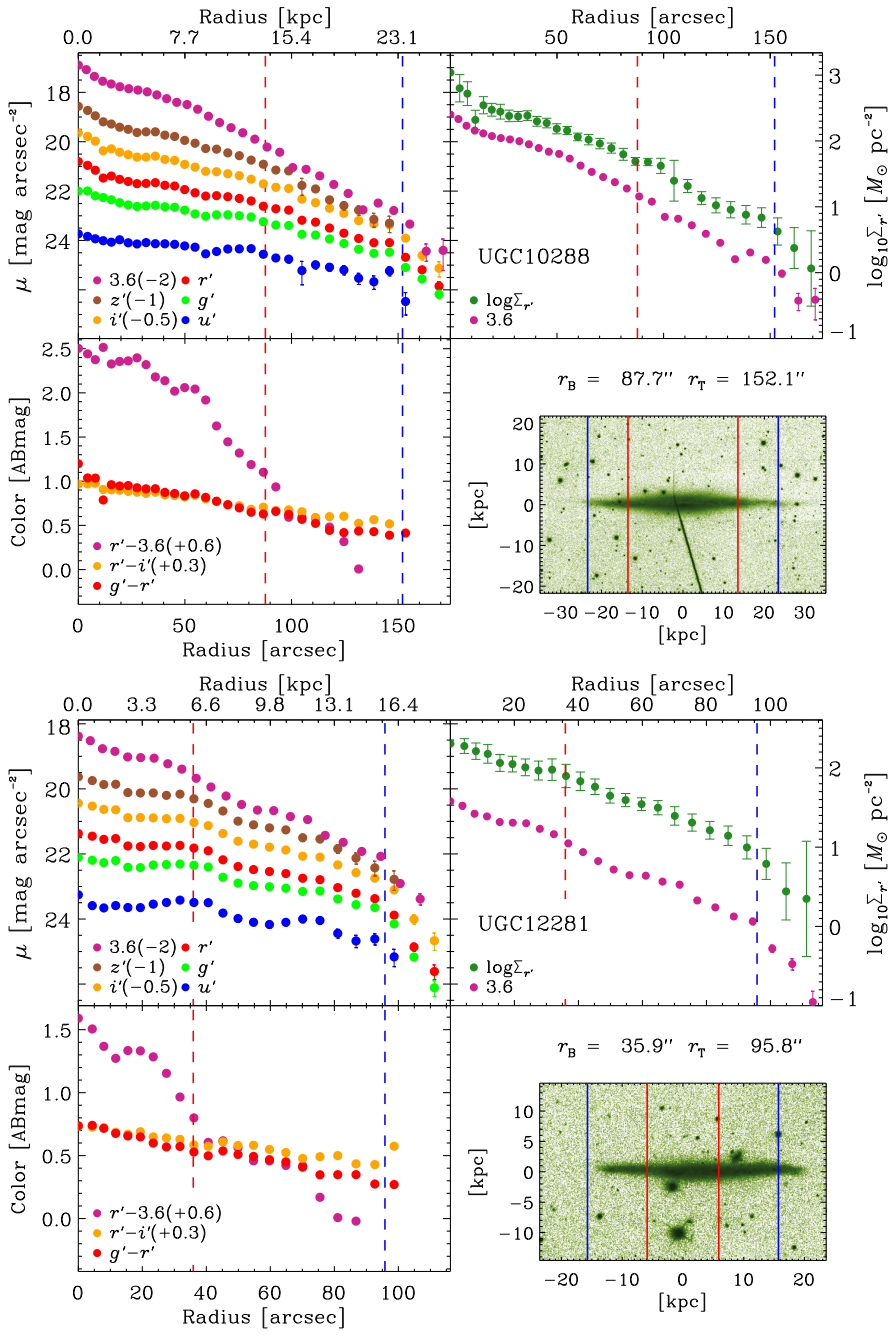
Radius [kpc]
Radius [arcsec]
μ [mag arcsec⁻²]
log10Σr' [M⊙ pc⁻²]
UGC10288
3.6(−2) r'
z'(−1) g'
i'(−0.5) u'
logΣr'
3.6
Color [ABmag]
r'−3.6(+0.6)
r'−i'(+0.3)
g'−r'
rB = 87.7'' rT = 152.1''
[kpc]
UGC12281
rB = 35.9'' rT = 95.8''

# B

# IMF radial profile of NGC 5557 (see Chapter 3)

As part of the same observing campaign with OSIRIS/10.4m GTC, we also acquired deep spectroscopic data for the high-mass ETG NGC 5557. Similar to NGC 4552, this galaxy shows no kinematic peculiarity within its effective radius, with a velocity dispersion profile that declines smoothly from $\sim 300\,\mathrm{kms}^{-1}$ in the centre, to $\sim 200\,\mathrm{km\,s}^{-1}$ at about one effective radius. We reduced the data for NGC 5557 in the same way as for NGC 4552 and NGC 4387. In particular, we extracted spectra in different radial bins, after removing the effect of the rotational velocity and velocity dispersion at each position along the slit. The radial bins were defined adaptively, in order to reach a target $S/N$ ratio $\geq 100$ per Å for each bin.

Unfortunately, due to the recession velocity of the galaxy, the spectrum of NGC 5557 is redshifted to an observed frame where both $TiO_1$ and (to a minor extent) $TiO_2$ are affected by telluric absorption. We evaluated this effect by applying (alternatively) two different telluric absorption models to the observed spectra of NGC 5557, at all radial positions (i.e. each row along the two-dimensional spectrum of the galaxy). The two models were constructed in a similar way as detailed below for NGC 4552 and NGC 4387 (see Sec. C.0.1, where the two models are referred to as $TELL1$ and $TELL2$, respectively). The TiO indices were re-measured on the corrected spectra, re-extracted in each radial aperture. For both telluric models, the correction was found to be relevant for the $TiO_1$ index, with a variation of up to $\sim$0.025 mag in the innermost radial bin (i.e. comparable to the entire dynamical range covered

by this index in panel b of Fig. 4.3). On the contrary, the effect of telluric absorption on the $TiO_2$ was very small, amounting to less than $\sim 0.003$ mag at all radial bins (i.e. about one tenth of the difference between $\Gamma_b = 0.3$ and $\Gamma_b = 3.3$).

For these reasons, we have analyzed the spectra of NGC 5557 with a different approach, by excluding $TiO_1$ from the $\chi^2$ minimization procedure (see Eq. 4.1). The $TiO_2$ index is also mildly contaminated by airglow, affecting only the central part of the feature, from 6224 to 6248 Å. We interpolated this spectral region both in models and observed data, for a consistent analysis. We point out that the effect of the interpolation is completely negligible, amounting to less than $\sim 0.002$ mag on the $TiO_2$ line-strengths, at all radial bins. Since there is a degeneracy between IMF slope and [Ti/Fe] abundance on a single TiO feature, for NGC 5557 we have minimised Eq. 4.1 by neglecting the effect of possible Ti abundance variations. This is motivated by the fact that, for NGC 4552, this residual abundance is found to have a minor effect on $TiO_2$ (see panel c of Fig. 4.3), both NGC 4552 and NGC 5557 showing a similar $TiO_2$ gradient ($\sim 0.025$ mag).

Figs. B.1 and B.2 show the fitting of line-strengths for NGC 5557 and the resulting gradient of IMF slope, respectively. The $\Gamma_b$ radial profile for our reference massive galaxy, NGC 4552 (see Fig. 4.4), is overplotted in Fig. B.2, in order to allow for a direct comparison of the two massive galaxies. As for NGC 4552, the Mg 4780 index of NGC 5557 deviates more than the other indices with respect to the best-fitting solution, although a radial gradient is detected for this feature (see panel c of Fig. B.1). Overall, the $\Gamma_b$ radial profile of NGC 5557 shows a similar behaviour as for NGC 4552, both profiles pointing to a decrease of IMF slope with galactocentric distance. However, one can notice that the $\Gamma_b$ values for NGC 5557 are systematically lower than those for NGC 4552. This might be due to the fact that we have analyzed these two galaxies with different sets of spectral features, or, alternatively, NGC 5557 might have a less bottom-heavy IMF than NGC 4552. For the purpose of the present chapter, the relevant point is that the analysis of NGC 5557 also points to a radial IMF gradient, with the bottom-heavy population confined to the galaxy central regions. We notice that Fig. B.2 suggests that the IMF radial gradient for NGC 5557 might be less significant than that for NGC 4552, mostly because of the relatively large error bars on $\Gamma_b$ in the outermost radial bins. To address this issue, we have fitted the $\Gamma_b$ vs. $R/R_e$ trend for NGC 5557 with a linear relation, adopting an ordinary least-squares fitting procedure with $\Gamma_b$ as dependent variable. We have repeated the fitting 10000 times, shifting each time the $\Gamma_b$ values according to their uncertainties. We estimated the probability, $P$, that $\Gamma_b$ does not decrease with radius, as the fraction of iterations

giving best-fitting lines with non-negative slope values. The $P$ turns out to be less than 1%, also in the case where $\log \mathrm{R/R_e}$, rather than $\mathrm{R/R_e}$, is adopted as independent variable in the fitting. Also, as a further test, we computed a further binned spectrum for NGC 5557, at a radial position of $\mathrm{R/R_e}$=0.7, i.e. the outest galactocentric distance explored for NGC 4552. For this bin, our fitting procedure gives $\Gamma_\mathrm{b} = 1.78 \pm 0.2$ (see red triangle in Fig.A2). Including only galactocentric distance less than 0.7 $\mathrm{R/R_e}$ for NGC 5557, we still find a probability less than 1% that $\Gamma_\mathrm{b}$ profile does not decrease with radius in this system. Notice that, as discussed in Sec. 4.4 for the reference massive galaxy NGC 4552, other ingredients in the stellar population modeling (e.g. individual elemental abundances) might contribute to further flatten the radial $\Gamma_\mathrm{b}$ trend for NGC 5557. However, the existence of a genuine radial IMF gradient for this galaxy is also supported by the NaI 8190 feature, as shown in Sec. C.0.1, as this feature breaks the degeneracy between IMF and other possible effects. Although our data suggest that the IMF gradient for NGC 5557 seems to be shallower than that for NGC 4552, together with analysis of NGC 4552 and NGC 4387, the results for NGC 5557 further support our conclusions that the enhanced fraction of low-mass stars in massive ellipticals is mostly located in their core regions. in their core regions.

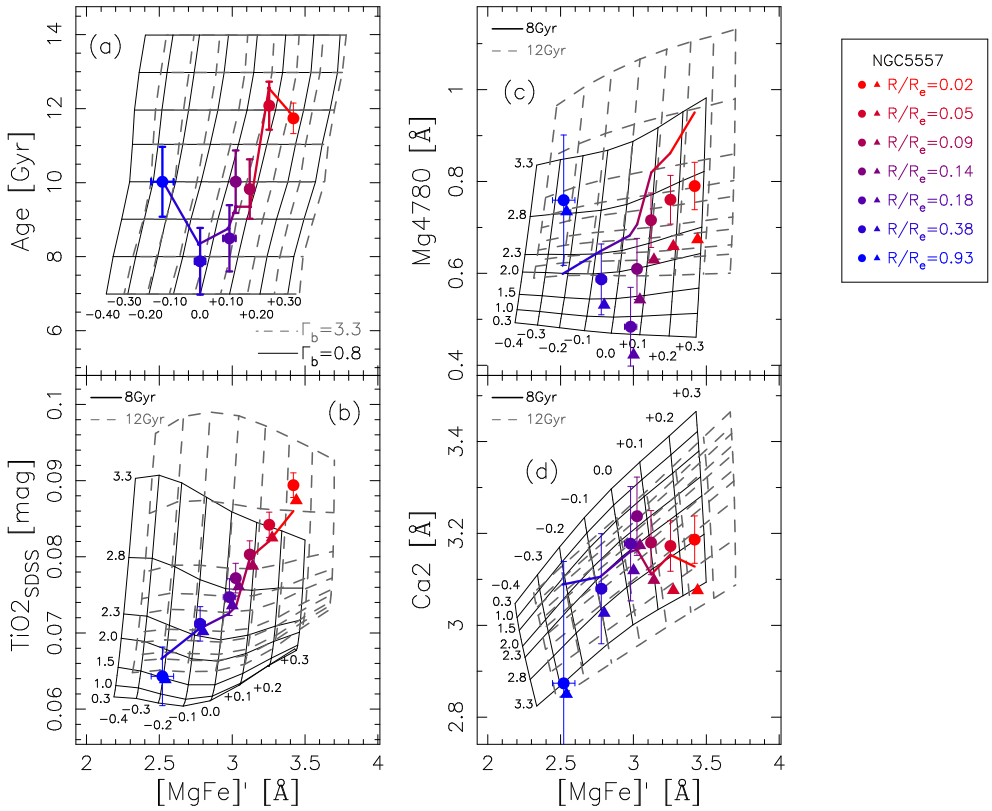


Figure B.1: Fitting of line strengths for the massive ETG NGC 5557. This Figure is similar to Fig. 4.3, but excluding the $TiO_1$ spectral feature, which is not reliable for this galaxy because of strong contamination from telluric absorption. Notice also that the solar-scale correction (difference between triangles and circles in panels b–d) does not include the effect of $\delta$Ti residual abundance, as for NGC 4387 and NGC 4552 in Fig. 4.3.

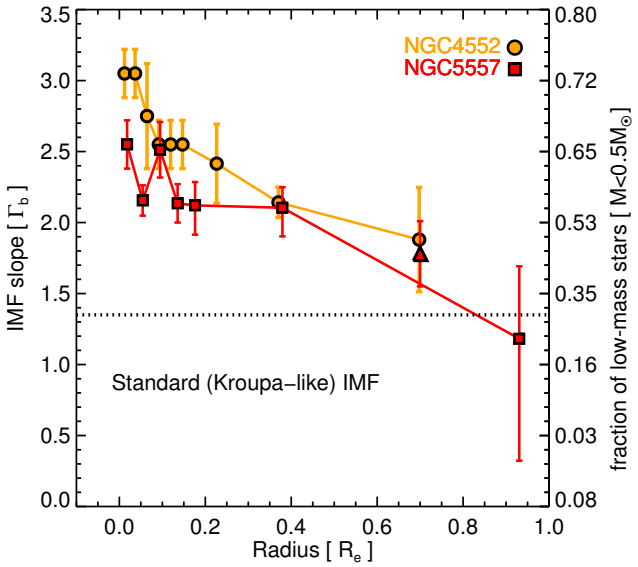


Figure B.2: Radial IMF-slope gradient for the massive galaxy NGC 5557 (orange circles), compared to that for our reference massive ETG, NGC 4552 (red squares). The trend for NGC 4552 is the same as in Fig. 4.3. Error bars denote 1 $\sigma$ uncertainties. Notice that error bars are asymmetric, reflecting the fact that gravity-sensitive features are more sensitive to high, relative to low, values of $\Gamma_b$. Because of the different fitting methodology (see the text), the results for NGC 5557 are only presented in this Appendix. Despite the relatively large error bars, the results for NGC 5557 also indicate a gradient of IMF slope, varying from bottom-heavy in the centre to Kroupa-like outwards (see dotted horizontal line), corroborating the result for our reference massive galaxy, NGC 4552. A radial bin at R = 0.7R$_e$ (red triangle) was calculated to compare directly both NGC 4552 and NGC 5557 IMF gradients at the same radial distance. Although this new bin is not independent from the original profile, it shows that the derived IMF gradient of NGC 5557 is not due to a larger error in the last radial bin.

# C

# Radial behaviour of additional gravity-sensitive features in the OSIRIS long-slit data (see Chapter 3)

### C.0.1 Radial trends of NaI 8190 and NaD

The near-infrared Na I doublet, at $\lambda$ ∼8200 Å, is a prominent feature in the atmospheres of low-mass dwarves, and it has been used, along with the Wing-Ford FeH band ($\lambda$ ∼9900 Å), to derive a significant excess of low-mass stars in the central regions of massive ETGs (van Dokkum & Conroy 2010). Unfortunately, for all the three galaxies observed with GTC-OSIRIS (Sec. 4.1), the NaI 8190 index is significantly contaminated by telluric absorption. No telluric standard is available for the same run as our observations, hampering the study of this line. However, since the *relative* absorption of flux is virtually the same at all radial positions for each galaxy, telluric absorption should not affect the amount of radial variation of the NaI 8190 EW, with only a constant shift in its absolute value. Since this statement is only exactly true in case of no radial rotational velocity, we have tested it directly by constructing two different telluric absorption models. The "synthetic" model (hereafter $TELL1$) is obtained, for each galaxy, as the ratio between a two-SSP model and the observed spectrum in the innermost radial bin. The model is obtained by fitting the spectrum, around the Na feature, with a linear combination of two SSPs, with age and metallicity being free fitting parameters, and IMF fixed to the result of our fiducial $\chi^2$ minimization procedure in the galaxy center (where we obtain con-

sistent results to our previous studies, targeting the central regions of ETGs with a variety of spectral features). The second absorption model (hereafter $TELL2$) relies on the spectrum of a telluric standard star, observed in a different observing run, but with the same instrumental setup as for NGC 4387 and NGC 4552. For each telluric model, we corrected the 2D galaxy spectra at each radial position, and re-extracted 1D spectra for all galacto-centric distance bins, re-measuring the NaI 8190 EWs. The same kind of analysis was performed for the optical Na doublet, $NaD$, at $\lambda \sim 5900$ Å, as well as other IMF-sensitive features (see below). The NaD feature turns out to be affected by telluric absorption, and to major extent, by sky emission. To test also the latter effect, we re-measured both Na features by performing sky subtraction with two different methods, i.e. either interpolating the sky from either sides of the slit, far from the galaxy center (hereafter method $SKY1$), or (method $SKY2$) performing a second iteration where the 2D spectrum of the galaxy (obtained from $SKY1$) is subtracted off from the original 2D frame, and the sky is re-estimated in a region closer to the galaxy center.

Fig. C.1 compares the radial gradients of NaI 8190 (upper panel) and NaD (lower panel), for our reference massive galaxy NGC 4552, among different methods used to treat telluric absorption and sky emission (see black curves with different line types, as labeled in the upper panel). Since the absolute value of the indices was found to be strongly dependent on the reduction procedure, we arbitrarily shifted all values, for a given method and each index, to match model predictions (from our best-fitting solution, see Sec. 4.3.2) in the outermost aperture. Notice that the amount of gradients in both indices is fairly consistent (considering the largest quoted error bars, i.e. for the outermost radial bin), among different methods (even when no telluric correction is applied at all), implying that the gradient of both Na features can be safely estimated. In both panels, different arrows plot the amount of expected variation of each index – when moving from the outermost to the innermost aperture – because of the gradients in different stellar population properties (metallicity, age, [$\alpha$/Fe], and IMF). Summing up all different contributions (orange plus magenta plus red arrows), we predict a radial gradient of $\sim 0.6$ Å and $\sim 3.4$ Å for NaI 8190 and NaD, respectively. From the black curves, we see that the observed gradients are $\sim$ 0.7–0.85 Å for NaI 8190 ($\pm$0.1 Å, considering the error bar in the outermost bin, and that on proxy correction) and $\sim$ 3.3–3.5 Å ($\pm$0.12) for NaD. Hence, within the uncertainties, an IMF radial variation reconciles both Na features (once the effect of other parameters, in particular that of metallicity, is taken into account). The effect of varying the temperature of giant stars, $T_{eff}$, in the stellar population models is also illustrated, with green arrows, in

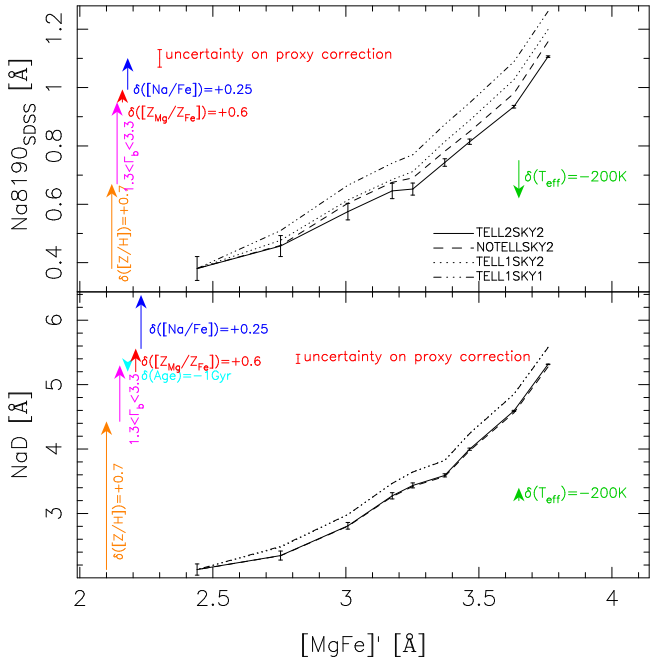


Figure C.1: The NaI 8190 (top panel) and NaD (bottom panel) index radial profiles of NGC 4552 are plotted as a function of the total metallicity indicator [MgFe]′. Black curves with different line types (see the black legend in the upper panel) correspond to different methods to treat telluric absorption, i.e. methods $TELL1$ and $TELL2$ (see the text) and no telluric correction ($NOTELL$), as well as different sky subtraction procedures (methods $SKY1$ and $SKY2$, see the text). Black error bars are the maximum uncertainties (among different methods), quoted at the 1 $\sigma$ level. In both panels, arrows show the expected variation of the indices (for SSP models) because of the metallicity (orange), IMF (magenta), age (cyan), and $[Z_{Mg}/Z_{Fe}]$ (red) gradients for NGC 4552 (Sec. 4.3.2). Notice that the effect of varying age is not shown for NaI 8190, as it is completely negligible for this index. The effect of varying [Na/Fe] abundance and $T_{eff}$ are also shown as blue and green arrows, respectively.

Fig. C.1. Decreasing $T_{eff}$ tends to decrease the model NaI 8190, i.e. it goes into an opposite direction to that of a more bottom-heavy IMF. On the other hand, NaD is insensitive to temperature variations, while TiO bands (panels b-c of Fig. 4.3) increase with decreasing $T_{eff}$. Therefore, while the effect of a radially varying IMF is consistent among all features (including the Na ones), a radial variation in the temperature is clearly ruled out when combining optical and NIR features. A similar argument applies to [Na/Fe] abundance (see blue arrows in the Figure, showing the effect of increasing [Na/Fe] by 0.25 dex, as estimated from Conroy & van Dokkum (2012b) stellar population models). To

mimic the effect of varying $\Gamma_b$ from 1.3 to 3.3 (consistent with our estimated gradient for NGC 4552, see Fig. 4.5), a change of $\sim$0.25 dex in [Na/Fe] would be required for NaD. However, this is far too small (by a factor of two) than that of a varying IMF on NaI 8190 (see magenta and blue arrows in the upper panel of Fig. C.1). Hence, an [Na/Fe] gradient is not able to explain the observed gradients of both Na features (see, e.g., Spiniello et al. 2015), Finally, it is worth noting that alternative explanations for the "unusual" strength of Na indices have also been proposed in the literature (Jeong et al. 2013).

As for NGC 4552, also for our reference low-mass galaxy, NGC 4387, we have found that the observed NaI 8190 gradients change very mildly, by $\widetilde{<}$0.1 Å, among different reduction procedures, meaning that the NaI 8190 gradients can be robustly estimated from our data. Fig. C.2 compares the radial gradients of NaI 8190 (whose EWs are estimated through methods $TELL2$ and $SKY2$, see above) for the low- and high-mass galaxy. A constant shift is arbitrarily applied for each galaxy, to match the IMF slope derived from our fiducial set of spectral indices (see Sec. 4.2.3) in the outermost radial bins. The Figure also plots the NaI 8190 gradient for the additional massive system, NGC 5557, observed as part of the same observational campaign as NGC 4387 and NGC 4552, but analyzed apart in Appendix B. Remarkably, for the low-mass ETG, no radial gradient in NaI8190 is detected, while a strong decrease is observed with galactocentric distance for the high-mass galaxies. As shown in Fig. C.2, the metallicity gradient of NGC 4552 cannot explain, by itself, the NaI 8190 gradient (as also seen by comparing the size of the orange arrow, to the range of values for the black curves, in the upper panel of Fig. C.1). Moreover, the NaI 8190 index is expected to decrease with [$\alpha$/Fe] (according to CvD12 stellar population models), whereas NGC 4552, as well as NGC 5557, *both* have high [$\alpha$/Fe] in the centre, and a very high NaI 8190 line-strength. In conclusion, the radial gradients of Na features, for high-mass galaxies, also point to a significant radial variation of the stellar IMF, with an excess of low-mass stars confined to their central regions.

### C.0.2 Radial trends of CaH1 and CaH2

We discuss here the radial behaviour of the two IMF-sensitive indices, CaH1 and CaH2, recently proposed by Spiniello et al. (2014). Both features (in particular CaH2) are affected by telluric absorption in the spectra of our reference high mass galaxy, NGC 4552. However, as done for Na features, we compare the radial gradients of both features among different reduction procedures, in order to gain further insights into the radial variation of stellar population properties for our reference massive galaxy. Fig. C.3 is similar to Fig. C.1,

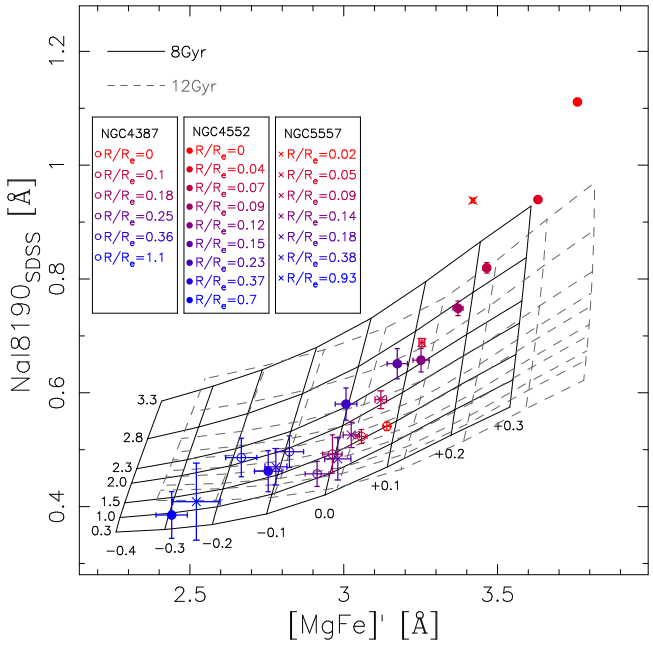


Figure C.2: The NaI 8190$_{\rm SDSS}$ line-strength is plotted as a function of the total metallicity indicator [MgFe]′, for NGC 4387 (empty circles), NGC 4552 (filled circles), and NGC 5557 (crosses; see Appendix B). Error bars are 1 $\sigma$ statistical uncertainties. Black and grey grids correspond to MILES SSP models with an age of 8 and 12 Gyr (i.e. the same as in Fig. 4.3), respectively. Notice that the NaI 8190 EWs are estimated with method $TELL2SKY2$, i.e. the same as for the black solid curve in Fig. C.1. The strong gradients of NaI 8190$_{\rm SDSS}$ for the high-mass galaxies contrast with the flat behaviour of this feature for the low-mass system, NGC 4387. A constant offset has been applied to the line-strengths of each galaxy, to account for the uncertainty on the absolute value of the indices, due to telluric absorption.

but plotting CaH2 (top) and CaH1 (bottom), rather than Na features, as a function of [MgFe]′ (both CaH features have been arbitrarely shifted in the Figure). As seen by the size of the cyan arrows, both indices are insensitive to age, consistent with Spiniello et al.(2014a, 2014b). CaH2 is also insensitive to total metallicity, while CaH1 shows a mild trend to decrease with increasing [Z/H]. Notice that according to our empirical approach, both indices (in particular CaH2) tend to *decrease* significantly with [Z$_{\rm Mg}$/Z$_{\rm Fe}$] (i.e. $[\alpha/Fe]$; see red arrows), at fixed total metallicity. As seen by summing up the orange, magenta, and red arrows in the upper panel of Fig. C.3, the radial behaviour of CaH2 is fully consistent with our results, i.e. a radial decrease of IMF slope in NGC 4552. For CaH1, the situation is more uncertain, as this index turns out

to be also significantly affected by airglow (see dot-dashed curve), and thus its radial gradient is either null or negative (i.e. decreasing outwards in the galaxy, leftwards in Fig. C.3), depending on the reduction procedure. We notice that, for a fixed IMF slope, the CaH1 gradient in NGC 4552 should be positive, as both metallicity and $[Z_{Mg}/Z_{Fe}]$ increase towards the galaxy center, CaH1 decreasing with both paramaters. Hence, regardless of the reduction procedure, our results for CaH1 also imply a radial decrease of IMF slope with radius in our reference massive galaxy. We notice that the radial gradient of CaH2 might also be explained by decreasing $T_{eff}$ in the models by $\sim 300$ K. However, this would be inconsistent, at fixed IMF, with the radial trend of CaH1, as the latter is insensitive to $T_{eff}$. In conclusion, also CaH features imply an IMF gradient for NGC 4552, ruling out a radial variation of $T_{eff}$.

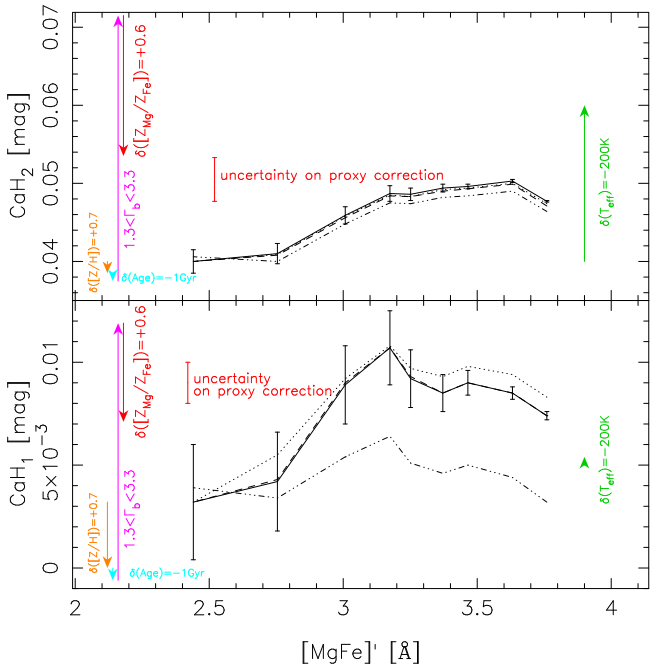


Figure C.3: CaH1 (bottom) and CaH2 (top) radial gradients for NGC 4552, i.e. the same as Fig. C.1 but for CaH, rather than Na, features. The telluric contamination of these indices does not allow us to trust the index absolute values. However, the radial gradient for CaH2 is robust, while for CaH1 we can exclude an increase of the index with radius (leftwards in the plot), as it would be the case for a constant IMF (see the text). Notice that CaH2 is fully consistent with our results of a varying IMF for NGC 4552. In general, because of the different sensitivity of the two indices to a variation in $T_{\rm eff}$ (green arrows), one cannot explain the behaviour of both CaH features without a varying IMF with radius.

### C.0.3 Radial trend of aTiO

Finally, we discuss the radial behaviour of the aTiO IMF-sensitive feature ($\lambda \sim 5500$ Å), also proposed by Spiniello et al. (2014). Being present in the atmospheres of both dwarf and giant stars, the aTiO is a potentially good IMF indicator. In our data, a strong sky emission line ($\lambda \sim 5780$ Å) lays within the central bandpass of the index. To overcome this problem, we have linearly interpolated both data and models over the affected region. The radial profile of aTiO for NGC 4552 is shown in Fig. C.4. In this case, since the feature is not affected by telluric absorption, we do not apply any shift to the line strenths. Also, since there is no difference among different reductions, only one black curve is shown in the Figure. Unfortunately, because of the large error bars, the aTiO has little constraining power on the radial variation of the IMF for NGC 4552, and thus we have not included it in our $\chi^2$ minimization procedure.

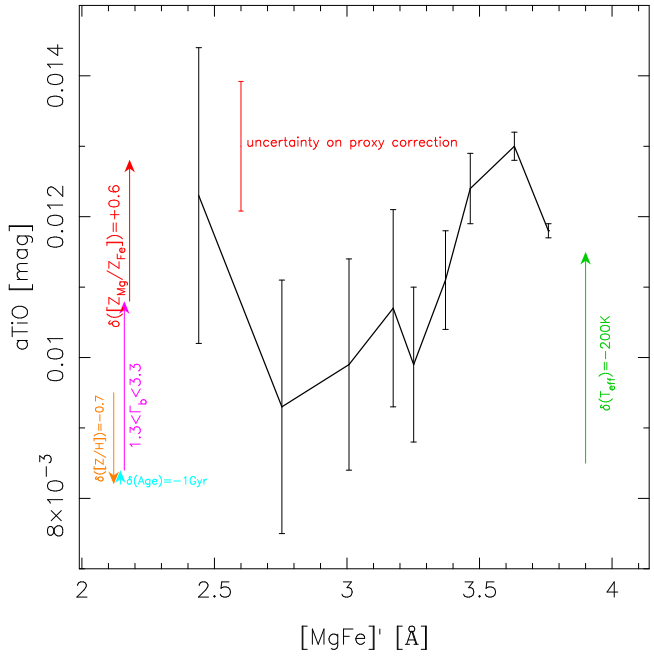


Figure C.4: Radial profile of the interpolated aTiO index for NGC 4552 (see the text). Notice the large error bars, in the outer radial bins (left in the plot) preventing us to use this index to significantly constrain the IMF gradient. Notice that because the index is not affected by telluric absorption, while airglow contamination is avoided by our interpolation procedure, no difference exists among different reduction procedures and we did not apply any rigid shift to the line strengths (as, e.g., in Figs. C.1 and C.3).

# D

# Correlated uncertainties on IMF and other parameters in the OSIRIS long-slit data (see Chapter 3)

In Fig. D.1, we show the PDF contours of our best-fitting solution for the second innermost and outermost radial bins of NGC 4552, in the $\Gamma_b$–*Age* (left) and $\Gamma_b$–$\delta$Ti (right) diagrams. Different line types show the impact of a number of effects, i.e. changing the modelling and fitting approach, as well as flux calibration issues (see details in §4.4), on our results. Notice that in all cases, a clear IMF radial gradient for NGC 4552 is detected. The left panel shows that there is very little correlation of best-fitting *Age* and $\Gamma_b$ values, i.e. our approach is able to break the *Age* vs. IMF slope degeneracy affecting spectral fitting at optical wavelengths alone. As seen from the black contours in the $\Gamma_b$–$\delta$Ti diagram (corresponding to the outermost radial bin of NGC 4552), the errors on $\Gamma_b$ and $\delta$Ti are significantly correlated, but the direction of this correlation is almost orthogonal to the radial variation of best-fitting $\Gamma_b$ and $\delta$Ti values. This ultimately results from the fact that the response of both $TiO_1$ and $TiO_2$ molecular features to [Ti/Fe] is comparable (Johansson et al. 2012) (i.e. $C_{TiO1} \sim C_{TiO2}$ in Eq. 4.1), while the observed radial gradient of $TiO_2$ in NGC 4552 is about twice that of $TiO_1$. It is worth noticing the strong dependence of $\delta$Ti on flux calibration, as shown by the red and black contours associated to the squares in the right panel. These contours are obtained after applying an artificial shift to TiO1 and TiO2, mimicking a possible uncertainty on flux calibration (see §4.4). This test shows that the absolute value of $\delta$Ti is

not trustable, but it might be significantly affected by the reduction procedure. On the other hand, the $\delta$Ti gradient is much more robust ($\Delta\delta\mathrm{Ti} \sim 0.4$ dex, for all different tests), and might be tracing a true radial variation of [Ti/Fe].

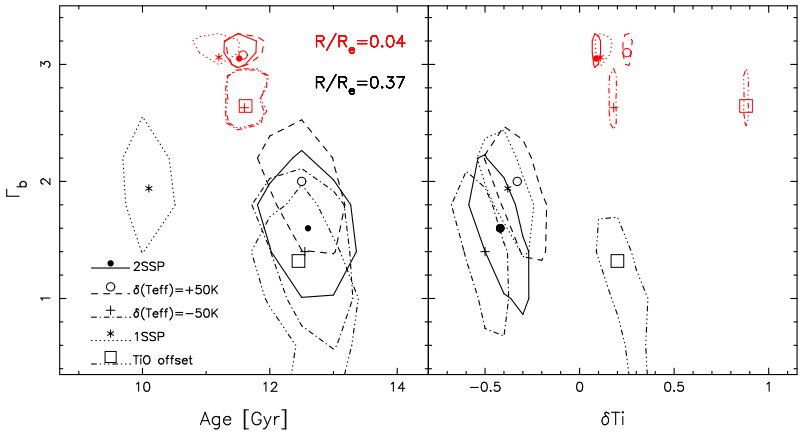


Figure D.1: Probability density contours of IMF slope vs. Age (left) and IMF slope vs. $\delta$Ti residual correction (right) for the second innermost (red) and outermost (black) radial bins of NGC 4552. The contours correspond to $1\sigma$ confidence levels. Different line-styles are the results of different tests, varying the modelling/fitting approach. The contours in the left panel show a mild correlated variation, illustrating how our method breaks the *Age*–IMF slope degeneracy. The right panel shows a correlated variation of IMF slope and $\delta$Ti. However, this trend is almost orthogonal to the radial IMF-slope gradient, proving that [Ti/Fe] cannot be responsible for the observed TiO gradients.